A study on a multi-physics design method for fluid MEMS using induced-charge electrokinetic phenomena

Hideyuki Sugioka

Contents

Abstract

Fluid micro-electro-mechanical systems (MEMS) using induced-charge electro-kinetic (ICEK) phenomena are important for promising biomedical applications such as a lab-on-a-chip (LOC) and micro-total-analysis systems (μTAS). This is because ICEK phenomena produce a large flow velocity ($\sim$mm/s) with a small voltage ($\sim$V) with simple structures and can prevent the occurrence of dc problems such as chemical reactions in an electrolytic solution. However, the designs of fluid MEMS using ICEK phenomena are difficult and challenging because we basically lack the complete knowledge of ICEK phenomena themselves. That is, to obtain the design method, we simultaneously need to clarify fundamental physics of ICEK phenomena by analyzing complex multi-physics problems coupled with fluid dynamics, electrostatics, and ion dynamics in the bounded domain. Moreover, to show the usefulness of our ICEK device designs, we also need to overcome a hydrodynamic resistance problem and a low Reynolds number problem in a micro-channel. In this thesis, from the unified view point of fundamental physics, we focus on a multi-physics design method for fluid MEMS using ICEK phenomena, and simultaneously demonstrate its usefulness by showing four kinds of design examples; i.e., a stacking pump, a rotary valve, a chaotic mixer, and a micro-column device. In particular, to consider a realistic bounded domain, we develop a multi-physics design method based on the boundary element method along with the thin electric double layer approximation. Further, to examine the validity of our design methods, we experimentally prove two key predictions obtained through our designs. By using the multi-physics design methods and microfluidic device designs, we believe that we can dramatically improve the size and performance of promising microfluidic systems in the future.

Chapter 1

Introduction

1.1 State of the art

1.1.1 Induced-charge electro-kinetic phenomena

In an ionic solution, metal is polarized and the polarized charge is screened by surrounding ions. Since an applied electric field $\boldsymbol{E}$ acts on its own induced diffuse charge, the representative slip velocity U_c on the metal surface is proportional to $\boldsymbol{E}^2$. This nonlinear phenomenon was termed induced-charge electro-kinetic (ICEK) phenomena by Bazant and Squires [5, 83, 84, 4, 82], and served a unified view point to understanding the wide range of problems of electrokinetics. It should be noted that ICEK phenomena include induced-charge electro-osmosis (ICEO) and induced-charge electrophoresis (ICEP) since they are intrinsically the same physical phenomena that are observed from different viewpoints.

Although it was not known largely in the West until recently, the pioneering work by Gamayunov et al. [29] first predicted quadrupolar flow due to ICEO around a polarizable sphere in a uniform electric field in 1986, and Murtsovkin et al. [55] observed the phenomenon using mercury drops in 1991. However, many crucial aspects remain unexplained from the beginning; for example, Gamayunov et al. [29] reported that the vortex flow around metal was sometimes in the opposite direction to the theory, although the flow reversal was conjectured to be due to Faradaic reactions [29, 4]. Further similar flows have also been studied on polarizable colloids [54], including the effect of such flows on dielectrophoresis [79]. In particular, Dukhin [24] reported that the surface condition in highly charged-colloids leads to other "non-equilibrium electrosurface phenomena" (NESP), and Mishchuk and Takhistov [53] reported that at very large voltage bulk space charge may also drive a "second-kind electrokinetic phenomena". However, these "large voltage problems" are still an unclear and challenging problem.

1.1.2 Diffused ion dynamics

To understand the flow reversal and large voltage problems, we need to explore diffusion ion dynamics based on the Poisson-Nernst-Plank (PNP) equations, since diffuse-charge dynamics plays an important role in the response of electrochemical and biological systems subject to time-dependent voltages or electric fields [6, 20, 44, 45, 90, 81]. In particular, Bazant et al. [6] showed a dc response of the diffuse-charge between electrodes by the one-dimensional (1D) PNP analysis in 2004, and afterwards Chu and Bazant [20] performed the two-dimensional (2D) PNP analysis. In addition, Kilic et al. demonstrated the steric effects of ions based on the PNP equations [44, 45], and explained the flow reversal at high frequencies [90]. Furthermore, Soestbergen et al. [81] demonstrated an ac response of the diffused-charge. Moreover, Zhao and Bau [104] showed the effect of ICEO flows on the movable particle near a wall by solving the PNP equations. However, the flow reversal at low frequencies ($<\sim$100 Hz) has not been explained clearly, and should be clarified to establish a fundamental understanding of ICEO phenomena.

1.1.3 AC electro-osmotic pump

Recently, pumps that use ac electro-osmotic flow (ACEO), which is intrinsically an ICEO flow that is generated not around conductive particles but near the surface of planar electrodes and driven using ac electric fields, were proposed in the context of microfluidics and have attracted considerable attention [97, 16, 66, 1, 57], because they have a large flow velocity ($\sim$mm/s) with a small voltage ($\sim$V) and can prevent the occurrence of dc problems such as chemical reactions in an electrolytic solution. In particular, Ramos et al. [67] first observed and modeled ACEO flows over a pair of micro-electrodes in 1999. Soon afterward, Ajdari [1] predicted ACEO pumping by asymmetric electrode arrays, which was demonstrated using planar electrodes of unequal widths and gaps [15, 66, 57]. In 2004, as related work, Lastockin et al. proposed a microfluidic pump and mixer designs based on ac Faradaic polarization [49].

In 2006, Bazant and Ben [7] predicted that the flow rates of ACEO pumps that have a three-dimensional (3D) stepped electrode are almost 20 times faster than the conventional planer ACEO pump, and Urbanski et al. [97] demonstrated dramatic improvements in flow rate by the 3D ACEO pump. Furthermore, Huang et al. [39] experimentally showed the high-pressure (1.3 kPa) of the 3D ACEO pumps using a long serpentine microchannel. Thus, ACEO and ICEO pumps that can be operated with small voltage with high speed are promising, since electroosmotic micropumps are emerging as a viable option for a number of applications such as micro-total-analysis systems (μTAS) as reviewed in Ref. [69]. However, since the density of the generation of the pumping pressure is lower than a porous electro-osmotic (EO) pump [102], the improvement of the pumping efficiency on the power density is still required.

1.2 Motivation

1.2.1 Fluid MEMS using ICEK phenomena

Micro-electro-mechanical systems (MEMS) are technologies produced naturally from the progress of integral circuit (IC) in the prosperous semiconductor industry, and they continue to provide innovative products such as the ink jet head for our printers, the inertia sensor for our cars, and the digital mirrors in digital light projectors. Although these technologies are matured to the commercial level, there is still plenty of room in this field. That is, as Richard Feynman predicted in 1959 [27], this field even now continues to tell us much of great interest about the strange phenomena that occur in complex situations in the miniaturized world, and a lot of new things that would happen that represent completely new opportunities for design.

In particular, fluid MEMS such as a lab-on-a-chip (LOC) and micro-total-analysis systems (μTAS) are promising, since they control not only flows of electrons in an electric circuit but also flows of substances in an fluidic circuit (channel); e.g., in a LOC, plural substances are moved into some chambers by micro-pumps through microfluidic channels, mixed with each other, and often reacted to obtain some valuable substances. Similarly, in (μTAS), small amount of substances such as blood are often flowed in microfluidic channels and analyzed by using various separation technique and high-sensitive small sensors. Of course, fluidic valves also important in those systems to stop and flow liquids in the micro-fluidic channels; it is something like a latched circuit or a transistor switch in the electric IC. Namely, micro-pump, -valves, -mixers are essential to control fluids and particles dynamically, and indispensable to perform innovative tasks in promising fluid MEMS.

In particular, fluid MEMS using ICEK phenomena are important for promising biomedical applications such as a LOC and μTAS. This is because ICEK phenomena produce a large flow velocity ($\sim$mm/s) with a small voltage ($\sim$V) with simple structures and can prevent the occurrence of dc problems such as chemical reactions in an electrolytic solution.

1.2.2 Challenging problems

However, the designs fluid MEMS using ICEK phenomena are difficult and challenging because we basically lack the complete knowledge of ICEK phenomena themselves; i.e., to obtain the design method, we simultaneously need to clarify fundamental physics of ICEK phenomena by analyzing complex multi-physics problems coupled with fluid dynamics, electrostatics, and ion dynamics in the bounded domain. Moreover, to show the usefulness of our ICEK device designs, we also need to overcome a hydrodynamic resistance problem and a low Reynolds number problem in a micro-channel.

Fortunately, ICEK concept implies the unified viewpoint that ICEK phenomena should

be calculated as the complex but classical physical response for the externally applied electric fields; i.e., the response of the system consisting of conductors and electric solutions are uniquely calculated from the physical conditions including boundary conditions. Namely, the zeta potential and electro-osmotic slip velocities around the conductors are uniquely calculated from the physical conditions including boundary conditions. That is, ICEK concept itself includes a clue to obtain the unified-multi-physics design method for fluid MEMS using ICEK phenomena.

In fact, analytical solutions in an unbounded domain can be obtained based on this fundamental ICEK concept, although to consider boundary conditions is essential to design real devices. It should be noted that this unified viewpoint is very different from that of classical linear electro-kinetics. Namely, in the classical electro-kinetics, the zeta potential is always obtained through experiments as the physical property of the material and thus we cannot predict anything without experiments. Thus, a study of a design method for fluid MEMS is interesting and challenging since there is a possibility that we can predict everything from the beginning based on the fundamental theory, although we need to overcome complexity of multi-physics problems and unknown physical problems.

1.2.3 Objective of this thesis

In this thesis, from the unified view point of fundamental physics, we focus on a multi-physics design method for fluid MEMS using ICEK phenomena. That is, to consider a bounded domain concerning real device designs, we mainly develop three kinds of design methods based on the boundary element method (BEM) along with the thin electric double-layer approximation; i.e., we develop following three methods;

Method 1: This method is a basic design method based on the BEM along with the analytical solutions of electro-kinetic slip velocities around elliptical conductive cylinders, and has a merit that it can consider the fluidic boundary conditions for the realistic fluid devices using ICEK phenomena. We believe that a series of proposals by Bazant and Squires [5] for micro-fluidic devices can be examined theoretically by this method as a first step. (See Chapter 2);

Method 2: This method is an advanced design method that uses a complete multi-physics calculation technique for both fluidic and electrostatic problems based on the BEM, and has a merit that it can consider the both fluidic and electrostatic boundaries completely. We believe that this method provides a complete design method for ICEK devices if we can neglect ion currents. (See Chapter 4);

Method 3: This method is another advanced design method to explore fundamental problems such as a reverse flow problem and a large voltage problem (mentioned in Sec. 1.1). In this method, we consider one-dimensional (1D) Poisson-Nernst-Planck equations to consider ion currents along with the two-dimensional (2D) analysis based on Method 2. (See also Chapter 4).

Further, to demonstrate their usefulness, we propose four kinds of innovative ICEK

devices, and examine their device performances theoretically. That is, by using the three methods, we propose a stacking pump, a rotary valve, a chaotic mixer, and a micro-column device, and clarify their design method. Furthermore, to examine the validity of our design methods based on the unified view point of ICEK phenomena, we experimentally prove two key predictions obtained through our designs. That is, by comparing theoretical predictions with experimental results, we prove that
(1) asymmetrical stacking structures produce asymmetrical vortex flows, and
(2) an elliptical conductor rotates even near the electrodes through ICEK flows.
Note that (1) and (2) are also key issues to realize an ICEK stacking pump and an ICEK rotary valve, respectively.

By using these multi-physics design methods and microfluidic device designs, we believe that we can dramatically improve the size and performance of promising microfluidic systems in the future.

1.3 Organization of this thesis

This thesis is presented in ten chapters. In Chapter 2, we describe basic theory based on the boundary element method. In Chapters 3 to 8, we propose a stacking pump, a rotary valve, a chaotic mixer, and a micro-column device and examine them theoretically, based on the basic and improved theories. In particular, in Chapters 4 and 6, we prove key predictions for the stacking pump and rotary valve, respectively. Following discussions in Chapter 9, our conclusions are summarized in Chapter 10.

Specifically, in Chapter 2, to analyze an ICEP flow in a microfluidic channel, we develop a calculation technique to model induced-charge electrophoresis using the boundary element method (BEM), and examine its validity. Using this method, we simulate a polarizable elliptical particle in a microfluidic channel in the presence of an electric field parallel to the flow channel, and find that a polarizable particle feels a strong repulsion force from the wall due to ICEP. Further, we find that two particles aligned in the direction of the electric field attract each other, while they repel each other when they are aligned perpendicular to the electric field. We believe that the presented method can largely contribute to develop a design tool for ICEP devices as a basic calculation method.

In Chapter 3, we propose ICEO pumps that remove reverse flows using asymmetrically stacked elliptical metal posts and numerically examine the pumping performance [92]. By the boundary element method along with double layer approximation (Method 1), we find that the asymmetrical stacking configuration efficiently suppresses the unwanted reverse flow and yields velocities of the order of a few millimeters per second, and this configuration is compatible with that of an optimized half-coating pump. Further, we propose a simple model for the stacking pump and predict that the velocity of such a stacking pump with a thin limit is larger than 67% of that of a circular cylindrical half-coating pump of the same length. Using this stacking pump, we can expect to significantly

improve the pumping performance.

In Chapter 4, following theoretical predictions in Chapter 3, we report experimental observations of asymmetrical reverse vortex flows around stacking structures of carbon posts with a large height ($\sim$110 μm) in water, prepared by the pyrolysis of a photoresist film in a reducing gas. Further, by the use of a coupled calculation method that considers boundary effects precisely (Method 2), the experimental results, except for the problem of anomalous flow reversal, are successfully explained. i.e., unlike previous predictions, the precise calculations here show that stacking structures accelerate a reverse flow rather than suppressing it for a microfluidic channel, because of the deformation of electric fields near the stacking portions; these structures can also generate a large net flow theoretically in the direction opposite to that of a previous prediction for a standard vortex flow. Furthermore, by solving the one-dimensional Poisson-Nernst-Plank (PNP) equations in the presence of ac electric fields (Method 3), we find that the anomalous flow reversal occurs by the phase retardation between the induced diffuse charge and the tangential electric field. In addition, we successfully explained the nonlinearity of the flow velocity on the applied voltage by the PNP analysis.

In Chapter 5, we consider using induced-charge electrophoresis (ICEP) to move actuators. We propose rotary microvalves in water using hydrodynamic force due to ICEP and numerically examine the performance of valves [95]. By the multi-physics coupled simulation technique between fluidics and electro-statics based on the boundary element method along with the thin double layer approximation (Method 2), we find that rotary valves using ICEP function effectively at high frequency. In the calculations, the electric and flow field problems in a bounded domain are solved, and the proper boundary conditions are discussed. By employing similar actuators using ICEP, we can dramatically improve the performance of promising microfluidic systems such as lab-on-a-chip.

In Chapter 6, by using an elliptical conductive carbon element fabricated by the pyrolysis of a photoresist film coated with gold, we experimentally demonstrate that microvalves can rotate near conductive electrodes. Namely, by numerically analyzing video data, we show the time evolution of the rotation angle, the flow field, and the center position of the microvalve. Further, we compare them with the theoretical results, and find that they are in good agreement qualitatively. In the future, by using ICEP valves as a latch device, we can significantly improve the size and processing speed of a fluidic integrated circuit.

In Chapter 7, we present an idea to generate mixing by "chaotic advection" in microscale geometries [36, 105]. That is, we consider using induced-charge electro-osmosis to generate a second flow and then modulate between the pressure-driven and induced-charge flows. By using the combined method consisting of the boundary element method (Method 2), the Lagrangian particle tracking method, and the random walk method, we analyze mixing efficiency, mixing time, and mixing length, with the effects of modulation frequency and molecular diffusivity, and compare our proposed mixer with other mixers. By this analysis, we find that chaotic mixing can be produced efficiently in a microfluidic channel by switching between pressure-driven and induced-charge flows in a wide range

of Peclet number under the specific condition of Strouhal number. By using our proposed mixer, we can expect to realize efficient chaotic mixing with minimum voltage in an ordinary flow channel with a simple structure without an oblique electric field even at large Peclet number.

In Chapter 8, a direct simulation of a dispersed system of metallic particles in water is performed to show that a microcolumn between electrodes is formed by the application of an ac electric field [93]. By the multi-physics coupled simulation technique between fluidics and electrostatics based on the boundary element method along with the double layer approximation (Method 2), we find that microcolumns are formed by the growth of clusters perpendicular to the electrodes under the condition that the number density of particles is larger than the percolation threshold. Further, we propose a simple model that efficiently explains the time dependence of the probability of the formation of a microcolumn by considering standard collision theory and percolation theory. By this analysis, we can greatly contribute to developments in studies on the self-organization of microcolumns and biosensors.

Then, following discussions in Chapter 9, our conclusions are summarized in Chapter 10.

Chapter 2

Basic Theory: Basic analysis of induced-charge electrophoresis using the boundary element method

Active control of fluids and particles by using induced-charge electrophoresis (ICEP) is important and promising. To analyze an ICEP flow in a microfluidic channel, we develop a calculation technique to model induced-charge electrophoresis using the boundary element method (BEM), and examine its validity. Using this method, we simulate a polarizable elliptical particle in a microfluidic channel in the presence of an electric field parallel to the flow channel, and find that a polarizable particle feels a strong repulsion force from the wall due to ICEP. Further, we find that two particles aligned in the direction of the electric field attract each other, while they repel each other when they are aligned perpendicular to the electric field. As a basic calculation method, the presented method can largely contribute to develop a design tool for ICEP devices.

2.1 Introduction

Active control of fluids and particles by using induced-charge electroosmosis (ICEO) and induced-charge electrophoresis (ICEP) is important and promising [5, 83, 84, 66, 1, 4, 82], because they have a large flow velocity (∼mm/s) with a small voltage (∼V) with simple structures and can prevent the occurrence of dc problems such as chemical reactions in an electrolytic solution [97]. ICEO and ICEP are different from classical electroosmosis and electrophoresis because they result from the interaction between the electric field and ions in the electric double layer formed by the polarizing effect of the electric field itself.

Recently, there has been increasing interest in using polarizable elliptical particles or

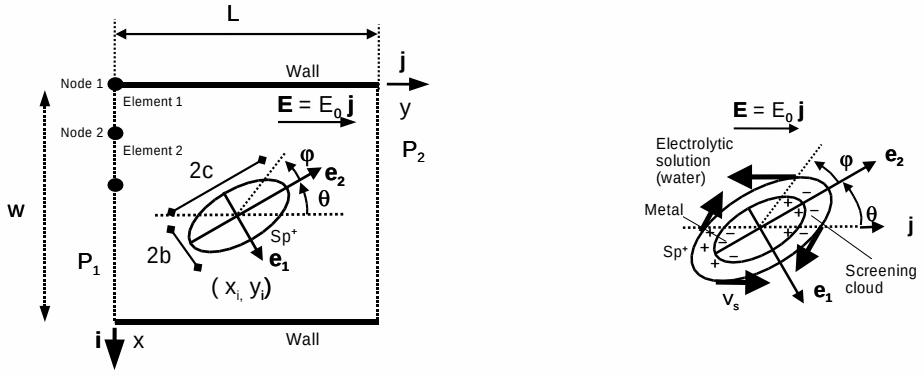

(a) BEM system (b) ICEP flow

Figure 2.1: Schematic view of the calculation system. In (a), the variables used in the ICEO-BEM formulation are shown. The semi-major axis is assumed to be along $\boldsymbol{e}_2$ and its length is c while the semi-minor axis has length b. In (b), thin electric double layer is shown around the elliptical conductive particle.

fibers in microfluidic systems, such as a lab-on-a-chip [42, 85]; e.g., a mixer which works at low Reynolds number has been proposed by Bazant and Squires [5, 83] using an array of conducting posts in a transverse ac electric field. The sedimentation of fibers with ICEP has been studied by [72, 73]. However, to design active control devices using ICEO and ICEP in a microfluidic channel, it is essential to consider the boundary effects, such as a wall effect and particle-particle interactions. Thus, in this study, we focus on the basic modeling and analysis of ICEP for a bounded domain, as a start point of more complex analysis presented in [92, 93, 95, 94].

This chapter is presented in five sections. In Sec. 2.2, we describe theory for a geometry model, a flow model, analytical solutions for an unbounded domain, and a simple model using the thin body theory (SBT). Based on these models, the results of the basic analysis for an elliptical conductive particle in the rectangular channel, are presented in Sec. 2.3. Following a discussion in Sec. 2.4, our conclusions are summarized in Sec. 2.5.

2.2 Theory

2.2.1 Geometry model

Figure 2.1 shows the schematic view of our calculation system. As shown in Fig. 2.1, we use the boundary element method (BEM) along with the analytical slip velocity (v_s) to calculate the flow around an elliptical conductive particle. In Fig. 2.1 (a), the variables used in the ICEP-BEM formulation are shown. The semi-major axis is assumed to be

along $\boldsymbol{e}_2$ and its length is c while the semi-minor axis has length b. Figure 2.1 (b) shows the schematic view of an ICEP flow, consisting of an elliptical particle suspended in an unbounded electrolytic solution with an applied electric field $\boldsymbol{E}_\infty = E_0\boldsymbol{j}$. In Fig. 2.1(b), thin electric double layer is shown around the elliptical conductive particle, and the slip velocities were generated around the particles.

2.2.2 Flow model

We consider a two dimensional (2D) quasi-static Stokes flow without Brownian movement, i.e. we consider the limit in which the Reynolds number $Re \to 0$ and the Peclet number is infinite. We assume the elliptical particles to be polarizable in an electrolytic solution under dc or ac electric field. The boundary conditions are zero velocity on the wall and given pressures at the inlet and outlet. We will discuss the boundary conditions at the surface of the particles below. The motion of the surrounding fluid must satisfy the following Stokes equations modified by the inclusion of an electrical stress ($\boldsymbol{\tau}^{\mathrm{e}}$) which results from the interaction of the applied electric field with the thin electric double layer at the particle's surface:

$$\text{Stokes' equations:} \quad \mu\nabla^2\boldsymbol{v} - \nabla p + \nabla\cdot\boldsymbol{\tau}^{\mathrm{e}} = 0, \quad \nabla\cdot\boldsymbol{v} = 0 \tag{2.1}$$

$$\left.\begin{aligned} \text{Boundary condition on } S_{\mathrm{p}}: &\quad \boldsymbol{v} = \boldsymbol{U} + \boldsymbol{\Omega}\times\boldsymbol{r} \\ \text{Boundary condition at } \infty: &\quad \boldsymbol{v} \to 0 \text{ for } \boldsymbol{r} \to \infty \end{aligned}\right\} \tag{2.2}$$

where $\boldsymbol{r} = \boldsymbol{x} - \boldsymbol{x}_{\mathrm{b}}$, $\boldsymbol{x}_{\mathrm{b}}$ is the center of the particle, μ is the viscosity, $\boldsymbol{v}$ is the velocity, $\boldsymbol{U}$ is the translational velocity, $\boldsymbol{\Omega}$ is the rotational angular velocity, and S_{p} denotes the surface of the particle. Assuming a constant permittivity for the fluid, we have $\nabla\cdot\boldsymbol{\tau}^{\mathrm{e}} = \rho_{\mathrm{e}}\boldsymbol{E}$ where $\rho_{\mathrm{e}}(\boldsymbol{r})$ is the charge density. The two additional relationships needed to solve for $\boldsymbol{U}$ and $\boldsymbol{\Omega}$ are that the net force and torque on the particle are zero.

In the electric double layer, if λ_{D} is small compared to the curvature of surface, the fluxes of charge and fluid are locally one-dimensional and parallel to the particle's surface. Therefore, using Eqs. (2.1), (2.2) and Poisson's equation, we obtain the following equations [26]:

$$\mu\frac{\partial^2\boldsymbol{v}}{\partial y^2} + \rho_{\mathrm{e}}\boldsymbol{E}_{\mathrm{s}} = 0, \qquad \rho_{\mathrm{e}} = -\epsilon\frac{\partial^2}{\partial y^2}(\Phi - \Phi_{\mathrm{s}}) \tag{2.3}$$

$$\text{On } S_{\mathrm{p}}: \quad \boldsymbol{v} = \boldsymbol{U} + \boldsymbol{\Omega}\times\boldsymbol{r} \tag{2.4}$$

where Φ is the electric potential, Φ_{s} ($= \lim_{\kappa y\to\infty}\Phi$) is the electric potential on the surface S_{p}, κ is Debye screening length, and $\boldsymbol{E}_{\mathrm{s}}$ ($= -\nabla\Phi_{\mathrm{s}}$) is the tangential component of the electric field on S_{p}.

Integrating Eq. (2.3) over y gives the following velocity on S_{p}^{+}:

$$\boldsymbol{v} = \boldsymbol{U} + \boldsymbol{\Omega} \times \boldsymbol{r} + \boldsymbol{v}^{(\mathrm{s})}, \quad \text{with} \tag{2.5}$$

$$\boldsymbol{v}^{(\mathrm{s})} = -\frac{\epsilon\zeta}{\mu}\boldsymbol{E}_{\mathrm{s}} \tag{2.6}$$

where $\boldsymbol{v}^{(\mathrm{s})}$ is the slip velocity, and S_{p}^{+} is the surface defined as the outer edge of the double layer.

Using a matched asymptotic expansion [26] for the outer region where the electrical stress tensor is negligible, Eqs. (2.1) and (2.2) reduce to the classical Stokes equations as follows:

$$\mu\nabla^2\boldsymbol{v} - \nabla p = 0, \qquad \nabla \cdot \boldsymbol{v} = 0 \tag{2.7}$$

$$\text{On } S_{\mathrm{p}}^{+}: \quad \boldsymbol{v} = \boldsymbol{U} + \boldsymbol{\Omega} \times \boldsymbol{r} + \boldsymbol{v}^{(\mathrm{s})} \quad \text{and } \boldsymbol{v} \to 0 \text{ for } \boldsymbol{r} \to \infty. \tag{2.8}$$

Initially, when the electric field is "switched" on, charges move along electric field lines and accumulate on the surface of the polarizable particle. As a result, in the thin electric double layer approximation, the effective boundary condition which needs to be applied is $\boldsymbol{n} \cdot \boldsymbol{E} = 0$, where $\boldsymbol{n}$ is the surface normal unit vector. The ζ potential is defined as $\Phi_0 - \Phi$ where Φ_0 is the native ζ potential (assumed to be zero in this work) and Φ is the electrostatic potential outside of the charge cloud. To obtain the tangential electric field $\boldsymbol{E}_{\mathrm{s}}$ and the ζ potential, we solve the Laplace equation with the following boundary conditions:

$$\nabla^2\Phi = 0, \qquad \text{on } S_{\mathrm{p}}^{+}: \quad \boldsymbol{n} \cdot \nabla\Phi = 0, \qquad \text{at infinity:} \quad \nabla\Phi \to -\boldsymbol{E}_{\infty}. \tag{2.9}$$

We used the solution for a 3D ellipsoid from [26] to obtain the 2D solution for an elliptical particle with semi-major axis c and semi-minor axis b. On the surface S_{p}^{+}:

$$\Phi = -\boldsymbol{x} \cdot \mathsf{G}_{\mathrm{p}}^{+} \cdot \boldsymbol{E}_{\infty}, \qquad \boldsymbol{E}_{\mathrm{p}}^{+} = \mathsf{G}_{\mathrm{p}}^{+} \cdot \boldsymbol{E}_{\infty}, \tag{2.10}$$

$$\mathsf{G}_{\mathrm{p}}^{+} = \left(1 + \frac{1}{\alpha}\right) \boldsymbol{e}_1 \otimes \boldsymbol{e}_1 + (1 + \alpha)\, \boldsymbol{e}_2 \otimes \boldsymbol{e}_2 \tag{2.11}$$

where $\alpha = b/c$ ($\alpha < 1$), $\boldsymbol{E}_{\mathrm{p}}^{+}$ is the surface electric field, $\boldsymbol{x}$ is the position on the surface, $\boldsymbol{e}_j$ is a unit coordinate vector. The symbol $\otimes$ is a tensor product so that $(\boldsymbol{e}_j \otimes \boldsymbol{e}_j) \cdot \boldsymbol{E}_{\infty} = (\boldsymbol{e}_j \cdot \boldsymbol{E}_{\infty})\, \boldsymbol{e}_j$. The tangential component of the electric field $\boldsymbol{E}_{\mathrm{s}}$ is obtained:

$$\boldsymbol{E}_{\mathrm{s}} = (I - \boldsymbol{n}\boldsymbol{n}) \cdot \mathsf{G}_{\mathrm{p}}^{+} \cdot \boldsymbol{E}_{\infty} = (\boldsymbol{t} \cdot \boldsymbol{E}_{\mathrm{p}}^{+})\, \boldsymbol{t} \tag{2.12}$$

where $\boldsymbol{t}$ is the unit tangential vector to the surface.

2.2.3 Summary of ICEP formulations

Following the notations on Fig. 2.1, we denote by θ the angle between $\boldsymbol{e}_2$ and the electric field $\boldsymbol{E} = E_0\boldsymbol{j}$. The vector $\boldsymbol{i}$ is such that $(\boldsymbol{i}, \boldsymbol{j})$ is an orthonormal basis with positive orientation. The surface of the elliptical particle is parametrized by φ with:

$$\boldsymbol{x} = -c\alpha \sin\varphi\ \boldsymbol{e}_1 + c\cos\varphi\ \boldsymbol{e}_2$$

From Eq. (2.6) for $\boldsymbol{v}^{(\mathrm{s})}$ and Eq. (2.12) for $\boldsymbol{E}_\mathrm{s}$, we obtain the following 2D-slip velocity $\boldsymbol{v}^{(\mathrm{s})}$, ζ potential and electric field $\boldsymbol{E}_\mathrm{p}^+$ for an elliptical particle:

$$\boldsymbol{v}^{(\mathrm{s})} = \left(\frac{\epsilon c E_0^2}{\mu}\right)\frac{(\alpha+1)^2}{q_0}\, g(\varphi,\theta)\ \boldsymbol{t}, \tag{2.13}$$

$$\zeta = c(1+\alpha)E_0\cos(\theta+\varphi), \tag{2.14}$$

$$\boldsymbol{E}_\mathrm{p}^+ = (1+\frac{1}{\alpha})E_0\sin\theta\ \boldsymbol{e}_1 + (1+\alpha)E_0\cos\theta\ \boldsymbol{e}_2, \tag{2.15}$$

where

$$g(\varphi,\theta) = \sin(\theta+\varphi)\cos(\theta+\varphi), \tag{2.16}$$

$$\boldsymbol{t} = -q_0^{-1}(\alpha\cos\varphi\ \boldsymbol{e}_1 + \sin\varphi\ \boldsymbol{e}_2), \tag{2.17}$$

$$q_0 = \sqrt{\alpha^2\cos^2\varphi + \sin^2\varphi}. \tag{2.18}$$

In addition, the following surface unit normal (pointing into the fluid) is needed in our calculations: $\boldsymbol{n} = q_0^{-1}(-\sin\varphi\ \boldsymbol{e}_1 + \alpha\cos\varphi\ \boldsymbol{e}_2)$.

It is important to note that the slip velocity in ICEP is proportional to E_0^2 as shown in Eq. (2.13). In particular, this means that even an ac field will generate some ICEP since the resulting slip velocity always points in the same direction irrespective of the sign of E_0.

2.2.4 Analytical solutions for an unbounded domain

In addition to developing a numerical scheme to model our system, we consider analytical formulas, used in particular to validate our numerical approach. In this section, we derive important theoretical results which we apply in the next section to ICEP flows. We start by deriving expressions for the stress on the surface of a translating and rotating elliptical particle in an unbounded domain. By calculating the stress of an elliptical particle in a Stokes flow $\boldsymbol{\sigma} = -p\mathbf{I} + \mu\boldsymbol{\nabla u} + \mu[\boldsymbol{\nabla u}]^T$ we can show that the differential stress on an element $\mathrm{d}\boldsymbol{l}(= \boldsymbol{n}dl)$ on the surface of the elliptical particle is equal to:

$$\mathrm{d}\boldsymbol{l}\cdot\sigma_\mathrm{tr} = \mu\,(\boldsymbol{n}\cdot\boldsymbol{x})\boldsymbol{K}\cdot\boldsymbol{U}\mathrm{d}l \tag{2.19}$$

where $\boldsymbol{U}$ is the velocity vector of the elliptical particle and $\boldsymbol{K}$ is a constant diagonal tensor related to the geophysical structure [48]. Note that although Brenner [14] and Jeffery [40] performed the calculation in 3D, we obtain the corresponding result in 2D. Assume that the elliptical particle is rotating with velocity $\boldsymbol{r} \times \boldsymbol{\Omega}$ the differential force on an element $\mathrm{d}\boldsymbol{l}$ is given by:

$$\mathrm{d}\boldsymbol{l} \cdot \boldsymbol{\sigma}_{\mathrm{rot}} = -\frac{2\mu}{bc}(\boldsymbol{n} \cdot \boldsymbol{x})\, \Omega\, (\boldsymbol{e}_3 \times \boldsymbol{x})\mathrm{d}l \tag{2.20}$$

As is done in [14] and [26], we can apply the Lorentz reciprocal theorem to find the total force and torque exerted on an elliptical particle with an arbitrary surface velocity $\boldsymbol{v}^{\mathrm{el}}$.

Translation. The Lorentz reciprocal theorem can be written in the form:

$$\int_{S_{\mathrm{p}}^+} \mathrm{d}\boldsymbol{l} \cdot \boldsymbol{\sigma}^{\mathrm{el}} \cdot \boldsymbol{U} = \int_{S_{\mathrm{p}}^+} \mathrm{d}\boldsymbol{l} \cdot \boldsymbol{\sigma}_{\mathrm{tr}} \cdot \boldsymbol{v}^{\mathrm{el}}$$

where $\boldsymbol{\sigma}_{\mathrm{tr}}$ is the stress associated with an elliptical particle translating with velocity $\boldsymbol{U}$, and $\boldsymbol{\sigma}^{\mathrm{el}}$ is the stress associated with the flow field satisfying the boundary condition $\boldsymbol{v}^{\mathrm{el}}$.

Now, $\int_{S_{\mathrm{p}}^+} \mathrm{d}\boldsymbol{l} \cdot \boldsymbol{\sigma}^{\mathrm{el}}$ is the total force, $\boldsymbol{F}^{\mathrm{el}}$, on the particle with boundary condition $\boldsymbol{v}^{\mathrm{el}}$. The force $\mathrm{d}\boldsymbol{l} \cdot \boldsymbol{\sigma}_{\mathrm{tr}}$ is given by Eq.(2.19). Since this holds for an arbitrary $\boldsymbol{U}$ we get that:

$$\boldsymbol{F}^{\mathrm{el}} = \int_{S_{\mathrm{p}}^+} \mu\, (\boldsymbol{n} \cdot \boldsymbol{x})\, \boldsymbol{K} \cdot \boldsymbol{v}^{\mathrm{el}}\, \mathrm{d}l = \mu \boldsymbol{K} \cdot \int_{S_{\mathrm{p}}^+} (\boldsymbol{n} \cdot \boldsymbol{x})\, \boldsymbol{v}^{\mathrm{el}}\, \mathrm{d}l \tag{2.21}$$

Rotation. We have in this case:

$$\int_{S_{\mathrm{p}}^+} \mathrm{d}\boldsymbol{l} \cdot \boldsymbol{\sigma}^{\mathrm{el}} \cdot (\Omega \boldsymbol{e}_3 \times \boldsymbol{x}) = \int_{S_{\mathrm{p}}^+} \mathrm{d}\boldsymbol{l} \cdot \boldsymbol{\sigma}_{\mathrm{rot}} \cdot \boldsymbol{v}^{\mathrm{el}}$$

Since this applies to an arbitrary Ω, we must have that the total torque is equal to:

$$\boldsymbol{T}^{\mathrm{el}} = -\frac{2\mu}{bc} \int_{S_{\mathrm{p}}^+} (\boldsymbol{n} \cdot \boldsymbol{x})\, (\boldsymbol{x} \times \boldsymbol{v}^{\mathrm{el}})\, \mathrm{d}l \tag{2.22}$$

Using the above results and $\boldsymbol{v}^{\mathrm{el}} = \boldsymbol{v}^{(s)}$, we are now going to show that the translational and angular velocities of a particle in an unbounded domain with an electric field $\boldsymbol{E} = E_0 \boldsymbol{j}$, are given by:

$$\boldsymbol{U}^{\mathrm{unbounded}} = \boldsymbol{0} \tag{2.23}$$

$$\boldsymbol{\Omega}^{\mathrm{unbounded}} = -\frac{\epsilon E_0^2}{\mu}\, \frac{1-\alpha^2}{1+\alpha^2}\, \sin 2\theta\, \boldsymbol{e}_3 \tag{2.24}$$

From those equations, we see that the particle will tend to align its major axis with the electric field. For a sphere, $\boldsymbol{\Omega}^{\mathrm{unbounded}} = \boldsymbol{0}$. The angular velocity is also zero if $\boldsymbol{E}$ is aligned with the major or minor axis of the elliptical particle. It is maximum when the electric field is at a 45° angle. Moreover we always have $|\boldsymbol{\Omega}^{\mathrm{unbounded}}| \leq \epsilon E_0^2/\mu$, the largest amplitude being achieved when $\alpha \to 0$.

2.2.5 Simple model using the SBT

If we consider a single thin elliptical particle (i.e., fiber) and neglect the perturbation of the flow near the wall due to this particle, we can find an expression for the translational and angular velocities. For 2D-Poiseuille flow in a rectangular channel, the steady background flow is

$$\boldsymbol{u}_\infty = -\frac{\Delta P}{2\mu L}\, x(w-x)\boldsymbol{e}_2 \tag{2.25}$$

where L is the length of channel, ΔP $(= p_2 - p_1)$ is the pressure difference, w is the width of the channel, and x is the component of $\boldsymbol{x}$ along $\boldsymbol{e}_1$. With this background flow and the slender body theory (SBT) of Batchelor [2, 3], the vectors $\boldsymbol{U}$ and $\boldsymbol{\Omega}$ must now satisfy:

$$\int_{S_\mathrm{p}^+} (\boldsymbol{n}\cdot\boldsymbol{x})\left(\boldsymbol{U} + \boldsymbol{v}^{(\mathrm{s})} - \boldsymbol{u}_\infty\right) \mathrm{d}l = 0$$

$$\int_{S_\mathrm{p}^+} (\boldsymbol{n}\cdot\boldsymbol{x})\left(|\boldsymbol{x}|^2\boldsymbol{\Omega} + \boldsymbol{x}\times(\boldsymbol{v}^{(\mathrm{s})} - \boldsymbol{u}_\infty)\right) \mathrm{d}l = 0$$

Those integrals can be computed analytically and we find that:

$$\boldsymbol{U} = -\frac{\Delta P}{2\mu L}\left(x_\mathrm{b}(w-x_\mathrm{b}) - \frac{1}{2}(b^2\cos^2\theta + c^2\sin^2\theta)\right)\boldsymbol{e}_2, \tag{2.26}$$

$$\boldsymbol{\Omega} = -\frac{\Delta P}{2\mu L}(w-2x_\mathrm{b})\,\frac{b^2\cos^2\theta + c^2\sin^2\theta}{b^2+c^2}\,\boldsymbol{e}_3 + \boldsymbol{\Omega}^{\mathrm{unbounded}}. \tag{2.27}$$

where x_b is the x coordinate of the center of the elliptical particle.

2.3 Result

Figure 2.2 shows analytical solutions for an unbounded domain. As shown in Fig. 2.2 (a), angular velocities obtained from Eq. (2.24) are decreasing as b/c approaches to one. Figure 2.2(b) shows $G_1 = 1 + c/b$ and $G_2 = 1 + b/c$ which are the first and second components of the diagonal tensor G_p^+ from Eq. (2.11). Contrary to the 3D electric field, the component 1 of the electric field $G_1 \cdot \boldsymbol{E}_\infty$ diverges when α approaches to zero. Because of this, the slip velocity near the ends of the particle (fiber) also diverges. However, this singularity is weak enough that the translational and rotational velocities of the particle remain bounded. Figures 2.3 (a) to (d) show the slip velocity $\boldsymbol{v}_s = (v_1, v_2)$ at α $(= b/c) = 0.25$. Figures 2.3 (e) to (f) show the flow fields around an elliptical particle in an unbounded domain $T_0 U_c/w = 0.02$, $T_0\Delta P/\mu = 0.002$, $b/c = 0.5$, $c/w = 0.2$, and $L/w = 1.0$. In Fig. 2.3 (e) and (f), the slip velocities are shown using arrows and was calculated from Eq. (2.13). By using these analytical solutions along with the BEM, we can realize a fast design tool that consider the boundary effects.

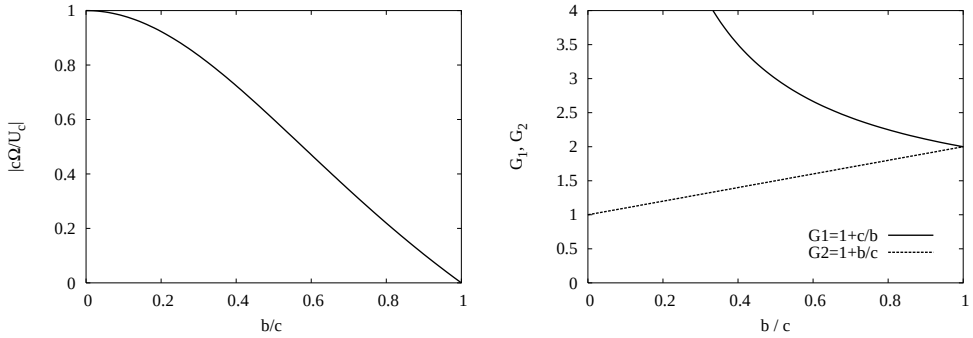

(a) Dependence of Ω on b/c (b) Dependence of G_1 and G_2 on b/c

Figure 2.2: Analytical solutions for an unbounded domain. In (a), angular velocities are obtained from Eq. (2.24) under the condition that $sin2\theta = 1$. In (b), the 2D-electric field tensor $\mathsf{G}_{\mathrm{p}}^{+}$ of Eq. (2.11) is diagonal and its first and second components are $G_1(= 1 + c/b)$ and $G_2(= 1 + b/c)$.

As a next step, we examine the validity of our boundary element formulation (i.e., ICEP-BEM) by comparing the numerical results with the analytical results. First, as shown in Fig. 2.4 (a), we compare the results of the ICEP-BEM with those of Eq. (2.24) for an elliptical particle in an unbounded domain. The results of two methods show close agreement with an error controlled by the number n_f of discretization nodes for the elliptical particle. Figure 2.4 (a) shows that many points are needed for small α $(= b/c)$. Second, as shown in Figs. 2.4 (b) and (c), we compare the results by the ICEP-BEM with those of Eqs. (2.26) and (2.27) (by the SBT) for the translational and rotational velocity U_y and Ω, respectively, in the rectangular channel with no electric field ($n_{\mathrm{f}} = 72$, $n_x = n_y = 32$, and $c = 0.1$). Despite the fact that the analytical result is approximate, the agreement is good under the condition that $\boldsymbol{E} = 0$. Third, as shown in Fig. 2.4 (d), we compare the results of ICEP-BEM with those of Eq. (2.27) (by the SBT) in the presence of an electric field: $T_0 U_c/w(= T_0 \epsilon c E_0^2/\mu/w) = 0.01$. As shown, these two methods yield good predictions for Ω in the presence of a weak electric field.

The analytical results of Eqs. (2.24), (2.26), and (2.27) is only approximate and does not account for the full particle-wall interactions. Figures 2.5 (a) and (b) show the hydrodynamic wall-particle interaction for a Poiseuille flow. In the absence of the wall (or far away from it), the particle translates only in the $\boldsymbol{j}$ direction. However because of the interaction with the wall, a net velocity in the $\boldsymbol{i}$ direction appears as shown in Figs. 2.5 (a) and (b): see [63], [86], and [76]. When the direction of the particle is normal or parallel to the wall, the hydrodynamic particle-wall interaction is zero. This is due to the fact that the stresslet [71, 76] created by the particle is zero for those two orientations. On the other hand, at about $\theta = 25^\circ$ and 65°, hydrodynamic wall-interaction exists. The interaction also becomes stronger as the particle approaches the wall. Figures 2.5 (c) and

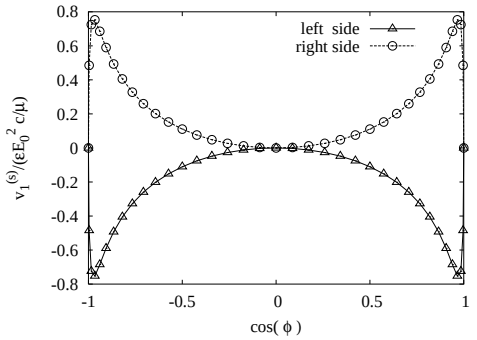

(a) Dependence of v_1 on φ ($\theta = 0°$)

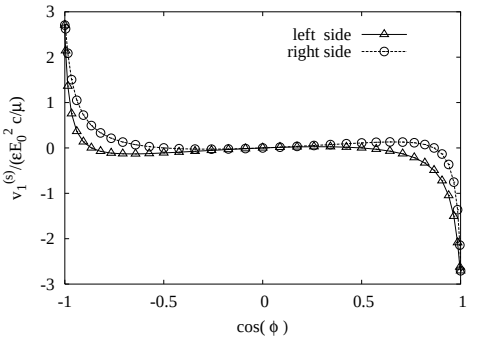

(b) Dependence of v_1 on φ ($\theta = 30°$)

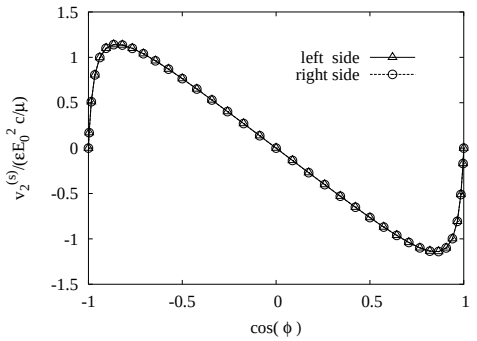

(c) Dependence of v_2 on φ ($\theta = 0°$)

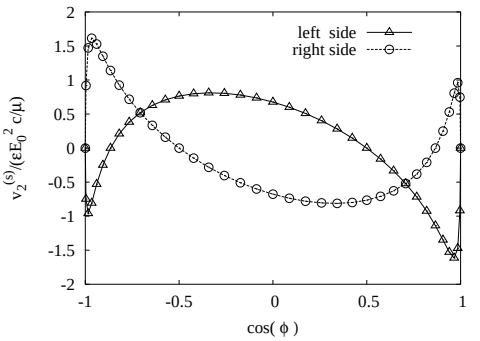

(d) Dependence of v_2 on φ ($\theta = 30°$)

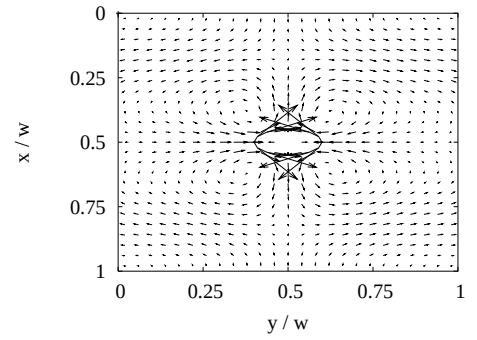

(e) Flow field ($\theta = 0°$)

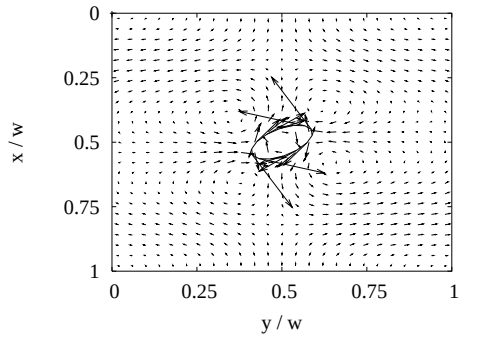

(f) Flow field ($\theta = 30°$)

Figure 2.3: Slip velocities and flow fields. In (e) and (f), $T_0 U_c/w = 0.02$, $U_c = \varepsilon c E_0^2$, $T_0 \Delta P/\mu = 0.002$, $n_x = n_y = 16$, $b/c = 0.5$, $c/w = 0.2$, and $L/w = 1.0$.

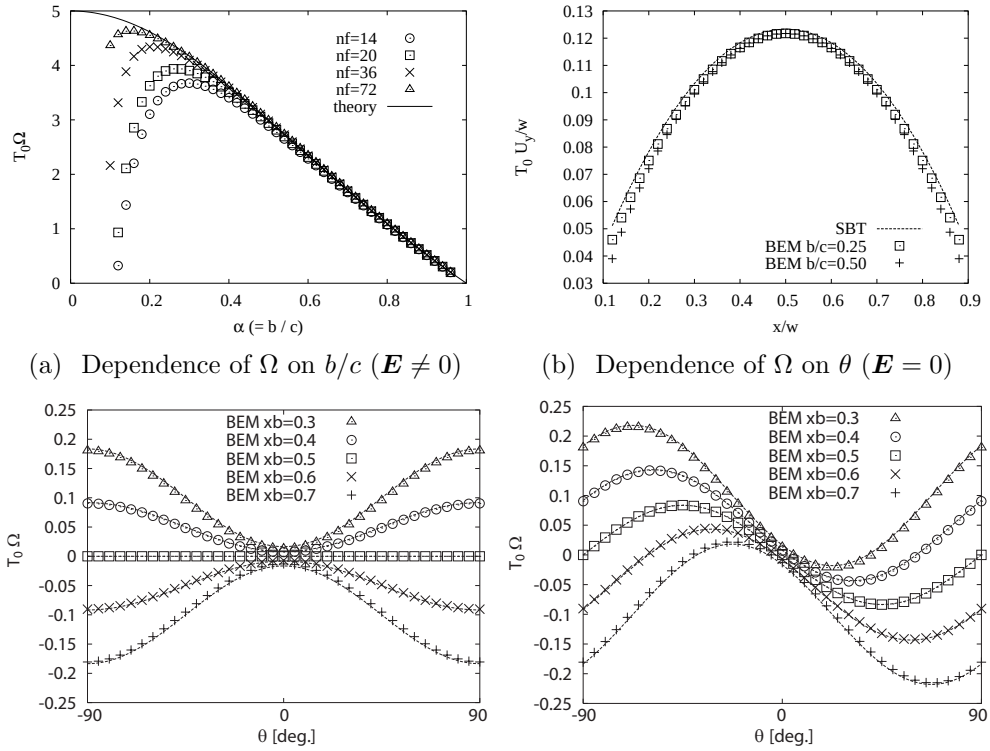

(a) Dependence of Ω on b/c ($\boldsymbol{E} \neq 0$)

(b) Dependence of Ω on θ ($\boldsymbol{E} = 0$)

(c) Dependence of Ω on θ ($\boldsymbol{E} = 0$)

(d) Dependence of Ω on θ ($\boldsymbol{E} \neq 0$)

Figure 2.4: Comparison between the numerical results and the analytical results. In (a), we compare the numerical results of the ICEP-BEM with those of Eq. (2.24), which is an analytical solution for an elliptical particle in an unbounded domain; Here, $T_0 U_c/w = 0.01$, $T_0 \Delta P/\mu = 1$, $c/w = 0.2$, and $L/w = 1$; e.g., $w = 100$ μm, $T_0 = 1$ ms, and $\mu = 1$ ms. In (b) and (c), we compare the results of the ICEP-BEM with those of Eqs. (2.26) and (2.27) for the translational and rotational velocity U_y and Ω, respectively, in the rectangular channel with no electric field; Here, $T_0 U_c/w = 0$, $T_0 \Delta P/\mu = 1$, $b/c = 0.3$, $c/w = 0.2$, $n_{\mathrm{f}} = 72$, $n_x = n_y = 32$, and $L/w = 1$. In (d), we compare the results of the ICEP-BEM with those of Eq. (2.27) for the rotational velocity Ω in the rectangular channel with a weak electric field; Here, $T_0 U_c/w = 0$, $T_0 \Delta P/\mu = 1$, $b/c = 0.3$, $c/w = 0.2$, $n_{\mathrm{f}} = 72$, $n_x = n_y = 32$, and $L/w = 1$.

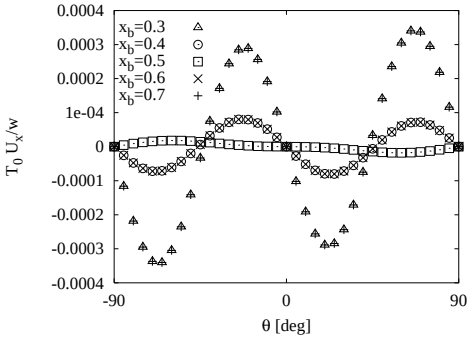

(a) Dependence of U_x on θ ($\boldsymbol{E} = 0$)

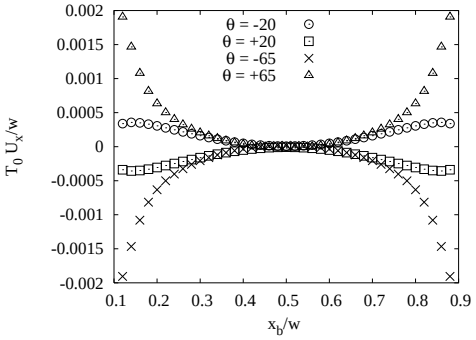

(b) Dependence of U_x on θ ($\boldsymbol{E} = 0$)

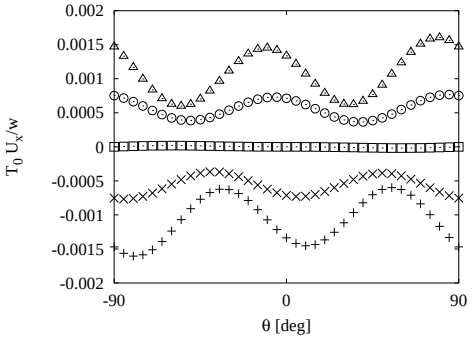

(c) Dependence of U_x on θ ($\boldsymbol{E} \neq 0$)

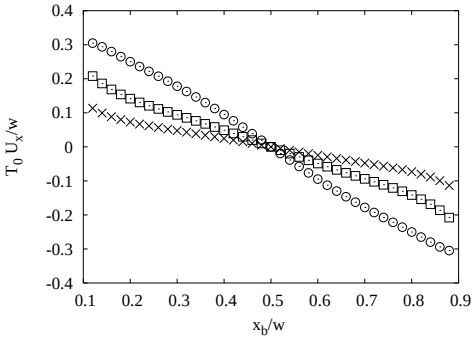

(d) Dependence of U_x on θ ($\boldsymbol{E} \neq 0$)

Figure 2.5: Wall-particle interactions. Here, $L/w = 1.0$, $c/w = 0.1$, and $T_0 \Delta P/\mu = 1$; In (a) and (b), $T_0 U_c/w = 0$; In (c) and (d), $T_0 U_c/w = 0.01$.

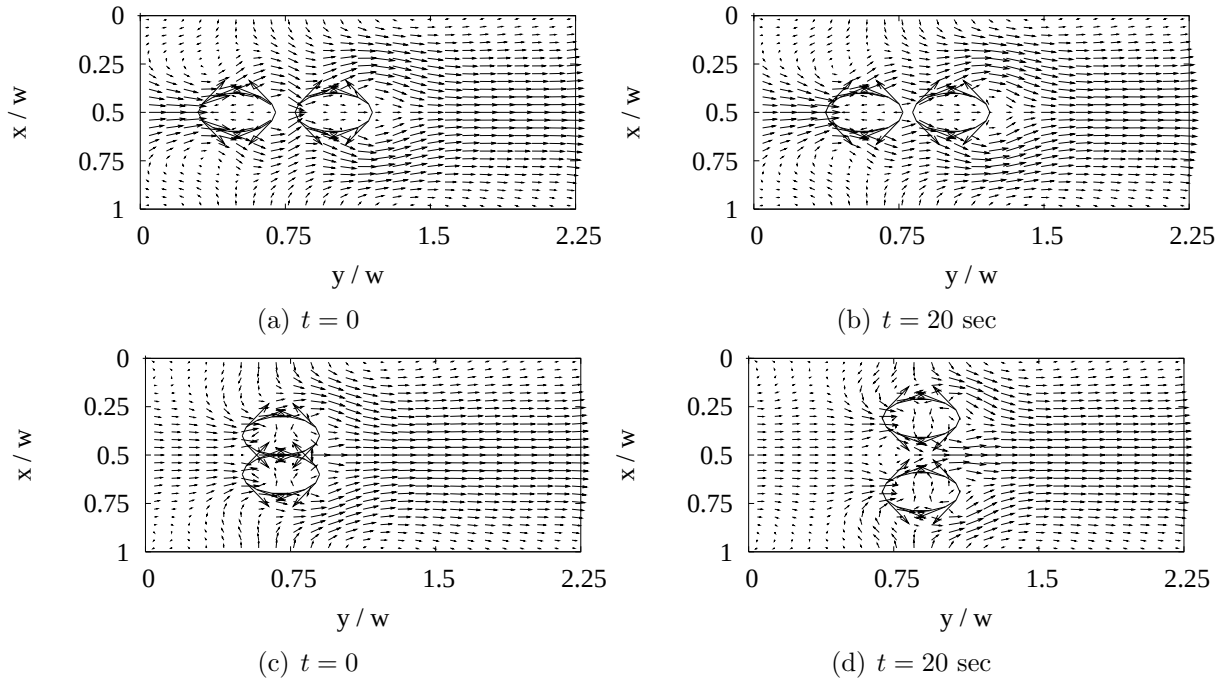

(a) $t = 0$ (b) $t = 20$ sec

(c) $t = 0$ (d) $t = 20$ sec

Figure 2.6: ICEP particle-particle interactions. Here, $n_f = 14$, $T_0 U_c/w = 0.02$, $b/c = 0.5$, $c/w = 0.2$, $T_0 \Delta P/\mu = 0.2$, and $L/w = 2.25$.

(d) show the ICEP wall-particle interaction. We see a strong repulsive force between the elliptical particle and the wall around $\theta \approx 0^\circ$ and $\pm 90^\circ$. This is a result of the slip velocity due to the electric field. Note that only in the presence of a wall the slip velocity result in a translation of the the particle. Different from hydrodynamic wall-particle interaction, ICEP wall-particle interaction increases almost linearly as a particle approaches the wall as shown in Fig. 2.5 (d).

Figure 2.6 shows particle-particle interactions when $T_0 U_c/w = 0.02$. On the one hand, when the vector joining the centers of the two particles is parallel to the electric field, there is an attractive force, as shown in Figs. 2.6 (a) and (b). On the other hand, when it is perpendicular, the particles are repelled from one another, as shown in Figs. 2.6 (c) and (d).

2.4 Discussion

For non-polarizable particles, hydrodynamic interactions between a wall and particles have been investigated by Pozrikidis [63] because of the wide range of applications, such as suspension flow, blood flow, flow cytometry and cell-based assays; e.g., Staben et al. [86, 87] have developed an accurate boundary element method formulation for cases

where the particle-wall gap is as small as 1.3% of the ellipsoid's major axis. They report an oscillating motion when the particle is near the midplane of the channel and a tumbling motion when their center is further from the midplane. Pozridis [65] studied the orbiting motion of a spheroid in a shear flow using a boundary element method. He observed that for oblate particles, the complete orbiting motion is suppressed when the particle is sufficiently close to the wall. Brebbia and Ingber [12] studied the motion of particles in a converging channel. However, for polarizable particles, especially for an ICEO flow, there has been no work that consider the BEM along with the thin double layer approximation, except our previous works [93, 94], as far as we know.

Previously, Fair and Anderson [26] studied how the electric stress due to the thin electric double layer can be modeled as a slip velocity in 3D. Besides, for fixed charged linear electrophoresis, they provided analytical formulas for the slip velocity for a single ellipsoid in an infinite region, and its translational and angular velocities. Similarly, we derive a slip velocity for 2D polarizable particles in an electric field and we model their motion in a microfluidic channel with arbitrary geometry using the boundary element method (BEM) [62, 61, 13, 100]. As the results of using the analytical formulations for slip velocities, the presented method becomes very attractive from the viewpoint of its calculation cost; e.g., Patankar and Hu [59] modeled electro-osmotic flows with the finite element method (FEM). They discretized the electric screening layer whose size is in the order of the Debye length (~ 1 μm). Thus, the calculation cost is quite high although their method has the advantage of being applicable to a more complex flow.

Further, the slender body theory (SBT) of Batchelor [2, 3] has been used for low Reynolds problems by Saintillan et al. [71, 77, 74, 78] and others [23, 22, 21, 18] to analyze large systems with fibers. The main idea of SBT is that the disturbance motion due to the presence of the body is approximated by a suitably chosen line distribution of Stokeslets. Based on the Stokesian dynamics of Brady [11], Saintillan et al. [71] proposed a fast method to model large systems with thin fibers. However, in the SBT, wall-fiber and fiber-fiber interactions due to ICEP are not completely considered, but just considered as a results of rotations through ICEP. Therefore, our presented method (ICEP-BEM) is important to analyze ICEP and ICEO for a bounded domain; i.e., our presented method can calculate wall-particle (wall-fiber) and particle-particle (fiber-fiber) interactions precisely for ICEP flows in microfluidic channels of arbitrary geometry, as a first start point of more complex analysis.

2.5 Conclusion

In conclusion, we have developed a calculation technique (ICEP-BEM) to model ICEP using the boundary element method, and examined its validity by comparing it with analytical solutions. Further, by this method, we have shown that (1) applying an electric field tends to align polarizable elliptical particles in the same direction as the electric field

thorough ICEP, even in the Poiseuille flow in a microfluidic channel; (2) in the presence of an electric field parallel to the flow channel, a polarizable elliptical particle near a wall always feels a repulsive force due to ICEP; (3) two polarizable elliptical particles are repelled each other in side-by-side conformation through ICEP, while they are attracted in head-and-tail conformation. We believe that our presented method gives the basis to analyze an ICEP flow and ICEP devices in the bounded domain, and can be applied to many design problems by little modifications; e.g., by the coupling with the Poisson equations, we can consider not only the fluidic boundary effects but also the electrostatic boundary effects along with ICEP and ICEO.

2.6 Appendix: Boundary element method coupled with ICEP

2.6.1 2D-Boundary integral equation

In Sec. 2.2, we described how the slip velocity can be computed for a given particle geometry and electric field. Eq. (2.13) for the slip velocity is combined with a boundary integral equation to obtain the ICEP-BEM formulation. In this section, we describe the ICEP-BEM formulation in detail.

A quasi static incompressible Stokes flow is described by the following governing equations:

$$\mu \sum_j \frac{\partial^2 u_i(\boldsymbol{x})}{\partial x_j \partial x_j} = \frac{\partial p(\boldsymbol{x})}{\partial x_i}, \qquad \sum_i \frac{\partial u_i(\boldsymbol{x})}{\partial x_i} = 0,$$

where u_i is ith component of the fluid velocity and p is the pressure. For the 2D Stokes problem, applying boundary formulation techniques, these equations can be transformed into the following integral equations [62]:

$$\begin{aligned} \sum_i C_{ji}\, u_i(\boldsymbol{x}_0) - \frac{1}{4\pi} \sum_{ik} \int_C{}^{\mathrm{PV}} u_i(\boldsymbol{x}) T_{ijk}(\boldsymbol{x}, \boldsymbol{x}_0) n_k(\boldsymbol{x}) \mathrm{d}l(\boldsymbol{x}) = \\ - \frac{1}{4\pi\mu} \sum_i \int_C f_i(\boldsymbol{x}) G_{ij}(\boldsymbol{x}, \boldsymbol{x}_0) \mathrm{d}l(\boldsymbol{x}), \end{aligned} \tag{2.28}$$

$$G_{ij} = -\delta_{ij} \ln r + \frac{r_i r_j}{r^2}, \qquad T_{ijk} = -4 \frac{r_i r_j r_k}{r^4}, \tag{2.29}$$

where $\boldsymbol{r} = \boldsymbol{x} - \boldsymbol{x}_0$ ($r = |\boldsymbol{r}|$); the normal vector $\boldsymbol{n}$ is directed into the control surface S; C is the boundary curve of S, C_{ji} the free term, G_{ij} the Green's function or 2D Stokeslet for an unbounded domain, and T_{ijk} the associated stress field.

2.6.2 Free term treatment using indirect method

We now explain how the tensor C in Eq. (2.28) can be computed. This tensor is constant for smooth boundaries but its value changes at corner points. We first present a simple technique to calculate C which has the drawback of potentially hiding coding errors in the program. Therefore we present another approach, more tedious to implement but which allows an independent verification of the computer code, which is obviously desirable.

Since Eq. (2.28) admits the solutions $u_1(\boldsymbol{x}) = 1$, $u_2(\boldsymbol{x}) = 0$, $f_i(\boldsymbol{x}) = 0$ and $u_1(\boldsymbol{x}) = 0$, $u_2(\boldsymbol{x}) = 1$, $f_i(\boldsymbol{x}) = 0$, we have:

$$C_{ji} = \frac{1}{4\pi} \sum_k \int_C^{\mathrm{PV}} T_{ijk}(\boldsymbol{x}, \boldsymbol{x}_0) n_k(\boldsymbol{x}) \mathrm{d}l(\boldsymbol{x}) \tag{2.30}$$

Once the system is discretized and a matrix T is assembled (see Eq. (2.40)), this equation allows computing C by summing up some of the entries in the corresponding rows of T.

2.6.3 Short-range repulsion forces

When an elliptical particle approaches a wall, it feels a weak repulsive force or lubrication force which prevents contact. However, in practice, unless a very high resolution is used (i.e. a very fine mesh and small time step), particles will collide with the wall. In order to prevent this from happening, following the work of [71] and [25], we add a short-range repulsion force acting on node i of particle f:

$$\boldsymbol{f}_i^{\text{particle-wall}} = \sum_{j=1}^{n_{\mathrm{w}}} a_0^{\mathrm{w}} \frac{\tau^{\mathrm{w}} \mathrm{e}^{-\tau^{\mathrm{w}} h_{ij}}}{1 - \mathrm{e}^{-\tau^{\mathrm{w}} h_{ij}}} \boldsymbol{n}_{ij}^{\mathrm{w}} \tag{2.31}$$

where n_{w} is the number of points on the wall. If we denote $\boldsymbol{x}_i^f$ the ith node on particle f and $\boldsymbol{x}_j^{\mathrm{w}}$ the jth node on the wall, then: $h_{ij} = |\boldsymbol{x}_i^f - \boldsymbol{x}_j^{\mathrm{w}}|$ and $\boldsymbol{n}_{ij}^{\mathrm{w}} = (\boldsymbol{x}_i^f - \boldsymbol{x}_j^{\mathrm{w}})/h_{ij}$. The parameter a_0^{w} needs to be tuned and is used to adjust the magnitude of the force; $1/\tau^{\mathrm{w}}$ is the distance beyond which the force becomes negligible.

A similar repulsion force is needed between particles. This is especially important since we will show later on that particles tend to pair up when an electric field is applied and consequently they often end up close to one another [72].

The short-range repulsive force on particle f due to all the other particles is equal to:

$$\boldsymbol{f}_i^{\text{particle-particle}} = \sum_{g=1}^{m_{\mathrm{f}}, g \neq f} \sum_{j=1}^{n_{\mathrm{f}}} a_0 \frac{\tau \mathrm{e}^{-\tau h_{ij}^g}}{1 - \mathrm{e}^{-\tau h_{ij}^g}} \boldsymbol{n}_{ij}^g \tag{2.32}$$

where m_{f} is the number of particles and n_{f} the number of points on each particle. As before, we denote $\boldsymbol{x}_i^f$ (resp. $\boldsymbol{x}_j^g$) the ith (resp. jth) node on particle f (resp. g), $h_{ij}^g = |\boldsymbol{x}_i^f - \boldsymbol{x}_j^g|$, and $\boldsymbol{n}_{ij}^g = (\boldsymbol{x}_i^f - \boldsymbol{x}_j^g)/h_{ij}^g$.

Therefore, the total artificial external force and torque on particle f are given as follows:

$$\boldsymbol{F}^{\text{ext}} = \sum_{i=1}^{n_{\text{f}}} \boldsymbol{f}_i^{ext}, \qquad \boldsymbol{T}^{ext} = \sum_{i=1}^{n_{\text{f}}} \boldsymbol{x}_i^f \times \boldsymbol{f}_i^{ext}, \tag{2.33}$$

where $\boldsymbol{f}_i^{ext} = \boldsymbol{f}_i^{\text{particle-wall}} + \boldsymbol{f}_i^{\text{particle-particle}}$.

2.6.4 Boundary conditions

The particles in our system are modeled as rigid bodies. This leads to the following equation for the fluid velocity on the surface S_{p}^+ of the particle:

$$\boldsymbol{u} = \boldsymbol{U} + \boldsymbol{\Omega} \times \boldsymbol{x} + \boldsymbol{v}^{(\text{s})}, \tag{2.34}$$

The other boundary conditions are: $\boldsymbol{u} = 0$ on the wall, $\boldsymbol{f} = \boldsymbol{f}_1$ $(= -p_1\boldsymbol{j})$ on the inlet, $\boldsymbol{f} = \boldsymbol{f}_2$ $(= p_2\boldsymbol{j})$ on the outlet ($\boldsymbol{f}_1$ and $\boldsymbol{f}_2$ are constant). In addition, the following zero force and moment conditions are required for the particle:

$$\int_{S_{\text{p}}^+} \boldsymbol{f}\mathrm{d}l + \boldsymbol{F}_t^{\text{ext}} = 0, \qquad \int_{S_{\text{p}}^+} \boldsymbol{x} \times \boldsymbol{f}\mathrm{d}l + \boldsymbol{T}_t^{\text{ext}} = 0. \tag{2.35}$$

For an elliptical particle with semi-minor axis b and semi-major axis c:

$$\mathrm{d}l = cq_0\mathrm{d}\varphi, \quad q_0 = \sqrt{\alpha^2\cos^2\varphi + \sin\varphi^2}. \tag{2.36}$$

2.6.5 Discretization

The boundary D can be discretized into n_e elements D_e. The velocity and traction vectors, $\boldsymbol{u}_k$ and $\boldsymbol{f}_k$, are defined at the nodes of the mesh. Inside, each element e, we use a local element numbering and denote the velocity and traction vectors using $\boldsymbol{u}_j^e$ and $\boldsymbol{f}_j^e$. We denote by ϕ_1 and ϕ_2 the iso-parametric elements of first degree :

$$\phi_1 = \frac{1}{2}(1-s), \qquad \phi_2 = \frac{1}{2}(1+s). \tag{2.37}$$

The velocity and traction vectors $\boldsymbol{u}$ and $\boldsymbol{f}$ are approximated inside element e by:

$$\boldsymbol{u}|_{D_e} \approx \sum_{j=1}^{2} \phi_j(s)\ \boldsymbol{u}_j^e, \qquad \boldsymbol{f}|_{D_e} \approx \sum_{j=1}^{2} \phi_j(s)\ \boldsymbol{f}_j^e. \tag{2.38}$$

Using a similar notation, the position vector $\boldsymbol{x}$ is approximated using $\boldsymbol{x}(s)|_{D_e} \approx \sum_{j=1}^{2} \phi_j(s)\ \boldsymbol{x}_j^e$.

2.6.6 Matrix equation

By substituting Eq. (2.38) into Eq. (2.28), we obtain the following equations at node i:

$$\begin{aligned}\mathsf{C}\,\boldsymbol{u}_i + \sum_{e=1}^{n_e}\sum_{j=1}^{2}\int_{D_e}\frac{(\boldsymbol{r}\cdot\boldsymbol{n})(\boldsymbol{r}\cdot\boldsymbol{u}_j^e)\,\boldsymbol{r}}{\pi r^4}\phi_j(s)\mathrm{d}l(\boldsymbol{x}) \\ = \sum_{e=1}^{n_e}\sum_{j=1}^{2}\int_{D_e}\frac{1}{4\pi\mu}\left[\ln r\;\boldsymbol{f}_j^e - \frac{(\boldsymbol{r}\cdot\boldsymbol{f}_j^e)\,\boldsymbol{r}}{r^2}\right]\phi_j(s)\mathrm{d}l(\boldsymbol{x}),\end{aligned} \tag{2.39}$$

where C is a tensor (see Eq. (2.28)) and $\boldsymbol{r} = \boldsymbol{x} - \boldsymbol{x}_i$. Here we switched the indexing to a node-based indexing.

We introduce 2×2 matrices T_{ik} and G_{ik}, such that the previous equation becomes:

$$\sum_k \mathsf{T}_{ik}\,\boldsymbol{u}_k + \sum_k \mathsf{G}_{ik}\,\boldsymbol{f}_k = 0. \tag{2.40}$$

Let us consider a system having the following boundaries: $D_\mathrm{s} = D_\mathrm{w}\cup D_\mathrm{i}\cup D_\mathrm{o}$ and D_p $(= S_\mathrm{p}^+)$, where D_w, D_i, and D_o correspond to the wall, the inlet, and the outlet, respectively. Eq. (2.40) can be re-ordered as follows:

$$\begin{bmatrix}[\mathsf{T}_{\mathrm{ss}}] & [\mathsf{G}_{\mathrm{ss}}] & [\mathsf{T}_{\mathrm{sp}}] & [\mathsf{G}_{\mathrm{sp}}]\\ [\mathsf{T}_{\mathrm{ps}}] & [\mathsf{G}_{\mathrm{ps}}] & [\mathsf{T}_{\mathrm{pp}}] & [\mathsf{G}_{\mathrm{pp}}]\end{bmatrix}\begin{Bmatrix}\{\boldsymbol{u}_\mathrm{s}\}\\ \{\boldsymbol{f}_\mathrm{s}\}\\ \{\boldsymbol{u}_\mathrm{p}\}\\ \{\boldsymbol{f}_\mathrm{p}\}\end{Bmatrix} = \{b\} \tag{2.41}$$

We use the [ ] notation to denote a matrix and { } to denote a column vector. $\{\boldsymbol{u}_\mathrm{s}\}$ and $\{\boldsymbol{f}_\mathrm{s}\}$ (resp. $\{\boldsymbol{u}_\mathrm{p}\}$ and $\{\boldsymbol{f}_\mathrm{p}\}$) are the unknown node vectors for the velocity and traction on D_s (resp. D_p). $[\mathsf{T}_{\mathrm{ss}}]$ corresponds to the integration over D_s for an observation point on D_s. Other T and G are similarly defined. Vector $\{b\}$ is defined by

$$\{b\} = -[\mathsf{T}_\mathrm{b}]\,\{\boldsymbol{u}_\mathrm{b}\} - [\mathsf{G}_\mathrm{b}]\,\{\boldsymbol{f}_\mathrm{b}\}$$

where $\{\boldsymbol{f}_\mathrm{b}\}$ and $\{\boldsymbol{u}_\mathrm{b}\}$ are the known node vectors for the velocity and traction on D_s (specified by the boundary conditions).

The zero net force and zero net torque condition (2.35) can be written as, using discretization (2.38) for $\boldsymbol{f}$:

$$\sum_{j=1}^{n_\mathrm{f}}\boldsymbol{f}_j\left(\sum_{i=1}^{g}\Delta\eta_i\,\left[\phi_2(\eta_i)q_0(\varphi_{j-1}(\eta_i)) + \phi_1(\eta_i)q_0(\varphi_j(\eta_i))\right]\right) = -\boldsymbol{F}_t^{\mathrm{ext}}, \tag{2.42}$$

$$\begin{aligned}\sum_{j=1}^{n_\mathrm{f}}\boldsymbol{f}_j\times\Big(\sum_{i=1}^{g}\Delta\eta_i\,\big[&\phi_2(\eta_i)q_0(\varphi_{j-1}(\eta_i))\;\boldsymbol{x}(\varphi_{j-1}(\eta_i))\\ &+\phi_1(\eta_i)q_0(\varphi_j(\eta_i))\;\boldsymbol{x}(\varphi_j(\eta_i))\big]\Big) = -\boldsymbol{T}_t^{\mathrm{ext}}.\end{aligned} \tag{2.43}$$

This corresponds to a uniform discretization along φ. The change of variable from s to φ is done using Eq. (2.36). n_f is the number of discretization nodes for each particle; g (equal to 10 in our simulations) is the number of Gauss points inside each element; η_i ($-1 \leq \eta_i \leq 1$) is the ith Gauss-integration point. If e is the element joining node j and $j+1$, $\varphi_j(\eta_i)$ is the polar angle corresponding to the ith Gauss point in element e; $\boldsymbol{x}(\varphi_j(\eta_i))$ is the corresponding position vector on the elliptical particle.

If we write symbolically Eqs. (2.42) and (2.43) as $[\mathsf{Z}]\{\boldsymbol{f}_\mathrm{p}\} = \{b_\mathrm{ext}\}$ and add this new equation to Eq. (2.41), we obtain the following matrix equation:

$$\begin{bmatrix} [\mathsf{T}_\mathrm{ss}] & [\mathsf{G}_\mathrm{ss}] & [\mathsf{T}_\mathrm{sp}] & [\mathsf{G}_\mathrm{sp}] \\ [\mathsf{T}_\mathrm{ps}] & [\mathsf{G}_\mathrm{ps}] & [\mathsf{T}_\mathrm{pp}] & [\mathsf{G}_\mathrm{pp}] \\ 0 & 0 & 0 & [\mathsf{Z}] \end{bmatrix} \begin{Bmatrix} \{\boldsymbol{u}_\mathrm{s}\} \\ \{\boldsymbol{f}_\mathrm{s}\} \\ \{\boldsymbol{u}_\mathrm{p}\} \\ \{\boldsymbol{f}_\mathrm{p}\} \end{Bmatrix} = \begin{Bmatrix} \{b\} \\ \{b_\mathrm{ext}\} \end{Bmatrix}. \tag{2.44}$$

2.6.7 Treatment of the ICEP slip velocity in ICEP-BEM

For simplicity, we describe only a system with a single particle. The extension to multiple particles is done in a similar fashion.

We decompose the velocity of the fluid around the particle into a rigid body motion and an ICEP slip velocity (see Eq. (2.5)):

$$\{\boldsymbol{u}_\mathrm{p}\} = \{\boldsymbol{u}'_\mathrm{p}\} + \{\boldsymbol{v}_\mathrm{p}^{(\mathrm{s})}\}, \tag{2.45}$$

where $\boldsymbol{u}'_\mathrm{p} = \boldsymbol{U} + \boldsymbol{\Omega} \times \boldsymbol{x}$. Even though the unknown velocity $\boldsymbol{u}'_\mathrm{p}$ is defined at many discretization nodes for a given particle, it really is only a function of three parameters (U, V, Ω) with $\boldsymbol{U} = U\boldsymbol{i} + V\boldsymbol{j}$, $\boldsymbol{\Omega} = \Omega\boldsymbol{k}$, and:

$$\{\boldsymbol{u}'_\mathrm{p}\} = [\mathsf{Q}] \begin{Bmatrix} U \\ V \\ \Omega \end{Bmatrix} \tag{2.46}$$

By substituting Eq. (2.45) and (2.46) into Eq. (2.44), we obtain the following matrix equation:

$$\begin{bmatrix} [\mathsf{T}_\mathrm{ss}] & [\mathsf{G}_\mathrm{ss}] & [\mathsf{T}'_\mathrm{sp}] & [\mathsf{G}_\mathrm{sp}] \\ [\mathsf{T}_\mathrm{ps}] & [\mathsf{G}_\mathrm{ps}] & [\mathsf{T}'_\mathrm{pp}] & [\mathsf{G}_\mathrm{pp}] \\ 0 & 0 & 0 & [\mathsf{Z}] \end{bmatrix} \begin{Bmatrix} \{\boldsymbol{u}_\mathrm{s}\} \\ \{\boldsymbol{f}_\mathrm{s}\} \\ \begin{Bmatrix} U \\ V \\ \Omega \end{Bmatrix} \\ \{\boldsymbol{f}_\mathrm{p}\} \end{Bmatrix} = \begin{Bmatrix} \{b\} \\ \{b_\mathrm{ext}\} \end{Bmatrix} - \begin{bmatrix} [\mathsf{T}_\mathrm{sp}] \\ [\mathsf{T}_\mathrm{pp}] \\ 0 \end{bmatrix} \{\boldsymbol{v}_\mathrm{p}^{(\mathrm{s})}\} \tag{2.47}$$

where $[\mathsf{T}'_\mathrm{sp}] = [\mathsf{T}_\mathrm{sp}][\mathsf{Q}]$ and $[\mathsf{T}'_\mathrm{pp}] = [\mathsf{T}_\mathrm{pp}][\mathsf{Q}]$.

Chapter 3

Pump 1 (Theory): Suppression of reverse flows in pumping by induced-charge electro-osmosis using asymmetrically stacked elliptical metal posts

Several researchers have analyzed pumps that employ induced-charge electro-osmosis (ICEO) using mainly coplanar electrode array structures in a lateral electric field. We propose ICEO pumps that remove reverse flows using asymmetrically stacked elliptical metal posts and numerically examine the pumping performance. By the boundary element method along with double layer approximation, we find that the asymmetrical stacking configuration efficiently suppresses the unwanted reverse flow and yields velocities of the order of a few millimeters per second, and this configuration is compatible with that of an optimized half-coating pump. Further, we propose a simple model for the stacking pump and predict that the velocity of such a stacking pump with a thin limit is larger than 67% of that of a circular cylindrical half-coating pump of the same length. Using this stacking pump, we can expect to significantly improve the pumping performance.

3.1 Introduction

In an ionic solution, metal is polarized and screened by surrounding ions. Since an applied field $\boldsymbol{E}$ acts on its own induced diffuse charge, the representative slip velocity U_b on the metal surface is proportional to $\boldsymbol{E}^2$. This nonlinear phenomenon is called induced-charge electro-osmosis (ICEO) [5, 83]. Recently, pumps that employ ICEO with broken symmetry were proposed, and they have attracted considerable attention [97, 16, 66, 1, 57] because

they have a large flow velocity (∼mm/s) with a small voltage (∼V) and can prevent the occurrence of dc problems such as chemical reactions in an electrolytic solution. These pumps are usually fabricated and analyzed by considering planar structures (structures made by a thin film process) because the fabrication of planar structures is easier than that of high-aspect-ratio structures (structures in which the ratio of the height to the width is high). However, by the development of process technologies such as deep reactive ion etching, the fabrication of high-aspect-ratio structures has also become a realistic option.

Bazant and Squires [5, 83] proposed the following high-aspect-ratio pumps using asymmetrical ICEO flow around metal posts: (1) a half-coating metal pump, (2) an irregular-shaped metal pump, and (3) an asymmetrical-channel pump. Further, motivated by these studies, Bazant et al. [97, 16] significantly improved pumping velocity by using three-dimensional (3D) stepped electrodes for suppressing reverse flow. However, thus far, no attempts have been made for removing reverse flow by using asymmetrically stacked structures. In fact, the suppression of reverse flow occurs when ellipse metal posts are very near. In this chapter, we focus on an ICEO pump that uses asymmetrical stacking as the origin for the suppression of the reverse flow, and we elucidate its design concept.

3.2 Theory

Figure 3.1 shows the schematic view of the hierarchically stacked asymmetrical ICEO pump considered in this study. As shown in Fig. 3.1, we place two 2nd-generation ellipses with lengths b to the left of a 1st-generation ellipse of length $2b$ in order to suppress the reverse flow of the 1st-generation ellipse. Similarly, we can suppress the reverse flow of the 2nd-generation ellipse by placing two 3rd-generation ellipses of lengths $b/2$ to the left of the 2nd-generation ellipse. By repeating this procedure, we can obtain a hierarchically stacked asymmetrical structure. A pump that includes ellipses from 1st-generation ellipses to Nth-generation ellipses is termed an Nth-generation pump. In the above explanation, we consider type-A stacking pump that suppresses the reverse flows of both sides of the 1st-generation ellipse; however, it is possible to consider other types of pumps (type-B and type-C, shown in Fig. 3.2) that suppress the reverse flow of one side of the 1st-generation ellipse by the wall of a channel, while the reverse flow of the other side is suppressed by the hierarchically stacked asymmetrical structure.

By considering the hierarchically stacked asymmetrical structure as the origin of the suppression of the reverse flow, we estimate the average flow velocity U_p of the pump as follows:

$$U_p \approx \frac{4}{3}(1-(\frac{1}{4})^{N-1})\eta_{\rm n}\eta_k^{\sigma_k}\eta_{k_1}\eta_0 v_{\rm s}^{\rm max} - 0.4\eta_n v_{\rm s}^{\rm max}\frac{\delta}{w} \tag{3.1}$$

where the first term ($U_p^{\rm forward}$) describes the forward pumping, the second term ($U_p^{\rm reverse}$) describes the reverse pumping that is a function of a gap δ ($= d - 2c$), $v_{\rm s}^{\rm max}$ is the maximum slip velocity of an ellipse, η_0 is the intrinsic efficiency of a half-coating pump,

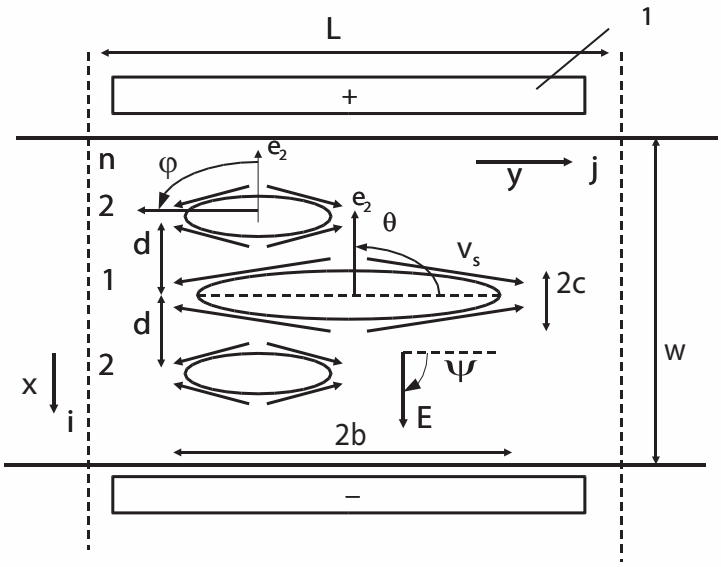

Figure 3.1: Schematic view of hierarchically stacked asymmetrical ICEO pump. 1: pair of electrodes. Here, $\psi = \theta = \pi/2$ rad, length $L = 2.25w$, width $w = 100$ μm, and $V_0 = 2.38$ V is applied to the electrodes. The ellipse has two semi-axes (b, c) with unit vectors $(\boldsymbol{e}_1, \boldsymbol{e}_2)$ that define the orientation of each semi-axis. Here, we place two 2nd-generation ellipses with lengths b to the left of a 1st-generation ellipse of length $2b$ in order to suppress the reverse flow of the 1st-generation ellipse.

$\eta_k(\approx (w-K)/w)$ and $\eta_{k_1}(\approx (w-K_1)/w)$ are the effect of narrowing of the channel, K and K_1 are the width of objects obstructing fluid flow ($K = 2c(2N-1) + 2\delta(N-1)$, $2cN + \delta(N-1)$, $4cN + 2\delta(N-1)$, $K_1 = 2c$, $2c+\delta$, $4c+2\delta$, $\sigma_k = 1.9$, 0.7, and 0.7 for Type-A, type-B, and type-C pumps, respectively), and $\eta_{\rm n}$ is the effect of the number of the elliptical metal posts ($\eta_{\rm n} = 1$ for type-A and type-C; $\eta_{\rm n} = 0.5$ for type-B pump). It should be noted that

$$U_{p0} \approx \eta_{k_1}^{0.7} \eta_0 v_{\rm s}^{\max} \tag{3.2}$$

is the the average flow velocity of the half-coating pump corresponding to the 1st-generation ellipse.

We consider a two-dimensional (2D) quasi-static Stokes flow without Brownian movement; that is, we consider the limit in which the Reynolds number Re tends to zero and the Peclet number is infinite. We assume the ellipse posts to be polarizable in an electrolytic solution under a dc or ac electric field. The motion of the surrounding fluid must satisfy the Stokes equations modified by the inclusion of an electrical stress. However, using a matched asymptotic expansion [26], we can reduce them to the classical Stokes equations as follows:

$$\mu \nabla^2 \boldsymbol{v} - \nabla p = 0, \qquad \nabla \cdot \boldsymbol{v} = 0, \tag{3.3}$$

$$\text{On metal}(\boldsymbol{E} \neq 0): \quad \boldsymbol{v} = \boldsymbol{v}_{\rm s}, \tag{3.4}$$

$$\boldsymbol{v}_{\rm s} = \frac{1}{2} U_b (\beta+1)^2 q_b^{-1} \sin 2(\psi + \varphi + \theta) \boldsymbol{t}, \tag{3.5}$$

where $q_b = \sqrt{\cos^2\varphi + \beta^2 \sin^2\varphi}$, U_b ($= \epsilon b E_0^2/\mu$) is the representative velocity, $\beta = c/b$, $\boldsymbol{x}$ ($= -b\sin\varphi\ \boldsymbol{e}_1 + c\cos\varphi\ \boldsymbol{e}_2$) is the surface position of metals parameterized by φ, $\boldsymbol{t} = -q_b^{-1}(\cos\varphi\ \boldsymbol{e}_1 + \beta\sin\varphi\ \boldsymbol{e}_2)$ is the tangential unit vector of the surface position, electric field $\boldsymbol{E} = \cos\psi \boldsymbol{j} + \sin\psi \boldsymbol{i}$, $\boldsymbol{e}_2 = \cos\theta \boldsymbol{j} - \sin\theta \boldsymbol{i}$, $\boldsymbol{e}_1 = \sin\theta \boldsymbol{j} + \cos\theta \boldsymbol{i}$, where $\boldsymbol{i}$ and $\boldsymbol{j}$ are orthogonal unit vectors of the Cartesian coordinate system, μ ($\sim$1 mPa·s) is the viscosity, $\boldsymbol{v}$ is the velocity, $\boldsymbol{v}_s$ is the slip velocity, p is the pressure, ϵ ($\sim 80\epsilon_0$) is the dielectric permittivity of the solvent (typically water), and ϵ_0 is the vacuum permittivity. It should be noted that the maximum absolute value of $\boldsymbol{v}_{\rm s}$ is

$$v_{\rm s}^{\max} = U_b (\beta+1)^2 \sin\varphi_0 / \sqrt{1+\beta} \tag{3.6}$$

at $\varphi_0 = \tan^{-1}\sqrt{1/\beta}$ when $\psi = \theta = \pi/2$. We calculate the flow fields of the ICEO pump by the boundary element method using Eqs. (3.3) and (3.4). In particular, to obtain a precise flow field near the wall and the metal surfaces, we use analytical integration to obtain the elements of the matrix of the boundary element method (50 to 72 elements for each ellipse). It is noteworthy that the Gauss integration produces a large error when ellipses are very near.

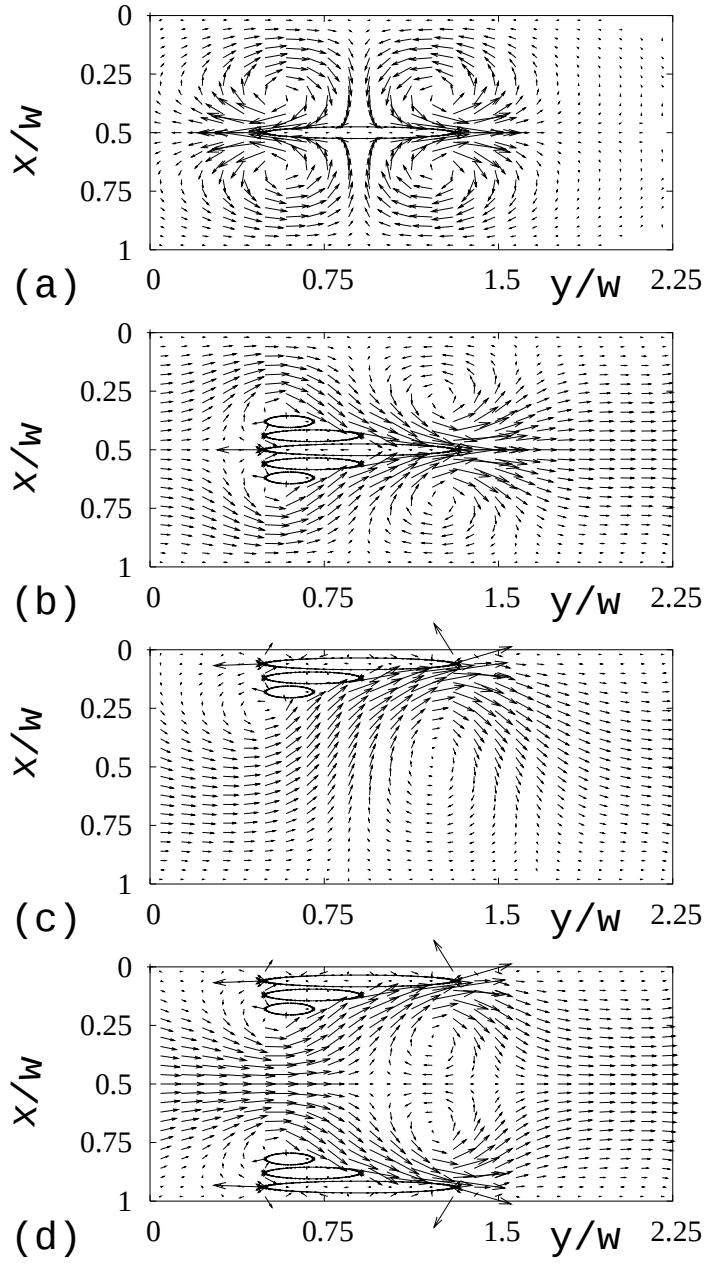

Figure 3.2: Flow field of stacking pump without coatings. (a) Type-A pump ($N = 1$, $U_p = 0$ mm/s). (b) Type-A pump ($N = 3$, $U_p = 1.31$ mm/s). (c) Type-B pump ($N = 3$, $U_p = 0.97$ mm/s). (d) Type-C pump ($N = 3$, $U_p = 1.52$ mm/s). Here, $U_b = 16$ mm/s, $E_0 = 23.8$ kV/m, $d/w = 0.06$, $\delta/w = 0.01$, and $c/w = 0.025$, where $\delta = d - 2c$. In the calculation, we used 50 to 72 elements for each ellipse.

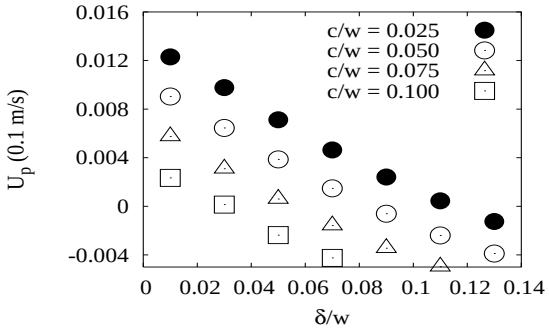

(a) U_p vs. δ for type-A pump at $N = 2$. At $\delta/w = 0.01$, the reverse flow is suppressed considerably.

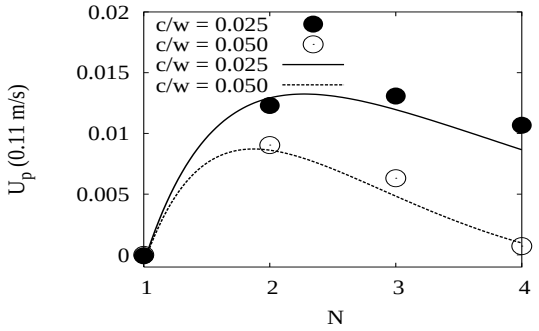

(b) U_p vs. N for type-A pump. The maximum performance is 1.31 mm/s at $N = 3$ when $c/w = 0.025$ and $b/w = 0.4$.

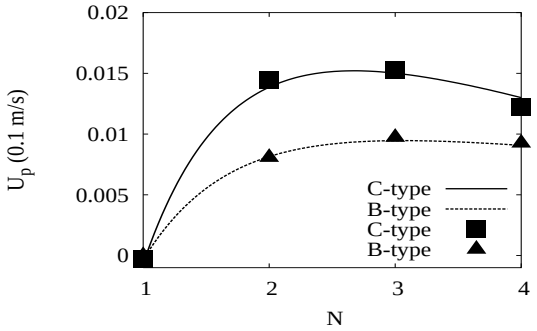

(c) U_p vs. N for type-B and type-C pumps. The maximum performances are 1.52 and 0.97 mm/s for type-C and type-B pumps, respectively, when $N = 3$, $b/w = 0.4$, and $c/w = 0.025$.

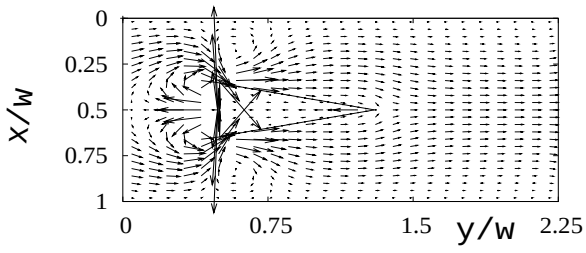

(d) Flow field of triangle metal post pump. Here, $w_h/w = 0.29$, $L_b/w = 0.8$, and $U_p = 0.11$ mm/s.

Figure 3.3: Performance of asymmetrical stacking pump ($E_0 = 23.8$ kV/m, $\eta_0 = 0.12$). The lines show the analytical results obtained by Eq. (3.1). The symbols show the numerical results obtained by the boundary element method.

3.3 Results

Figure 3.2 shows the flow field for the stacking pump when $b/w = 0.4$, $c/w = 0.025$, $U_b = 16$ mm/s ($E_0 = 23.8$ kV/m), $d/w = 0.06$, and $\delta/w = 0.01$. On the one hand, for the 1st-generation pump shown in Fig. 3.2(a), we observe a symmetrical quadrupolar electroosmotic flow around an ellipse post, and the net flow is zero because the forward flow of the left-hand part of the ellipse cancels the reverse flow of its right-hand part. On the other hand, the type-A, type-B, and type-C stacking pumps (whose flow fields are shown in Figs. 3.2(a)-3.2(c), respectively) function efficiently, i.e., the reverse flow is suppressed by the hierarchically stacked asymmetrical alignment of the ellipses, probably because the amount of the reverse pumping is limited in the level of $0.4 v_s^{\max} \delta$. Further, the forward flow is stimulated by the increase of the surface of the forward slip velocity.

Figure 3.3 shows the performance of the asymmetrical stacking pump. As shown in

Fig. 3.3(a), the suppression of the flow diminishes as the gap increases. Further, as predicted in Eq. (3.1), the reverse flow is considerably suppressed at the small gap ($\delta/w = 0.01$). Here, U_p is almost a strait line at least for $\delta/w < 0.1$ without depending on the value of c/w. The ultimate reason for having this behavior is the reverse pumping is just proportional to δ/w because the amount of reverse flow is limited by the narrowest gap δ without depending on the curvature of elliptical posts. Further, a kind of adjustment mechanism works for the changes of the gradient $dU_p/d(\delta/w)$ when c/w changes as predicted in Eq. (3.1). That is as c/w increases from 0.025 to 0.1, $dU_p^{\text{forward}}/d(\delta/w)$ changes from -6 to -3 mm/s, whereas $dU_p^{\text{reverse}}/d(\delta/w)$ increases from 7 to 8 mm/s. Thus. $|dU_p^{\text{inverse}}/d(\delta/w)|$ becomes approximately constant ($\sim$12 mm/s) without depending on the value of c/w. Here, we set $\eta_0 = 0.12$, and U_p is calculated on the boundary of the inlet ($y = 0$ and $0 < x < w$). Thus, we believe that the suppression of the reverse flow in the stacking pump occurs because a small gap limits the amount of the reverse pumping. Although the reverse flow is not completely suppressed for finite δ, a small gap that keeps unwanted slip velocities is intrinsically required to suppress the reverse flow. If there is no gap, the reverse flow in the x direction remains on the left-hand part of the pump, and it degrades the performance of the pump. Figures 3.3(b) and 3.3(c) show the dependence of the U_p values of the type-A, type-B, and type-C pumps on N. We compare the numerical results with theoretical results obtained using the simple model expressed in Eq. (3.1). Although these results are not in complete agreement with each other, both show that the effect of flow resistance is dominant. If we neglect the narrowing of the channel, U_p increases monotonously as N increases. However, in reality, U_p attains the maximum value at an optimum N in a real channel because flow resistance also increases. When $N = 3$, $b/w = 0.4$, and $c/w = 0.025$, the maximum $U_p = 1.31$, 0.97, and 1.52 mm/s for type-A, type-B, and type-C pumps, respectively. Note that a triangle metal post pump which shape and size are similar to 3rd-generation stacking pump changes the direction of reverse flow and shows the pumping performance ($U_p = 0.11$ mm/s) as shown in Fig. 3.3(d). However, the triangle metal pump cannot suppress the reverse flow considerably. Here, w_h ($= 2c(2N-1) + 2\delta(N-1) = 0.29w$) and L_h ($= 2b = 0.8w$) are the base length and the height of the triangle. Thus, the stacking pump is conceptually different from the irregular-shaped metal pump.

Figure 3.4 shows the performance of the half-coating pump. Figure 3.4(a) shows the flow of the optimum single half-coating pump at $c/w = 0.15$ when $b/w = 0.4$. Figure 3.4(b) shows the dependence of U_p on c. For this case, we compare the numerical results with the theoretical results obtained by the simple model expressed in Eq. (3.2). Here, $K_1 = 2c$. Although these results are not in complete agreement, both show that the effect of flow resistance is dominant. In a real channel, the pumping performance is the optimum at an optimum c because flow resistance also increases. As observed in Fig. 3.4(b), the maximum performances of the half-coating pump are $U_p = 2.13$, 1.72, and 1.34 mm/s at $c/w = 0.15$, 0.2, and 0.25 under the conditions $b/w = 0.4$, 0.3, and 0.2, respectively, when we apply $V_0 = 2.38$ V to a channel with a width $w = 100$ μm. Therefore, the

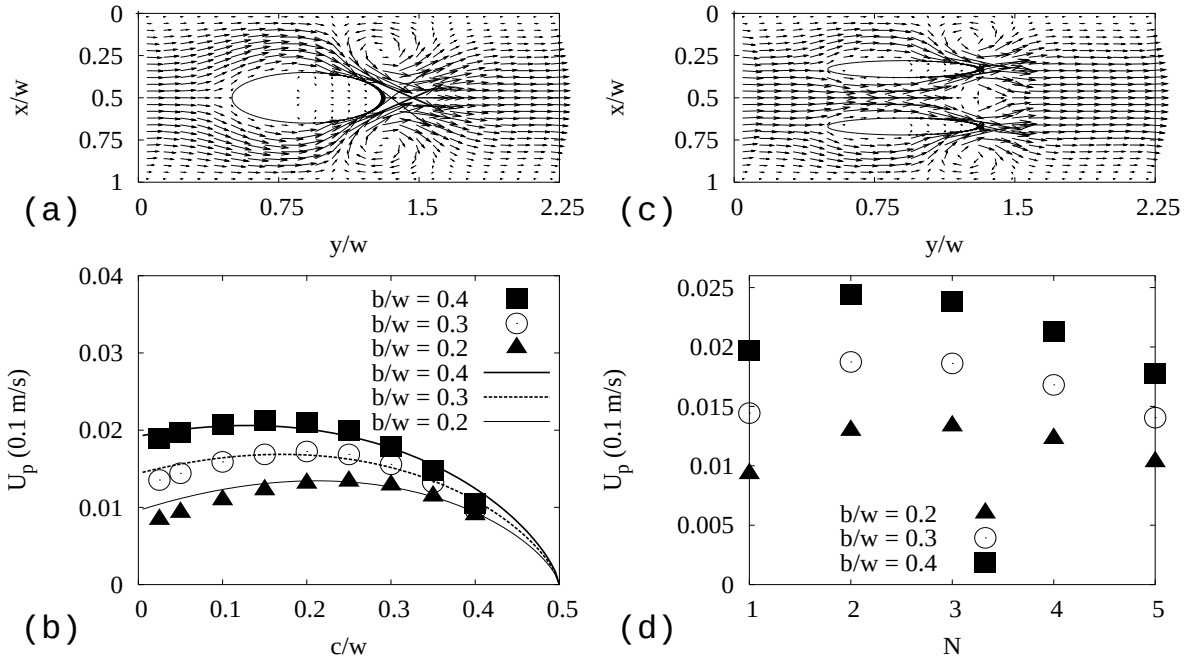

Figure 3.4: Performance of half-coating pump ($E_0 = 23.8$ kV/m, $\eta_0 = 0.12$). (a) Flow of optimum single half-coating pump. Here, $c/w = 0.15$, $b/w = 0.4$, and $U_b = 16$ m/s. (b) U_p vs. c for the single half-coating pump. The U_p value is the maximum (2.13 mm/s) at $c/w = 0.15$ when $b/w = 0.4$. (c) Flow of optimum multiple half-coating pump. Here, $N = 2$, $b/w = 0.4$, and $c/w = 0.025$. (d) U_p vs. N for multiple half-coating pump. The U_p value is the maximum (2.44 mm/s) at $N = 2$ when $b/w = 0.4$ and $c/w = 0.025$. The left-hand part of the ellipse was coated by insulators. The lines show the analytical results obtained by Eq. (3.2). The symbols show the numerical results obtained by the boundary element method.

performances of the type-C, type-A, and type-B stacking pumps are evaluated to be approximately 71%, 61%, and 46%, respectively, of the performance of the optimum half-coating pump. Figure 3.4(c) shows the flow of the optimum multiple half-coating pump when $N = 2$, $c/w = 0.025$, and $b/w = 0.4$. Figure 3.4(d) shows the dependence of U_p on the number N of multiple half-coating pumps under the condition $c/w = 0.025$. Here, the distance between the ellipses is $w/(N + 1)$. If we neglect the flow resistance, U_p increases as N increases. However, because of the flow resistance, U_p has the maximum value in a real channel; The maximum values of U_p are 2.44, 1.72, and 1.34 mm/s at $N = 2$, 2, and 3 when $b/w = 0.4$, 0.3, and 0.2, respectively. Similarly, lateral arrangements also face a flow resistance problem because of the potentially large width of an ellipse.

3.4 discussion

The performance of hierarchically stacked asymmetrical pumps (46% to 71%) is good because they can be fabricated without coating. Further, from Eqs. (3.1) and (3.6) we can estimate $U_p \approx 1.33 U_b \eta_0$ for type-A and type-C pumps in the limits $c \to 0$ and $N \to \infty$, whereas $U_{p0} \approx 2 U_b \eta_0 \eta_{k_1}^{0.7}$ for the half-coating pump at $c/b = 1$. Because $\eta_{k_1}^{0.7} < 1$, the velocity of the stacking pump with a thin limit with infinite N is larger than 67% of that of the half-coating pump of the circular cylinder of the same length $2b$. Obviously, we can place such thin pumps in a channel with high density, large slip velocity, and small flow resistance. Further, such thin limit pumps with asymmetrically stacked metal posts can be used for planar structures, though insulator may be required. Therefore, the stacking pump can dramatically improve the pumping performance in terms of flow rate, applied voltage, and applied electric field.

3.5 Conclusion

In conclusion, we have proposed ICEO pumps that employ asymmetrically stacked structures to suppress the reverse flow and examined the pumping performance by the boundary element method in conjunction with the double layer approximation and a simple model. The following are the conclusions of the numerical calculations. (1) The asymmetrical stacking configuration efficiently suppresses the reverse flow and yields ∼mm/s velocity, which is 46% to 71% of the performance of an optimum half-coating pump. (2) The velocity of the stacking pump with a thin limit with infinite N is larger than 67% of that of the half-coating pump of the circular cylinder of the same length. The use of this stacking pump is expected to dramatically improve the pumping performance in terms of flow rate, applied voltage, and applied electric field. In the future, we intend to evaluate other stacking structures for suppressing reverse flow.

Chapter 4

Pump 2 (Theory and Experiment): Asymmetrical reverse vortex flow due to induced-charge electroosmosis around carbon stacking structures

Broken symmetry of vortices due to induced-charge electroosmosis (ICEO) around stacking structures is important for the generation of a large net flow in a microchannel. Following theoretical predictions in our previous study, we herein report experimental observations of asymmetrical reverse vortex flows around stacking structures of carbon posts with a large height ($\sim$110 μm) in water, prepared by the pyrolysis of a photoresist film in a reducing gas. Further, by the use of a coupled calculation method that considers boundary effects precisely, the experimental results, except for the problem of anomalous flow reversal, are successfully explained. That is, unlike previous predictions, the precise calculations here show that stacking structures accelerate a reverse flow rather than suppressing it for a microfluidic channel, because of the deformation of electric fields near the stacking portions; these structures can also generate a large net flow theoretically in the direction opposite to that of a previous prediction for a standard vortex flow. Furthermore, by solving the one-dimensional Poisson-Nernst-Plank (PNP) equations in the presence of ac electric fields, we find that the anomalous flow reversal occurs by the phase retardation between the induced diffuse charge and the tangential electric field. In addition, we successfully explain the nonlinearity of the flow velocity on the applied voltage by the PNP analysis. In the future, we expect to improve the pumping performance significantly by using stacking structures of conductive posts along with a low-cost process.

4.1 Introduction

In this chapter, we focus on the experimental proof of the generation of asymmetrical vortex flow due to ICEO around the stacking structures consisting of conductive posts in an aqueous solution, as the basis of stacking ICEO pump. Furthermore, since the conductive post is very near to the other conductive posts, 2D electric and flow field problems in the bounded domain are solved precisely and discussed by considering proper boundary conditions in the dc limit by the coupled calculation method [95]. Furthermore, to explain the anomalous flow reversal, we solve 1D problems of an electrolyte cell bounded by two parallel walls in the presence of ac electric fields by using the PNP equations, and compare the theoretical results with the experimental results concerning the dependence of the flow velocity on the applied voltage.

This chapter is presented in five sections. In Sec. 4.2, we describe methods for a geometry model, fabrications of carbon structures, observations of asymmetrical vortex flow, a 2D flow analysis using the coupled simulations, and a diffuse-charge analysis using the 1D PNP equations. Based on these methods, the fabrication results of high-aspect-ratio carbon structures, the observation results of asymmetrical vortex flows, the analysis results of the 2D flow calculations using the coupled simulation method, and the analysis results of the 1D flow calculations using the PNP equations, are presented in Sec. 4.3. Following a discussion in Sec. 4.4, our conclusions are summarized in Sec. 4.5.

4.2 Method

4.2.1 Geometry model

Figure 4.1 shows the schematic view of the asymmetrical stacking structure considered in this study. As shown in Fig. 4.1, we consider a rocket-shaped stacking structure consisting of one larger elliptical conductive cylinder of length $2b$ and width $2c$ at the center $[(x_1/w,\ y_1/w) = (0.5,\ 0.9)]$ and two smaller conductive cylinders of length $1b$ and width $2c$ placed on the upper and lower left-hand sides $[(x_2/w,\ y_2/w) = (0.5 - 2c/w - \delta/w,\ 0.9 - b/2w)$, $(x_3/w,\ y_3/w) = (0.5 + 2c/w + \delta/w,\ 0.9 - b/2w)]$ in a rectangular channel of length L and width w; here, δ is the gap between the conductive cylinders and $(x_i/w,\ y_i/w)$ are the centers of the cylinders. Since the stacking structure is symmetric for the plane of $x/w = 0.5$ and asymmetric for the plane of $y/w = 0.9$, we can predict an asymmetrical ICEO flow for the plane of $y/w = 0.9$ with a symmetrical flow for the plane of $x/w = 0.5$.

4.2.2 Fabrication method

To test this prediction in the first experimental study of an ICEO stacking pump, several stacking structures ($w = 0.2$ to 1.6 mm, $c/w = 0.025$ to 0.1) consisting of elliptical carbon

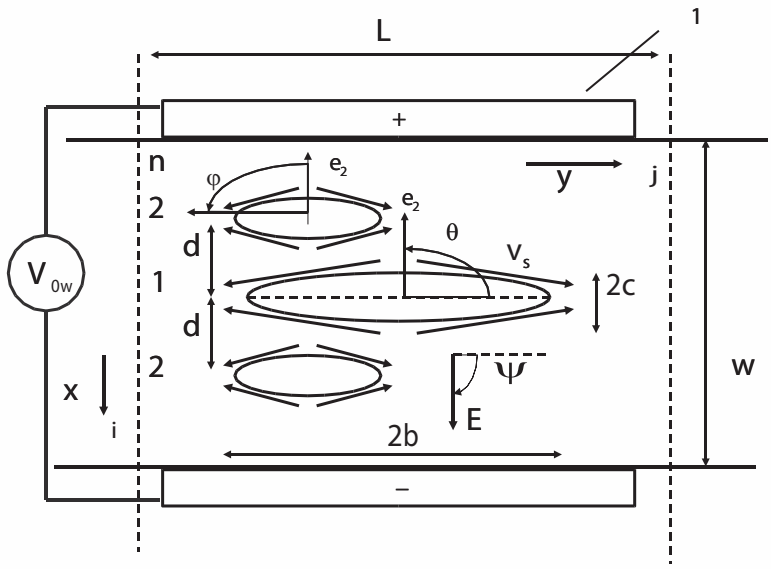

Figure 4.1: Schematic view of ICEO stacking pump. 1: pair of electrodes. Here, $\psi = \theta = \pi/2$ rad, L is the length, w is the width, and V_{0w} is the voltage applied to the electrodes. The ellipse has two semi-axes (b, c) with unit vectors $(\boldsymbol{e}_1, \boldsymbol{e}_2)$ that define the orientation of each semi-axis. Here, we place two 2nd-generation ellipses with lengths b to the left of a 1st-generation ellipse of length $2b$ in order to suppress the reverse flow of the 1st-generation ellipse.

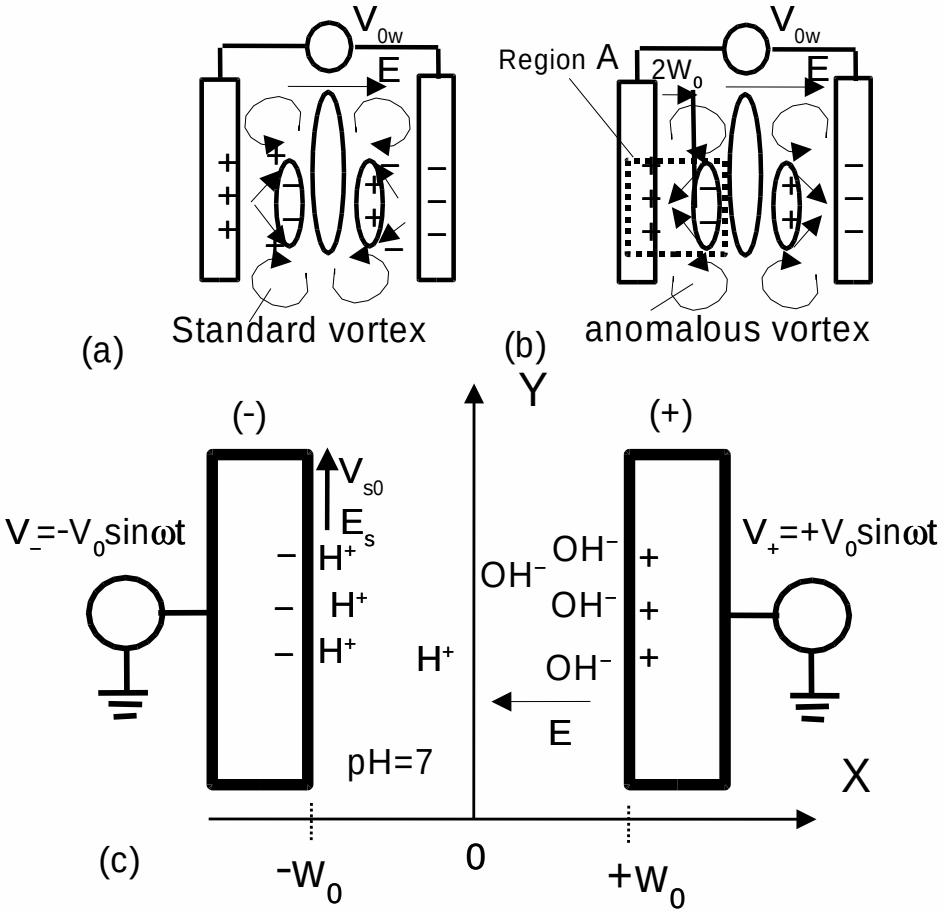

Figure 4.2: Schematic view of a calculation system for 1D-PNP analysis. Standard and anomalous vortex flows are shown in (a) and (b), respectively, and we modeled region A as (c). In (c), $2V_0 \sin \omega t$ is the applied voltage to the electrodes, V_{s0} is a slip velocity on the electrode, and $2W_0$ is the width between electrodes.

cylinders with a large hight ($\sim$110 μm) were microfabricated on a silicon substrate with highresistivity (greater than 1000 Ωcm) by the pyrolysis of a photoresist film with a large hight ($\sim$130 μm) in a reducing forming gas [98]. That is, we used the epoxy-based negative photoresist SU-8 2100 (Microchem Corp., Newton, MA) and spin-coated it on a silicon substrate with a speed of 2000 rpm for 30 s, after spin-coating hexamethyldisilazane (HMDS) on the substrate. The resist was then exposed to UV light through a contact mask. A latent image was developed using the developer and rinsed. After the post- and hard-baking processes, the photoresist was pyrolyzed in a closed-tube furnace in a forming gas atmosphere (98% N_2, 2% H_2) that was introduced into the furnace under a vacuum pressure of 4.1×10^{-4} Pa. Here, the photoresist on the substrate was heated at a rate of approximately 1.5°C/min to 300°C, held at 300°C for 1 h, then heated again at the same rate to 900°C, held at 900°C for 1 h, and cooled down to room temperature. It should be noted that if the vacuum pressure is not sufficiently low in the setting up of the atmosphere or if we use just N_2 gas instead of the forming gas, the resists will burn out.

4.2.3 Observation method

Diluted fluorescent particle suspensions (red fluorescence; Thermo Scientific Co.; $\sim$0.01–0.05% solids; $\sim$1 μm ϕ) were injected into the channel between the electrodes, and then covered with a cover glass placed under a microscope equipped with a digital video camera; that is, the fabricated carbon structures were immersed in deionized water ($\sim$18 MΩcm) containing fluorescent particles that can visualize flow fields for the observation of an ICEO flow around a stacking structure under ac electric fields. We measured the flow fields quantitatively by particle image velocimetry (PIV), which yields a velocity vector at a point by calculating the correlation function between two images at different times [50].

4.2.4 2D flow model in the dc limit

Numerically, we consider a 2D quasi-static Stokes flow without Brownian motion: i.e., we consider the limit in which the Reynolds number Re tends to zero and consider the Peclet number to be infinite. We assume the posts of the conductive cylinder to be polarizable in an electrolytic solution under a dc or ac electric field. The motion of the surrounding fluid must satisfy Stokes equations modified by the inclusion of an electrical stress. However, by using matched asymptotic expansion [26], we can reduce them to the classical Stokes equations as follows:

$$\mu \nabla^2 \boldsymbol{v} - \nabla p = 0, \qquad \nabla \cdot \boldsymbol{v} = 0, \tag{4.1}$$

$$\text{on } S_{\mathrm{p}}^{+(j)}: \quad \boldsymbol{v}^{(j)} = \boldsymbol{v}_{\mathrm{s}}^{(j)}. \tag{4.2}$$

where $S_{\mathrm{p}}^{+(j)}$ is the surface defined as the outer edge of the double layer on the j-th conductive post ($j = 1, 2, \ldots, N$). Further, $\boldsymbol{x}^{(j)}$ ($= -\sin\varphi\ \boldsymbol{i} + \cos\varphi\ \boldsymbol{j}$) is the surface position of the j-th conductive post parameterized by φ, $\boldsymbol{i}$ and $\boldsymbol{j}$ are orthogonal unit vectors in the Cartesian coordinate system, μ ($\sim$1 mPa·s) is the viscosity, $\boldsymbol{v}$ is the velocity, and p is the pressure. Under a wide range of conditions, the local slip velocity $\boldsymbol{v}_s^{(j)}$ is given by the Helmholtz-Smoluchowski formula:

$$\boldsymbol{v}_s^{(j)} = -\frac{\varepsilon\zeta^{(j)}}{\mu}\boldsymbol{E}_{\mathrm{s}}{}^{(j)}, \tag{4.3}$$

where $\boldsymbol{E}_{\mathrm{s}}{}^{(j)}$ is the tangential component of the electric field, ε ($\sim 80\varepsilon_0$) is the dielectric permittivity of the solvent (typically water), and ε_0 is the vacuum permittivity. Here, a zetapotential $\zeta^{(j)}$ around the j-th conductive post is generally defined as $\zeta^{(j)} = \phi_i^{(j)} - \phi_f^{(j)}$, where $\phi_f^{(j)}$ and $\phi_i^{(j)}$ are the final and initial potentials, respectively.

Before calculating the flow field, we solve the electric potential by the boundary element method based on the following Laplace equation: $\nabla^2\phi = 0$. Here, on the one hand, we use the Dirichlet boundary condition for the upper and lower walls (electrodes); that is, $\phi = +0.5V_0$ at $x = 0$ and $\phi = -0.5V_0$ at $x = w$, where V_0 is the voltage applied across the channel. On the other hand, we use the Neumann boundary condition for the left and right walls (i.e., $\boldsymbol{n}\nabla\phi = 0$ at $y = 0$ and L, where $\boldsymbol{n}$ is the surface normal unit vector). In addition to these boundary conditions, to obtain the final potential, we use the Neumann boundary condition (i.e., $\boldsymbol{n}\nabla\phi = 0$) on the metal surface. Furthermore, to obtain the initial potential, we use the condition that the j-th conductive post has an unknown surface potential $\phi_i^{(j)}$ and requires the electrical neutral condition $\oint_{(j)}(\boldsymbol{n}\nabla\phi)ds = 0$. Thus, on the basis of Eqs. (4.1)–(4.3), we can numerically calculate a flow field for a bounded domain. It should be noted that we use the boundary condition that the velocity on the wall of the channel is zero and that the pressures of the inlet and outlet are P_1 and P_2, respectively. (Here, $P_1 = P_2 = 0$ and $\Delta P = P_2 - P_1 = 0$.) In this paper, we will refer to this method as method B, while we will refer the previous method [see Chapter 3] [92] as method A.

4.2.5 1D flow model using the PNP equations

Figures 4.2(a) and (b) show a standard and anomalous vortex flow around conductive posts, respectively. Usually, we believe that a net negative (positive) charge that cancels the positive (negative) induced-charge on the conductive posts exists near the surface of the left-hand side (right-hand side) of the conductive posts under the presence of the external electric field from the left to the right. Thus, as a standard vortex flow, we expect clockwise (CW) and counter clockwise (CCW) vortex flows in the lower and upper left-hand sides, respectively, while one expects CCW and CW vortex flow in the lower and

upper right-hand sides, respectively, as shown in Fig. 4.2(a). However, experimentally, we observe an anomalous reverse vortex flow, as shown in Fig. 4.2(b).

What happens in region A in Fig. 4.2(b)? To the best of our knowledge, there is no design method that explains the flow reversal associated with the stacking structures of conducting posts generally. However, at least in the case of the rocket-shaped structures illustrated in Figs. 4.1, 4.2(a), and 4.2(b), ion dynamics in region A can be analyzed as a 1D problem of an electrolyte cell as a fist step. In other words, if we can assume that elliptical posts are oblate enough to be considered as a flat electrode, we can analyze the ion distribution in region A as the 1D problem, although we need to correct the charging time and applied voltage by considering the total electric circuit. Note that we believe that the requirement of the flatness is very weak and even the circular cylinder can be analyzed, since the main path of the electric field between the smaller post and the electrode is basically 1D during the charging process. Further, as discussed later on Fig. 4.5, a dominant driving force in region A seems to exist on the surface of the smaller elliptical post. Thus, if we can assume that the effective tangential electric field (E_s) that contributes to the maximum slip velocity is the order of the applied electric field between the smaller post and the electrode, the order of the maximum slip velocity on the surface of a smaller elliptical post can be calculated by the integration similar to the procedure of the thin double layer approximation [26].

Thus, to analyze the anomalous reverse vortex flow, we consider the 1D problem of an electrolyte cell bounded by two parallel walls (at $X = \pm W_0$), filled with a $z : z$ electrolyte, at concentration c_0, as shown in Fig. 4.2(c); that is, we consider the dimensionless 1D PNP equations as follows:

$$\frac{1}{\epsilon}\frac{\partial c_p}{\partial t} = -\frac{\partial}{\partial x}(-\frac{\partial c_p}{\partial x} - c_p\frac{\partial \phi}{\partial x}), \tag{4.4}$$

$$\frac{1}{\epsilon}\frac{\partial c_n}{\partial t} = -\frac{\partial}{\partial x}(-\frac{\partial c_n}{\partial x} + c_n\frac{\partial \phi}{\partial x}), \tag{4.5}$$

$$-\epsilon^2\frac{\partial^2 \phi}{\partial x^2} = \rho \tag{4.6}$$

where $c_p = C_p/C_0$ ($c_n = C_n/C_0$) is a non-dimensional concentration of positive (negative) ion, ϕ is a non-dimensional potential, C_p (C_n) is a dimensional concentration of positive (negative) ion, $\rho = c_p - c_n$, $x = X/W_0$, and $\epsilon = \lambda_D/W_0$. Here, λ_D ($= 1$ μm for water at pH $= 7$) is the Debye screening length and $2W_0$ is the width of the gap between electrodes for a 1D PNP problem in Fig. 4.2. We solve Eqs. (4.4)–(4.6) under the boundary condition that

$$\phi = v_\pm \mp \delta_0\epsilon\frac{\partial \phi}{\partial x}, \text{ at } x = \pm 1, \tag{4.7}$$

where $\delta_0 = \lambda_s/\lambda_D$ and λ_s is a length characterizing the compact-layer surface capacitance (e.g., due to a Stern mono layer). Note that we cast the PNP equations in a dimensionless

form using W_0 as the reference length scale, $\tau_c = \lambda_D W_0/D$ as the reference time scale, $\phi_c = kT/ze$ ($\simeq 25$ mV) as the reference potential, and $f_c = 1/\tau_c$ as the reference frequency. Here, D is the ion diffusivity, k is the Boltzmann constant, T is the temperature, and e is the electric charge. We calculate the time evolutions of $c_p(x)$, $c_n(x)$, $\rho(x)$, and $\phi(x)$ in the presence of a dc or ac applied voltage ($v_\pm = v_0$ or $v_\pm = \pm v_0 \sin 2\pi f_0 t$, respectively) by the finite element method (FEM) [for Eq. (4.6)] and the control-volume difference method (CVDM) [for Eqs. (4.4)–(4.5)], since the FEM is convenient for dealing with the mixed boundary condition of Eq. (4.7) and the CVDM is useful to preserve the number of ions precisely. Note that the CVDM is a numerical method for solving partial differential equations that calculates the values of the conserved variables averaged across the volume and thus preserves the number of ions well, while ordinary numerical methods often do not preserve the number of ions.

Now, we evaluate the order of the maximum slip velocities on the smaller elliptical post from the results of the 1D PNP analysis by assuming the existence of the artificial tangential electric filed $E_s = -V_+/W_0$. Note that λ_D is smaller than the radius of curvature of the surface. Thus, in the electric double layer, the charge flux is locally 1D and the flow is parallel to the conductive post. Thus, using the Stokes equations modified by the inclusion of an electrical stress term ($\Delta \boldsymbol{\tau}^e = \rho_e \boldsymbol{E}_s$), we obtain the following equation [26] near the electrodes (or the surface of conductive post):

$$\mu \frac{\partial^2 v_y}{\partial X^2} + \rho_e E_s = 0, \tag{4.8}$$

where ρ_e is a dimensional net charge. Therefore, by integrating Eq. (4.8) under the condition that $v_y = 0$ and $\partial v_y/\partial X = 0$ at $X = -W_0 + \tilde{\lambda}_c$, we obtain the dimensional slip velocity:

$$V_s = -\int_{-W_0+\tilde{\lambda}_c}^{0} \int_{-W_0+\tilde{\lambda}_c}^{0} \rho_e E_s dX' dX/\mu. \tag{4.9}$$

Note that from Eq. (4.9) we can derive Eq. (4.3) if we can assume the ζ potential in the dc limit, and $\tilde{\lambda}_c (= \lambda_c W_0)$ is a length of a condensed layer in which a tangential flow velocity v_y is assumed to be zero. From Eq. (4.9), by using $v_{s,c} = (C_0 N_0 ze)(W_0^2)(kT/zeW_0)/\mu$ as the reference slip velocity, we obtain the non-dimensional time dependent slip velocity:

$$v_s(t) = -\int_{-1+\lambda_c}^{0} \int_{-1+\lambda_c}^{0} \rho e_s(t) dx' dx, \tag{4.10}$$

where $e_s(t) = -v_0 \sin \omega t$ and $-v_0$ for an ac and dc problem, respectively. Further, we define the average slip velocity, the total charge, and the related value as

$$< v_s > = -\int_{t_1}^{t_2} v_s(t) dt/(t_2 - t_1), \tag{4.11}$$

$$C_{t1}(t) = -\int_{-1+\lambda_c}^{0} \rho(x)dx, \tag{4.12}$$

and

$$C_{t2}(t) = -\int_{-1+\lambda_c}^{0}\int_{-1+\lambda_c}^{0} \rho(x)dx'dx, \tag{4.13}$$

respectively. Although we can calculate C_{t2} by using the values of ϕ, we prefer to calculate it by Eq. (4.13); i.e., in the same manner as Eqs. (4.10) and (4.11). Note that in this paper we set $t_2 = 4$ and $t_1 = 2/f_0$ for $f_0 = 1$; for other frequencies, we set $t_2 = 2$ and $t_1 = 2/f_0$.

Generally, a 2D flow velocity $\boldsymbol{v}$ is a function of f, V_{0w}, and $\boldsymbol{x}$, where f is a frequency, V_{0w} is an applied voltage, and $\boldsymbol{x}$ is a position [i.e., $\boldsymbol{v} \equiv \boldsymbol{v}(f, V_{0w}, \boldsymbol{x})$]. Since $\boldsymbol{v}(f, V_{0w}, \boldsymbol{x}) \equiv [\boldsymbol{v}(f, V_{0w}, \boldsymbol{x})/v_A(f, V_{0w})]v_A(f, V_{0w})$, we can generally write the 2D flow velocity as

$$\boldsymbol{v}(f, V_{0w}, \boldsymbol{x}) = v_A(f, V_{0w})\boldsymbol{f}_A(\boldsymbol{x})^{\rm 2D}, \tag{4.14}$$

where v_A is a flow velocity of point A that is the center of region A and $\boldsymbol{f}_A(\boldsymbol{x})^{\rm 2D} \equiv \boldsymbol{v}(f, V_{0w}, \boldsymbol{x})/v_A(f, V_{0w})$. Furthermore, if we can assume that a dominant driving force in region A is the maximum slip velocity on the surface of the smaller elliptical post, the velocity of point A (v_A) is proportional to the maximum slip velocity of the surface of the smaller elliptical post (v_s); i.e., $v_A(f, V_{0w}) = C_A v_s(f, V_{0w})$, where C_A is a constant. Therefore, we can write the 2D flow velocity as $\boldsymbol{v}(f, V_{0w}, \boldsymbol{x}) \simeq v_s(f, V_{0w})\boldsymbol{f}_A(\boldsymbol{x})^{\rm 2D}$ under the condition that $C_A \simeq 1$. Thus, by assuming that $v_s(f, V_{0w}) \simeq v_s^{\rm 1D}$ and $\boldsymbol{f}_A(\boldsymbol{x})^{\rm 2D} \simeq \boldsymbol{f}_A(\boldsymbol{x})^{\rm 2D}_{\rm methodB}$, we can obtain the following equation:

$$\boldsymbol{v}(f, V_{0w}, \boldsymbol{x}) \simeq v_s^{\rm 1D}(f, V_{0w})\boldsymbol{f}_A(\boldsymbol{x})^{\rm 2D}_{\rm methodB}, \tag{4.15}$$

where $v_s^{\rm 1D}(f, V_{0w})(\equiv < v_s >)$ is the maximum slip velocity calculated by the 1D PNP analysis and $\boldsymbol{f}_A(\boldsymbol{x})^{\rm 2D}_{\rm methodB}$ is the 2D flow velocity vector that was calculated by the coupled simulation method (method B) and normalized by the value of point A. Here, we selected the sign of $\boldsymbol{f}_A(\boldsymbol{x})^{\rm 2D}_{\rm methodB}$ so that it represents the standard vortex flow illustrated in Fig. 4.2(a).

To compare the experimental results performed for the 2D system in Fig. 4.2(b) and the theoretical results performed for the 1D system in Fig. 4.2(c), we need to reconsider a charging time and an applied voltage as a whole circuit. Namely, we assume that the concerning system is a voltage divider consisting of four resistors ($R_1 = \rho_b 2W_0/hb$, $R_2 = \rho_b\delta/hb$, $R_3 = \rho_b\delta/hb$, and $R_4 = \rho_b 2W_0/hb$, where ρ_b is the bulk resistivity). Thus, the applied voltage ($2v_0kT/ze$) between the smaller post and the electrode is $\sqrt{2}V_{0w}2W_0/(4W_0 + 2\delta)$ [i.e., $v_0 = \sqrt{2}(\frac{2W_0}{4W_0+2\delta})V_{0w}/2(\frac{kT}{ze})$]. Note that V_{0w} is the effective value and $2v_0kT/ze$ is a peak to peak value. Of course, W_0 is obtained from the geometrical conditions [i.e., $W_0 = (w - 6c - 2\delta)/4$]. Furthermore, under the assumption

that $L \gg 2b$, we approximate the charging time of a 2D system τ_c^{2D} by the RC relaxation time [6] for the whole electrolyte cell bounded by two parallel walls with the distance w [i.e., $\tau_c^{2D} \simeq \lambda_D w/2D$]. Thus, we assume that $f_0 = f/f_c^{2D} = f\tau_c^{2D}$ [e.g., $f_0 = 40$, $\epsilon(= \lambda_D/W_0) = 0.005$, $\tau_c^{2D} = 0.8$ s, and $W_0 = 0.2$ mm, when $w = 1.6$ mm, $\delta/w = 0.05$, $c/w = 0.065$, $D = 1.0 \times 10^{-9}$ m^2/s, $f = 50$ Hz, and $\lambda_D = 1$ μm]. Here, $\delta_0(= \lambda_s/\lambda_D)$ can be fixed as $\delta_0 \sim 1$, since λ_s is conceptually a similar parameter to λ_c. It should be noted that we packed most of the errors into λ_c [i.e., we use just one adjusting parameter λ_c to describe the flow field].

Although we derived Eq. (4.15) as a better approximation for an exact formulation of Eq. (4.14), Eq. (4.15) is suitable for analyzing the problem of reverse flow, because the 2D flow model in the dc limit is reliable to some extent to obtain a spatial distribution of the flow velocity and the 1D PNP model can describe an ion distribution in the presence of ac electric fields. Thus, under the assumption that there is no flow normal to the conductive surface near the surface and the ion distribution normal to the surface near the surface is described by 1D PNP equations, Eq. (4.15) is justified. In other words, our 1D PNP model coupled with the Stokes equation [Eq. (4.8)] can be used to explain the phenomena associated with a 2D conducting post under the thin double electric layer approximation. Fortunately, the above assumption or the thin double electric layer approximation is usually satisfied in the concerning system, since the length of a diffused layer is always much smaller than the concerning gap length ($2W_0$). Actually, Eq. (4.15) is a natural correction of the thin double electric layer theory described by Eqs.(4.1) to (4.3).

4.3 Results

4.3.1 Fabrication results

Figure 4.3 summarizes the fabrication results of the carbon structures. We first fabricated a photoresist structure made of SU-8 with a large height ($h = 130$ μm) by the standard process [in Fig. 4.3(a)]; then, we obtained a carbon stacking structure by pyrolysis in a reducing gas [in Fig. 4.3(b)]. Figure 4.3(b) shows an example of fabricated carbon stacking structures with carbon electrodes. In Fig. 4.3(b), the upper and lower black structures are carbon electrodes. However, we cannot use them for the observations because they break easily during preparation. Thus, we used copper electrodes ($h \sim 100$ μm) that were attached after removing the carbon electrodes in the subsequent observations of ICEO flow fields. Further, as shown in Figs. 4.3(a) and (b), the edge of the fabricated carbon structures is deformed by shrinkage during pyrolysis, whereas the edge of the resist structure before carbonization is sharp. Figure 4.3(c) shows the side view of the fabricated carbon cylinder. From this photograph, we measured the height of the carbon structures as $h \sim 110$ μm. Figure 4.3(d) shows an example of fabricated carbon stacking structures with broken carbon electrodes. Unfortunately, as shown in Fig. 4.3(d), those carbon

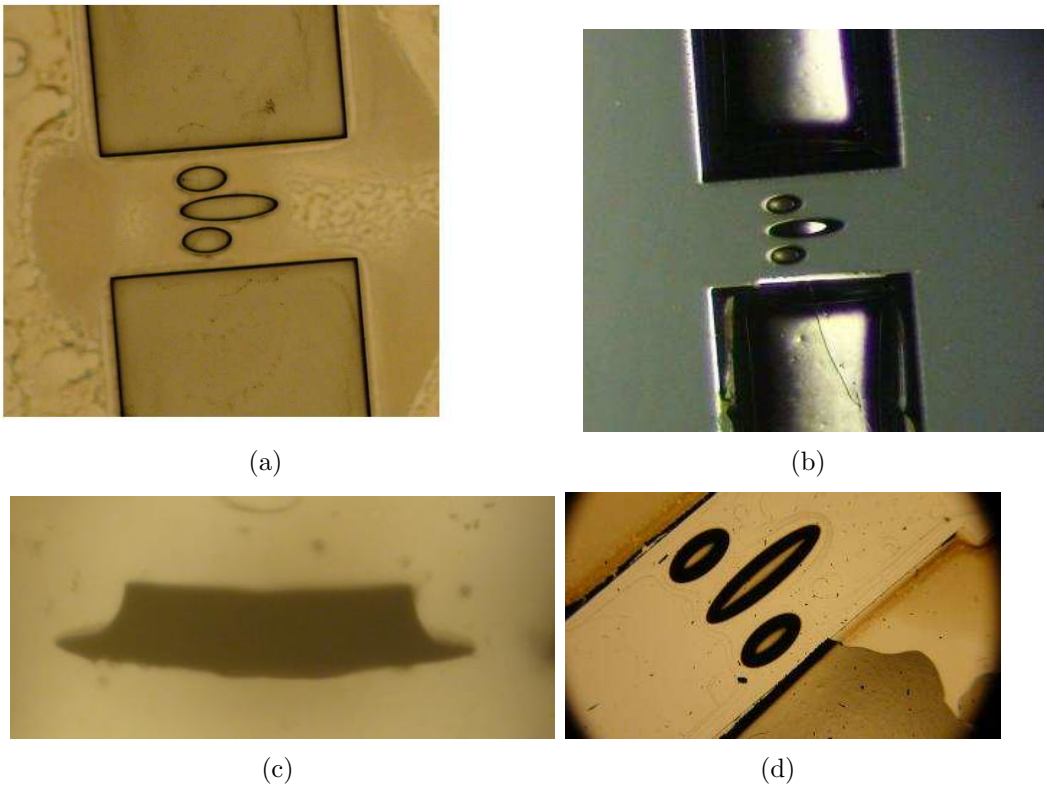

Figure 4.3: (Color online) Fabrication results of carbon stacking structures by pyrolysis of photoresists in reducing gas (98% N_2; 2% H_2; maximum temperature of 900°C). (a) Micrograph of SU-8 photoresist structure before carbonization ($h = 130$ μm, $w = 400$ μm, $b = 160$ μm, $c = 40$ μm, and $\delta = 20$ μm). (b) Micrograph of carbon stacking structure with carbon electrodes ($h = 110$ μm and $w = 400$ μm). (c) Side view of carbon structure. (d) Micrograph of carbon structure with broken electrodes ($h = 110$ μm and $w = 1.6$ μm).

electrodes having a fairly large area were usually broken because of the residual stress in the pyrolysis and the weakness of the adhesive force between the substrate and the carbon structure. Furthermore, those carbon stacking structures having a relatively high aspect ratio ($w = 200$ to 800 μm for $h \sim 110$ μm) often broken down by the electrostatic rotational force during the experiment, and they often broke down just because of the surface tension caused by the introduction of an aqueous solution. Thus, we used a carbon stacking structure having a low aspect ratio ($w = 1600$ μm for $h \sim 110$ μm) between copper electrodes ($h \sim 100$ μm) in the observations of ICEO flow fields.

4.3.2 Observations of asymmetrical reverse vortex flows

Figure 4.4 shows the results of experimental observations and their data analysis. As shown in Fig. 4.4, we find that two strong reverse vortex flows are generated on the left-hand side of the stacking structure (in the rear of the rocket-shaped formation) by the application of a large ac voltage (∼15 V) at a low frequency (50 Hz) for the large-width channel ($w = 1.6$ mm), whereas just an ICEO flow exists along a carbon post ($h \sim 110$ μm) on the right-hand side. Namely, our basic prediction that an asymmetrical stacking structure causes asymmetrical vortex flows [see Chapter 3] [92] is proved experimentally. However, there are three major differences from the previous predictions. (1) The direction of vortices in the experiments is in the opposite to that of the theory; (2) the observed flow velocities of the vortices are much smaller than those of the theory; (3) two strong vortices appear on the left-hand side of the stacking structure in the experiment, while they appear on the right-hand side in the previous theory.

Figure 4.5 shows the transient flow around ac 8 V when the applied voltage is increased from 0 to 15 V. As shown in Fig. 4.5, two flow fronts are pushed out from the upper and lower carbon surfaces toward the upper and lower electrodes, respectively, as a transient flow. Thus, we believe that the flows originate not from a bulk force due to a bulk charge but from a surface force due to a surface charge; that is, although temperature-induced inhomogeneities in medium conductivity and permittivity due to Joule heating sometimes generate electrothermal (ET) flow [28], we believe that our observed flow is an ICEO flow originating from the slip velocity due to ICEO on the surface of carbon posts. Furthermore, in the initial stage of the experiment, we observed the generation of bubbles as shown in Figs. 4.4(a) and 4.5, but it ceased under the condition that $V_{0w} < 20$ V; thus, we could continue to carry out our observations smoothly. Moreover, from this fact, we believe that the observed flow reversal in our experiments dose not relate to the Faradaic reactions.

4.3.3 Results of 2D flow analysis by the coupled simulation

Figure 4.6 shows the results of theoretical calculations performed by the coupled calculation method (method B) that yields more precise results than previous predictions [see

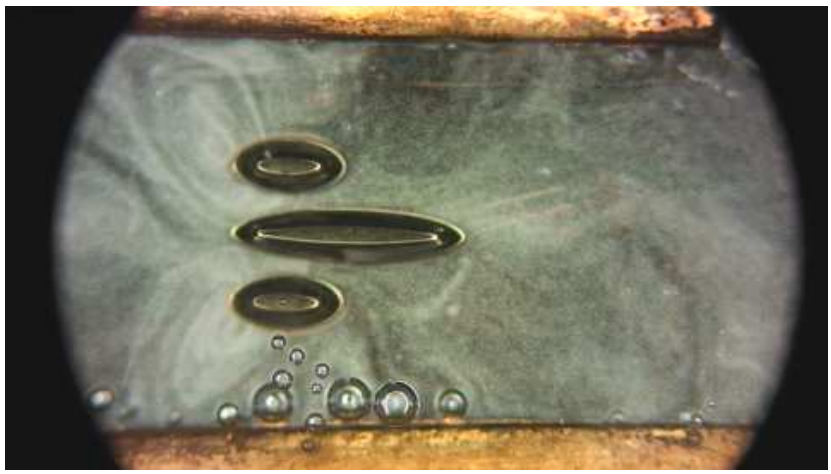

(a)

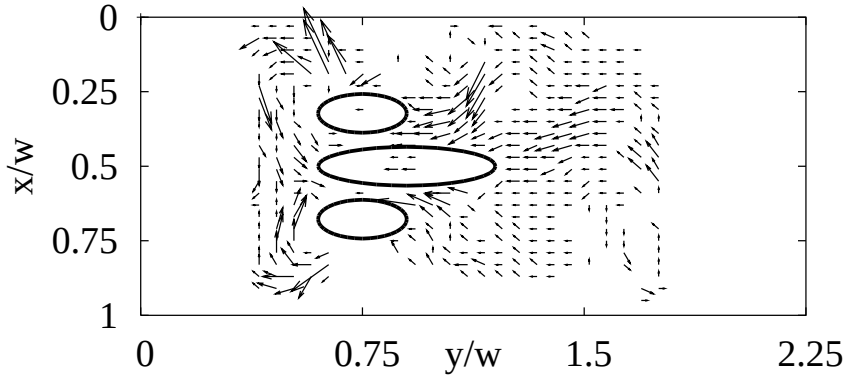

(b)

Figure 4.4: (Color online) Experimental observations of asymmetrical reverse vortex flows around a carbon stacking structure. (a) Micrograph of asymmetrical vortex flow ($V_{0w} = 15$ V); (b) Experimental flow field obtained by PIV. ($V_{0w} = 15$ V). Here, $V_{0w} = 15$ V, $f = 50$ Hz, $w = 1.6$ mm, $c/w = 0.065$, $b_1/c = 4.6$, $b_2/c = 2.3$, $\delta/w = 0.05$, $t_s U_c/w = 0.00405$, and $E_0 = 9.4$ kV/m.

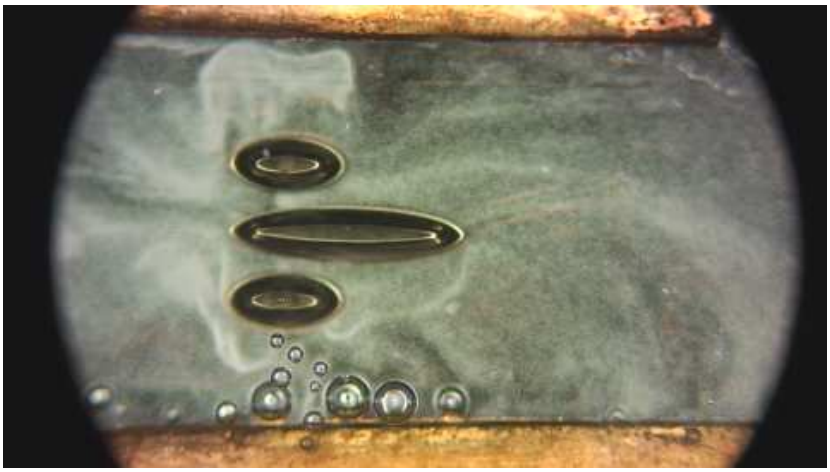

Figure 4.5: (Color online) Micrograph of transient flow around $V_{0w} \sim 8$ V, when V_0 is increased from 0 to 15 V. Here, $V_{0w} = 15$ V, $f = 50$ Hz, $w = 1.6$ mm, $c/w = 0.065$, $b_1/c = 4.6$, $b_2/c = 2.3$, $\delta/w = 0.05$, $t_s U_c/w = 0.00405$, and $E_0 = 9.4$ kV/m.

Chapter 3] [92]. As shown in Fig. 4.6(a), unlike previous predictions, the precise calculations in this study show that stacking structures accelerate a reverse flow rather than suppressing it for a microfluidic channel. This is because the potential and electric fields are largely deformed by the stacking structure as shown in Figs. 4.6(b) and (c); thus, the ζ potentials and slip velocities around the conductive posts are also largely deformed, as shown in Figs. 4.6(d) and (e). In particular, the slip velocity of a bounded domain of an upper conductive post (triangle) around $\varphi = 70°$ becomes approximately three times that of an unbounded domain (broken line), and consequently, a reverse flow seems to be accelerated rather than suppressed. Although there is a qualitative difference between the experimental flow fields [in Fig. 4.4] and the theoretical flow fields [in Fig. 4.6(a)], we believe that this is mainly because of the difference between the experimental and theoretical conditions of the flow resistance (i.e., unlike in the calculation, we cannot expect an ideally short channel in the actual experiment). Thus, we believe that the experimental flow fields [in Figs. 4.4 and 4.6(a)] are explained theoretically, except for the problem of the anomalous reverse vortex flow, by using the coupled calculation method that considers the boundary effects precisely.

Further, Fig. 4.6(f) shows the comparison between the experimental results and the theoretical results obtained by method B in the dependence of v_y on x/w at $y/w = 0.55$ and 1.25 when $V_{0w} = 15$ V. As shown in Fig. 4.6(f), they also just agree with each other fairly well. Further, $U_p^{\text{method B}} = -1.28$ mm/s, $\Lambda_{\text{eff}}^{\text{method B}} = -0.0025$, and $U_p^{\text{eff,method B}} (= \Lambda_{\text{eff}}^{\text{method B}} U_p^{\text{method B}}) = +3.2$ μm/s, while $U_p^{\text{experiment}}$ is approximately -3 μm/s; i.e., $U_p^{\text{eff,method B}}$ is not consistent with $U_p^{\text{experiment}}$. Nonetheless, we believe that method B is more precise method than method A, since method B considers boundary

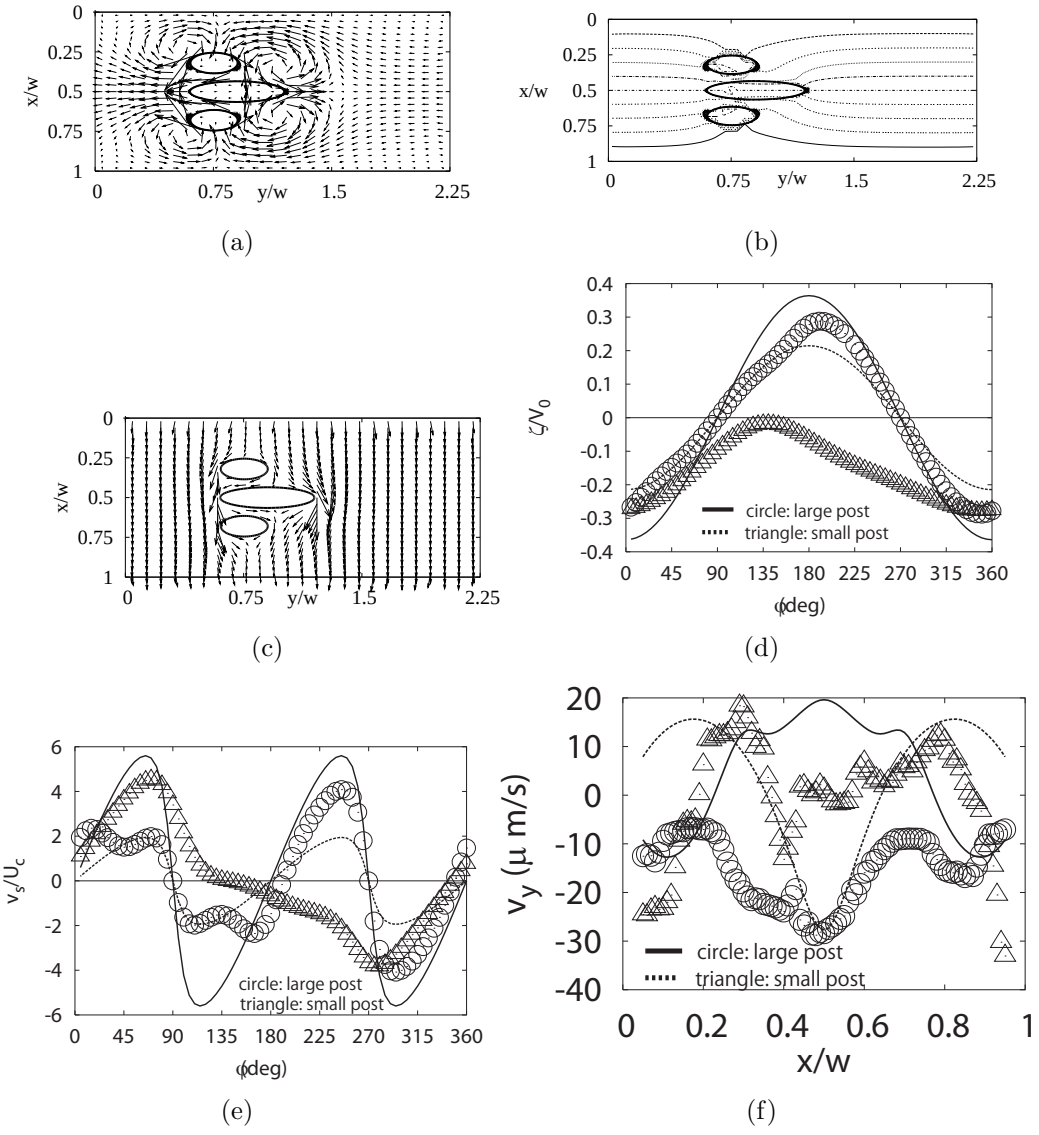

Figure 4.6: Theoretical results obtained by the coupled calculation method (method B) that considers precise boundary conditions for a bounded domain. (a) Theoretical flow field (method B); (b) potential map; (c) electric field; (d) ζ potential; (e) slip velocity; (f) dependence of v_y on x/w ($V_{0w} = 15$ V). In (d) and (e), the open circles and triangles (the solid and broken lines) show the results around larger and smaller elliptical posts, respectively, for a bounded domain (for an unbounded domain). In (f), the triangles and circles (solid and broken lines) show the experimental (theoretical) results of v_y at $y/w = 0.55$ and 1.25, respectively, and $\Lambda_{\rm eff}(\equiv v_y^{\rm experiment}/v_y^{\rm method\ B}) = -0.0025$; $t_s U_p^{method\ B}/w = -8.02 \times 10^{-4}$; e.g., $U_p^{\rm method\ B} = -1.28$ μm/s and $U_p^{\rm eff,method\ B}(= \Lambda_{\rm eff} U_p^{\rm method\ B}) = +3.2$ μm/s.

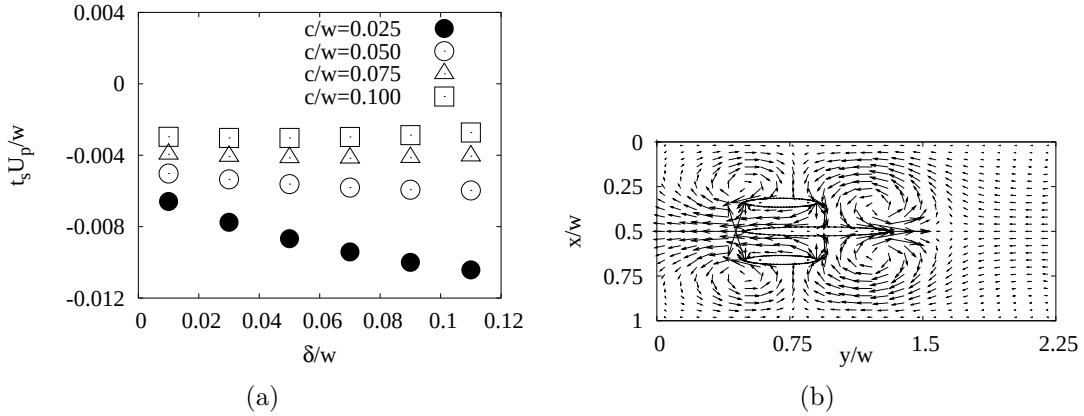

(a) (b)

Figure 4.7: Design of the ICEO stacking pumps by the coupled calculation method (method B) that considers precise boundary conditions for a bounded domain. (a) U_p vs. δ; (b) theoretical flow field ($c/w = 0.025$ and $\delta/w = 0.11$); Here, $c/w = 0.025$ to 0.100, $b_1/w = 0.4$, $b_2/w = 0.2$, $T_0U_c/w = 0.02$, and $U_c = \epsilon c E_0^2/\mu$; e.g., if $T_0 = 1$ ms, $\mu = 1$ mPa·s, and $w = 0.1$ mm, then $E_0 = 21$ kV/m.

conditions precisely. Probably, the small value of U_p has a large error.

Figure 4.7 shows the design of the ICEO stacking pumps by the coupled calculation method (method B). As shown in Fig. 4.7(a), the absolute value of U_p increases monotonically as the gap distance δ increases, and the sign of U_p is negative. Surprisingly, these results are contrary to the previous results obtained by method A (Fig. 3.3(a) in Chapter 3; Fig. 3 in Ref. [92]) (i.e., method A suggested that U_p decreases monotonically as δ increases, and the sign of U_p is positive). However, method B also predicts that stacking structures can generate a large net flow to the level of the previous prediction. In particular, when c/w is small and δ/w is large, we theoretically obtain a large net flow. Figure 4.7(b) shows the flow field by method B under the conditions that $\delta/w = 0.11$, $c/w = 0.025$, and $T_0U_c/w = 0.02$. In this case, we theoretically obtain a large net flow that $T_0U_p^{\text{method B}}/w = -1.0$; e.g., $U_p^{\text{method B}} = -1.0$ mm/s when $V_{0w} = 2.1$ V, $w = 100$ μm, $T_0 = 1$ ms, and $\mu = 1$ mPa·s.

4.3.4 Results of nonlinear dependence of $|\boldsymbol{v}|$ on V_{0w}

To examine our 1D PNP model and the predictions (that will be explained in detail in Sec. 4.3.5), we re-measured the same sample again in detail, unfortunately after keeping it for a long period (∼5 months) in the air. Figure 4.8(a) shows the typical observation results of the stream lines at $V_{0w} = 16$ V, and Fig. 4.8(b) shows its flow fields measured by PIV. Figures 4.8(a) and (b) show the similar results to those of Figs. 4.4(a) and (b), respectively, and show the same characteristics [i.e., we also find the asymmetrical reverse

(a)

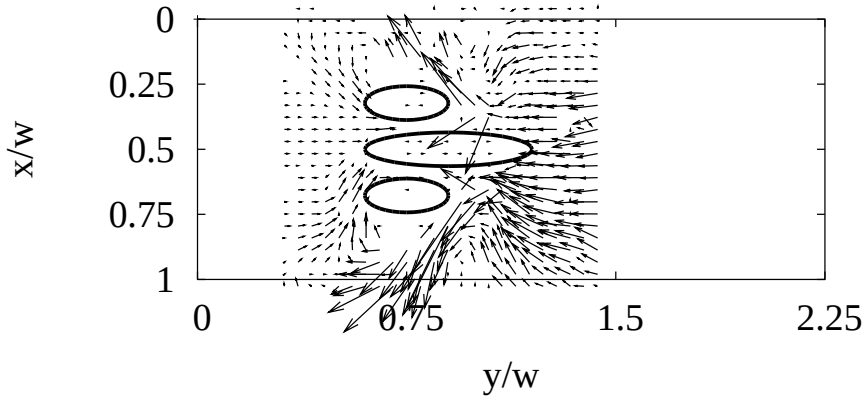

(b)

Figure 4.8: (Color online) Experimental observations at $V_{0w} = 16$ V. (a) Micrograph of asymmetrical vortex flow ($V_{0w} = 16$ V); (b) experimental flow field by PIV ($V_{0w} = 16$ V); Here, $f = 50$ Hz, $w = 1.6$ mm, $c/w = 0.065$, $b_1/c = 4.6$, $b_2/c = 2.3$, and $\delta/w = 0.05$.

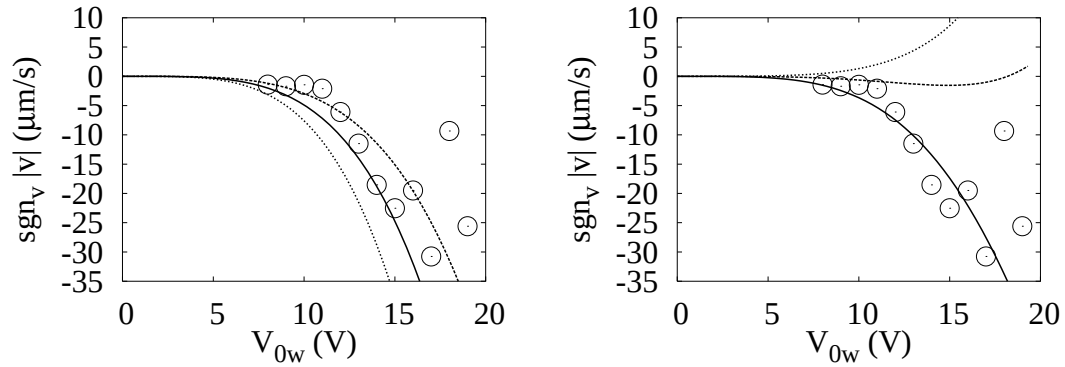

Figure 4.9: Comparison between the experimental results and theoretical results using Eq. (4.14) by the 1D PNP equations and 2D flow analysis. (a) Dependence of $sgn_v|v|$ on V_{0w} at $\lambda_c = 0.20$, 0.22, and 0.25. ($f_0 = 40$, $\epsilon = 0.0050$, and $\delta_0 = 1$); (b) Dependence of $sgn_v|v|$ on V_{0w} at $f_0 = 37$, 38, and 40. ($\lambda_c = 0.20$, $\epsilon = 0.0045$, and $\delta_0 = 1$); Here, the circle shows the experimental results of $\mathrm{sgn}_v|v|$ at point A [$(x_A/w, y_A/w) = (0.1375, 0.75)$]. In (a), the dashed, solid, and broken lines are the theoretical results at $\lambda_c = 0.20$, 0.22, and 0.25, respectively. In (b), the dashed, broken, and solid lines are the theoretical results at $f_0 = 37$, 38, and 40, respectively. In (a) and (b), "sgn_v" represents the sign of $\boldsymbol{v}$, and the sign is defined as positive (negative) for the direction of the standard (anomalous) vortex flow; $w = 1.6$ mm, $c/w = 0.065$, $b_1/c = 4.6$, $b_2/c = 2.3$, $\delta/w = 0.05$, $\tau_c^{2D} \simeq 0.8$ s, $W_0 = 0.2$ mm, $D = 1.0 \times 10^{-9}$ m^2/s, $\lambda_D = 1$ μm, and $\Delta t = 0.001$.

vortex flow in Figs. 4.8(a) and (b)]. It should be noted that, as shown in Fig. 4.8(a), there was no bubble between electrodes, since we operated under the condition that $V_{0w} < 20$ V.

Figure 4.9 (a) shows the comparison between the experimental results of $\boldsymbol{v}$ and theoretical results using Eq. (15) by the 1D PNP equations and 2D flow analysis. In Fig. 4.9 (a), the circle shows the experimental results of $\mathrm{sgn}_v|v|$ at point A [$(x_A/w, y_A/w) = (0.1375, 0.75)$], while the broken, solid, and dashed lines are the theoretical results at $\lambda_c = 0.20$, 0.22, and 0.25, respectively. Here, "$\mathrm{sgn_v}$" represents the sign of $\boldsymbol{v}$, and the sign is defined as positive (negative) for the direction of the standard (anomalous) vortex flow. In this analysis, λ_c is an only adjusting parameter when we fix $\delta_0 = 1$. Namely, other parameters are determined by the experimental conditions (i.e., $f_0 = 40$, $\epsilon = 0.005$, $\tau_c^{2\mathrm{D}} = 0.8$ s, $W_0 = 0.2$ mm, $w = 1.6$ mm, $\delta/w = 0.05$, $c/w = 0.065$, $D = 1.0 \times 10^{-9}$ m^2/s, $f = 50$ Hz, $\lambda_D = 1$ μm. and $|\boldsymbol{f}(x_A)^{2\mathrm{D}}| = 1$). Thus, as shown in Fig. 4.9 (a), we find that the theoretical flow velocities by the 1D PNP equations agree with the experimental results fairly well. when we assume that $\lambda_c = 0.22$. In particular, we find that the 1D PNP theory succeeds in predicting the flow reversal at 50 Hz and the order of the flow velocities correctly. Thus, $v_s^{1\mathrm{D}}$ in Eq. (8.15) is reliable; i.e., Eq. (8.15) [$\boldsymbol{v}(f, V_{0w}, \boldsymbol{x}) = v_s^{1\mathrm{D}}(f, V_{0w})\boldsymbol{f}_A(\boldsymbol{x})^{2\mathrm{D}}_{\mathrm{methodB}}$] is reliable to some extent, since we already showed that $\boldsymbol{f}_A(\boldsymbol{x})^{2\mathrm{D}}_{\mathrm{methodB}}$ is reliable to some extent. Further, we find instability in the experimental results of $|\boldsymbol{v}|$ in the range that $16 \leq V_{0w} \leq 19$ as shown in Fig. 4.9 (a); We think that this is a sign that a Faradaic reaction start to affect an ICEO flow, since we rely on the stability of our PIV results that use about 70 pair images for ensemble averaging.

The good agreement between the experimental and theoretical predictions in Fig. 4.9 (a) is surprising since we did not assume that the relation between the voltage and the velocity is quadratic. In other words, the relation between the voltage and the velocity is very complex and generally has a strong nonlinearity as mentioned later on Figs. 4.13(b) and 4.14(b), and thus it is very difficult to obtain a suitable dependence of $sgn_v|\boldsymbol{v}|$ on V_{0w}, a suitable order of the magnitude, and a suitable sign at the same time with one adjusting parameter λ_c, although the value of λ_c may have a large error due to the inaccuracy of C_A (= 1). In fact, the estimation of charging time affects seriously as shown in Fig. 4.9 (b). In Fig. 4.9 (b), the dashed, broken, and solid lines are the theoretical results at $f_0 = 37$, 38, and 40, respectively, when $\lambda_c = 0.20$, $\epsilon = 0.0045$, and $\delta_0 = 1$. Namely, although a slight decrease (∼10 %) of ϵ affects just limitedly the functional form (solid line), a slight decrease (∼5-8 %) of f_0 results in the dramatic change on its functional form and sign (broken and dashed lines). Thus, we believe that our assumptions for the charging time and applied voltage are appropriate as a first attempt, and the 1D PNP analysis is valid to explain the generation of the flow reversal around the stacking structures of elliptical conductive posts.

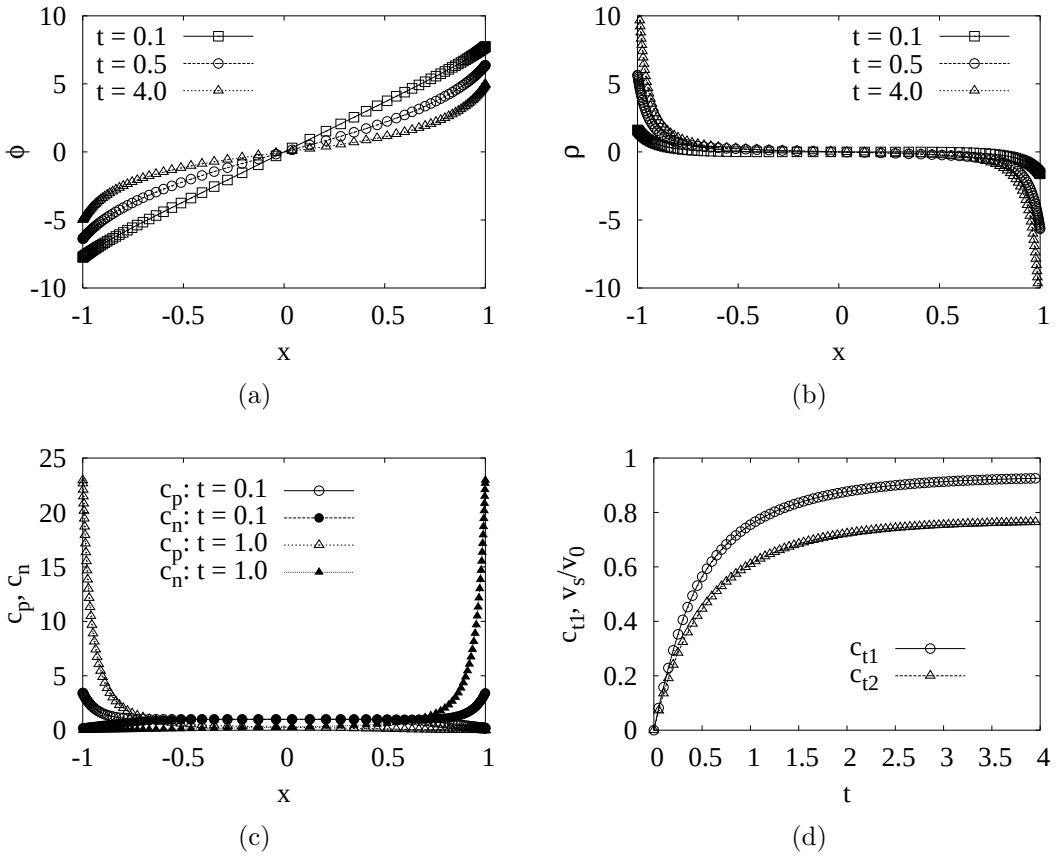

Figure 4.10: Results of dc analysis by the 1D PNP equations. (a) Potential distribution; (b) charge distribution; (c) ion density distribution; and (d) time evolutions of c_{t1} and v_s/v_0; Here, $\epsilon = 0.2$, $\delta_0 = 1.0$, $v_0 = 10$ (dc), and $\Delta t = 0.001$.

4.3.5 Results of diffused-charge analysis by the 1D PNP equations

Figure 4.10 shows the results of dc analysis by the 1D PNP equations. By applying a dc voltage at the initial time ($t = 0$), the distributions of the potential and charge are changing as shown in Fig. 4.10(a) and (b), respectively, for $\epsilon = 0.2$, $\delta_0 = 1.0$, $\lambda_c = 0$, and $v_0 = +10$ (dc). As shown in Fig. 4.10(b), the region ($x < -0.8$) near the negative electrode (the electrode of the left-hand side) charged plus, while the region ($x > +0.8$) near the positive electrode (the electrode of the right-hand side) charged minus, since the positive (negative) ions moves toward the left (right) in the presence of the electric field from the right to left as shown in Fig. 4.10(c). Thus, the potential in the bulk region ($-0.8 < x < +0.8$) approaches zero by the screening effect of the induced-charge as t increases, as shown in Fig. 4.10(a). These results are similar to the results of those

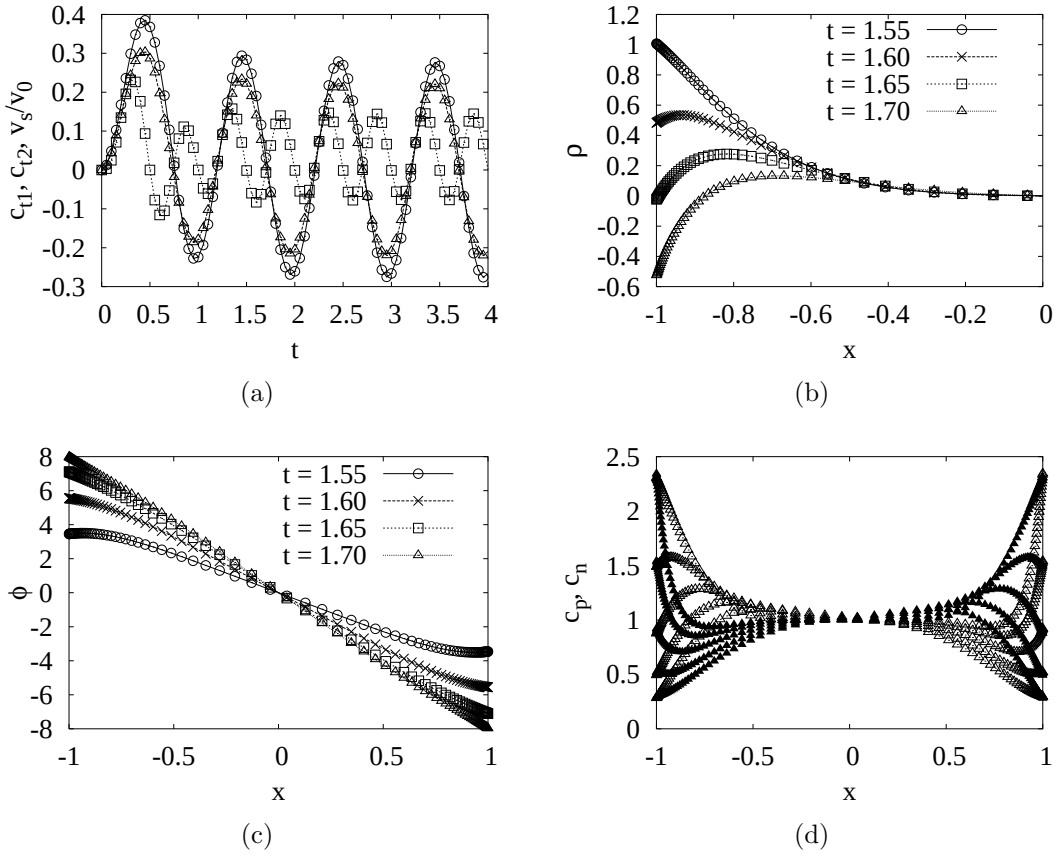

Figure 4.11: Results of ac analysis at a low voltage with a low frequency by the 1D PNP equations. (a) Time dependence of c_{t1}, c_{t2}, and v_s/v_0; (b) charge distribution; (c) potential distribution; and (d) ion density distribution; Here, $\epsilon = 0.2$, $\delta_0 = 1.0$, $v_0 = 100$ (ac), $f_0 = 1$, and $\Delta t = 0.001$. In (a), the circle, triangle, and square show c_{t1} c_{t2}, and v_s, respectively. In (d), the open and closed triangles show c_p and c_n, respectively, at $t = 1.55$, 1.60, 1.65, 1.70, and 1.75.

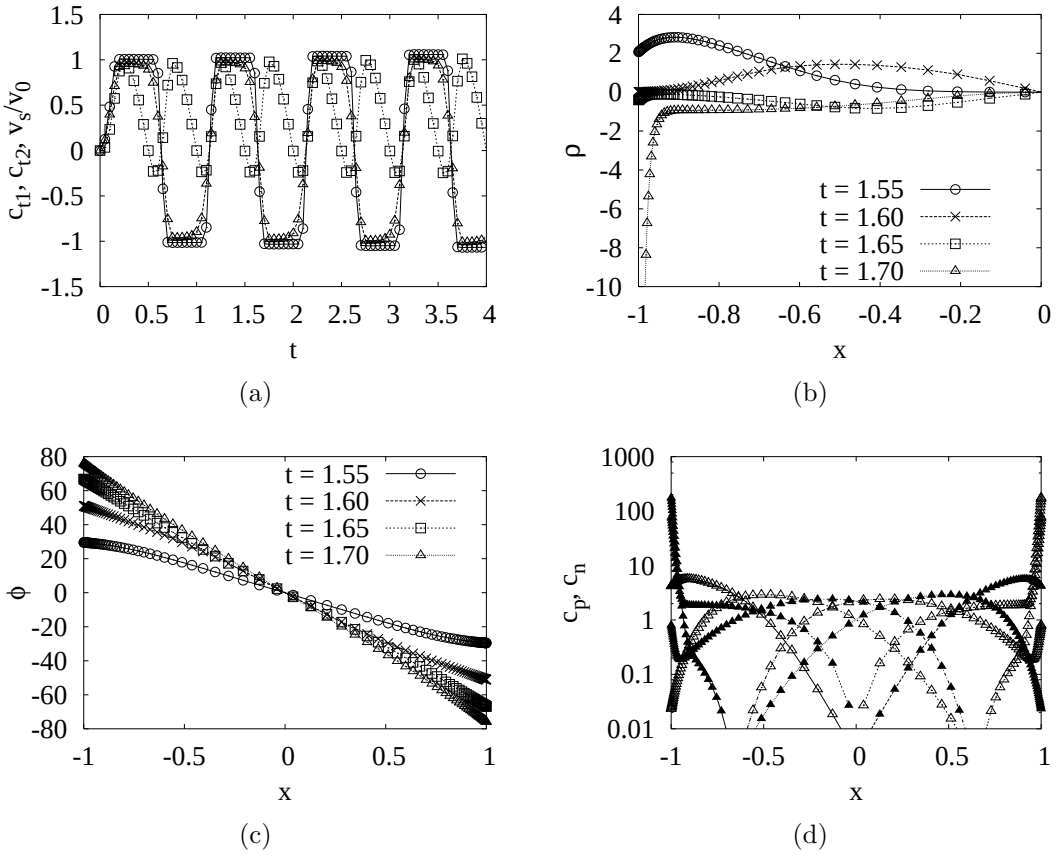

Figure 4.12: Results of ac analysis at a high voltage with a low frequency by the 1D PNP equations. (a) Time dependence of c_{t1}, c_{t2}, and v_s/v_0; (b) charge distribution; (c) potential distribution; and (d) ion density distribution; Here, $\epsilon = 0.2$, $\delta_0 = 1.0$, $v_0 = 100$ (ac), $f_0 = 1$, and $\Delta t = 0.001$. In (a), the circle, triangle, and square show c_{t1} c_{t2}, and v_s, respectively. In (d), the open and closed triangles show c_p and c_n, respectively, at $t = 1.55$, 1.60, 1.65, 1.70, and 1.75.

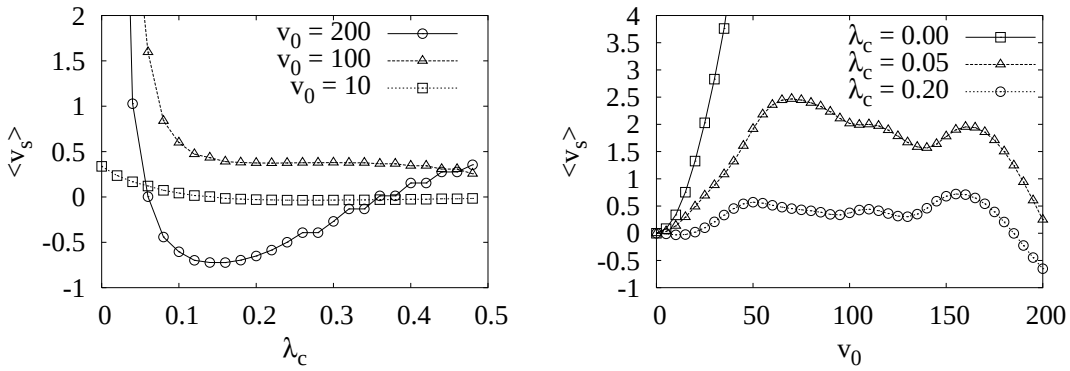

Figure 4.13: Results of average slip velocities at a low frequency by the 1D PNP equations. (a) the dependence of $< v_s >$ on λ_c ($f_0 = 1$) and (b) the dependence of $< v_s >$ on v_0 ($f_0 = 1$); Here, $\epsilon = 0.2$, $\delta_0 = 1.0$, $f_0 = 1$, and $\Delta t = 0.001$.

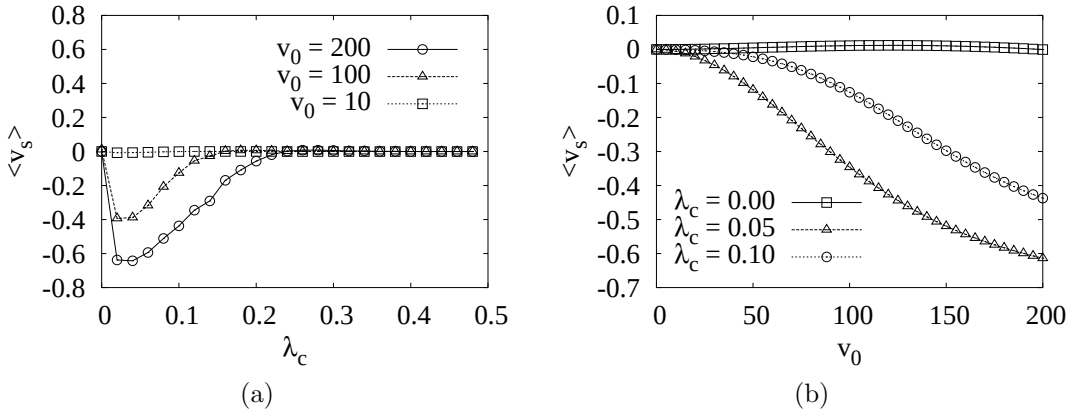

Figure 4.14: Results of average slip velocities at a high frequency by the 1D PNP equations. (a) the dependence of $< v_s >$ on λ_c ($f_0 = 50$); (b) the dependence of $< v_s >$ on v_0 ($f_0 = 50$); Here, $\epsilon = 0.2$, $\delta_0 = 1.0$, and $\Delta t = 0.0001$.

found in Refs. [6, 45]. Further, as shown in Fig. 4.10(d), the total charge c_{t1} increasing monotonously, and of course the sign of slip velocity is always plus.

Figure 4.11 shows the results of ac analysis at a low voltage ($v_0 = 10$) with a low frequency ($f_0 = 1$). As shown in Fig. 4.11(a), by applying an ac voltage at $t = 0$, the total charge c_{t1} ($\bigcirc$) and related value c_{t2} ($\triangle$) alternate the signs, and the slip velocity v_s also alternates its sign since the phase is different between a induced-charge and an applied field. Figure 4.11(b) shows the anomalous positive charge remained near the electrode of the left-hand side after the sign of the applied electric field changed from plus to minus. Figure 4.11(c) shows that the screening effect does not work sufficiently for the ac applied voltage and thus the bulk electric field does not become zero. Figure 4.11(d) shows the time evolutions of c_p and c_n during the transition period. In Fig. 4.11(d), the open and closed triangles show c_p and c_n, respectively, at $t = 1.55$, 1.60, 1.65, 1.70, and 1.75. Although the plus-ion rich region is replaced by the minus-ion rich region by the inversion of the applied electric field as shown in Fig. 4.11(d), the phase retardation between the induced-charge and applied electric field occurs since the diffusion velocity of ions is very slow. We believe that the remaining opposite charge due to the phase retardation is a natural origin of the flow reversal phenomena.

Figure 4.12 shows the results of ac analysis at a high voltage ($v_0 = 100$) with a low frequency ($f_0 = 1$). The results are intrinsically the same as the results of Fig. 4.8 except that ions are exhausted because of the large voltage as shown in Fig. 4.12(d), and thus c_{t1} and c_{t2} have flat periods. At room temperature, $v_0 = 100$ corresponds to $V_0 = 2.5$ V. It should be noted that the "ion crowding" and "steric effects" [90, 44, 45, 4] probably do not happen in our situation, since the concentration of ions ($C_0 = 10^{-7}$ mol/l for water) is much smaller than the concentration of the water ($C_w \simeq 55.6$ mol/l).

Figure 4.13 shows the results of the average slip velocities $< v_s >$ at a low frequency ($f_0 = 1$). As shown in Fig. 4.13(a), we cannot obtain the negative value of $< v_s >$ at $\lambda_c = 0$ (i.e., if we do not assume the existence of the condensed layer, we cannot explain the generation of flow reversal at low frequency). Figure 4.13(b) shows the dependence of $< v_s >$ on v_0. We find that complex nonlinearities of $< v_s >$ on v_0 exist at a low frequency, as shown in Fig. 4.13(b).

Figure 4.14 shows the results of average slip velocities at a high frequency ($f_0 = 50$) by the 1D PNP equations. As shown in Fig. 4.14(a), we find a reverse flow in the range that $0 < \lambda_c < 0.2$, and only in the range $| < v_s > |$ has a large value, since the moving distance of ions decreases as the frequency increases. Furthermore, as shown in Fig. 4.14(b), we find that simpler nonlinearities of $< v_s >$ on v_0 exist at a higher frequency than those at a low frequency (i.e., the sign of $< v_s >$ is always negative and $| < v_s > |$ increases largely at a threshold voltage; but the increasing rate is suppressed around a high voltage region).

4.4 discussion

Stacking ICEO pumps are important because of their potential to improve the obtainable pressure of ICEO pumps to the level of porous dc electroosmotic pumps [102], since the intrinsic density of a working surface of stacking structures is larger than that of planar structures and equivalent to that of porous structures. Thus, the experimental observations of the broken symmetry of vortex flows around the stacking structures are important as the first step toward such an improvement. Furthermore, we have shown that nonreactive and conductive carbon structures fabricated by pyrolysis [98] are useful for realizing an ICEO device having a large-height conductive structures between electrodes by a simple process. Furthermore, although the flow reversal at low frequencies (<100 Hz) is often conjectured to be due to Faradaic reactions [29], we first show that the phase retardation of the diffuse-charge can cause the flow reversal at low frequencies.

In a simple ICEO model, counterions that cancel the induced charge on the conductive surface slip along to the surface by the tangential component of electric fields on the surface. However, as pointed out in Ref. [4], in many situations involving high induced voltages, this simple ICEO model often cannot predict even the direction of ICEO flow correctly. In our experiment, because of a high applied voltage ($v \equiv \frac{ze|V_{0w}|}{kT} \sim 600$), the thickness of the unmovable "condensed" layer of counterions (l_c) is probably very large as predicted in Ref. [44]; Namely, from Eq. (4.21) in Ref. [44], we can evaluate that $l_c \sim \lambda_D\sqrt{2\nu v} \sim 2.4\lambda_D$ at $\nu = 0.005$ and $v = 600$, where ze is the charge, k is the Boltzmann constant, T is the absolute temperature, and ν is the mean volume fraction of ions in bulk (i.e., $l_c \sim 2.4$ μm since $\lambda_D \sim 1$ μm in deionized water of pH = 7). Therefore, in our theory, the assumption of a condensed layer that is introduced as an unmovable layer in Eq. (4.9) is reasonable as a phenomenological assumption.

It should be noted that we did not consider the steric effects [90, 44, 45, 4] and the obtained experimental value of $\tilde{\lambda}_c$ (~ 40 μm) is much larger than l_c (~ 2.4 μm). However, we are not surprised at the large value. Rather, we think that the value is reasonable since it includes all errors as an adjusting parameter. Further, as discussed in Fig. 4.12, the steric effects probably do not happen in our situation, since the concentration of ions ($C_0 = 10^{-7}$ mol/l for water) is much smaller than the concentration of the water ($C_w \simeq 55.6$ mol/l). Probably, we need to consider other mechanisms that cause a dramatic increase of viscosity near the surface (e.g, surface roughness may work as an effective unmovable layer [52]). Or, as a practical approach, we might need to introduce an artificial viscosity. Actually, even by the modified Poisson-Nernst-Planck (MPNP) equations [44], an unrealistically large value of ν is usually required to explain flow reversal. Thus, although we have not known well why the unmovable or condensed layer exits, we can say that the unmovable or condensed layer plays an important role even for low frequency problems to cause a reverse flow.

In addition, since $\sqrt{DT/2}$ ($\sim$3.2 μm) $\ll w$ ($= 1600$ μm) and $\sqrt{DT/2} \sim l_c$ ($\sim$2.4 μm) for typical ion diffusivity $D = 10^{-9}$ m^2/s and a half period time $T/2 = 10$ ms (i.e.,

frequency of 50 Hz), we cannot expect the equilibrium state that is realized at a dc limit even for low ac frequencies ($\sim$ 50 Hz). Thus, we can naturally believe that the phase retardation of diffuse charge occurs (i.e., even at low ac frequencies, ions cannot follow the changes of an applied electric field, and thus it generates time dependent reverse and forward flows near the surface of conductive posts). Therefore, the observed flow velocity can be small because of the cancellation between the reverse and forward flows. Furthermore, the existence of some unmovable layer can break the balance between reverse and forward flows, and can produce a net anomalous reverse flow. This is a qualitative explanation for the anomalous reverse flow, and is consistent with the results of our 1D PNP analysis.

4.5 Conclusion

In conclusion, (1) we have experimentally shown that asymmetrical vortices due to ICEO are generated around stacking structures consisting of conductive posts in an aqueous solution. (2) By considering boundary effects precisely, except for the problem of anomalous reverse vortex flow, we have successfully explained the experimental results that stacking structures accelerate a reverse flow rather than suppressing it. (3) By the 1D PNP analysis, we find that the anomalous flow reversal in low frequency occurs owing to the phase retardation between an induced diffuse charge and a tangential electric field, and successfully explained the observed nonlinearity of the flow velocity on the applied voltage. (3) We have shown that a large-height structure consisting of carbon posts fabricated by pyrolysis of photoresists is useful for the fabrication of an ICEO device because of its simplicity and nonreactive nature.

We believe that the use of this stacking pump can dramatically improve the pumping performance in terms of flow rate, applied voltage, and applied electric field.

Chapter 5

Valve 1 (Theory): High-speed rotary microvalves in water using hydrodynamic force due to induced-charge electrophoresis

The development of a high-speed microactuator in water is difficult because of electrostatic problems and hydrodynamic resistance. To overcome these problems, we consider using induced-charge electrophoresis (ICEP) to perform actuators. We propose rotary microvalves in water using hydrodynamic force due to ICEP and numerically examine the performance of valves. By the multi-physics coupled simulation technique between fluidics and electro-statics based on the boundary element method along with the thin double layer approximation, we find that rotary valves using ICEP function effectively at high frequency. In the calculations, the electric and flow field problems in a bounded domain are solved, and the proper boundary conditions are discussed. By employing similar actuators using ICEP, we can dramatically improve the performance of promising microfluidic systems such as lab-on-a-chip.

5.1 Introduction

A hydrodynamic resistance due to viscosity increases rapidly in a microchannel as the width of the channel decreases. Thus, the development of a high-speed microactuator in water is challenging, though the development of a high-speed microactuator in air by using electrostatic force is common in the field of microelectromechanical systems (MEMS). In particular, it is very challenging to develop microvalves that function in water at high-speeds similar to those of an electrostatic valve in air because valves are indispensable for controlling flows in microchannels with mixers and pumps in promising biomedical

applications such as lab-on-a-chip [51] and they are intrinsically movable devices. Note that large pressure-driven valves are still used reluctantly for the design of lab-on-a-chip.

Recently, several researchers [30, 70] have observed motion in water using induced-charge electrophoresis (ICEP). ICEP is different from classical electrophoresis because it results from the interaction between the electric field and ions in the electric double layer formed by the polarizing effect of the electric field itself [5, 83, 84, 97, 16, 30, 6, 20, 90, 17, 66, 1, 57]. In particular, Gangwal et al. [30] have observed the motion of a half-coated metal sphere using ICEP and suggested its application to various devices. Moreover, the rotation of micrometallic rods has been studied theoretically [75] and experimentally [70]. However, no attempt has been made to analyze microvalves that use ICEP. To overcome the problems faced by actuators in water, we consider using ICEP to move valves and then stop and release the flow of the channel. In particular, rotary-ICEP valves have the potential to avoid viscosity problems since they are expected to move smoothly by using the slip velocity on the surface. Thus, in this chapter, we focus on the development of a rotary-ICEP valve in water using hydrodynamic force due to ICEP and elucidate its design concept. In particular, we consider a rotary-ICEP valve that can be opened by the pressure gradient without an electric field, and can be closed by an electric field perpendicular to the channel wall to avoid complex geometries for electrodes. Further, for the valve problem, the conductive (metal) cylinder is very close to the wall in order to sufficiently stop the flow. Thus, in the calculations, the electric and flow field problems in the bounded domain are solved, and the proper boundary conditions are discussed.

This chapter is presented in five sections. In Sec. 5.2, we describe theory for a geometry model, a flow model, a slip velocity model for bounded and unbounded domains, an electrorotational torque model for bounded and unbounded domains, and a simple model for a multi rotary-ICEP valve. Based on these models, the results for the boundary effects on ICEP, the basic design of Nth rotary-ICEP valve, the performance of a single rotary-ICEP valve, and the performance of a twin rotary-ICEP valve, are presented in Sec. 5.3. Following a discussion in Sec. 5.4, our conclusions are summarized in Sec. 5.5.

5.2 Theory

5.2.1 Geometry model

Figure 5.1 shows the schematic view of the rotary-ICEP valve considered in this study. In Fig. 5.1, we place an elliptical conductive (metal) cylinder of length $2b$ and width $2c$ in a rectangular channel of length $L = 2.25w$ and width $w = 100$ μm. The center of the cylinder of a single rotary valve is anchored near the center of the channel but is free for rotation. Similarly, we can consider other valves using multi elliptical cylinders, as shown in Figs. 5.2 and 5.16. Note that these rotary-ICEP valves have an intrinsically two-dimensional (2D) structure. Moreover, we can probably neglect the friction between

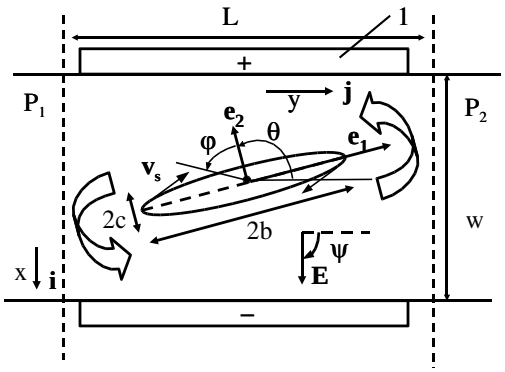

Figure 5.1: Schematic view of rotary-ICEP valve. 1: pair of electrodes. Here, $\psi = 0$ and $\pi/2$ rad for parallel and vertical electric fields, respectively; length $L = 2.25w$ and width $w = 100$ μm. The ellipse has two semi-axes (b, c) with unit vectors $(\boldsymbol{e}_1, \boldsymbol{e}_2)$ that define the orientation of each semi-axis.

the substrate and the elliptical cylinder by considering a hydrodynamic repulsion that considerably reduces the friction between a spindle of the valve and a bearing.

5.2.2 Flow model

We consider a 2D quasi-static Stokes flow without Brownian motion: i.e., we consider the limit in which the Reynolds number Re tends to zero and the Peclet number is infinite. We assume the posts of the elliptical cylinder to be polarizable in an electrolytic solution under a dc or ac electric field. The motion of the surrounding fluid must satisfy Stokes equations modified by the inclusion of an electrical stress. However, by using matched asymptotic expansion [26], we can reduce them to the classical Stokes equations as follows:

$$\mu\nabla^2\boldsymbol{v} - \nabla p = 0, \qquad \nabla\cdot\boldsymbol{v} = 0, \tag{5.1}$$

$$\text{On } S_{\mathrm{p}}^{+}: \quad \boldsymbol{v} = \boldsymbol{U} + \boldsymbol{\Omega}\times\boldsymbol{x} + \boldsymbol{v}_{\mathrm{s}}, \tag{5.2}$$

$$\int_{S_{\mathrm{p}}^{+}} \boldsymbol{f}\mathrm{d}l + \boldsymbol{F}_t^{\mathrm{ext}} = 0, \qquad \int_{S_{\mathrm{p}}^{+}} \boldsymbol{x}\times\boldsymbol{f}\mathrm{d}l + \boldsymbol{T}_t^{\mathrm{ext}} = 0. \tag{5.3}$$

where S_{p}^{+} denotes the surface defined as the outer edge of the double layer, $\boldsymbol{U}$ is the translational velocity, $\boldsymbol{\Omega}$ is the rotational angular velocity, $\boldsymbol{f}$ is the traction vector, $\boldsymbol{F}_t^{\mathrm{ext}}$ and $\boldsymbol{T}_t^{\mathrm{ext}}$ are the total external force and torque, respectively, on the elliptical conductive (metal) cylinder, $\boldsymbol{x}$ is the surface position of metals parameterized by φ, μ ($\sim$1 mPa·s) is the viscosity, $\boldsymbol{v}$ is the velocity, $\boldsymbol{v}_s$ is the slip velocity, and p is the pressure. Note that we use the boundary condition that velocity on the wall of the channel is zero and that the pressures of the inlet and outlet are P_1 and P_2, respectively. (Here, $\Delta P = P_2 - P_1$.)

We calculate the flow fields of the ICEP valve using the boundary element method based on Eqs. (5.1)-(5.3). In particular, to obtain a precise flow field near the wall and the conductive surfaces, we use analytical integration to obtain the matrix elements of the boundary element method. Moreover, to evaluate the valve performance we define U_p as the average flow velocity at the inlet.

5.2.3 Slip velocity model for a bounded domain

The basic phenomena of ICEP can be understood by considering initial potential state and final potential state when we apply an external field [83, 84]. Immediately after an external field $\boldsymbol{E} = E_0\boldsymbol{i}$ is applied to a conductive cylinder, an electric field is set up so that field lines intersect conducting surfaces at right-angles because the cylinder works as conductive material. Although this represents the steady-state vacuum field configuration, mobile ions in electrolytic solutions move in response to applied fields. A current $\boldsymbol{J} = \sigma\boldsymbol{E}$ drives positive ions into a charge cloud on one side the conductor, and negative ions to the other, inducing an equal and opposite surface charge on the conducting surface. A dipolar charge cloud grows as long as a normal field injects ions into the induced double layer, and steady state is achieved when no field lines penetrate the double layer if the induced charge is so small that the surface conduction is negligible. Thus, a zeta-potential ζ around a conductor is generally defined as follows :

$$\zeta = \phi_i - \phi_f \tag{5.4}$$

where ϕ_i is the electric potential of the cylinder that is equal to the electric potential without the double layer or the initial potential defined in this manuscript, and ϕ_f is the electric potential just outside the double layer or the final potential defined in this manuscript; i.e., the zeta-potential is the difference between the potential in the conductor and the potential just outside the double layer. To model an ICEP-valve problem under a bounded condition, we solve the electric potential at every time step before calculating a flow field by the boundary element method based on the following Laplace's equation,

$$\nabla^2\phi = 0. \tag{5.5}$$

On the one hand, we use the Dirichlet boundary condition for the upper and lower walls (electrodes); i.e., $\phi = +0.5V_0$ at $x = 0$, $\phi = -0.5V_0$ at $x = w$, where V_0 is an applied voltage across the channel. On the other hand, we use the Neumann boundary condition for the left and right walls; i.e., $\boldsymbol{n}\cdot\nabla\phi = 0$ at $y = 0$ and L, where $\boldsymbol{n}$ is the surface normal unit vector. In addition to those boundary conditions, to obtain a final potential, we also use the Neumann boundary condition (i.e., $\boldsymbol{n}\cdot\nabla\phi = 0$) on the cylinder's surface. Further, to obtain an initial potential, we use the condition that j's conductive cylinder have an unknown surface potential $\phi_i^{(j)}$, and require the electrical neutral condition that $\oint_{(j)}(\boldsymbol{n}\cdot\nabla\phi)ds = 0$. It should be noted that we are assuming that the ellipsoid is a "floating

conductor", i.e., the total charge does not change with time. The ellipsoid does change its potential ϕ_i with time, though it does not change its charge.

Under a wide range of conditions, the local slip velocity is given by the Helmholtz-Smoluchowski formula,

$$\boldsymbol{v}_s = -\frac{\varepsilon\zeta}{\mu}\boldsymbol{E}_{\mathrm{s}} \tag{5.6}$$

where $\boldsymbol{v}_s$ is the slip velocity, and S_{p}^{+} is the surface defined as the outer edge of the double layer, and $\boldsymbol{E}_{\mathrm{s}}$ is the tangential component of the electric field. Thus, we can numerically calculate a flow field and an angular velocity of a elliptical cylinder for a bounded domain ($\Omega^{\mathrm{ICEP,bounded}}$).

5.2.4 Slip velocity model for an unbounded domain

By using an analytical solution of $\boldsymbol{E}_{\mathrm{s}}$ for an unbounded domain in Appendix A, we can obtain formulation of a slip velocity and a zeta-potential as follows:

$$\boldsymbol{v}_{\mathrm{s}}^{unbounded} = \frac{1}{2}U_c(\alpha+1)^2 q_0^{-1}\sin 2(\psi+\varphi+\theta)\boldsymbol{t}, \tag{5.7}$$

$$\zeta^{unbounded} = c(\alpha+1)E_0\cos(\psi+\varphi+\theta) \tag{5.8}$$

where $q_0 = \sqrt{\alpha^2\cos^2\varphi+\sin^2\varphi}$, U_c $(=\varepsilon c E_0^2/\mu)$ is the representative velocity, $\alpha = b/c$, $\boldsymbol{x} = -b\sin\varphi\ \boldsymbol{e}_1 + c\cos\varphi\ \boldsymbol{e}_2$, $\boldsymbol{t} = -q_0^{-1}(\alpha\cos\varphi\ \boldsymbol{e}_1 + \sin\varphi\ \boldsymbol{e}_2)$ is the tangential unit vector of the position, electric field $\boldsymbol{E} = \cos\psi\boldsymbol{j} + \sin\psi\boldsymbol{i}$, $\boldsymbol{e}_2 = \cos\theta\boldsymbol{j} - \sin\theta\boldsymbol{i}$, $\boldsymbol{e}_1 = \sin\theta\boldsymbol{j} + \cos\theta\boldsymbol{i}$, where $\boldsymbol{i}$ and $\boldsymbol{j}$ are orthogonal unit vectors of the Cartesian coordinate system, $E_0 = |\boldsymbol{E}|$, μ ($\sim$1 mPa·s) is the viscosity, ε ($\sim 80\varepsilon_0$) is the dielectric permittivity of the solvent (typically water), and ε_0 is the vacuum permittivity. Further, from Eqs. (5.1)-(5.3) and based on the 3D formulation of [26], we find that the 2D angular velocity of the elliptical cylinder in unbounded domain is

$$\boldsymbol{\Omega}^{\mathrm{ICEP}} = -\frac{1}{\pi bc(b^2+c^2)}\int_{S_{\mathrm{p}}^{+}}(\boldsymbol{n}\cdot\boldsymbol{x})\,(\boldsymbol{x}\times\boldsymbol{v}_s)\,\mathrm{d}l. \tag{5.9}$$

Thus, by using Eqs. (5.7) and (5.9), we find that the 2D angular velocity of the elliptical cylinder in an unbounded domain is

$$\boldsymbol{\Omega}^{\mathrm{ICEP,unbounded}} = \frac{\varepsilon E_0^2}{\mu}\,\frac{\alpha^2-1}{\alpha^2+1}\,\sin 2(\theta+\psi)\,\boldsymbol{e}_3. \tag{5.10}$$

Note that we will prove Eq. (5.10) in Appendix B.

Furthermore, a slip velocity $\boldsymbol{v}_s$ can be calculated by the electric field calculations using Eqs. (5.4)-(5.6) for a bounded domain. Therefore, we can also obtain an angular velocity

$\boldsymbol{\Omega}^{\text{method-A}}$ that is predicted by Eqs. (5.4)-(5.6) and (5.9); i.e., by using the slip velocity obtained by the bounded electric field calculation and the analytical prediction for angular velocity using a integral form of Eq. (5.9). Note that $\boldsymbol{\Omega}^{\text{method-A}}$ is useful for separating a boundary effect due to the electric field boundary conditions from that due to the flow field boundary conditions. Similarly, we can obtain an angular velocity ($\Omega^{\text{method-B}}$) predicted by Eqs. (5.1)-(5.3) and (5.7); i.e., by using the analytical slip velocity of Eq. (5.7) and the numerical flow calculation for the bounded domain.

5.2.5 Electrorotational torque model for a bounded domain

Squires and Bazant [84] and Saintillan et al. [75] compute two contributions to the angular velocity: one due to the electrokinetic flow (ICEP torque) and the other due to the electrorotational torque [dielectrophoretic (DEP) torque]. Thus, to complete our analysis, we need to consider the DEP torque due to the parallel electric field around a cylindrical conductor; i.e., in thin-double-layer approximation, the Maxwell stress tensor just outside the double layer leads to an element of torque equal to $d\boldsymbol{T}^{DEP} = \boldsymbol{x} \times (-\frac{1}{2}\varepsilon {\boldsymbol{E}_s}^2)\boldsymbol{n}dl$, where $\boldsymbol{E}_s$ is purely tangential to surface S_{p}^{+}. In general, the DEP torque

$$\boldsymbol{T}^{\text{DEP}} = \int \boldsymbol{x} \times (-\frac{1}{2}\varepsilon {\boldsymbol{E}_s}^2)\boldsymbol{n}dl \tag{5.11}$$

on S_{p}^{+} is different from zero. That is, the external torque in Eq.(5.3) is different from zero and it is equal to the DEP torque. Note that for a bounded problem, we refer the method that considers both the DEP and ICEO torques (i.e., $\boldsymbol{T}_t^{ext} = \boldsymbol{T}^{DEP}$) as method-D, while we refer the method that considers just the ICEO torque (i.e., $\boldsymbol{T}_t^{ext} = 0$) as method-C.

5.2.6 Electrorotational torque model for an unbounded domain

By using Eq. (5.24) in Appendix A and Eq. (5.11), we find that the electrorotational torque of the elliptical cylinder in an unbounded domain is

$$\boldsymbol{T}_t^{\text{DEP,unbounded}} = \frac{\pi}{2}\, \varepsilon c^2 E_0^2\, (\alpha^2 - 1)\, \sin 2(\theta + \psi)\, \boldsymbol{e}_3. \tag{5.12}$$

Note that Eq. (5.12) is the same as the result provided in the classical book of W.R. Smythe [80] with zero relative dielectric constant, which gives electric field lines purely tangential to surface S_{p}^{+}. Since $\boldsymbol{\Omega} = \boldsymbol{T}/2\pi(b^2 + c^2)\mu$ for the elliptical cylinder in the Stokes flow [26], the angular velocity due to the DEP is

$$\boldsymbol{\Omega}^{\text{DEP,unbounded}} = \frac{1}{4}\, \frac{\varepsilon E_0^2}{\mu}\, \frac{\alpha^2 - 1}{\alpha^2 + 1}\, \sin 2(\theta + \psi)\, \boldsymbol{e}_3. \tag{5.13}$$

Thus, from Eqs. (5.10) and (5.13), we can estimate that the total angular velocity is

$$\Omega_t^{\text{unbounded}} = \frac{5}{4}\, \frac{\varepsilon E_0^2}{\mu}\, \frac{\alpha^2 - 1}{\alpha^2 + 1} \sin 2(\theta + \psi)\, \boldsymbol{e}_3. \tag{5.14}$$

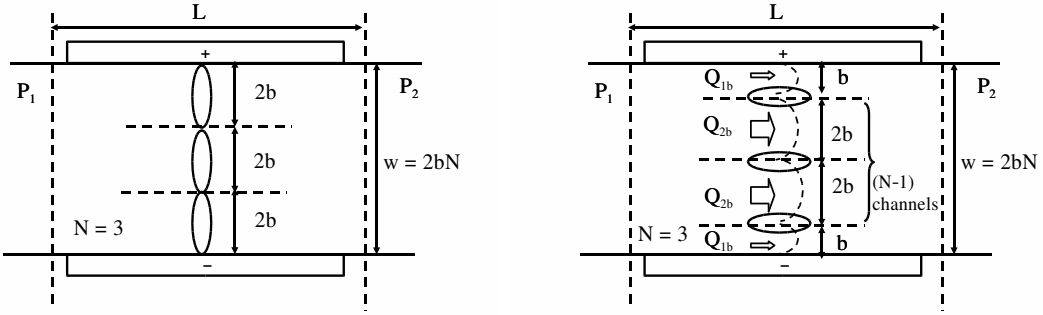

(a) Close state (b) Open state

Figure 5.2: Schematic view of multi rotary-ICEP valve ($N = 3$).

5.2.7 Simple model for a multi rotary-ICEP valve

Fundamental requirements for the design of a rotary-ICEP valve are to achieve a maximum average flow velocity for an open state and to close at a minimum leak with a maximum angular velocity. Here, we consider a simple model for the design of a multi (Nth) rotary-ICEP valve that has N elliptical cylinders with half lengths $b = w/2N$ as shown in Fig. 5.2(a). The Nth rotary valve has $N-1$ channels with a width $2b$ and two channels with a width b for an open state at the thin body limit of elliptical cylinders as shown in Fig. 5.2(b). By considering 2D Poiseuille flow, we can estimate that the flow amounts of the divided channels with a width $2b$ and b are $\frac{2}{3\mu}(\frac{\Delta P}{L})b^3$ and $\frac{2}{3\mu}(\frac{\Delta P}{L})(\frac{b}{2})^3$, respectively. Therefore, the total flow amount of the Nth rotary valve is $Q^{(N)} = 2\frac{2}{3\mu}(\frac{\Delta P}{L})(\frac{b}{2})^3 + (N-1)\frac{2}{3\mu}(\frac{\Delta P}{L})b^3 = \frac{2}{3\mu}(\frac{\Delta P}{L})b^3(N-0.75)$. Thus, by considering $b = w/2N$, we can estimate a maximum average flow velocity U_p ($= Q^{(N)}/w$) of the Nth rotary-ICEP valve in an open state as follows:

$$U_p^{\text{open}} \simeq \frac{w^2}{12\mu}\frac{\Delta P}{L}\frac{N-0.75}{N^3} \tag{5.15}$$

Further, an angular velocity of a rotary valve has a maximum value at $\theta = 45$ and 135 deg when $\psi = 90$ deg from Eq. (5.14). Note that $|\sin 2(\pi/4+\pi/2)| = |\sin 2(3\pi/4+\pi/2)| = 1$. Therefore, from Eq. (5.14), we can estimate a maximum angular velocity of the Nth rotary-ICEP valve in a closing motion as follows:

$$\Omega^{\text{close}} \simeq \frac{5}{4}\frac{\varepsilon E_0^2}{\mu}\frac{\alpha^2-1}{\alpha^2+1}. \tag{5.16}$$

It should be noted that α ($= b/c$) $= w/2Nc$ if c is constant for the Nth rotary valve. If the electrorotational torque is neglected intrinsically because of a bounded effect for the

valve problems we can obtain that

$$\Omega^{\text{close}} \sim \frac{\varepsilon E_0^2}{\mu} \frac{\alpha^2 - 1}{\alpha^2 + 1}. \tag{5.17}$$

5.3 Results

5.3.1 Boundary effects on ICEP

Figure 5.3 shows the boundary effects on electrophoresis when $\theta = 135$ deg, $c/w = 0.2$, and α $(= b/c) = 2.3$. Figures 5.3(a) and 5.3(b) show a potential and electric field in the rectangular channel, respectively. In Fig. 5.3(a), the symbols of "+" and "-" inside the domain stand for the induced charge and ion by the application of an electric field. In Fig. 5.3(b), an electric field around a conductive cylinder is parallel to the surface on the conductor because of the boundary condition. In this case, an elliptical conductive cylinder is very close to both the upper and lower electrodes. Therefore, the boundary condition due to the existence of a thin double layer on the cylinder affects the surface charge distributions on the upper and lower walls as shown in Fig. 5.3(c). On the contrary, the charges of the surface on the upper and lower walls affect the zeta potential around a conductive cylinder as shown in Fig. 5.3(d). Here, the maximum zeta potential of a bounded domain ($\zeta_{\max}^{\text{bounded}}/V_0 = 0.47$ at $\phi = 135$ deg) is approximately 71% of that of an unbounded domain ($\zeta_{\max}^{\text{unbounded}}/V_0 = 0.66$ at $\phi = 135$ deg). Further, Figs. 5.3(e) and 5.3(f) show the flow field and slip velocity, respectively. As shown in Fig. 5.3(e), ions of the outer edge of the double layer slips along the tangential electric field and make a flow around a conductive cylinder. Here, the maximum slip velocity of a bounded domain ($v_{s,\max}^{\text{bounded}}/U_c = 1.2$ at $\phi = 0$ deg) is approximately 50% of that of an unbounded domain ($\zeta_{\max}^{\text{unbounded}}/V_0 = 2.4$ at $\phi = 0$ deg) as shown in Fig. 5.3(f). Thus, peak values of a zeta potential and a slip velocity around a cylinder are suppressed by the effects of electric field deformations when $2c \sim w$. Furthermore, although we use method-D that considers both the ICEO and DEP flow in the calculation of Fig. 5.3(e), the flow field is the almost same as that by method-C because of the suppression of electrorotational torque due to the bounded effect.

Figures 5.4(a) and 5.4(b) show the dependence of ζ and v_s on φ when $c/w = 0.02$ and α $(= b/c) = 2.3$. As shown in Figs. 5.4(a) and 5.4(b), the values of a zeta potential and a slip velocity around a cylinder in a bounded domain agree well with those of an unbounded domain when $c/w = 0.02$. It should be noted that this verifies that our numerical code is correct. Figures 5.4(c) and 5.4(d) show the dependence of ζ and Ω on c/w when α $(= b/c) = 2.3$. As shown in Figs. 5.4(c), as c/w decreases, ζ (at $\phi = 135$ deg) of a bounded condition asymptotically approach the values predicted with the thin electric double layer approximation in an unbounded domain [i.e, the values predicted by Eqs. (4.8)]. Thus, the effects of the electric field deformations are negligible if $c \ll w$.

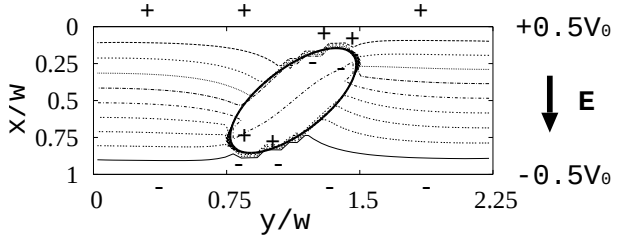

(a) Potential field ($c/w = 0.2$)

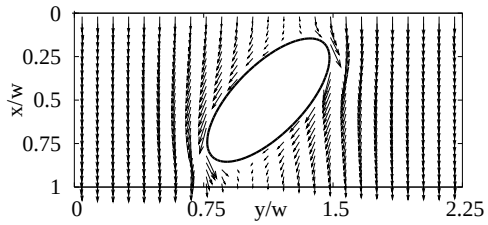

(b) Electric field ($c/w = 0.2$)

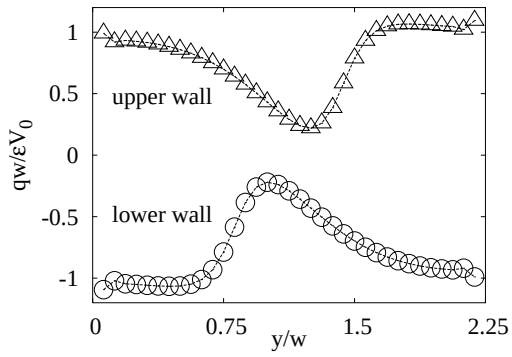

(c) Surface charge ($c/w = 0.2$)

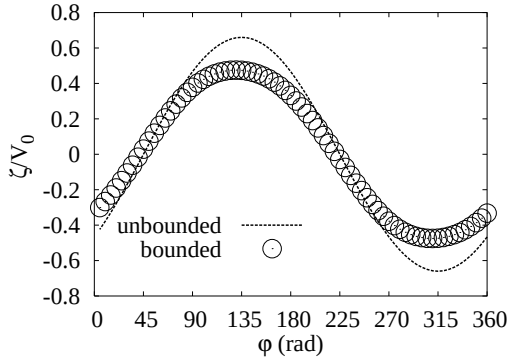

(d) Zeta potential ($c/w = 0.2$)

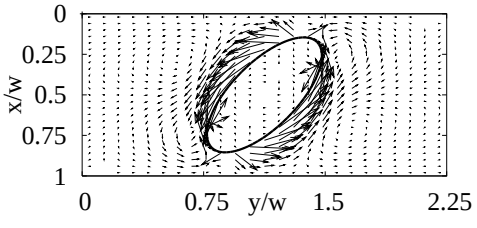

(e) Flow field ($c/w = 0.2$)

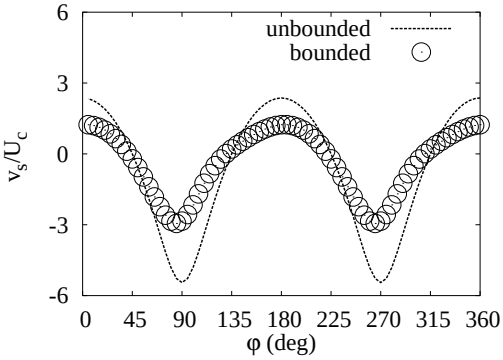

(f) Slip velocity ($c/w = 0.2$)

Figure 5.3: Boundary effects. Here, $c/w = 0.2$, $\theta = 3\pi/4$, $T_0\Delta P/\mu = 0$, $\alpha\ (= b/c) = 2.3$, and $T_0 U_c/w = 0.01$, where T_0 is representative velocity; Through this paper, we use a set of typical values that $\mu = 1.0$ mPa·s, $w = 100$ μm, and $T_0 = 1$ ms; Here, we obtain the values that $U_c = 1.0$ mm/s, $\Delta P = 0$ Pa, and $E_0 = 11.9$ kV/m.

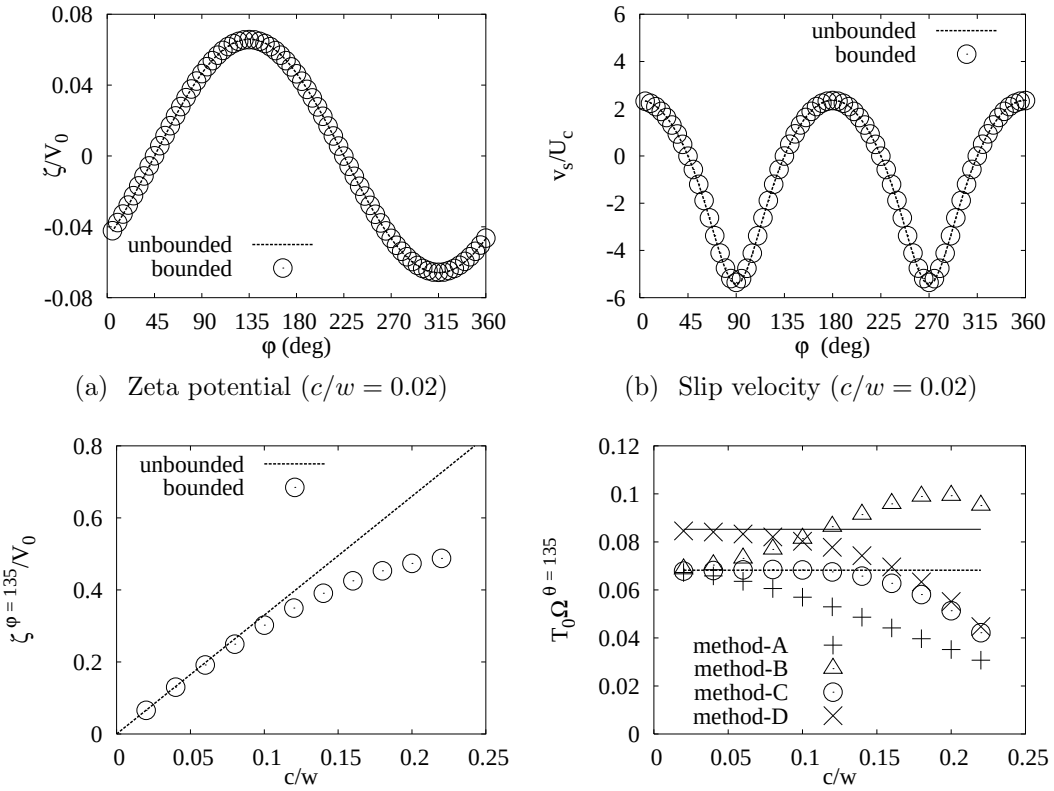

(a) Zeta potential ($c/w = 0.02$)

(b) Slip velocity ($c/w = 0.02$)

(c) Zeta potential vs c/w

(d) Angular velocity vs c/w

Figure 5.4: Boundary effects on c/w. Here, $T_0\Delta P/\mu = 0$, α $(= b/c) = 2.3$, and $T_0 U_c/w = 0.01$; e.g., $\mu = 1.0$ mPa·s, $w = 100$ μm, $T_0 = 1$ ms, $\Delta P = 0$ Pa, $U_c = 1.0$ mm/s, and $E_0 = 11.9$ kV/m; In (d), broken and solid lines show the analytical results by Eq. (5.10) and (5.14), respectively (i.e., $\Omega^{\mathrm{ICEP,unbounded}}$ and $\Omega_t^{\mathrm{unbounded}}$, respectively).

Further, in Fig. 5.4(d), broken and solid lines show the analytical results by Eq. (5.10) and (5.14), respectively (i.e., $\Omega^{\mathrm{ICEP,unbounded}}$ and $\Omega_t^{\mathrm{unbounded}}$, respectively), while plus (+), open triangle ($\triangle$), open circle ($\bigcirc$), and cross ($\times$) show the numerical results by method-A, B, C, and D, respectively. As shown in Fig. 5.4(d), the numerical results by method-C and D tend to the analytical results by Eq. (5.10) and (5.14), respectively, for c/w going to zero. Furthermore, from Fig. 5.4(d), we can find that in a perpendicular electric field, the boundary effect due to a fluid boundary condition accelerates the angular velocity of a elliptical conductive cylinder, whereas the boundary effect due to an electric boundary condition decelerates the angular velocity of a elliptical conductive cylinder. In particular, we can find that as c/w increases, the value of the DEP torque decreases and approaches zero.

Figure 5.5 shows the boundary effects on x_b/w when $\theta = 135$ deg, $c/w = 0.1$, and $\alpha\ (= b/c) = 2.3$. Here, (x_b, y_b) is a position of the center of an elliptical conductive cylinder. Figures 5.5(a) and 5.5(b) show potential and flow fields, respectively, for the cylinder's positions $x/w = 0.75$. In this case, we can find an asymmetrical zeta potential and slip velocity around a cylinder as shown in Fig. 5.5(c) and 5.5(d). This is the result from the redistribution of a surface charge on the lower electrode near the cylinder; i.e., when an elliptical conductive cylinder approaches the lower wall as shown in Fig. 5.5(a), the negative surface charge on the lower electrode near the metal reduces considerably because of the repulsion due to the existence of the negative ions on the metal surface near the lower electrode as shown in Fig. 5.5(e). Figure 5.5(f) shows the dependence of Ω on x_b/w. Further, Fig. 5.6 shows the dependence of ϕ_i on x_b/w. It should be noted that the dependence of ϕ_i on x_b/w is slightly nonlinear, and depended slightly on $\alpha\ (= b/c)$.

Figure 5.7 shows the dependence of ζ at $\phi = 135$ deg and Ω on $\alpha\ (= b/c)$ when $c/w = 0.1$, $\theta = 135$ deg, and $x_b/w = 0.5$. As shown in Fig. 5.7(a), the $\zeta^{bounded}$ asymptotically approaches the $\zeta^{unbounded}$ as $\alpha\ (= b/c)$ decreases. In Fig. 5.7(b), the angular velocities by method-C and D asymptotically approach $\Omega^{\mathrm{ICEP,unbounded}}$ and $\Omega_t^{\mathrm{unbounded}}$, respectively.

5.3.2 Basic design of Nth rotary-ICEP valve

Figure 5.8 shows the results of a basic design of a Nth rotary-ICEP valve by using Eqs. (5.15), (5.16), and (5.17). Here, $w = 100$ μm, $L/w = 2.25$, $\Delta P = 4$ Pa, $E_0 = 11.9$ kV/m, and $\mu = 1$ mPa·s. As shown in Fig. 5.8(a), the maximum U_p in an open state decreases rapidly as N increases. Further, as shown in Fig. 5.8(b), the maximum angular velocity in a closing motion Ω^{close} decreases as N increases if c/w is constant. Thus, selecting a small N number has advantages to obtain a large U_p in an open state and a large angular velocity in a closing motion. Therefore, as a realistic problem, considering a single or twin valve is enough to overview a design concept of a rotary-ICEP valve. Note that open circle and cross in Fig. 5.8 show the numerical results by method-C and D, respectively. In Fig. 5.8, the agreement of U_p between the numerical simulations and the thin limit is good, while the agreement of Ω is poor. This is because Eq. (5.16) just gives

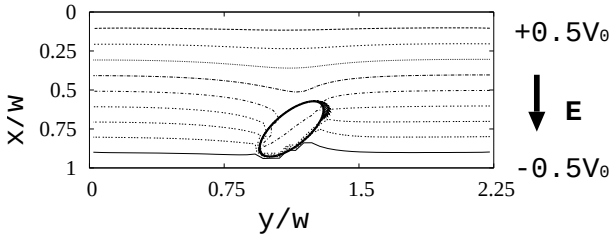

(a) Potential field ($c/w = 0.1$, $x_b/w = 0.75$)

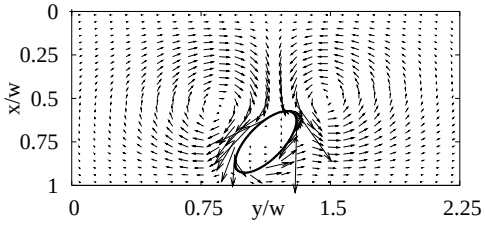

(b) Flow field ($c/w = 0.1$, $x_b/w = 0.75$)

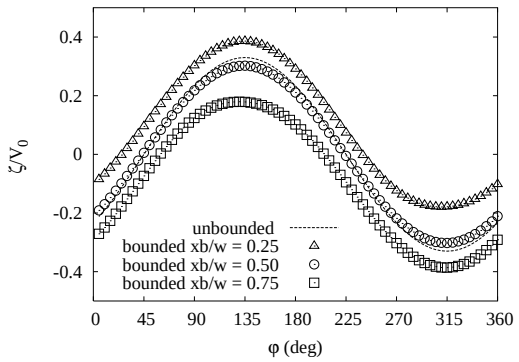

(c) Zeta potential ($c/w = 0.1$, α ($= b/c$) = 2.3)

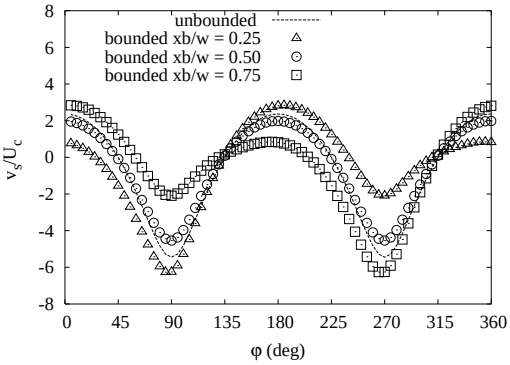

(d) Slip velocity ($c/w = 0.1$, α ($= b/c$) = 2.3)

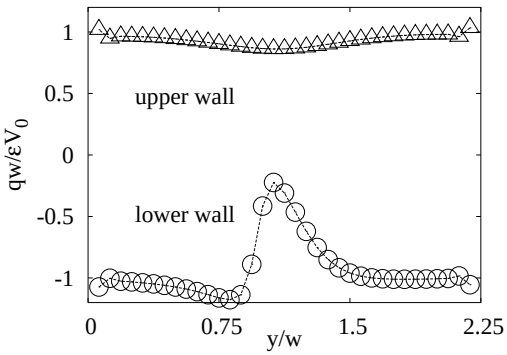

(e) Surface charge ($c/w = 0.2$)

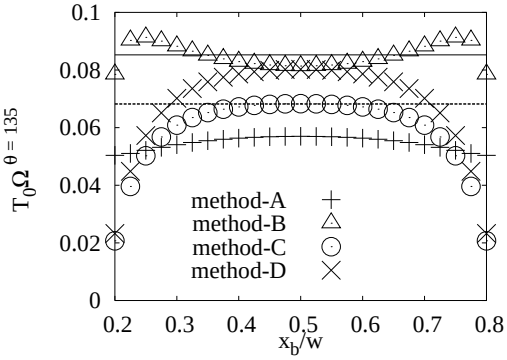

(f) Dependence of Ω on x_b

Figure 5.5: Boundary effects on x_b/w. Here, $T_0\Delta P/\mu = 0$, α ($= b/c$) = 2.3, and $T_0 U_c/w = 0.01$; e.g., $\mu = 1.0$ mPa·s, $w = 100$ μm, $T_0 = 1$ ms, $\Delta P = 0$ Pa, $U_c = 1.0$ mm/s, and $E_0 = 11.9$ kV/m; In (f), broken and solid lines show the analytical results by Eq. (5.10) and (5.14), respectively (i.e., $\Omega^{\mathrm{ICEP,unbounded}}$ and $\Omega_t^{\mathrm{unbounded}}$, respectively).

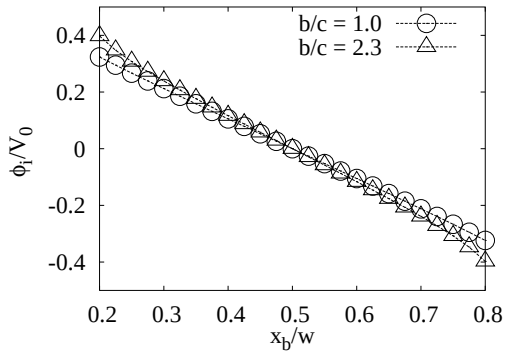

Figure 5.6: Dependence of ϕ_i on x_b/w. Here, $c/w = 0.1$, and $T_0 U_c/w = 0.01$; e.g., $w = 100$ μm, $T_0 = 1$ ms, $U_c = 1.0$ mm/s, and $E_0 = 11.9$ kV/m.

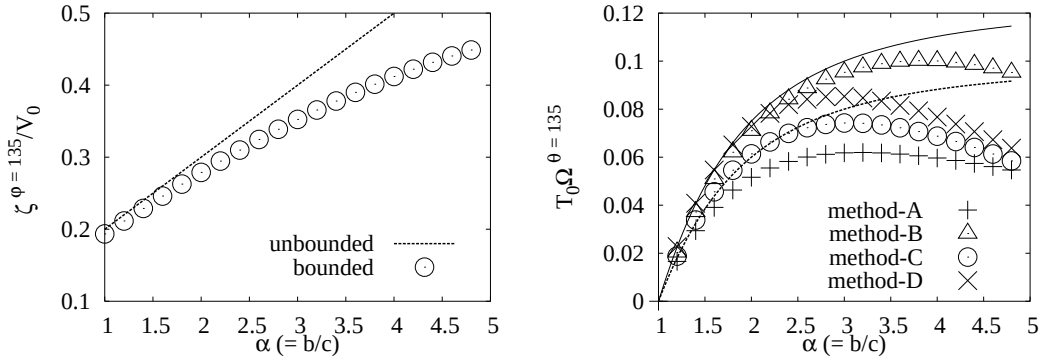

(a) Dependence of ζ on α $(= b/c)$ (b) Dependence of Ω on α $(= b/c)$

Figure 5.7: Boundary effects on α $(= b/c)$. Here, $\theta = 3\pi/4$, $c/w = 0.1$, $T_0 \Delta P/\mu = 0$, and $T_0 U_c/w = 0.01$; e.g., $\mu = 1.0$ mPa·s, $w = 100$ μm, $T_0 = 1$ ms, $\Delta P = 0$ Pa, $U_c = 1.0$ mm/s, and $E_0 = 11.9$ kV/m; In (b), broken and solid lines show the analytical results by Eq. (5.10) and (5.14), respectively (i.e., $\Omega^{\mathrm{ICEP,unbounded}}$ and $\Omega_t^{\mathrm{unbounded}}$, respectively).

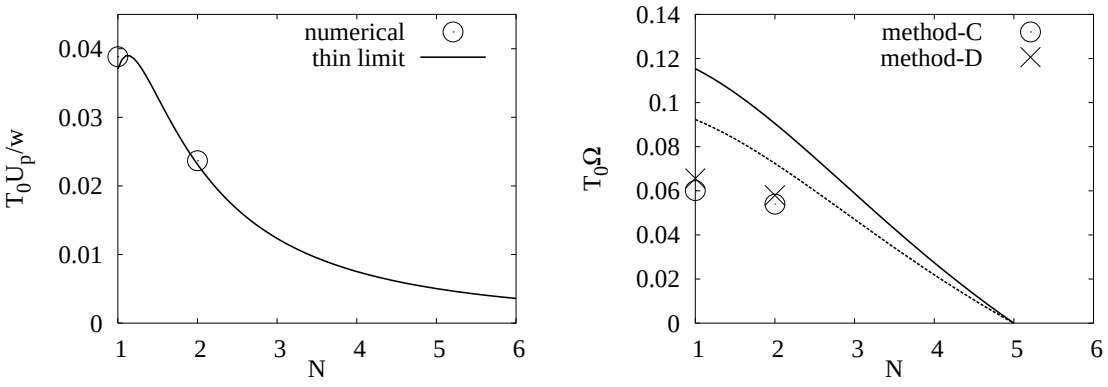

(a) U_P vs N (b) Ω vs N

Figure 5.8: Basic design of Nth rotary-ICEP valve. In (a), the symbol (◯) shows the numerical results by the boundary element method, and the solid line shows the analytical results predicted by Eqs. (5.15) (i.e., $U_p^{open} = \frac{w^2}{12\mu}\frac{\Delta P}{L}\frac{N-0.75}{N^3}$). In (b), open circle (◯) and cross (×) show the numerical results by method-C and D, respectively, and solid and broken lines show the analytical results predicted by Eqs. (5.16) and (5.17),respectively [i.e., $\Omega^{\rm close} \simeq \frac{\varepsilon E_0^2}{\mu}\left[1+\frac{(\alpha+1)^2}{16\alpha}\right]\frac{\alpha^2-1}{\alpha^2+1}$ and $\Omega^{\rm close} \simeq \frac{\varepsilon E_0^2}{\mu}\frac{\alpha^2-1}{\alpha^2+1}$]. Here, $c/w = 0.1$. Here, $L/w = 2.25$, $T_0\Delta P/\mu = 4$, and $T_0U_c/w = 0.01$; e.g., $\mu = 1.0$ mPa·s, $w = 100$ μm, $T_0 = 1$ ms, $\Delta P = 4$ Pa, $U_c = 1.0$ mm/s, and $E_0 = 11.9$ kV/m.

rough predictions based on the solution for an unbounded domain, while Eq. (5.15) gives good predictions based on the precise solution for 2D Poiseuille flows. In particular, the prediction of Eq. (5.16) that considers both the DEP and ICEP torques overestimates the angular velocity worse than that of Eq. (5.17) that just considers the ICEP torque, since the DEP torque is intrinsically small for the valve problem because of the bounded effect.

Figure 5.9 show the results of a basic design of a single rotary-ICEP valve when $c/w = 0.1$, α $(= b/c) = 4.6$, $x_b = 0.47$, and $U_c = 1$ mm/s. Figures 5.9(a) and 5.9(b) show the potential and flow fields of a single rotary-ICEP valve, respectively. Here, an elliptical conductive cylinder is positioned off the center of the channel. Thus, the distribution of a surface charge is slightly asymmetrical between the upper and lower electrodes as shown in Fig. 5.9(c). Further, a zeta potential is biased to the positive direction as shown in Fig. 5.9(d). Here, if a conductive cylinder locates at the center of the channel, the conductive cylinder will not rotate from the closed state, and thus the single rotary-ICEP valve will not realize an open state in the presence of the pressure difference. It should be noted that the hydrodynamic force will always force the cylinder to be aligned with the flow field. However, because of a balance of clockwise torque and counterclockwise torque, the elliptical cylinder at $\theta = 0$ deg will not rotate in the 2D Poiseuille flow if we do not assume an artificial fluctuation. In Fig. 5.9(e), the maximum angular velocities of a bounded domain by method-C and D are 60 and 66 rad/s, which are 65 and 49% of those of an unbounded domain, respectively. Figure 5.9(f) shows the dependence of U_p on θ when $\Delta P = 4$ Pa. In Fig. 5.9(f), the maximum and minimum velocities are 3.9 mm/s and 0.3 mm/s at $\theta = 90$ and 0 deg, respectively.

Figures 5.10 show the results of a basic design of a twin rotary-ICEP valve when $c/w = 0.1$, α $(= b/c) = 2.3$, and $U_c = 1$ mm/s. Figures 5.10(a) and 5.10(b) show the potential and flow fields of a twin rotary-ICEP valve, respectively. Here, we assume that $\theta^{\text{upper metal}} = -\theta^{\text{lower metal}}$, where $\theta^{\text{upper metal}}$ and $\theta^{\text{lower metal}}$ are the θ of the upper and lower conductive (metal) cylinders, respectively. Further, two elliptical conductive cylinders are positioned at $x_b/w = 0.25$ and 0.75. Thus, the distribution of a surface charge is symmetrical between the upper and lower electrodes as shown in Fig. 5.10(c). In Fig. 5.10(d), $\zeta/V_0 = -0.249$ and $+0.249$ at $\phi = 90$ and 270 deg, respectively, when $\theta = 0$ deg, whereas $\zeta/V_0 = -0.240$ and $+0.245$ at $\phi = 90$ and 270 deg when $\theta = 15$ deg, respectively; i.e., Because of the symmetrical geometry that $\theta^{\text{upper metal}} = -\theta^{\text{lower metal}}$, the characteristics of the surface of one conductive (metal) cylinder near the electrode and near the other metal cylinder are similar, but slightly different. In Fig. 5.10(e), the maximum angular velocities of a bounded domain by method-C and D are 54 and 58 rad/s, which are 75 and 61% of those of an unbounded domain [by Eq. (5.10) and (5.14)], respectively. Figure 5.10(f) shows the dependence of U_p on θ when $\Delta P = 4$ Pa. In Fig. 5.10(f), the maximum and minimum velocities are 2.4 mm/s and 0.1 mm/s at $\theta = 90$ and 0 deg, respectively.

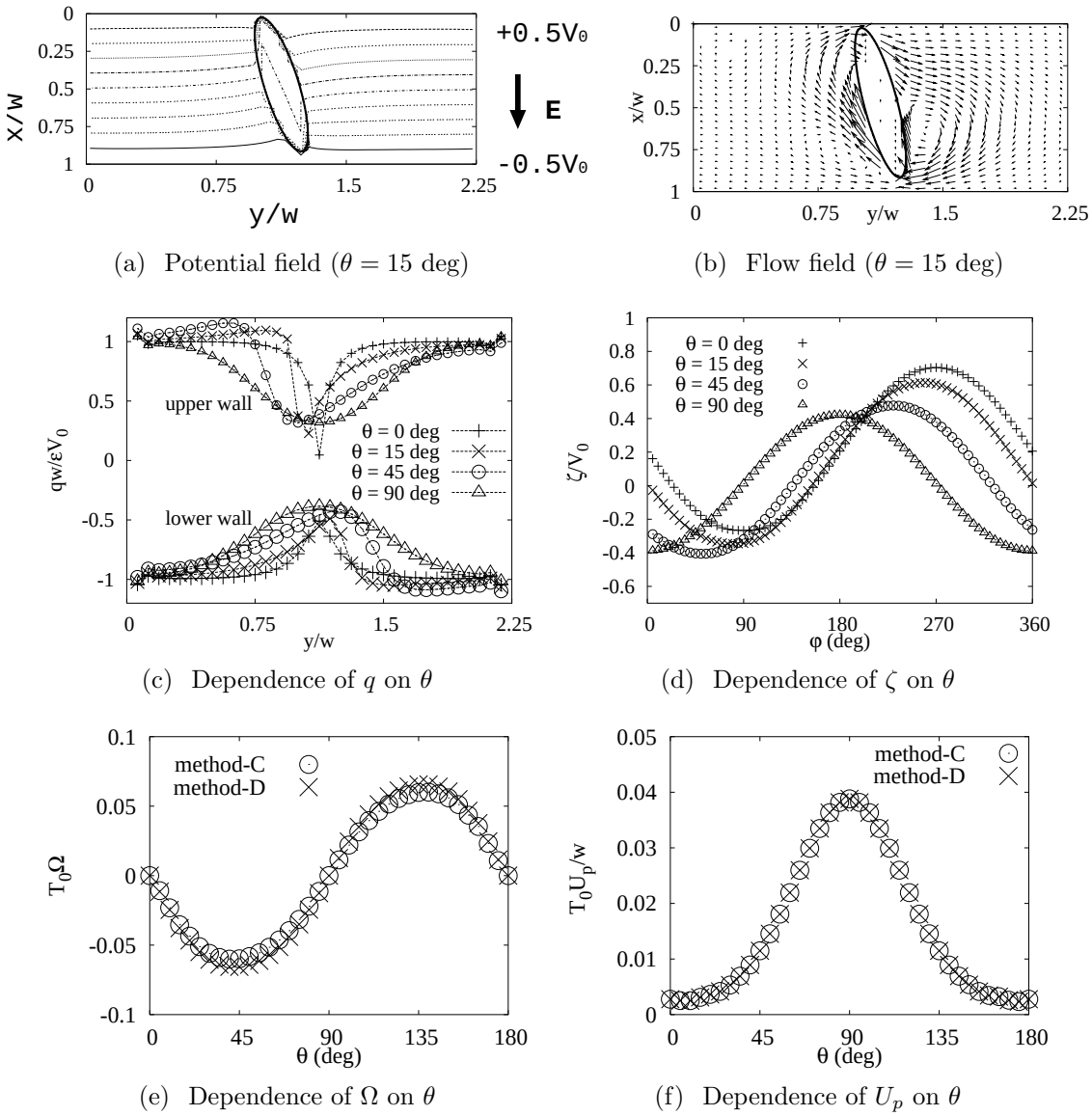

(a) Potential field ($\theta = 15$ deg)

(b) Flow field ($\theta = 15$ deg)

(c) Dependence of q on θ

(d) Dependence of ζ on θ

(e) Dependence of Ω on θ

(f) Dependence of U_p on θ

Figure 5.9: Basic design of single rotary-ICEP valve. Here, the center of the single valve is anchored at $(x/w, y/w) = (0.47,\ 1.125)$; α $(= b/c) = 4.6$ and $c/w = 0.1$; In (a)-(e), $T_0\Delta P/\mu = 0$ and $T_0 U_c/w = 0.01$; In (f), $T_0\Delta P/\mu = 4$ and $T_0 U_c/w = 0$; e.g., $T_0 = 1$ ms, $\mu = 1$ mPa·s, and $w = 100$ μm.

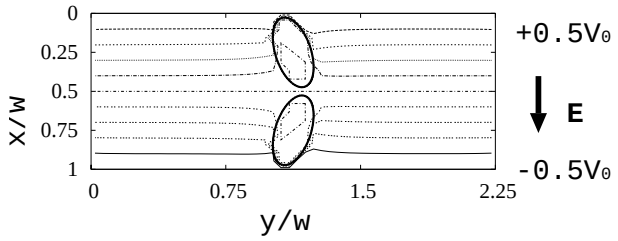

(a) Potential field ($\theta = 15$ deg)

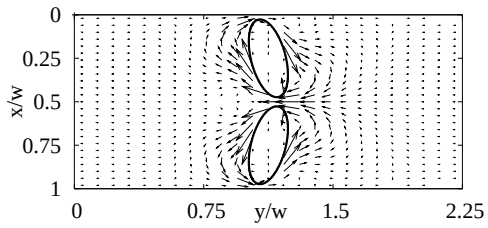

(b) Flow field ($\theta = 15$ deg)

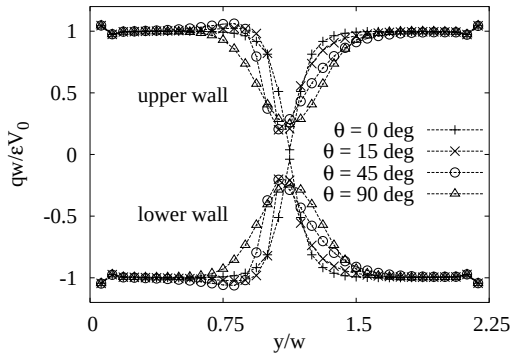

(c) Dependence of q on θ

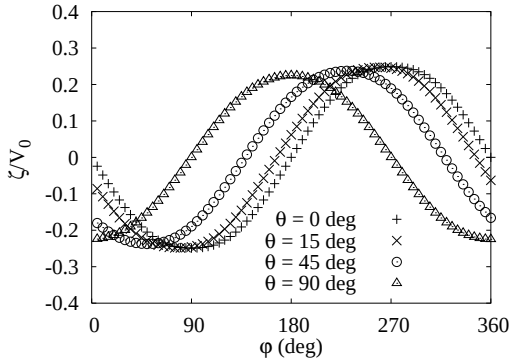

(d) Dependence of ζ on θ

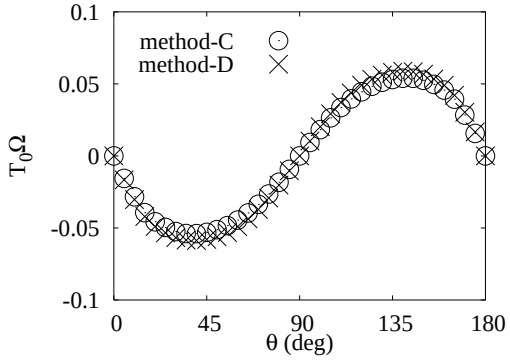

(e) Dependence of Ω on θ

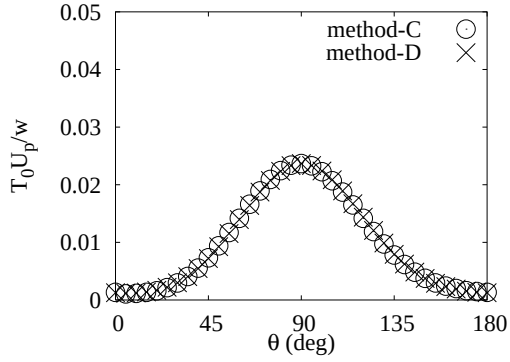

(f) Dependence of U_p on θ

Figure 5.10: Basic design of twin rotary-ICEP valve. Here, the centers of the twin valve are anchored at $(x/w, y/w) = (0.25,\ 1.125)$ and $(0.75,\ 1.125)$, respectively; $\alpha\ (= b/c) = 2.3$ and $c/w = 0.1$; In (a)-(e), $T_0\Delta P/\mu = 0$ and $T_0U_c/w = 0.01$; In (f), $T_0\Delta P/\mu = 4$ and $T_0U_c/w = 0$; e.g., $T_0 = 1$ ms, $\mu = 1$ mPa·s, and $w = 100$ μm.

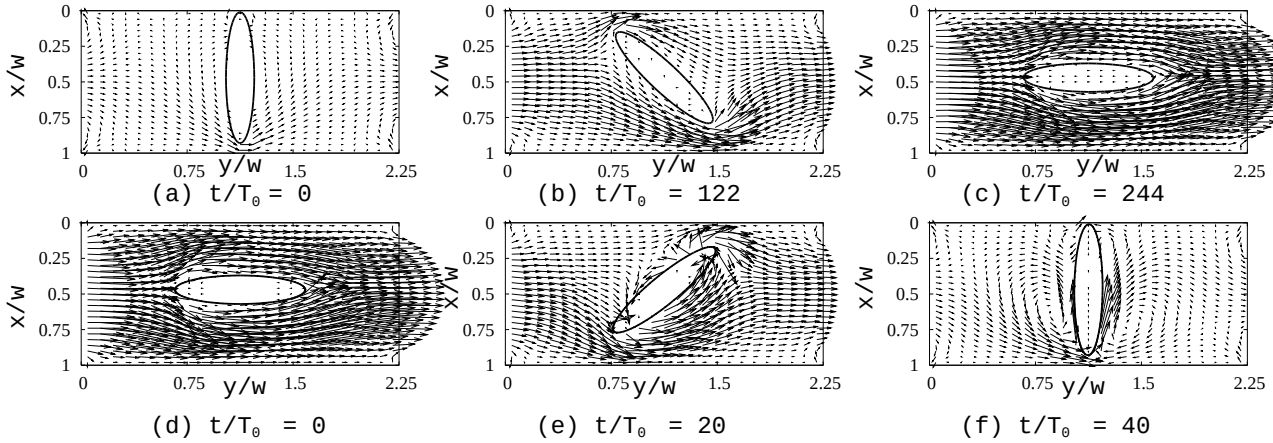

Figure 5.11: Opening [(a), (b), and (c) without an electric field] and closing [(d), (e), and (f) with an electric field ($T_0U_c/0 = 0.01$)] motions and flow fields of single rotary-ICEP valve. Here, we use method-D that considers both ICEO and DEP effects due to the parallel electric field on the conductive cylinder, and the center of the single valve is anchored at $(x/w, y/w) = (0.47,\ 1.125)$; $T_0\Delta P/\mu = 4$, $\alpha\ (= b/c) = 4.6$, and $c/w = 0.1$; e.g., $T_0 = 1$ ms, $\mu = 1$ mPa·s, and $w = 100$ μm.

5.3.3 Performance of single rotary-ICEP valve

Figure 5.11 shows the opening [(a), (b), and (c) without an electric field] and closing [(d), (e), and (f) with an electric field $E_0 = 11.9$ kV/m] motions and the flow fields for the single rotary-ICEP valve. As shown in Figs. 5.11(a), 5.11(b), and 5.11(c), an elliptical cylinder of the single valve continues to rotate counterclockwise by the presence of the pressure difference $\Delta P = 4$ Pa without an electric field because we place it slightly above the center line of the channel. As shown in Figs. 5.11(d), 5.11(e), and 5.11(f), an elliptical cylinder of the single valve closes in a vertical electric field ($E_0 = 11.9$ kV/m). Though a single rotary valve that is placed on the center line of the channel (i.e., $x_b/w = 0.5$) has a problem that no torque due to an ICEP works if $\theta = 90$ deg at $t = 0$ ms, we can avoid the problem by placing a valve slightly above the center line of the channel. Figure 5.12 shows the time evolution of a potential field[(a), (b), and (c)] and a electric field [(d), (e), and (f)] in a vertical electric field. Figure 5.13 shows the time evolution of a zeta potential [(a), (b), and (c)] and a slip velocity [(d), (e), and (f)] in a vertical electric field.

Figure 5.14 shows the performance of a single rotary-ICEP valve for an opening motion [(a), (b), and (c)] and a closing motion [(d), (e), and (f)] when $x_b/w = 0.47$, 0.48, and 0.49. Figures 5.14(a), 5.14(b), and 5.14(c) [Figs. 5.14(d), 5.14(e), and 5.14(f)] show the dependences of U_p, θ, and Ω on time t, respectively, in an opening motion [in a closing motion]. On the one hand, for the conditions $x_b/w = 0.47$, 0.48, and 0.49, a single rotary valve in an opening motion has local maximum values of $U_p = 3.88$, 3.86, and 3.84 mm/s

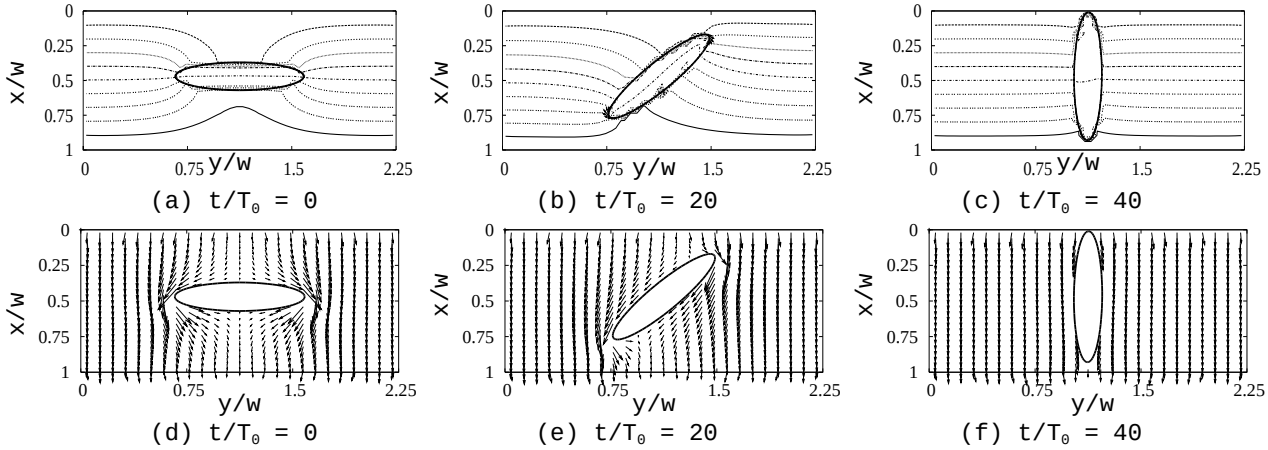

Figure 5.12: Time evolution of potential field[(a), (b), and (c)] and electric field [(d), (e), and (f)] in a closing motion in a vertical electric field. Here, we use method-D that considers both ICEO and DEP effects due to the parallel electric field on the conductive cylinder, and the center of the single valve is anchored at $(x/w, y/w) = (0.47,\ 1.125)$; $T_0\Delta P/\mu = 4$, $\alpha\ (= b/c) = 4.6$, $c/w = 0.1$, $T_0 U_c/w = 0.01$; e.g., $T_0 = 1$ ms, $\mu = 1$ mPa·s, $w = 100$ μm, $U_c = 1$ mm/s, and $E_0 = 11.9$ kV/m.

at $t\ (= t_r^{\text{opening}}) = 244$, 359, and 699 ms, respectively, without an electric field as shown in Fig. 5.14(a). Here, t_r^{opening} is a response time in an opening motion, and the rotation of a single valve generates a pulsating flow with period $t_p^{\text{opening}}\ (= 2t_r^{\text{opening}})$. On the other hand, for the conditions $x_b/w = 0.47$, 0.48, and 0.49, a single rotary valve close with $t\ (= t_r^{\text{closing}}) = 33$, 36, and 41 ms, respectively, by the application of a vertical electric field $E_0 = 11.9$ kV/m as shown in Fig. 5.14(d). Here, t_r^{closing} is a response time in an closing motion. Note that if we use method-C in stead of method-D, $t\ (= t_r^{\text{closing}}) = 35$, 39, and 44 ms, respectively; i.e., if we neglect the DEP torque, we underestimate closing times about 10%. It should be noted that the angular velocities of the triangle symbols ($x_b = 0.47$) in Fig. 5.14(c) spread wide around $t = 0$, 500, and 1000 ms corresponding to $\theta = 0$, 180, 360 deg in Fig. 5.14(b) because there are various factors that increase and decrease the angular velocities in the small range near the angles due to the extremely small gap (0.01 w) between the upper wall ($w = 0$) and elliptical cylinder. That is we can expect a large counterclockwise torque at $\theta = 0$ because we can neglect the flow through the small gap. However, by the small rotation of the elliptical cylinder, clockwise torque generates because of the flow between the upper wall and elliptical cylinder. Thus, the angular velocity decreases rapidly. Moreover, by the additional small rotation, we can expect another local maximum because of increase of counterclockwise torque due to the flow distribution of 2D Poiseuille flow, and so on.

Figure 5.15 shows the dependence of U_p and t_r on x_b/w for a single rotary-ICEP

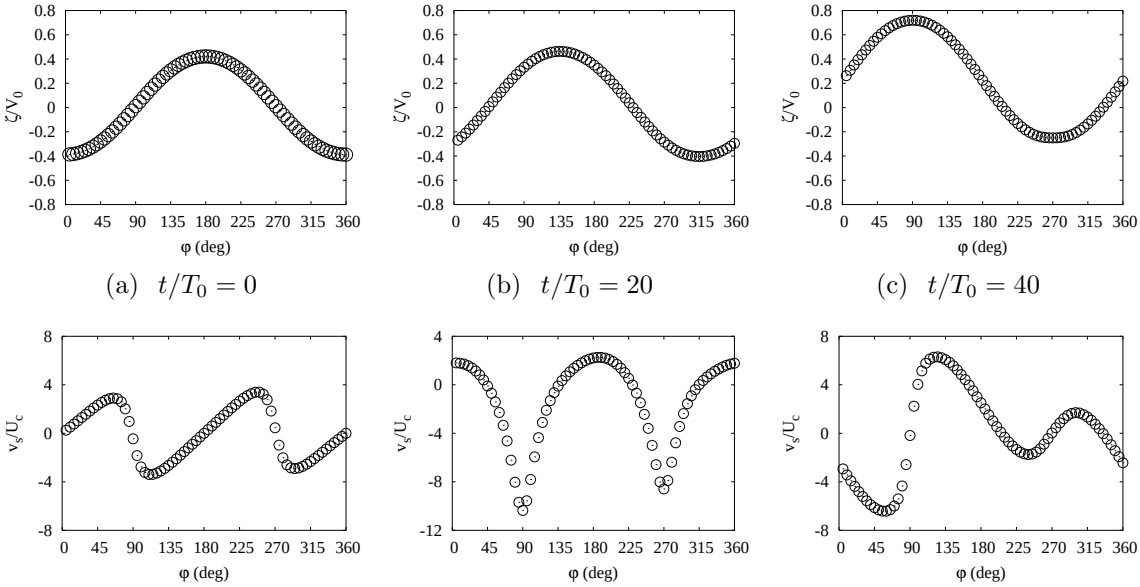

(a) $t/T_0 = 0$ (b) $t/T_0 = 20$ (c) $t/T_0 = 40$

(d) $t/T_0 = 0$ (e) $t/T_0 = 20$ (f) $t/T_0 = 40$

Figure 5.13: Time evolution of zeta potential [(a), (b), and (c)] and slip velocity [(d), (e), and (f)] in a closing motion in a vertical electric field. Here, we use method-D that considers both ICEO and DEP effects due to the parallel electric field on the conductive cylinder, and the center of the single valve is anchored at $(x/w, y/w) = (0.47,\ 1.125)$; $T_0\Delta P/\mu = 4$, $\alpha\ (= b/c) = 4.6$, $c/w = 0.1$, $T_0 U_c/w = 0.01$; e.g., $T_0 = 1$ ms, $\mu = 1$ mPa·s, $w = 100$ μm, $U_c = 1$ mm/s, and $E_0 = 11.9$ kV/m.

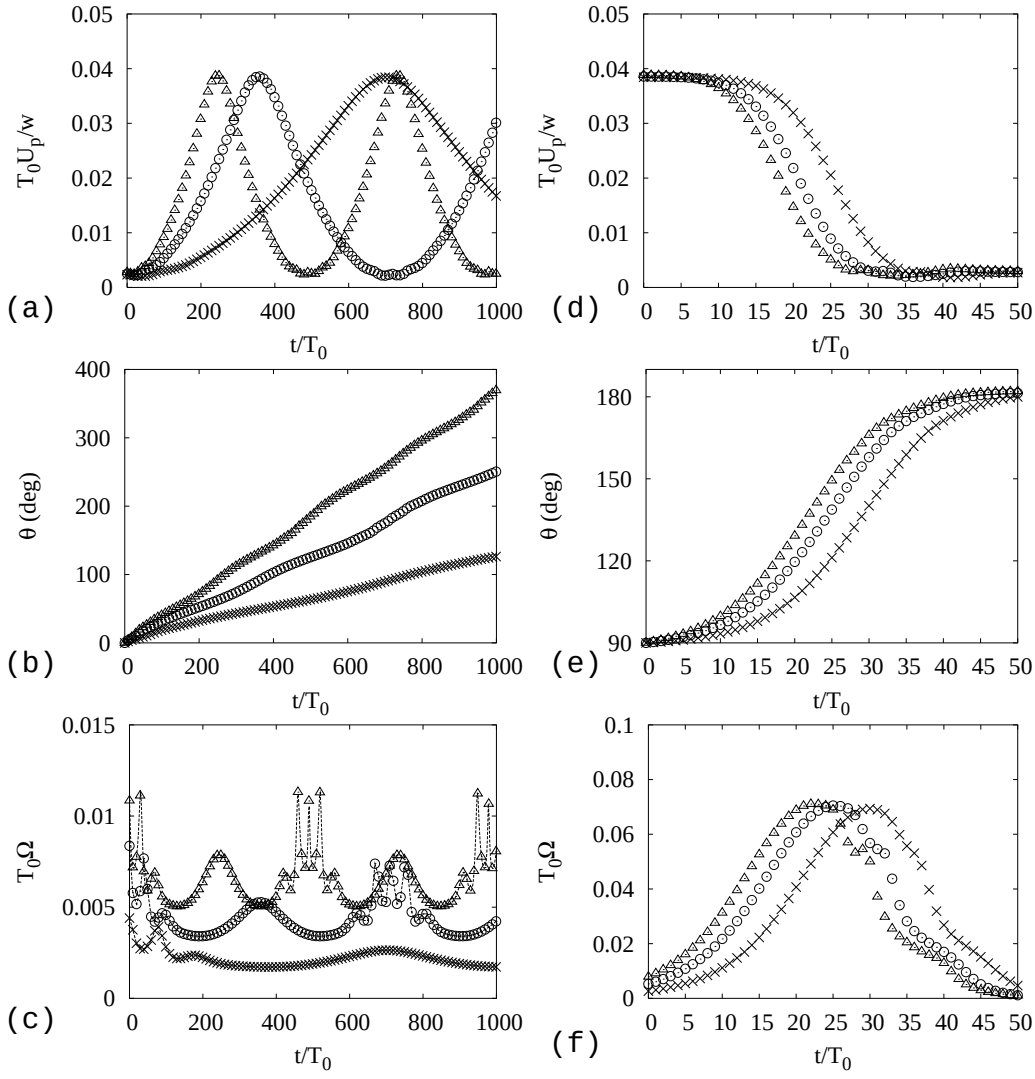

Figure 5.14: Performance of single rotary-ICEP valve for an opening motion [(a), (b), and (c) without an electric field] and a closing motion [(d), (e), and (f) with an electric field ($T_0U_c/w = 0.01$)]. Here, we use method-D that considers both ICEO and DEP effects due to the parallel electric field on the conductive cylinder, and open triangle, open circle, and cross show the numerical results for the single valve which center is anchored at $(x/w, y/w) = (0.49,1.125)$, $(0.48,1.125)$, and $(0.47,1.125)$, respectively; $T_0\Delta P/\mu = 4$, α $(= b/c) = 4.6$, and $c/w = 0.1$.

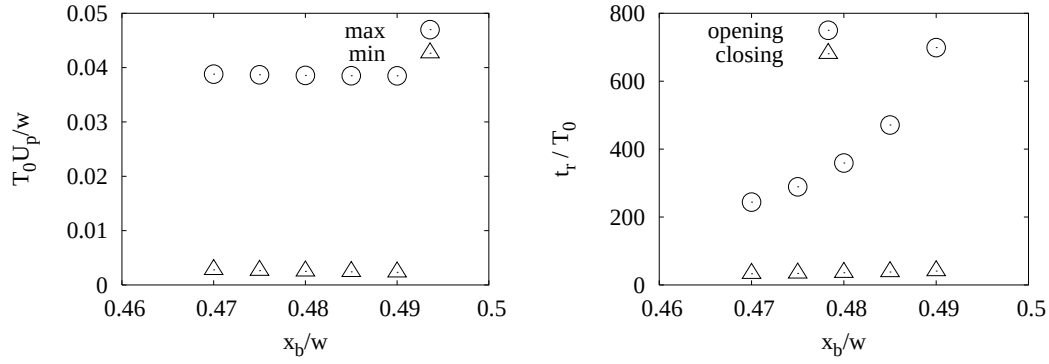

(a) U_P vs x_b/w ($T_0U_c/w = 0$) (b) t_r vs x_b/w ($T_0U_c/w = 0.01$)

Figure 5.15: Dependence of U_p and t_r on x_b/w for single rotary-ICEP valve. Here, we use method-D that considers both ICEO and DEP effects due to the parallel electric field on the conductive cylinder; $T_0\Delta P/\mu = 4$, α ($= b/c$) $= 4.6$, and $c/w = 0.1$; e.g., $T_0 = 1$ ms, $\mu = 1$ mPa·s, and $w = 100$ μm.

valve. As shown in Fig. 5.15(a), both $U_p^{\max}$ and $U_p^{\min}$ are almost constant though they decrease gradually as x_b increases. As shown in Fig. 5.15(b), t_r^{opening} increases rapidly as x_b/w increases, whereas t_r^{closing} increase gradually from 33 to 41 ms. Thus, a single rotary-ICEP valve that is positioned off the center works well; i.e., it closes at high speed ($\sim$15 Hz) and can control the pulsating flow ($\sim$3.9 mm/s for open state).

5.3.4 Performance of twin rotary-ICEP valve

Figure 5.16 shows the opening [(a), (b), and (c)] and closing [(d), (e), and (f)] motions and the flow fields for a twin rotary-ICEP valve. As shown in Figs. 5.16(a), 5.16(b), and 5.16(c) the upper and lower cylinders of the twin valve continue to rotate counterclockwise and clockwise, respectively, in an opening motion by the presence of the pressure difference $\Delta P = 4$ Pa without an electric field because of the torque due to the Poiseuille flow. As shown in Figs. 5.16(d), 5.16(e), and 5.16(f), an elliptical cylinder of the twin valve closes in a vertical electric field ($E_0 = 11.9$ kV/m). Figure 5.17 shows the time evolution of a potential field [(a), (b), and (c)] and a electric field [(d), (e), and (f)] in a vertical electric field. Figure 5.18 shows the time evolution of a zeta potential [(a), (b), and (c)] and a slip velocity [(d), (e), and (f)] in a vertical electric field.

Figure 5.19 shows the performance of a twin rotary-ICEP valve for an opening motion [(a), (b), and (c)] and a closing motion [(d), (e), and (f)] when α ($= b/c$) $= 1.7$, 2.0, and 2.3. Figures 5.19(a), 5.19(b), and 5.19(c) [Figs. 5.19(d), 5.19(e), and 5.19(f)] show the dependences of U_p, θ, and Ω on time t, respectively, in an opening motion (in a closing motion). On the one hand, a twin rotary valve in an opening motion has local maximum values of $U_p = 2.83$, 2.61, and 2.42 mm/s at t ($= t_r^{\text{opening}}$) $= 24$, 34, and 60 ms,

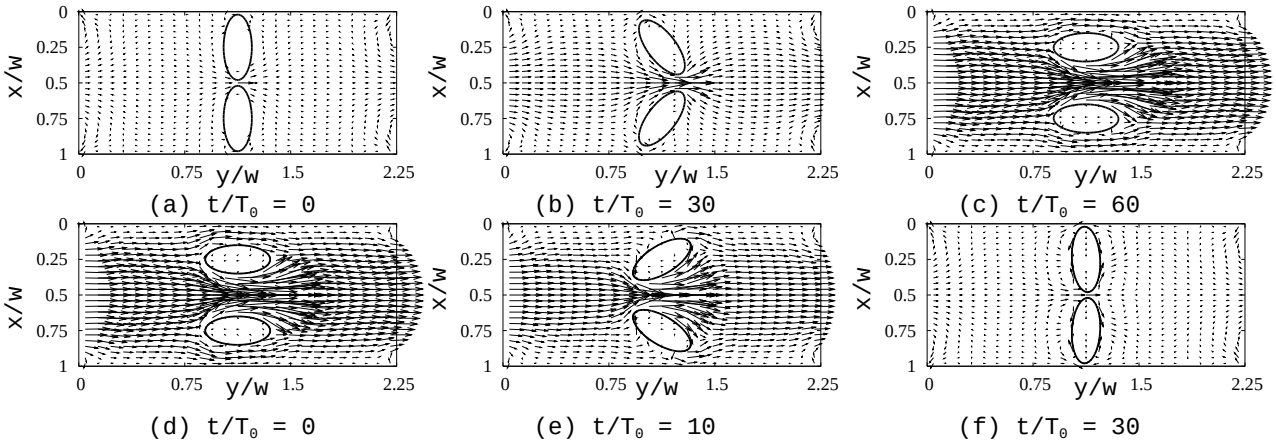

Figure 5.16: Opening [(a), (b), and (c) without an electric field] and closing [(d), (e), and (f) with an electric field $E_0 = 11.9$ kV] motions of twin rotary-ICEP valve. Here, we use method-D that considers both ICEO and DEP effects due to the parallel electric field on the conductive cylinder, and the centers of the twin valve are anchored at $(x/w, y/w)$ = (0.25,1.125) and (0.75,1.125), respectively; $T_0\Delta P/\mu = 4$, α $(= b/c) = 2.3$, and $c/w = 0.1$; e.g., $T_0 = 1$ ms, $\mu = 1$ mPa·s, and $w = 100$ μm.

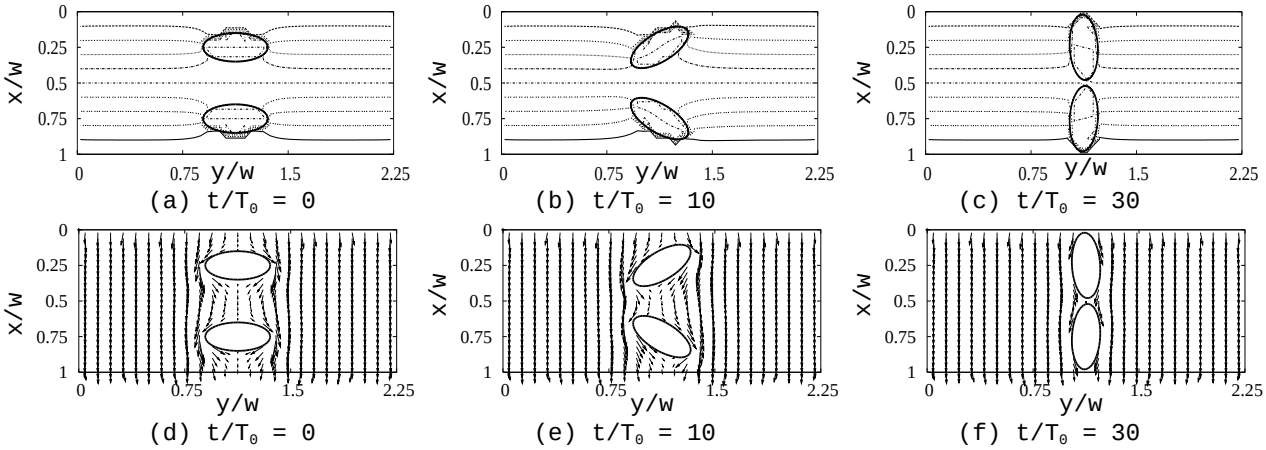

Figure 5.17: Time evolution of potential and electric fields of twin rotary-ICEP valve by the application of a vertical electric field in an opening motion. Here, we use method-D that considers both ICEO and DEP effects due to the parallel electric field on the conductive cylinder, and the centers of the twin valve are anchored at $(x/w, y/w)$ = (0.25, 1.125) and (0.75, 1.125), respectively; $T_0\Delta P/\mu = 4$, α $(= b/c) = 2.3$, $c/w = 0.1$, and $T_0U_0/w = 0.01$; e.g., $T_0 = 1$ ms, $\mu = 1$ mPa·s, and $w = 100$ μm.

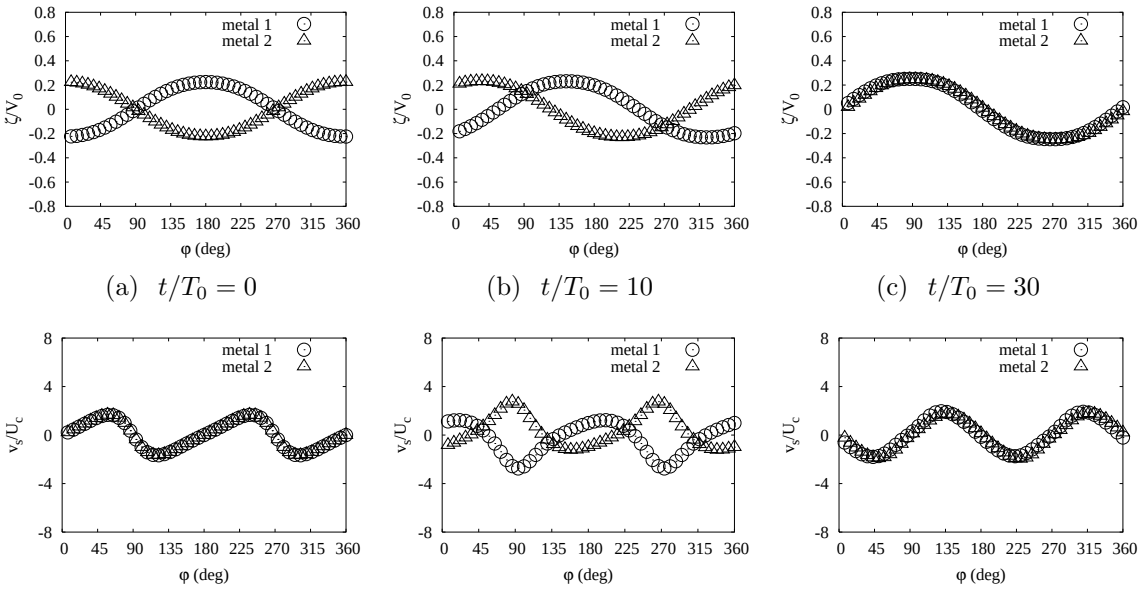

(a) $t/T_0 = 0$ (b) $t/T_0 = 10$ (c) $t/T_0 = 30$

(d) $t/T_0 = 0$ (e) $t/T_0 = 10$ (f) $t/T_0 = 30$

Figure 5.18: Time evolution of a zeta potential and a slip velocity of twin rotary-ICEP valve by the application of a vertical electric field. Here, we use method-D that considers both ICEO and DEP effects due to the parallel electric field on the conductive cylinder, and the centers of the twin valve are anchored at $(x/w, y/w) = (0.25,1.125)$ and $(0.75,1.125)$, respectively; $T_0\Delta P/\mu = 4$, α $(= b/c) = 2.3$, $c/w = 0.1$, and $T_0 U_c/w = 0.01$; e.g., $T_0 = 1$ ms, $\mu = 1$ mPa·s, and $w = 100$ μm.

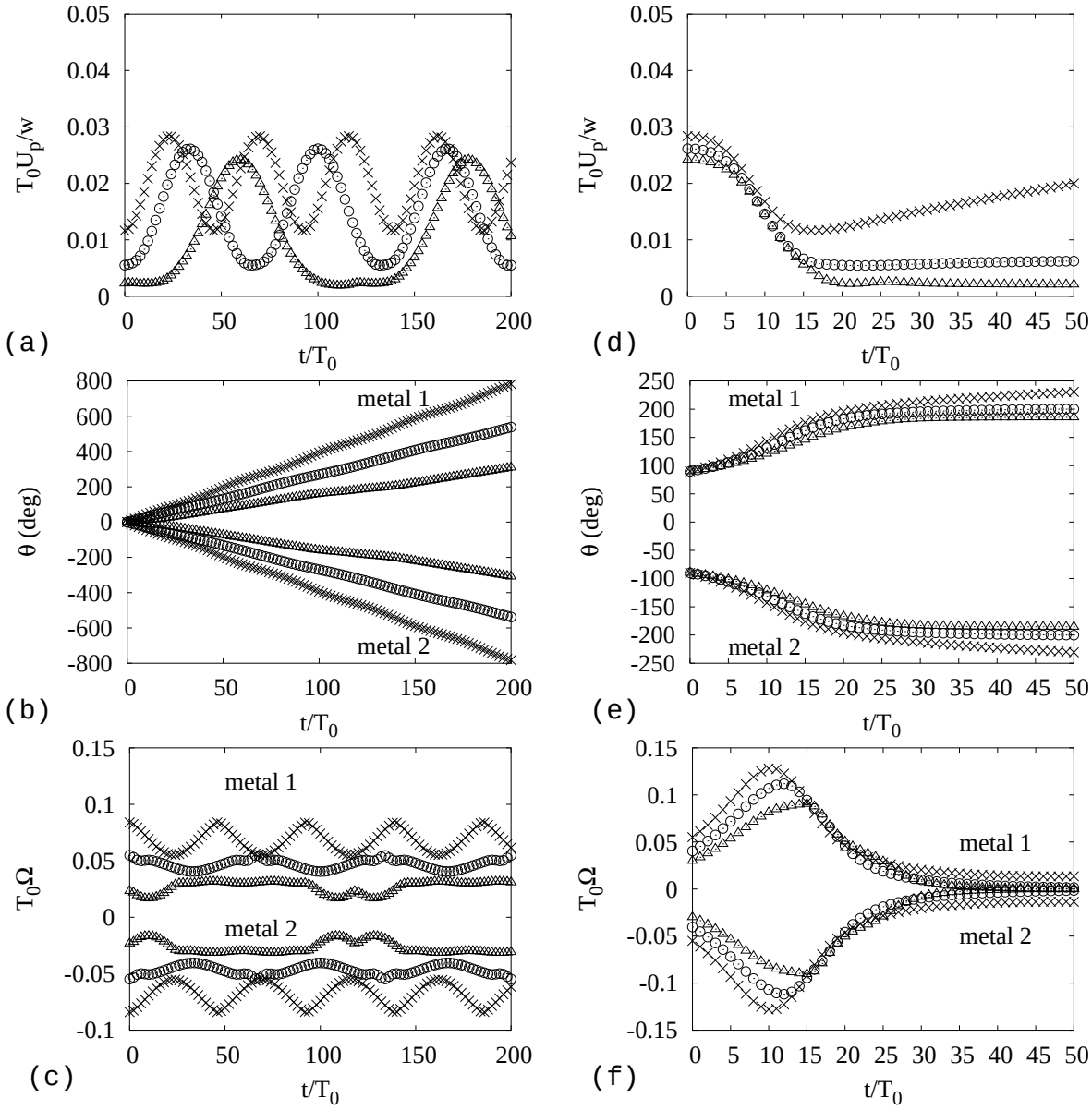

Figure 5.19: Performance of twin rotary-ICEP valve for an opening motion [(a), (b), and (c) without an electric field] and a closing motion [(d), (e), and (f) with an electric field ($T_0U_c/w = 0.01$)]. Here, we use method-D that considers both ICEO and DEP effects due to the parallel electric field on the conductive cylinder, and the centers of the twin valve are anchored at $(x/w, y/w)$ = (0.25,1.125) and (0.75,1.125), respectively; $T_0\Delta P/\mu$ = 4, α (= b/c) = 2.3, and c/w = 0.1; e.g., T_0 = 1 ms, μ = 1 mPa·s, and w = 100 μm; The symbols show the numerical results for a bounded domain; i.e., open triangle, open circle, and cross show the numerical results at b/c = 2.3, 2.0, and 1.7, respectively.

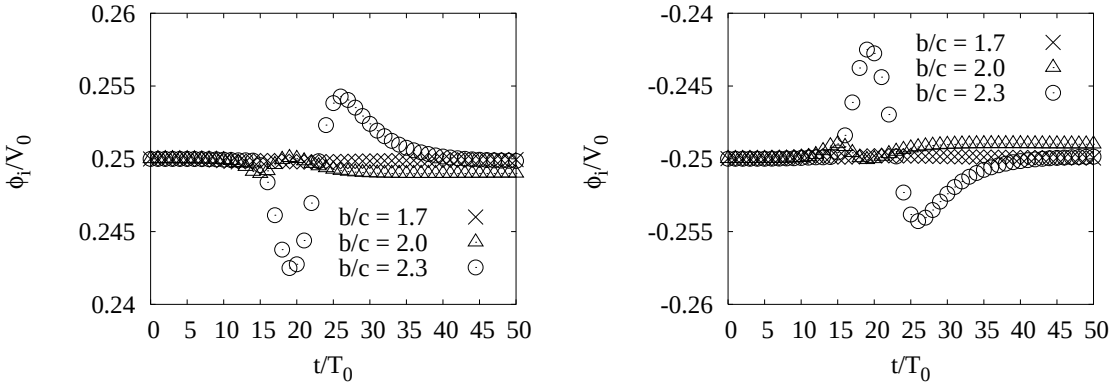

(a) Upper metal (metal 1) (b) Lower metal (metal 2)

Figure 5.20: ϕ_i vs t. Here, the centers of the twin valve are anchored at $(x/w, y/w)$ = (0.25,1.125) and (0.75,1.125), respectively; $T_0\Delta P/\mu = 4$, $c/w = 0.1$, and $T_0 U_c/w = 0.01$; e.g., $T_0 = 1$ ms, $\mu = 1$ mPa·s, $w = 100$ μm, $U_c = 1$ mm/s, and $E_0 = 11.9$ kV/m.

respectively, without an electric field as shown in Fig. 5.19(a). On the other hand, for the conditions α (= b/c) = 2.0 and 2.3, a twin rotary valve close with t (= t_r^{closing}) = 22 and 21 ms, respectively, by the application of an electric field $E_0 = 11.9$ kV/m as shown in Fig. 5.19(d). Note that if we use method-C, t (= t_r^{closing}) = 23 and 22 ms, respectively. It should be noted that the rotary-ICEP valve that α (= b/c) = 1.7 will not close by the application of an electric field $E_0 = 11.9$ kV/m because of the shortage of the torque due to an ICEP. Further, Figs. 5.20(a) and 5.20(b) show the time evolution of ϕ_i for the upper and lower cylinders (metal), respectively, in a closing motion. As shown in Figs. 5.20(a) and 5.20(b), ϕ_i changes remarkably in the range that 17 ms $< t <$ 35 ms when α (= b/c) = 2.3.

Figure 5.21 shows the dependence of U_p and t_r on α (= b/c) for a twin rotary-ICEP valve. As shown in Fig. 5.21(a), both $U_p^{\max}$ and $U_p^{\min}$ decrease as α (= b/c) increases. As shown in Fig. 5.21(b), t_r^{opening} increase rapidly as b/c increases. It should be noted that the twin rotary-ICEP valve close in the range that α (= b/c) $\geq$ 2.0. Thus, the twin rotary-ICEP valve closes at high frequency (∼24 Hz) and a weak electric field (11.9 kV/m) in a microfluidic channel of 100 μm width and can control the pulsating pressure flow (∼2.4 mm/s for open state).

5.3.5 Best rotary-ICEP valve

As a practical consideration, a valve often needs to work against external pressure gradient. Figure 5.22 shows the maximum pressure head our proposed valves can operate against. From Figs. 5.22(a) and (b), controllable maximum pressures for the single and twin rotary-ICEP valves of channel length $L = 2.25$ μm are 32 and 8 Pa, respectively;

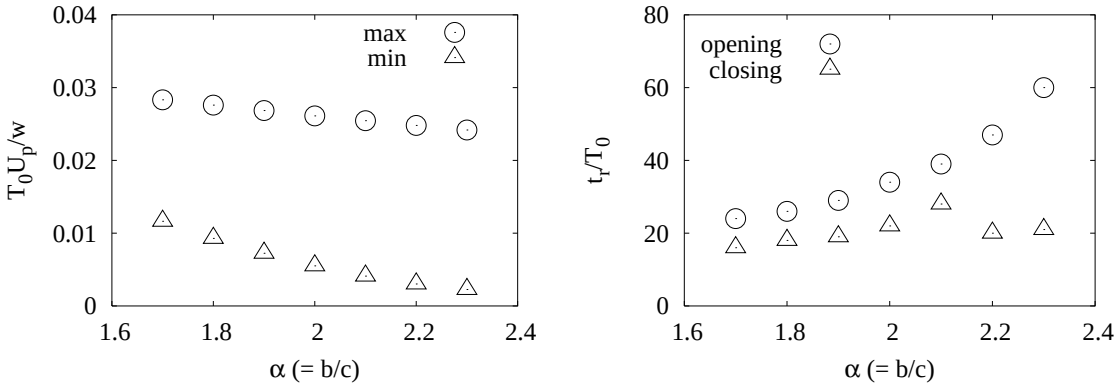

(a) U_P vs α $(= b/c)$ (b) t_r vs α $(= b/c)$

Figure 5.21: Dependence of U_p and t_r on α $(= b/c)$ for twin rotary-ICEP valve. Here, we use method-D that considers both ICEO and DEP effects due to the parallel electric field on the conductive cylinder, and the centers of the twin valve are anchored at $(x/w, y/w)$ = (0.25,1.125) and (0.75,1.125), respectively; $T_0\Delta P/\mu = 4$, $T_0U_c/w = 0.01$, and $c/w = 0.1$; e.g., $T_0 = 1$ ms, $\mu = 1$ mPa·s, and $w = 100$ μm.

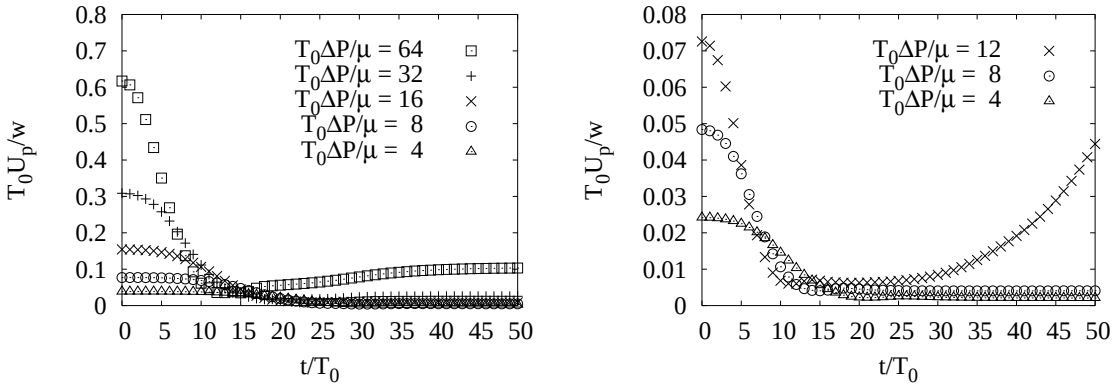

(a) U_P vs *time* for single ICEP valve (b) t_r vs *time* for twin ICEP valve

Figure 5.22: Controllable maximum pressure. (a) The center of the single valve is anchored at $(x/w, y/w) = (0.48,1.125)$; (b) The centers of the twin valve are anchored at $(x/w, y/w) = (0.25,1.125)$ and $(0.75,1.125)$, respectively; In (a) and (b), $T_0\Delta P/\mu = 4$, $T_0U_cw = 0.01$, $L/w = 2.25$, and $c/w = 0.1$; e.g., $T_0 = 1$ ms, $\mu = 1$ mPa·s, $w = 100$ μm, $\Delta P = 4$ Pa, $E_0 = 11.9$ kV/m, $U_c = 1$ mm/s. Here, we use method-D that considers both ICEO and DEP effects due to the parallel electric field on the metal cylinder,

i.e., controllable maximum pressure gradients of the single and twin rotary-ICEP valves are 142 and 36 kPa/cm, respectively. Note that we mainly use the condition that ΔP = 4 Pa for $L = 2.25$ μm ($\Delta P/L = 18$ kPa/cm) throughout calculations except Fig. 5.22 so that an average flow velocity for open state is approximately αU_c (= 4.6 mm/s) that is a maximum flow value to be expected. Further, in Fig. 5.22, maximum and minimum average flow velocities for the single valve (at $T_0 \Delta P/\mu = 4$) are 3.9 and 0.19 mm/s, while those velocities for the twin valve are 2.2 and 0.26 mm/s; i.e., the values of $U_p^{\max}/U_p^{\min}$ for the single and twin rotary-ICEP valves are 20.1 and 8.4, respectively. Furthermore, a single rotary-ICEP valve is simpler than a twin rotary-ICEP valve. Therefore, from the view point of practical applications, we believe that a single rotary-ICEP valve is better than a twin rotary-ICEP valve and any other multi rotary-ICEP valves, although the response frequency of a twin valve is larger than that of a single valve. Thus, we believe that a single rotary-ICEP valve is the best rotary-ICEP valve.

5.4 Discussion

Boundary effects on electrophoresis of colloidal cylinders have been analyzed by Keh et al. [43], and the effect of induced electro-osmosis on cylindrical particle next to a surface has been analyzed by Zhao and Bau [104]. However, the effect of ICEP on the rotation of a elliptical conductive cylinder near a conductive surface in a flow channel has first been analyzed in this paper by the multi-physics coupled simulation technique between fluidics and electro-statics based on the boundary element method along with the thin double layer approximation. Based on the analysis of boundary effects on ICEP, we have first extended ICEP to design a microfluidic system's component including a movable part, albeit the induced-charge electro-osmosis (ICEO) has been utilized to enhance mixing in principle [105, 5, 83], and it can also be exploited to pump the liquid [1, 5, 83, 84, 34, 66, 97, 30, 16, 90, 17, 92]. Namely, we have first shown that by the application of an electric field perpendicular to the flow channel, the elliptical conductive cylinder in the channel rotates to be aligned with the electric field due to ICEP and the elliptical cylinder can block the flow, which serves as a valve. It should be noted that though the angular velocity of a elliptical cylinder due to ICEP is diminished by the electric boundary effects, it is accelerated by the fluidic boundary effects.

Further, from Eq. (5.17), we can estimate $\Omega^{\max} = \varepsilon E_0^2/\mu$ in the thin limit ($\alpha = b/c \to 0$) in water in an unbounded domain. Thus, if we consider a rotational electric field such as $\sin 2(\theta + \psi) = 1$, the response time is $t_{\rm r}^{\min} = \pi\mu/2\varepsilon E_0^2$ and the response frequency is $f_{\rm r}^{\max} = 1/2t_{\rm r}^{\min}$: i.e., for $E_0 = 11.9$ kV/m, $t_{\rm r}^{\min} = 16$ ms and $f_{\rm r}^{\max} = 32$ Hz are ideal values. Therefore, the response frequencies 15 and 24 Hz for the single and twin rotary-ICEP valves in a microfluidic channel are 44% and 69% of the ideal value (32 Hz).

We assume that boundary conditions at the two electrodes ($x = 0$ and w) are those of fixed potential for the electrical problem and zero slip velocity for the mechanical

problem. In order to have an electric field in the electrolyte, electrical current should go from one electrode to the other and, consequently, there must be Faradaic reactions at the electrodes. This will surely generate problems such as bubbles generation, changes in the electrolyte species, etc., although the problems are reduced to some extent by the application of ac electric fields. In addition, the electrodes might need to be ideally non-polarizable in this context. In this case, one of the possibilities might be to have the electrodes further apart (to put the problems "the electrodes" outside the channel where the valve is) and to use porous walls, although we cannot deny that we still see that there could be fluid motion generated at the boundaries $x = 0$ and w because of concentration polarization. In other words, if the channel walls are conducting so that electric field can be applied, the polarization of the electrolyte near the electrodes ($x = 0$, w) will lead to shielding of the imposed dc electric field. In particular, a small voltage, such as 1.19 V (= 11.9 kV/m $\times$ 100 μm), might be particularly susceptible to polarization near the electrodes. Nevertheless, we believe that our predictions are still valid mainly because there are various ways for applying an electric field to the device; e.g., we can use the difference of charging time between electrodes and elliptical cylinders. Further, real electrodes are not ideally non-polarizable and polarizable [9] and it is realistic assumption that there is no tangential electric field that drives fluid as an ICEO flow at the boundaries $x = 0$ and w. Furthermore, if the double layer is thin and Faradaic reaction is fast, potential drop across the double layer will be uniform and the constant potential boundary condition is still applicable, although the electrode will attract counter ions and form electric double layer due to the electrostatics as long as there exists an electric potential on the electrode.

However, it is true that there are some difficulties if we consider dc electric fields. Thus, we need to consider ideally polarizable electrodes with ac electric fields, rather than ideally non-polarizable electrodes with dc electric fields. Figure 5.23(a) shows the schematic view of the electric circuit model considered in this discussion. As shown in Fig. 5.23, ideally polarizable electrodes at $x = 0$ and w are modeled [83, 6, 67] as the two capacitors of the capacitance $C_{e0} = \varepsilon L' d/\lambda_D$, where λ_D ($\sim$1nm in water) is the Debye screening length, L' ($\gg 2b$) is the length of electrodes, and d is a depth of the channel. Further, the polarizable elliptical cylinder is approximately modeled as the two capacitors of the capacitance $C_{p0} = \varepsilon 2bd/\lambda_D$. Furthermore, the resistance between electrodes is modeled as $R_e = w/\sigma_b L' d$, and the resistance between the electrode and elliptical cylinder is modeled as $R_p = \overline{w}/\sigma_b 2bd$, where $\sigma_b = \varepsilon D/\lambda_D^2$ is the bulk conductivity, D ($\sim 10^3 \mu\text{m}^2/\text{s}$) is an ion diffusivity, and $\overline{w}$ is the effective gap length between the electrode and elliptical cylinder. Since the gap length between the electrode and elliptical cylinder is $w - 2c$ (80 μm) and $w - 2b$ (8 μm) for $\psi = 90$ and 0 deg, respectively, we can approximate $\overline{w}$ as $\overline{w} \simeq \sqrt{(w-2c)(w-2b)} \sim 25$ μm as a first attempt. Therefore, we can simplify the electrical circuit model as shown in Fig. 5.23(b). From the standard ac analysis, we obtain the complex internal voltage $\tilde{V}_0$ (= $V_0 e^{j\omega t}$) that is applied to the bulk region between two

thin double layers of the electrodes as follows:

$$\tilde{V}_0 = \frac{j\omega C_e R_e[j\omega C_p(R_e + R_p) + 1]}{j\omega C_e R_e(j\omega C_p R_p + 1) + [j\omega C_p(R_e + R_p) + 1]}\tilde{V}_{\rm in}, \tag{5.18}$$

where $\tilde{V}_{\rm in}$ is the complex external voltage that is applied between the electrodes including thin double layers, and ω is a driving angular velocity of the ac external voltage. By considering $R_p \gg R_e$ (because of $L' \gg 2b$ and $w \sim \overline{w}$), we can approximate $\tilde{V}_0$ as $\tilde{V}_0 \simeq \frac{j\omega\tau_e}{j\omega\tau_e+1}\tilde{V}_{\rm in}$, where $\tau_e = R_e C_e = \lambda_D w/2D$ ($\simeq 1\text{nm}\times 100\mu\text{m}/2\times 10^{-9}\text{m}^2/\text{s} \sim 0.05$ ms) is a charging time for the electrode. Thus,

$$|\tilde{V}_0| \simeq \frac{\omega\tau_e}{\sqrt{(\omega\tau_e)^2 + 1}}|\tilde{V}_{\rm in}|. \tag{5.19}$$

Further, the complex voltage $\tilde{V}_p$ across C_p is $\tilde{V}_p = \frac{1}{j\omega\tau_p+1}\tilde{V}_0 \simeq \frac{1}{j\omega\tau_p+1}\frac{j\omega\tau_e}{j\omega\tau_e+1}\tilde{V}_{\rm in}$, where $\tau_p = R_p C_p = \lambda_D\overline{w}/2D$ ($\simeq 1\text{nm}\times 25\mu\text{m}/2\times 10^{-9}\text{m}^2/\text{s} \sim 0.01$ ms) is a charging time for the elliptical cylinder. Thus,

$$|\tilde{V}_p| = \frac{1}{\sqrt{(\omega\tau_p)^2 + 1}}|\tilde{V}_0| \simeq \frac{1}{\sqrt{(\omega\tau_p)^2 + 1}}\frac{\omega\tau_e}{\sqrt{(\omega\tau_e)^2 + 1}}|\tilde{V}_{\rm in}|. \tag{5.20}$$

Figure 5.23(c) shows the dependence of $\tilde{V}_p$ on ω by using Eq. (5.20). From Fig. 5.23(c) or Eq. (5.20), our proposed device can work well around $\omega_0 = (\tau_p^{-1} - \tau_e^{-1})/2 \sim 0.4 \times 10^5$ rad/s ($f_0 = \omega_0/2\pi \sim 6$ kHz). Note that the ICEO flow around the elliptical cylinder is set into motion exponentially over the cylinder charging time τ_p, but is terminated exponentially over the longer electrode charging time τ_e as the bulk field is screened at the electrodes. In other words, electric fields persist in the bulk solution when the driving frequency is high enough ($\omega\tau_e > 1$) that induced double layers do not have time to develop near the electrodes; Induced-charge electro-osmotic flows driven by applied ac fields can thus persist only in a certain band of driving frequencies, $\tau_e^{-1} < \omega < \tau_p^{-1}$. (Note that these kinds of arguments are seen in [83, 6].)

By introducing dimensionless valuables $\hat{\boldsymbol{v}} = \boldsymbol{v}/U_0$, $\hat{\boldsymbol{x}} = \boldsymbol{x}/L_0$, $\hat{\boldsymbol{t}} = \boldsymbol{t}/T_0$, and $\hat{\boldsymbol{p}} = L_0 p/\mu U_0$, we can obtain the dimensionless form of Navier-Stoles equation [64] without an external force $\boldsymbol{g}$ as follows:

$$\beta\frac{\partial\hat{\boldsymbol{v}}}{\partial t} + Re\hat{\boldsymbol{v}}\cdot\hat{\nabla}\hat{\boldsymbol{v}} = -\hat{\nabla}\hat{p} + \hat{\nabla}^2\hat{\boldsymbol{v}}, \tag{5.21}$$

where $\beta = \rho L_0^2/\mu T_0$ is unsteadiness parameter (the Stokes number), $Re = \rho U_0 L_0/\mu$ is the Reynolds number, and ρ is the density of the solution. Note that U_0, L_0, and T_0 are representative velocity, length, and time, respectively. The reciprocal number of frequency of rotation or equivalently the time of rotation is of the order of 10 ms. Thus, calculations may not be totally correct because of two quasi-static approximations; mechanical and

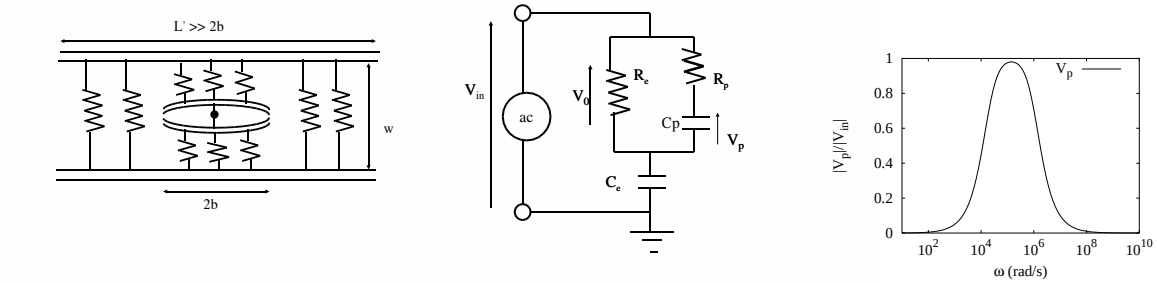

(a) Schematic view of electro circuit model for ICEO valve (b) Simple electro circuit model (c) Dependence of $\tilde{V_p}$ on ω for ICEO valve

Figure 5.23: Ac analysis using a simple circuit model.

electrical approximations. (a) The Reynolds and Stokes numbers associated to the angular frequency are not much smaller than one under the condition that $w = 100$ μm and $E_0 = 11.9$ kV/m; i.e., $Re = \rho\Omega^{\max}b^2/\mu \sim \rho\alpha U_c b/\mu \sim 1000\text{kg/m}^3 \times 5\text{mm/s} \times 50\mu\text{m}/1\text{mPa}\cdot\text{s} \sim 0.25$, and $\beta = \rho b^2/\mu T_0 \sim 1000\text{kg/m}^3 \times (50\mu\text{m})^2/1\text{mPa}\cdot\text{s} \sim 0.25$. Therefore, under the condition that $w = 100$ μm and $E_0 = 11.9$ kV/m, the term $\beta\frac{\partial\hat{\boldsymbol{v}}}{\partial t} + Re\hat{\boldsymbol{v}}\cdot\hat{\nabla}\hat{\boldsymbol{v}}$ might be present in Eq. (5.21) to calculate more correctly. Or, we should reduce w; e.g., $Re \sim 0.0025$ and $\beta \sim 0.0025$ under the condition that $w = 10$ μm and $E_0 = 11.9$ kV/m. However, it is customary in microfluidic and colloidal systems to neglect the unsteady term $(\rho\partial\boldsymbol{v}/\partial t)$ in the Stokes equations, because ions diffuse more slowly than vorticity by a factor of $\rho D/\mu \simeq 10^{-3}$ [83]. Further, the condition that $w = 100$ μm and $E_0 = 11.9$ kV/m ($V_0 = 1.19$ V) is the most interesting condition for the wide range of biomedical applications. (b) The two typical time for charging a metal/electrolyte double layer are RC times, τ_p and τ_e. As mentioned before, these times are $\tau_p = \lambda_D\overline{w}/2D \sim 0.01$ ms and $\tau_e = \lambda_D w/2D \sim 0.05$ ms for water. Therefore, it seems that to use an electrical quasi-static approximation is justified for water. However, solutions that are used in biomedical applications have various values of λ_D in the range that 1 to 100 nm. Thus, there is a possibility that to use an electrical quasi-static approximation may not be justified; e.g., if $\lambda_D = 100$ nm, $\tau_p \sim 1$ ms and $\tau_e \sim 5$ ms. In such a case, the electrical problem may need the following boundary condition at the surface of ellipsoid and electrodes; $\partial q/\partial t = j_n$, where $\partial q/\partial t$ is the derivative of surface charge in the double layer and j_n is the normal current arriving at them. Because of these two points, we may need to say that our calculations are a first approach to the problem.

5.5 Conclusion

In conclusion, we have proposed rotary-ICEP microvalves in water using hydrodynamic force due to induced-charge electrophoresis and numerically examined their performance.

By the multi-physics coupled simulation technique between fluidics and electro-statics based on the boundary element method along with the thin double layer approximation, we find that (1) for the general problem, an angular velocity of an elliptical conductive cylinder is accelerated by the fluidic boundary effect, and is decelerated by the electric boundary effect; (2) for the valve problem, the electric boundary effect is stronger than the fluidic boundary condition and thus it usually decelerates the angular velocity of the valve, because the elliptical conductive cylinder is very close to the electrode; (3) to obtain a large average velocity in an opening state and a large angular velocity in a closing motion, single or twin rotary-valves have more advantages than the multi ($N \geq 3$) rotary-ICEP valves; (4) a single rotary-ICEP valve that is positioned off the center closes at high frequency ($\sim$15 Hz) and a weak electric field (11.9 kV/m) in a microfluidic channel and can control the pulsating pressure flow in an opening state; (5) a twin rotary-ICEP valve closes at high frequency ($\sim$24 Hz) and a weak electric field (11.9 kV/m) in a microfluidic channel and can control the pulsating pressure flow in an opening state. We believe that actuators using ICEP will revolutionize the design concept of fluidic MEMS and can greatly contribute to many promising biomedical applications. In the future, we intend to evaluate other actuators using ICEP.

5.6 Appendix A: Tangential component of the electric field

We used the solution for a 3D ellipsoid from [26] to obtain the 2D solution for an ellipse with semi-major axis c and semi-minor axis b. On the surface S_{p}^{+}:

$$\phi = -\boldsymbol{x} \cdot \mathsf{G}_{\mathrm{p}}^{+} \cdot \boldsymbol{E}_{\infty}, \qquad \boldsymbol{E}_{\mathrm{p}}^{+} = \mathsf{G}_{\mathrm{p}}^{+} \cdot \boldsymbol{E}_{\infty}, \tag{5.22}$$

$$\mathsf{G}_{\mathrm{p}}^{+} = \left(1 + \frac{1}{\alpha}\right) \boldsymbol{e}_1 \otimes \boldsymbol{e}_1 + (1+\alpha)\, \boldsymbol{e}_2 \otimes \boldsymbol{e}_2 \tag{5.23}$$

where $\alpha = b/c$, $\boldsymbol{E}_{\mathrm{p}}^{+}$ is the surface electric field, $\boldsymbol{x}$ is the position on the surface, $\boldsymbol{e}_j$ is a unit coordinate vector. The symbol $\otimes$ is a tensor product so that $(\boldsymbol{e}_j \otimes \boldsymbol{e}_j) \cdot \boldsymbol{E}_{\infty} = (\boldsymbol{e}_j \cdot \boldsymbol{E}_{\infty})\, \boldsymbol{e}_j$. The tangential component of the electric field $\boldsymbol{E}_{\mathrm{s}}$ is obtained thanks to:

$$\boldsymbol{E}_{\mathrm{s}} = (I - \boldsymbol{n}\boldsymbol{n}) \cdot \mathsf{G}_{\mathrm{p}}^{+} \cdot \boldsymbol{E}_{\infty} = (\boldsymbol{t} \cdot \boldsymbol{E}_{\mathrm{p}}^{+})\, \boldsymbol{t} \tag{5.24}$$

where $\boldsymbol{t}$ is the unit tangential vector to the surface.

Proof. For completeness, we provide a proof of this result. Using Eqs. (5.21) in [26], we have in 2D:

$$\mathsf{G}_{\mathrm{p}}^{+} = \left[1 - \frac{bc}{2} W(b)\right]^{-1} \boldsymbol{e}_1 \otimes \boldsymbol{e}_1 + \left[1 - \frac{bc}{2} W(c)\right]^{-1} \boldsymbol{e}_2 \otimes \boldsymbol{e}_2$$

$$W(u) = \int_0^{\infty} \frac{1}{(u^2+\lambda)\sqrt{(b^2+\lambda)(c^2+\lambda)}}\, d\lambda$$

These integrals can be computed analytically:

$$\begin{aligned}\frac{bc}{2}W(b) &= \frac{bc}{2}\int_0^\infty \frac{d\lambda}{(b^2+\lambda)^{3/2}(c^2+\lambda)^{1/2}} \\ &= bc\left[\frac{\sqrt{c^2+\lambda}}{(b^2-c^2)\sqrt{b^2+\lambda}}\right]_0^\infty \\ &= \frac{bc}{b^2-c^2} - \frac{c^2}{b^2-c^2} \\ &= \frac{1}{\alpha+1}.\end{aligned}$$

Similarly, $bcW(c)/2 = \alpha/(\alpha+1)$. Thus,

$$\mathsf{G}_{\mathrm{p}}^{+} = \left(1+\frac{1}{\alpha}\right)\boldsymbol{e}_1\otimes\boldsymbol{e}_1 + (1+\alpha)\,\boldsymbol{e}_2\otimes\boldsymbol{e}_2.$$

5.7 Appendix B: 2D angular velocity of the elliptical cylinder in an unbounded domain

Proof. The translational and rotational parts of the motion can be treated separately.

For the translational part, we write the velocity on the surface of the ellipse as $\boldsymbol{U}^{\text{unbounded}} + \boldsymbol{v}_s$. There should be no net force on the cylinder so that:

$$\int_{S_{\mathrm{p}}^{+}} (\boldsymbol{n}\cdot\boldsymbol{x})\,(\boldsymbol{U}^{\text{unbounded}} + \boldsymbol{v}_s)\,\mathrm{d}l = 0 \tag{5.25}$$

The integral of $(\boldsymbol{n}\cdot\boldsymbol{x})$ can be computed easily using Green's theorem and we find that:

$$\boldsymbol{U}^{\text{unbounded}} = -\frac{1}{2A_{\mathrm{p}}}\int_{S_{\mathrm{p}}^{+}} (\boldsymbol{n}\cdot\boldsymbol{x})\,\boldsymbol{v}_s\,\mathrm{d}l$$

where $A_{\mathrm{p}} = \pi bc$ is the area of the ellipse.

Similarly there should be no net torque on the cylinder so that:

$$\int_{S_{\mathrm{p}}^{+}} (\boldsymbol{n}\cdot\boldsymbol{x})\,(|\boldsymbol{x}|^2\boldsymbol{\Omega}^{\text{unbounded}} + \boldsymbol{x}\times\boldsymbol{v}_s)\,\mathrm{d}l = 0 \tag{5.26}$$

From this equation, we obtain:

$$\boldsymbol{\Omega}^{\text{unbounded}} = -\frac{1}{A_{\mathrm{p}}(b^2+c^2)}\int_{S_{\mathrm{p}}^{+}} (\boldsymbol{n}\cdot\boldsymbol{x})\,(\boldsymbol{x}\times\boldsymbol{v}_s)\,\mathrm{d}l$$

We can now prove Eq. (4.10) using Eq. (4.7) for $\boldsymbol{v}_s$. Recall that $\boldsymbol{x}$ and $\boldsymbol{n}$ are equal to:

$$\begin{aligned}\boldsymbol{x} &= -c\alpha \sin\varphi\ \boldsymbol{e}_1 + c\cos\varphi\ \boldsymbol{e}_2\\ \boldsymbol{n} &= q_0^{-1}(-\sin\varphi\ \boldsymbol{e}_1 + \alpha\cos\varphi\ \boldsymbol{e}_2)\end{aligned}$$

from which $\boldsymbol{n}\cdot\boldsymbol{x} = bq_0^{-1}$. The slip velocity $\boldsymbol{v}_s$ is given by Eq. (5.7). The length element can be shown to be equal to $\mathrm{d}l = cq_0\mathrm{d}\varphi$.

Here, we can set that $\boldsymbol{U}^{\text{unbounded}} = \boldsymbol{0}$ because of the anchoring condition of our valves. However, we can show that $\boldsymbol{U}^{\text{unbounded}} = \boldsymbol{0}$ even if we do not consider the anchoring condition. To show that $\boldsymbol{U}^{\text{unbounded}} = \boldsymbol{0}$, we need to calculate the following integral:

$$\int_0^{2\pi} q_0^{-1} g\ \boldsymbol{t}\mathrm{d}\varphi,$$

where $g = g(\varphi) = \frac{1}{2}\sin 2(\theta+\psi+\varphi) = \sin(\theta+\psi+\varphi)\cos(\theta+\psi+\varphi)$. However, we notice that $[q_0^{-1}g](\varphi+\pi) = [q_0^{-1}g](\varphi)$ while $\boldsymbol{t}(\varphi+\pi) = -\boldsymbol{t}(\varphi)$. Therefore this integral is equal to 0.

Moving on to $\boldsymbol{\Omega}^{\text{unbounded}}$, the cross product with $\boldsymbol{x}$ is equal to:

$$\boldsymbol{x}\times\boldsymbol{v}^{(\mathrm{s})} = \frac{\varepsilon bcE_0^2(1+\alpha)^2 g}{\mu q_0^2}\boldsymbol{e}_3$$

We therefore need to calculate the following integral:

$$\boldsymbol{\Omega}^{\text{unbounded}} = -\frac{\varepsilon E_0^2 b(1+\alpha)^2}{\mu\pi c(1+\alpha^2)}\left[\int_0^{2\pi}\frac{g}{q_0^2}\mathrm{d}\varphi\right]\boldsymbol{e}_3$$

The integral of g/q_0^2 can be computed analytically:

$$\frac{g}{q_0^2} = \frac{\sin(\theta+\psi+\varphi)\cos(\theta+\psi+\varphi)}{\alpha^2\cos^2\varphi+\sin^2\varphi}$$

If we expand $\sin(\theta+\psi+\varphi)\cos(\theta+\psi+\varphi)$, we obtain three terms, with $\cos^2\varphi$, $\sin^2\varphi$, and $\cos\varphi\sin\varphi$. Because of the anti-symmetry $\cos(-\varphi)\sin(-\varphi) = -\cos\varphi\sin\varphi$, the last term makes no contribution. We are left with:

$$\frac{\sin 2(\theta+\psi)}{2}\int_0^{2\pi}\frac{\cos^2\varphi-\sin^2\varphi}{\alpha^2\cos^2\varphi+\sin^2\varphi}\mathrm{d}\varphi = \pi\sin 2(\theta+\psi)\ \frac{1-\alpha}{\alpha(1+\alpha)}$$

Inserting this result for $\int g/q_0^2$ into the previous equation for $\boldsymbol{\Omega}^{\text{unbounded}}$, we finally obtain:

$$\boldsymbol{\Omega}^{\text{unbounded}} = -\frac{\varepsilon E_0^2}{\mu}\ \frac{1-\alpha^2}{1+\alpha^2}\sin 2(\theta+\psi)\ \boldsymbol{e}_3$$

Chapter 6

Valve 2 (Theory and Experiment): Rotation of a microvalve near conductive electrodes via induced-charge electrophoresis

In this chapter, by using an elliptical conductive carbon element fabricated by the pyrolysis of a photoresist film coated with gold, we experimentally demonstrate that microvalves can rotate near conductive electrodes. Namely, by numerically analyzing video data, we show the time evolution of the rotation angle, the flow field, and the center position of the microvalve. Further, we compare them with the theoretical results, and find that they are in good agreement qualitatively. In the future, by using ICEP valves as a latch device, we can significantly improve the size and processing speed of a fluidic integrated circuit.

6.1 Introduction

To the best of our knowledge, no attempt has been made to analyze microvalves that rotate via ICEP, except for our previous study [95]. In our previous study, we proposed a rotary-ICEP valve in water using hydrodynamic force due to ICEP and theoretically demonstrated its design. To overcome the problems faced by actuators in water, we adopted ICEP to move valves in order to stop and release the flow of the channel, and we concluded that rotary-ICEP valves function effectively at high frequencies, in spite of the electrostatic boundary effect (of the conductive electrodes) that suppresses the torques due to ICEP and dielectrophoresis (DEP). Note that the flow resistance of ICEP valves in a small channel is much smaller than that of ordinary valves that use an external torque because ICEP valves can move smoothly at the velocity that is proportional to the slip velocity on the surface, while structures in a viscous flow usually feel a strong

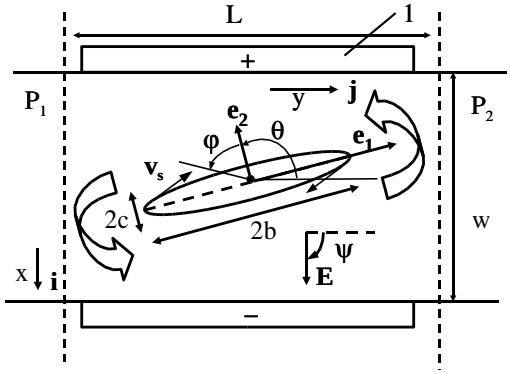

Figure 6.1: Schematic view of ICEO stacking pump. 1: pair of electrodes. Here, $\psi = \theta = \pi/2$ rad, L is the length, w is the width, and V_0 is the voltage applied to the electrodes. The ellipse has two semi-axes (b, c) with unit vectors $(\boldsymbol{e}_1, \boldsymbol{e}_2)$ that define the orientation of each semi-axis.

repulsion force when they move (with pushing water) since the pressure-driven flow rate through small channels decreases with the third or fourth power of channel size. Further, in the absence of ICEP torque, an elliptical cylinder cannot rotate near the walls because the DEP torque is theoretically negligible. Thus, our investigation of the rotation of an elliptical conductive cylinder near the walls under the application of an ac electric field constitutes the first experimental study of an ICEP rotary valve. In this chapter, we experimentally prove that a microvalve can rotate near conductive walls. In particular, we experimentally demonstrate the time evolution of the rotation angle of an elliptical carbon cylinder, and compare it with theoretical results.

6.2 Method

Figure 6.1 shows the schematic view of the rotary-ICEP valve employed in this study. We placed an elliptical metal cylinder [major axis and minor axis of length $2b$ (= 1.42 mm) and $2c$ (= 0.34 mm), respectively] in a rectangular channel having a width w (= 1.7 mm) and length L (= $2.25w$). Although the center of the cylinder of a single rotary valve is usually anchored near the center of the channel to function as a valve, we assume that the center (x_b, y_b) of the elliptical cylinder is not fixed, both theoretically and experimentally, to analyze the effects of the walls during rotation. We neglect the hydrodynamic and electrostatic frictions between the substrate and the elliptical cylinder as a first attempt since we can assume a hydrodynamic repulsion (due to an ICEO flow) that hovers the elliptical cylinder and considerably reduces those frictions.

We fabricated an elliptical gold-coated carbon cylinder ($w = 1.7$ mm, $c/w = 0.1$, and

$b/w = 0.43$) having a large height ($\sim$110 μm) on a silicon substrate of high resistivity (>1000 Ωcm) by the pyrolysis of a photoresist film having a large height ($\sim$130 μm), in a reducing forming gas [98]. That is, we employed the epoxy-based negative photoresist SU-8 2100 (MicroChem Corp., Newton, MA) and spin-coated it on a silicon substrate at a speed of 2000 rpm for 30 s, after spin-coating hexamethyldisilazane (HMDS) on the substrate. The resist was then exposed to UV light through a contact mask. A latent image was developed using the developer, after which it was rinsed. After the post- and hard-baking processes, the photoresist was coated with a gold film having a thickness of 100 nm. Then, the photoresist was pyrolyzed in a closed-tube furnace in a forming gas atmosphere (98% N_2 and 2% H_2 with a flow rate of 10 sccm) introduced into the furnace under a vacuum pressure of 4.1×10^{-4} Pa. Here, the photoresist on the substrate was heated to 300°C at approximately 1.5°C/min to 300°C, maintained at 300°C for 1 h, heated again at the same rate to 900°C, maintained at 900°C for 1 h, and finally cooled down to room temperature. It should be noted that if the vacuum pressure is not sufficiently low while setting up the atmosphere, or if we use only N_2 gas instead of the forming gas, the resist will burn out. Fortunately, because of the weak contact between the fabricated carbon cylinder and the substrate, we could separate the elliptical cylinder by applying ac 60 V (50 Hz) three times for several tens of seconds in water. Further, the gold film was coated to increase the surface conductivity of the elliptical cylinder.

Diluted fluorescent particle suspensions (red fluorescence; Thermo Scientific Co.; $\sim$0.01% solids; $\sim$1 μm ϕ) were injected into the channel between the electrodes, and then, covered with a cover glass and placed under a microscope equipped with a digital video camera. That is, the fabricated elliptical carbon cylinder was immersed in deionized water (mill-Q, $\sim$18 MΩcm) containing fluorescent particles that facilitate the visualization of flow fields, and hence ICEO flow around the elliptical cylinder was observed under ac electric fields. We quantitatively measured the flow fields via particle image velocimetry (PIV), which yields a velocity vector at a point by calculating the correlation function between two images at different times [50]. Further, we obtained the time evolutions of rotational angles and center positions of the elliptical cylinder via numerical analysis of the video images captured during the rotations. After binarization with a suitable threshold to detect the edges of the elliptical cylinder, we set a suitable window that included only the elliptical cylinder as a black image, and we obtained the maximum and minimum x (y) values of the black image as x_{max} and x_{min} (y_{max} and y_{min}), respectively. Then, we obtained $\theta'(\equiv |90 - \theta|) = \frac{1}{2}\tan^{-1}[\tan 2\alpha \cos[\sin^{-1}(\frac{\sin 2\chi}{\sin 2\alpha})]$ if $0 \leq \theta' < 45$ and $\theta' = \frac{1}{2}\tan^{-1}[\tan 2\alpha \cos[\sin^{-1}(\frac{\sin 2\chi}{\sin 2\alpha})] + 90$ if $45 \leq \theta' \leq 90$, where $\chi = \tan^{-1} b/c$ and $\alpha = \tan^{-1}|(x_{max} - x_{min})/(y_{max} - y_{min})|$.

Numerically, we use the coupled calculation method [95] that solves the Stokes equations and the Laplace equation, iteratively, by the boundary element method (BEM) along with the correct boundary conditions; i.e., After calculating slip velocities $\boldsymbol{v}_s$ on the conductive cylinder (in the presence of applied voltage V_0) by the Laplace equation

(a) $t = 2.3$ s (b) $t = 3.3$ s (c) $t = 4.3$ s

Figure 6.2: (Color online) Micrographs showing rotation of rotary microvalve by application of ac 15 V at frequency 50 Hz across channel. Here, $h \simeq 0.11$ mm, $w = 1.7$ mm, $c/w = 0.1$, and $b/w = 0.42$.

($\nabla^2\phi = 0$), we calculate flow fields by the Stokes equations:

$$\mu\nabla^2\boldsymbol{v} - \nabla p = 0, \qquad \nabla \cdot \boldsymbol{v} = 0, \tag{6.1}$$

$$\text{On } S_{\mathrm{p}}^{+}: \quad \boldsymbol{v} = \boldsymbol{U} + \boldsymbol{\Omega} \times \boldsymbol{x} + \boldsymbol{v}_{\mathrm{s}}, \tag{6.2}$$

$$\int_{S_{\mathrm{p}}^{+}} \boldsymbol{f}\mathrm{d}l + \boldsymbol{F}_t^{\mathrm{ext}} = 0, \qquad \int_{S_{\mathrm{p}}^{+}} \boldsymbol{x} \times \boldsymbol{f}\mathrm{d}l + \boldsymbol{T}_t^{\mathrm{ext}} = 0. \tag{6.3}$$

where S_{p}^{+} denotes the surface defined as the outer edge of the double layer, $\boldsymbol{U}$ is the translational velocity, $\boldsymbol{\Omega}$ is the rotational angular velocity, $\boldsymbol{f}$ is the traction vector, $\boldsymbol{F}_t^{\mathrm{ext}}$ and $\boldsymbol{T}_t^{\mathrm{ext}}$ are the total external force and torque, respectively, on the elliptical metal cylinder, $\boldsymbol{x}$ is the surface position of metals parameterized by φ, μ ($\sim$1 mPa·s) is the viscosity, $\boldsymbol{v}$ is the velocity, and p is the pressure. It should be noted that we adopted the boundary condition wherein the velocity on the wall of the channel is zero and the pressures of the inlet and outlet are P_1 and P_2, respectively. (Here, $P_1 = P_2 = 0$ and $\Delta P = P_2 - P_1 = 0$.) Further, we assumed both the DEP and the ICEP torques (forces) by setting $\boldsymbol{T}_t^{ext} = \boldsymbol{T}^{DEP}$ ($\boldsymbol{F}_t^{ext} = \boldsymbol{F}^{DEP}$) in Eq. (6.3), where $\boldsymbol{T}^{\mathrm{DEP}} = \int \boldsymbol{x} \times (-\frac{1}{2}\varepsilon {\boldsymbol{E}_s}^2)\boldsymbol{n}dl$, $\boldsymbol{F}^{\mathrm{DEP}} = \int(-\frac{1}{2}\varepsilon {\boldsymbol{E}_s}^2)\boldsymbol{n}dl$, and $\boldsymbol{E}_s$ is purely tangential to surface S_{p}^{+}. Note that in our case, since the DEP force and torque are just calculated from the maxwell stress around the elliptical cylinder, they are calculated by the above equations.

6.3 Results

Figure 6.2 shows the micrographs obtained during the rotation of an elliptical conductive cylinder in water by the application of ac 15 V. Here, the elliptical conductive cylinder was fabricated by the pyrolysis of a photoresist coated with gold and the height (h) of the elliptical carbon post is approximately 110 μm. As shown in Fig. 6.2, the edge of the fabricated carbon structures was slightly deformed owing to shrinkage during pyrolysis, and the carbon surface was covered with gold, which increased the surface conductivity.

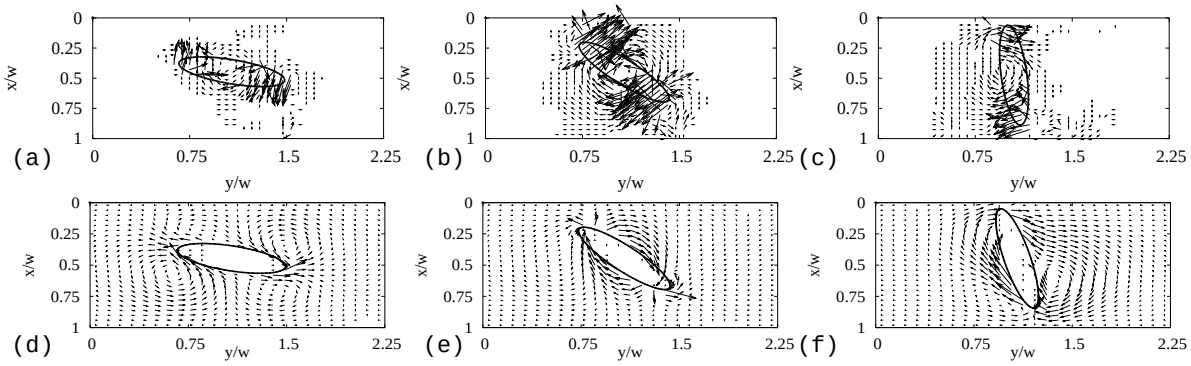

Figure 6.3: Flow fields. Comparison between experimental fields [(a) to (c)] and theoretical fields [(d) to (f)]. Here, $V_0 = 15$ V (50 Hz), $h \simeq 0.11$ mm, $w = 1.7$ mm, $c/w = 0.1$, and $b/w = 0.42$.

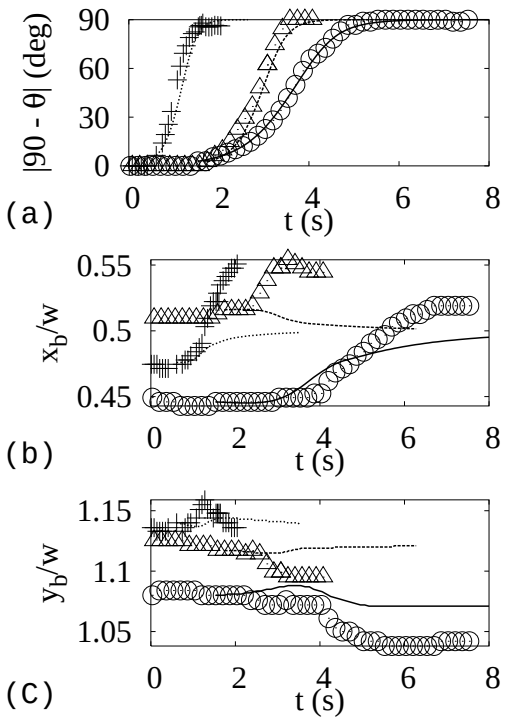

Figure 6.4: Time evolution of θ, x_b, and y_b. Here, $h \simeq 0.11$ mm, $w = 1.7$ mm, $c/w = 0.1$, and $b/w = 0.42$; circle, triangle, and cross (solid,broken, and dotted lines) denote the experimental results (the theoretical results) by the application of ac 15, 20, and 25 V, respectively; $\Lambda = 0.018$; Dependence of rotation angle (a), x_b position (b), and y_b position (c) on time.

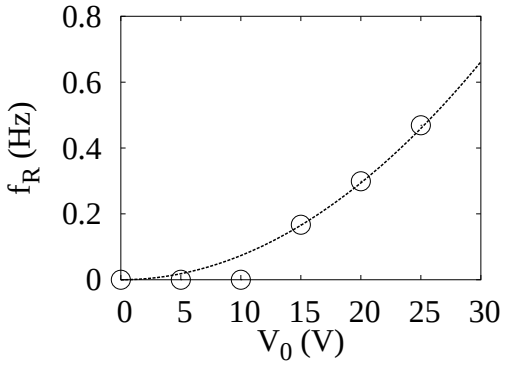

Figure 6.5: Response frequency. Here, $h \simeq 0.11$ mm, $w = 1.7$ mm, $c/w = 0.1$, and $b/w = 0.42$. The circles denote the experimental results, and the broken line denotes the theoretical results obtained by the equation $f_R = \Lambda f_{R0} V_0^2$, where $\Lambda = 0.018$ and $f_{R0} = 0.041$ Hz/V^2.

Further, the microvalve rotated smoothly without streamlines of fluorescent particles; however, we observed a slight disturbance in the flow near the electrodes. Moreover, the conductive element seemed to hover slightly during the application of ac voltage, probably because of a hydrodynamic repulsion; thus, the conductive element frequently deviated from the axis during rotation, even though we set the hole of the elliptical cylinder on the axis.

Figure 6.3 shows the comparison between the flow fields obtained experimentally from the data analysis via PIV [(a) to (c)] and those obtained theoretically from the coupled calculation method via the BEM [(d) to (f)]. In Figs. 6.3(a) to (c), we can see large body velocity of the elliptical cylinder corresponding to its rotation, because the PIV method calculates velocities without distinguishing between fluids and solids. Further, in both the experimental and the theoretical results, we find a pair of opposite flows, which probably is the origin of rotational torque, at the both sides of the elliptical cylinder. It should be noted that the flow velocities around the elliptical post are much smaller than those at the edge of the elliptical cylinder. We believe that this is because the elliptical cylinder slips smoothly in the same topological surface by ICEP.

Figures 6.4 (a), (b), and (c) show the time evolutions of θ, x_b, and y_b, respectively, by the application of ac 15–25 V at a frequency 50 Hz. The circle, triangle, and cross (solid, broken, and dotted lines) denote the experimental results (the theoretical results) obtained by the application of ac 15, 20, and 25 V, respectively. As shown in Fig. 6.4(a), the experimental results of the time evolution of θ are in good agreement with the theoretical results; the correction factor Λ, which indicates the difference between the experimental and the theoretical values, is very small ($\Lambda = 0.018$) corresponding to a large difference between the two. However, the experimental results of the time evolutions of x_b and y_b

are not in good agreement with the theoretical results, as shown in Figs. 6.4(b) and (c), even though the initial movements tend to follow the theoretical results. This is probably because numerous complex subtle balances exist between the fluidic boundary effects and the electrostatic boundary effects, as discussed in [95]; e.g., the fluidic boundary effects accelerate the angular velocity of an elliptical cylinder, whereas the electrostatic boundary effects decelerate it. It should be note that, theoretically, the center of the elliptical cylinder gradually moves to the center of the channel with the left and right motions during rotation, as shown in Figs. 6.4(b) and (c).

Figure 6.5 shows the response frequencies defined by $f_R = 1/2T_R$. The circles and the broken line denote the experimental and theoretical results, respectively. As shown in Fig. 6.5, the response frequency of the ICEP rotary valve tends to be proportional to the square of the applied voltage. Here, although the number of the measuring points are a very few, they are supported by a lot of data as shown in Fig.6.4(a) and reliable. Thus, we believe that the observed rotations are caused by the non-linear phenomena discussed in our previous analysis [95], although $\Lambda = 0.018$. Since Λ is often very small as reported by many researchers [4], our results are reasonable. Probably, the condensation of diffused ion due to the large applied voltage ($V_0 = 15$ to 25 V) is a main reason for small Λ [4], although the fluidic resistance between the cylinder and substrate also may affect the reduction of the response frequency.

6.4 discussion

The application of ICEP to actuators in water, especially in microfluidics, is important because of its potential to improve the response time of the actuators to the level of actuators in air. Thus, experimental observations of the rotation of microvalves near conductive electrodes constitute the first step toward such an improvement; albeit, there were observations of the rotation of metal rods in the bulk region [70, 69], and observations of the wall effects on a half-coated metal particle [30]. Note that if the major driving torque is the DEP torque, it is difficult to improve Λ, because the DEP torque is intrinsically suppressed near the conductive electrodes. Further, Λ is originally introduced as $\Lambda \equiv 1/(1+\delta)$, with $\delta = C_D/C_S = (\epsilon_D/\lambda_D)/(\epsilon_S/h_S) = \epsilon_D h_S/\epsilon_S\lambda_D$, where C_D is the diffuse-layer capacitance, ϵ_D is the permittivity of the diffuse layer, λ_D is the Debye screening length, and h_S, ϵ_S, and C_S are the thickness, permittivity, and capacitance of the Stern (condensed) layer, respectively [4, 58]. Thus, $\Lambda = 0.018$ indicated that $h_S \simeq 54.5\epsilon_S\lambda_D/\epsilon_D$; i.e., if we can assume that $\epsilon_D/\epsilon_S \simeq 80/4.6 \simeq 17.4$ [58], h_S is approximately 3 times larger than the Debye length [typically, tens of nanometer in water] as a result of the condensation of ions by the large applied voltage ($\sim$20 V $\ll$ kT/e = 25 mV) [4]. Therefore, we can improve the performance of the ICEP rotary valve by making a smaller device (e.g., $w \simeq 100$ to 500 μm) that works at a lower voltage. Moreover, a clean surface is also important to improve Λ because contamination of the inducing surface is the major

cause of ICEO flow suppression [58]. Furthermore, we have shown that nonreactive and conductive carbon structures fabricated by pyrolysis [98] are useful for realizing ICEP actuators having conductive structures of large height between electrodes, by a simple process; in particular, the simplicity of the removal of the movable portion from the substrate by applying a high ac voltage is useful.

6.5 Conclusion

In conclusion, (1) by using an elliptical carbon conductive cylinder coated with gold, we experimentally showed that microvalves rotate near the conductive electrodes in deionized water. (2) The time evolution of the rotation angle of the elliptical conducive cylinder was obtained experimentally from the numerical analysis of an experimental image and successfully compared with the theoretical results using the multiphysics coupled simulation technique; the correction factor was very small ($\Lambda = 0.018$). (3) We have shown that a carbon cylinder of large height fabricated by the pyrolysis of a photoresist is useful for the fabrication of an ICEP device because of the simplicity of its removal from the substrate. In the future, we believe that the use of ICEP actuators can significantly enhance the response times of actuator devices in water.

Chapter 7

Mixer 1 (Theory): Chaotic mixer using electro-osmosis at finite Peclet number

Two pressure-driven streams of two miscible liquids can only mix by diffusion in microfluidic channels because of the low Reynolds number. We present an idea to generate mixing by "chaotic advection" in microscale geometries. That is, we consider using induced-charge electro-osmosis to generate a second flow and then modulate between the pressure-driven and induced-charge flows. By using the combined method consisting of the boundary element method, the Lagrangian particle tracking method, and the random walk method, we analyze mixing efficiency, mixing time, and mixing length, with the effects of modulation frequency and molecular diffusivity, and compare our proposed mixer with other mixers. By this analysis, we find that chaotic mixing can be produced efficiently in a microfluidic channel by switching between pressure-driven and induced-charge flows in a wide range of Peclet number under the specific condition of Strouhal number. By using our proposed mixer, we can expect to realize efficient chaotic mixing with minimum voltage in an ordinary flow channel with a simple structure without an oblique electric field even at large Peclet number.

7.1 Introduction

Two pressure-driven streams of two miscible liquids mix only through diffusion in microgeometries. This is because the flows typically have low Reynolds numbers and the residence times are typically too small for efficient molecular diffusion to occur. Hence, efficient mixers are important in the microfluidic applications; e.g., in the homogenization of solutions of regents used in chemical reactions. Because of this importance, several methods for microfluidic mixing have been reported, typically based upon clever geometries

[91, 19], miniature stirrers [103, 46], or external agitations using external fields [10, 89].

Recently, mixers that employ a vortex flow around metal posts due to induced-charge electro-osmosis (ICEO) [5, 83, 84] are proposed, and they have attracted considerable attention in the context of microfluidic applications [37, 105, 97, 16, 30, 66, 1, 57, 92, 93] because they can produce a large vortex flow for mixing and a large net flow for pumping ($\sim$mm/s) with a small voltage ($\sim$V) by the simple structure. ICEO is different from classical electro-osmosis, because it results from the interaction between the electric field and ions in the electric double layer formed by the polarizing effect of the electric field itself [5, 83, 84, 6, 20, 90]; i.e., the velocity of resulting flow is proportional to the square of the electric field, and thus ICEO can avoid many dc problems such as chemical reactions in an electrolyte.

Aref [36] demonstrated that, when flow patterns form closed orbits, one can induce Lagrangian chaos and effective stirring by alternating periodically between two or more flow patterns. In this context, Zhao and Bau [105] have proposed a chaotic mixer using ICEO in a closed chamber on the basis of Aref's method that uses chaotic advection. In the mixer, periodic switching between a vertical and an oblique electric field is used to produce two kinds of vortex flows around a circular metal cylinder. The chaotic mixer using chaotic advection is important because simple vortex mixers never work in microfluidic channels in the absence of molecular diffusivity (i.e., at infinite Peclet number), because the vortex flow is also a laminar flow.

However, mixing must be produced in a directional microfluidic channel in many realistic applications such as micro total analysis systems (microTAS) and biological diagnostic systems. Further, to satisfy the requirements for miniaturization and low-voltage design, we require an ICEO mixer that can be operated in the absence of an oblique electric field. Apparently, the design concept of an ICEO mixer in a flow channel is different from that of the closed chamber. Thus, a chaotic ICEO mixer operated in a directional flow channel without an oblique electric field is important as the simplest chaotic mixer that works well in a wide range of Peclet number.

Nevertheless, thus far, no attempt has been made for producing chaotic mixing by using a directional flow itself along with a vortex flow. Thus, we consider using induced-charge electro-osmosis to generate a second flow and then modulates between the pressure-driven and induced-charge flows. In this study, we focus on a chaotic ICEO mixer that switches between a pressure-driven directional flow and a vortex flow produced by the application of a vertical electric field, and elucidate its design concept by using the boundary element method combined with the thin double layer approximation. Further, because Peclet number is not truly infinite in a real channel, we consider finite Peclet number by using the random walk method along with Lagrangian particle tracking method. Furthermore, we compare our proposed chaotic ICEO mixer with other several ideas that have been proposed to mix two miscible streams.

This chapter is presented in five sections. In Sec. 7.2, we describe theory for a geometry model, a flow model, the Lagrangian particle tracking method with the box counting

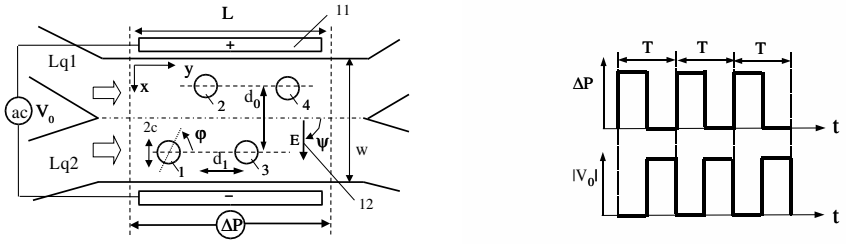

(a) Geometry (b) switching method

Figure 7.1: Schematic diagram of chaotic ICEO mixer. 1 to 4: metal posts that induce quadruple electro-osmotic flow, 11: pair of electrodes, 12: electric field. Here, $L = 2.25w$ and $w = 100$ μm are the length and width of the periodic part of the rectangular channel. Lq1 and Lq2 are two liquids, and $c = 0.1w$ is the radius of the metal posts; $x_1 = x_3 = 0.5w + d_0/2$, $x_2 = x_4 = 0.5w - d_0/2$, $y_1 = d_1$, $y_2 = 2d_1$, $y_3 = 3d_1$, $y_4 = 4d_1$, $d_0 = 0.6w$, $d_1 = 0.45w$, where (x_i, y_i) are the coordinates of the ith number.

method, the random walk method for the analysis of finite molecular diffusivity, and a simple model at infinite Peclet number. Based on these models, the results for the basic performance of chaotic ICEO mixers at infinite Peclet number, the effect of switching period, and the effect of molecular diffusivity, are presented in Sec. 7.3. Following a discussion in Sec. 7.4, our conclusions are summarized in Sec. 7.5.

7.2 Theory

7.2.1 Geometry model

Figure 7.1 shows a schematic diagram of the chaotic ICEO mixer that uses a pressure-driven directional flow and a vortex flow. In Fig. 7.1(a), we assume that two liquids (Lq1, Lq2) mix in the rectangular channel. As shown in Fig. 7.1(a), to produce a vortex flow due to ICEO, we typically place four circular metal cylinders of radius $c = 0.1w$ at the positions (x_i, y_i) in a rectangular channel of length $L = 2.25w$ and width $w = 100$ μm, where x_i and y_i are the coordinates of the center of the cylinder of the ith number; e.g., $x_1 = x_3 = 0.5w + d_0/2$, $x_2 = x_4 = 0.5w - d_0/2$, $y_1 = d_1$, $y_2 = 2d_1$, $y_3 = 3d_1$, $y_4 = 4d_1$, $d_0 = 0.6w$, and $d_1 = 0.45w$. In Fig. 7.1, the vortex flow produced by the zig-zag structure is characterized by d_0 and d_1. As shown in Fig. 7.1(b), we alternate between period 1 ($\Delta P \neq 0$, $V_0 = 0$) and period 2 ($\Delta P = 0$, $V_0 \neq 0$) to produce chaotic mixing, where ΔP is a pressure difference between the inlet and outlet, and V_0 is the voltage applied to the

electrodes.

7.2.2 Flow model

Numerically, we consider a 2D quasi-static Stokes flow without Brownian motion [93, 43, 104]: i.e., we consider the limit in which the Reynolds number Re tends to zero and the Peclet number is infinite. We assume the posts of the metal cylinder to be polarizable in an electrolytic solution under a dc or ac electric field. The motion of the surrounding fluid must satisfy Stokes equations modified by the inclusion of an electrical stress. However, by using matched asymptotic expansion [26], we can reduce them to the classical Stokes equations as follows:

$$\mu\nabla^2\boldsymbol{v} - \nabla p = 0, \qquad \nabla\cdot\boldsymbol{v} = 0, \tag{7.1}$$

$$\text{On } S_{\mathrm{p}}^{+(j)}\ (\boldsymbol{E}\neq 0): \quad \boldsymbol{v}^{(j)} = \boldsymbol{v}_{\mathrm{s}}^{(j)}, \tag{7.2}$$

$$\text{On } S_{\mathrm{p}}^{+(j)}\ (\boldsymbol{E}= 0): \quad \boldsymbol{v}^{(j)} = 0 \tag{7.3}$$

where $S_{\mathrm{p}}^{+(j)}$ denotes the surface defined as the outer edge of the double layer, on the j's metal cylinder (j = 1,2,...,N). Further, N is the number of the metal cylinders, $\boldsymbol{E}$ is the electric field, $\boldsymbol{v}$ is the velocity, and p is the pressure. Under a wide range of conditions, the local slip velocity $\boldsymbol{v}_s^{(j)}$ is given by the Helmholtz-Smoluchowski formula,

$$\boldsymbol{v}_s^{(j)} = -\frac{\epsilon\zeta^{(j)}}{\mu}\boldsymbol{E}_{\mathrm{s}}{}^{(j)} \tag{7.4}$$

where $\boldsymbol{E}_{\mathrm{s}}{}^{(j)}$ is the tangential component of the electric field, μ ($\sim$1 mPa·s) is the viscosity, ϵ ($\sim 80\epsilon_0$) is the dielectric permittivity of the solvent (typically water), and ϵ_0 is the vacuum permittivity. Here, a zeta-potential $\zeta^{(j)}$ around the j's metal is generally defined as $\zeta^{(j)} = \phi_i^{(j)} - \phi_f^{(j)}$, where $\phi_i^{(j)}$ is the electric potential of the metal cylinder that is equal to the electric potential without double layer, and $\phi_f^{(j)}$ is the electric potential just outside the double layer

To consider the slip velocity under a bounded condition, we solve the electric potentials ($\phi_i^{(j)}$ and $\phi_f^{(j)}$) before calculating a flow field by the boundary element method based on the following Laplace's equation, $\nabla^2\phi = 0$. On the one hand, we use the Dirichlet boundary condition for the upper and lower walls (electrodes); i.e., $\phi = +0.5V_0$ at $x = 0$, $\phi = -0.5V_0$ at $x = w$, where V_0 is an applied voltage across the channel. On the other hand, we use the Neumann boundary condition for the left and right walls; i.e., $\boldsymbol{n}\cdot\nabla\phi = 0$ at $y = 0$ and L, where $\boldsymbol{n}$ is the surface normal unit vector. In addition to those boundary conditions, to obtain a final potential, we also use the Neumann boundary condition (i.e., $\boldsymbol{n}\cdot\nabla\phi = 0$) on the metal surface. Further, to obtain a initial potential, we use the condition that j's metal cylinder have an unknown surface potential $\phi_i^{(j)}$, and require the electrical neutral

condition that $\oint_{(j)}(\boldsymbol{n}\cdot\nabla\phi)ds = 0$. Thus, we can numerically calculate a flow field for a bounded domain. It should be noted that we use the boundary condition that the velocity on the wall of the channel is zero and that the pressures of the inlet and outlet are P_1 and P_2, respectively. On the basis of Eqs. (7.1)-(7.4), we calculate the flow fields of the ICEO mixer for a bounded domain by the boundary element method. Further, it is convenient to define the representative velocity of a vortex as $\boldsymbol{U}_0$ $(= cE_0^2/\mu)$ [5], where c is the radius of the metal posts and $E_0 =\mid \mathbf{E} \mid = V_0/w$. Note that to obtain a precise flow field near the wall and the metal surfaces, we use analytical integration to obtain the matrix elements of the boundary element method because the Gauss integration produces a large error near the wall.

7.2.3 Lagrangian particle tracking method with box counting method

The Lagrangian particle tracking method in mixing is an analyzing method to visualize a mixing state by tracking passive (tracer) particles in flow velocity fields on the basis of the Lagrangian analysis of motion [46, 105]. i.e. $d\mathbf{r}/dt = \mathbf{v}(\mathbf{r}, t)$. In the simulation, we switch between two flow patterns during a period T; we apply the first flow pattern for $0 < t < T/2$ and then the second pattern for $T/2 < t < T$. This process is repeated continuously over time, and passive particles are moved and spread. Note that we use periodical condition when we move the particles to consider a long channel with a short channel. By the Lagrangian particle tracking method, we obtain images of the distribution of particles and visually evaluate the performance of the mixer for various parameters.

To evaluate the mixing performance quantitatively, we use the box counting method [46]; we define the stirring index ε as $\varepsilon_j = \sum_{i=1}^{i=K}\omega_{ij}/K$, where $\omega_{ij} = n_{ij}/n_{\mathrm{ave,j}}$ if $n_{ij} < n_{\mathrm{ave,j}}$, and $\omega_{ij} = 1$ if $n_{ij} \geq n_{\mathrm{ave,j}}$. Here, $n_{\mathrm{ave,j}} = N_j/K$, N_j is the total number of particle j, K is the number of boxes, and n_{ij} is the number of particle j in the ith box. Note that particle 1 and 2 are corresponding to upper (red) and lower (blue) particles, respectively, and particle 0 is a red or blue particle; i.e., $n_{i0} = n_{i1} + n_{i2}$ and $N_0 = N_1 + N_2$. Similarly, we can define ε_3 as the stirring index corresponding to $n_{i3} = \sqrt{n_{i1}n_{i2}}$ and $N_3 = \sqrt{N_1N_2}$. Through this paper, we use the values that $N_0 = 20 \times 40 \times 2 = 1600$, $N_1 = N_2 = 20 \times 40 = 800$, $N_3 = 800$, and $K = 10 \times 20 = 200$. In this case, $n_{\mathrm{ave},0} = 8$, $n_{\mathrm{ave},1} = n_{\mathrm{ave},2} = 4$, and $n_{\mathrm{ave},3} = 4$.

If particles are concentrated in a small region, few overpopulated boxes (boxes under the condition that $n_{ij} > n_{\mathrm{ave,j}}$ and $\omega_{ij} = 1$) and many empty boxes (boxes under the condition that $n_{ij} = 0$ and $\omega_{ij} = 0$) are created. In this case, ε approaches 0. However, if particles are distributed uniformly throughout the channel, many boxes containing the average number of particles (boxes under the condition that $n_{ij} \sim n_{\mathrm{ave,j}}$ and $\omega_{ij} \sim 1$) are created. In this case, ε_j approaches 1. Hence, ε_j is interpreted as the stirring index. In particular, ε_3 is useful to evaluate the degree of mixing between particle 1 and 2.

7.2.4 Random walk method for the analysis of finite molecular diffusivity

Random walks are strongly related to diffusive process [99]; i.e., normal diffusion of tracers in liquids is result of the random walks, and that the variance of the ensemble of tracers spreads as

$$\sigma^2(t) = \left\langle x^2(t) \right\rangle - \left\langle x(t) \right\rangle^2 = 2Dt, \tag{7.5}$$

where D is the molecular diffusivity [$x(t)$ represents one dimensional motion]. If the tracer particles take step length l, with a probability distribution function (PDF) for step lengths

$$P_{\rm rw}(l) = \frac{1}{\sqrt{2\pi}\sigma} e^{-\frac{l^2}{2\sigma^2}}, \tag{7.6}$$

the central limit theorem shows that

$$D = \frac{\langle l^2 \rangle - \langle l \rangle^2}{2\Delta t}, \tag{7.7}$$

where $< l^n >$ are the moments of $P_{\rm rw}$, and Δt is the time between each step.

Thus, molecular diffusion is simulated by the random walk method combined with Lagrange particle tracking method; i.e., at each time step, after moving particles as $\mathbf{r}_{\rm L}(t) \simeq \mathbf{r}(t-\Delta t) + \mathbf{v}(\mathbf{r}, t-\Delta t)\Delta t$, we move tracer particles as $\mathbf{r}(t) = \mathbf{r}_{\rm L}(t) + \Delta \mathbf{r}_{\rm rw}$, where $\Delta \mathbf{r}_{\rm rw} = (\Delta x, \Delta y)$. Here, Δx and Δy are the random numbers that satisfy Eq (7.5), and they are generated by the box-muller method. In the algorithm of the random walk process, if a fluid particle moves into the region of circular cylinders, we do not move the particle.

7.2.5 Simple model at infinite Peclet number

As a first attempt, we can assume that

$$\varepsilon(t) = \varepsilon_{\rm max}(1 - e^{-t/\tau_m}), \tag{7.8}$$

where $\varepsilon_{\rm max}$ is a maximum or saturated value and τ_m is a time constant of the mixing phenomenon. If we define a mixing time t_m as the time when $\varepsilon(t)$ reaches $0.95\varepsilon_{\rm max}$, $t_m/\tau_m = -ln0.05 \sim 3$. To modulate between flows, we consider that considerable motions of fluid particles are required such that $U_0 T > d_0$ and $U_1 T > d_1$; i.e, $1/St_0 \equiv U_0/fd_0 > 1$ and $1/St_1 \equiv U_1/fd_1 > 1$, where f is a switching frequency and U_1 is an average velocity of a pressure-driven flow. Here, St_0 and St_1 are Strouhal numbers related to a vortex flow and a pressure-driven flow, respectively. Strouhal number is a dimensionless number oscillating flow mechanisms. Thus, we propose following phenomenological formulations as a first attempt;

$$\varepsilon_{\rm max} = C_1(1 - e^{-1/St_1})(1 - e^{-1/St_0}), \tag{7.9}$$

$$t_m/T_0 = C_2 + C_3 e^{-1/St_0 f(T)} + C_4 e^{-1/St_1 f(T)}, \tag{7.10}$$

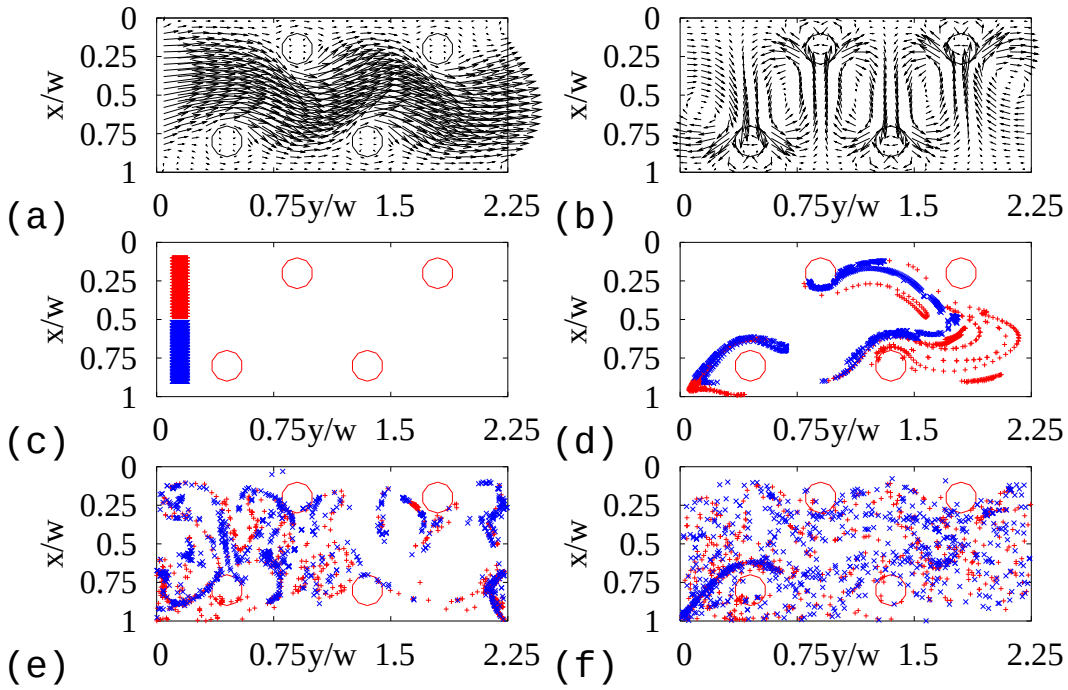

Figure 7.2: Performance of chaotic ICEO mixer that has a zig-zag structure of four metal posts (type A). (a) Flow 1 ($E_0 = 0$); (b) Flow 2 ($E_0 \neq 0$, $\psi = 90°$); (c) $t/T_0 = 0$; (d) $t/T_0 = 100$; (e) $t/T_0 = 200$; (f) $t/T_0 = 500$. Here, $d_0/w = 0.6$ and $d_1/w = 0.45$. (a)-(b): Two flow fields; (a) a directional flow resulting from a pressure difference $T_0\Delta P/\mu$ (= 2.4) when $\boldsymbol{E} = 0$ and (b) a vortex flow resulting from electro-osmosis induced around cylindrical metal posts by the application of an electric field $\boldsymbol{E} = E_0\boldsymbol{i}$ ($T_0U_0/w = T_0cE_0^2/w\mu = 0.04$) when $T_0\Delta P/\mu = 0$. If $T_0 = 1$ mm/s, $\mu = 1$ mPa·s, and $w = 100$ μm, a directional flow and a vortex flow are driven by $\Delta P = 2.4$ Pa and $E_0 = 2.38$ V/m ($U_0 = 4$ mm/s), respectively. (c)-(f): Distribution of passive tracer particles at $T/2T_0 = 20$.

$$L_m = U_1 t_m, \tag{7.11}$$

where T_0 is a time scale. Here, C_1, C_2, C_3, and C_4 are constant parameters, while $f(T)$ is a function of T.

7.3 Results

7.3.1 Basic performance of chaotic ICEO mixers at infinite Peclet number

Figure 7.2 shows the performance of the chaotic ICEO mixer that has a zig-zag structure of four metal posts (type A). Here, $d_0/w = 0.6$ and $d_1/w = 0.45$. Figures 7.2(a) and 2(b) show two flow fields: (a) a directional flow resulting from a pressure difference $T_0\Delta P/\mu$ (= 2.4) when $\boldsymbol{E} = 0$ and (b) a vortex flow resulting from electro-osmosis induced around cylindrical metal posts by the application of an electric field $\boldsymbol{E} = E_0\boldsymbol{i}$ ($T_0U_0/w = T_0cE_0^2/w\mu = 0.04$) when $T_0\Delta P/\mu = 0$, where T_0 is a time scale; e.g., if $T_0 =$ 1 mm/s, $\mu = 1$ mPa·s, and $w = 100$ μm, a directional flow and a vortex flow are driven by $\Delta P = 2.4$ Pa and $E_0 = 2.38$ V/m ($U_0 = 4$ mm/s), respectively. In Fig. 7.2(a), we observe a typical pressure flow with viscosity; however, it resembles a winding flow of the presence of metal posts near the wall. In Fig. 7.2(b), we observe large vortices across the channel; they are produced by the presence of a pair of upper and lower metal posts. In Figs. 7.2 (c)-(f), we show the dispersion of 1600 particles at various times. As shown in Figs. 7.2 (c)-(f), chaotic mixing is produced by switching between the two flows. Here, the time interval is $T/2T_0 = 20$. In Fig. 7.2(c), to examine the mixing between the two liquids emanating from the left of the channel, we place particle 1 (red) and particle 2 (blue) near the inlet; particle 1 (red) region, $0.1 \leq x/w < 0.5$; particle 2 (blue) region, $0.5 < x/w \leq 0.9$. The simulation begins from the interval in which the directional flow is generated. The particles move from the left to the right along the streams of the directional flow shown in Fig. 7.2(a). After the interval, the particles are subjected to the vortex flow shown in Fig. 7.2(a). Figure 7.2(d) shows the distribution of the particles at $t/T_0 = 100$. Although the particles are subjected to the directional flow 3 times and the vortex flow 2 times across the channel, the switching times are not sufficient for mixing. Figure 7.2(e) shows that mixing at $t/T_0 = 200$ is also not sufficient for achieving a uniform distribution of particles. Figure 7.2(e) shows that at $t/T_0 = 500$, the particle 1 (red) and particle 2 (blue) spread over the entire mixing domain. An efficient mixer should be capable of producing such a result. Note that we consider a periodic boundary condition in order to represent a long channel as a short channel.

Figure 7.3 shows the performance of the ICEO mixer that has a linear geometry of four metal posts (type B). As shown in Fig. 7.3, both particles do not mix each other, although upper (red) and lower (blue) particles are dispersed independently in upper and lower regions, respectively, Namely, a symmetrical structure in which the plane of symmetry is at $x = w/2$ has a drawback in that it divides the flow into two symmetrical regions; i.e., the upper and lower regions. Figure 7.4 shows the performance of ICEO mixer that has 8 posts (type C). As shown in Fig. 7.4, it is disadvantageous to place many small metal posts across the channel, because they create small vortices separated from each other and do not contribute to large-scale mixing. Thus, we believe that the

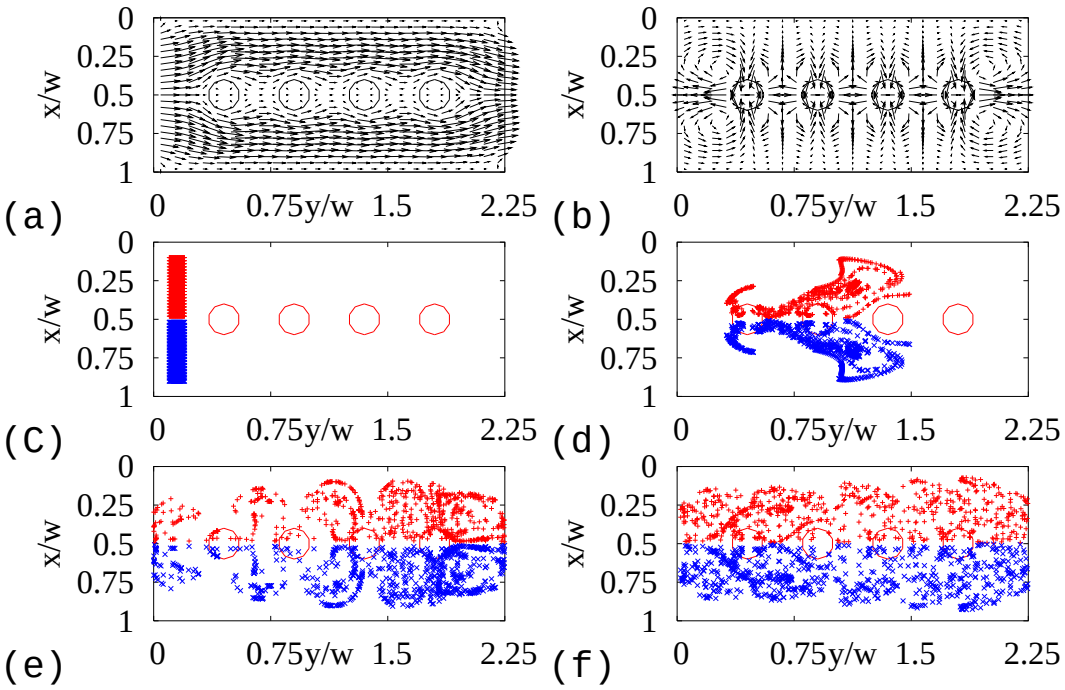

Figure 7.3: Performance of ICEO mixer that has a linear geometry of four metal posts (type B). (a) Flow 1 ($E_0 = 0$); (b) Flow 2 ($E_0 \neq 0$, $\psi = 90°$); (c) $t/T_0 = 0$; (d) $t/T_0 = 100$; (e) $t/T_0 = 200$; (f) $t/T_0 = 500$. Here, $d_0/w = 0.6$ and $d_1/w = 0.45$. (a)-(b): Two flow fields; (a) directional flow resulting from a pressure difference $T_0\Delta P/\mu = 2.4$ when $\boldsymbol{E} = 0$ and (b) vortex flow resulting from electro-osmosis induced around cylindrical metal posts when $\boldsymbol{E} = E_0\boldsymbol{i}$ $T_0U_0/w = T_0cE_0^2/w\mu = 0.04$, and $T_0\Delta P/\mu$=0; Typically, $T_0 = 1$ mm/s, $\mu = 1$ mPa·s, and $w = 100$ μm. (c)-(f): Distribution of passive tracer particles at $T/2T_0 = 20$.

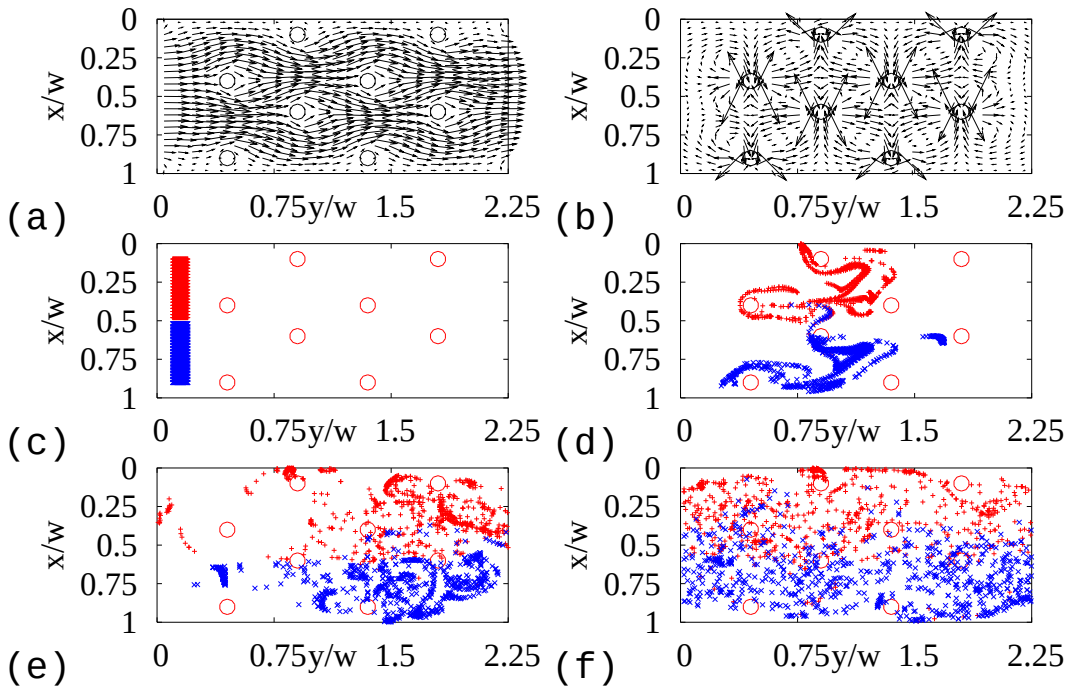

Figure 7.4: Performance of ICEO mixer that has 8 posts (type C). (a) Flow 1 ($E_0 = 0$); (b) Flow 2 ($E_0 \neq 0$, $\psi = 90°$); (c) $t/T_0 = 0$; (d) $t/T_0 = 100$; (e) $t/T_0 = 200$; (f) $t/T_0 = 500$. Here, $d_0/w = 0.6$ and $d_1/w = 0.45$. (a)-(b): Two flow fields; (a) directional flow resulting from a pressure difference $T_0\Delta P/\mu = 2.4$ when $\boldsymbol{E} = 0$ and (b) vortex flow resulting from electro-osmosis induced around cylindrical metal posts when $\boldsymbol{E} = E_0\boldsymbol{i}$, $T_0U_0/w = T_0cE_0^2/w\mu = 0.04$, and $T_0\Delta P/\mu$=0; Typically, $T_0 = 1$ mm/s, $\mu = 1$ mPa·s, and $w = 100$ μm. (c)-(f): Distribution of passive tracer particles at $T/2T_0 = 20$. Here, $x_1/w = x_3/w = 0.4$, $x_2/w = x_4/w = 0.1$, $x_5/w = x_7/w = 0.9$, $x_6/w = x_8/w = 0.6$, $y_1/w = x_5/w = 0.45$, $y_2/w = x_6/w = 0.90$, $x_3/w = x_7/w = 1.35$, and $x_4/w = x_8/w = 1.80$.

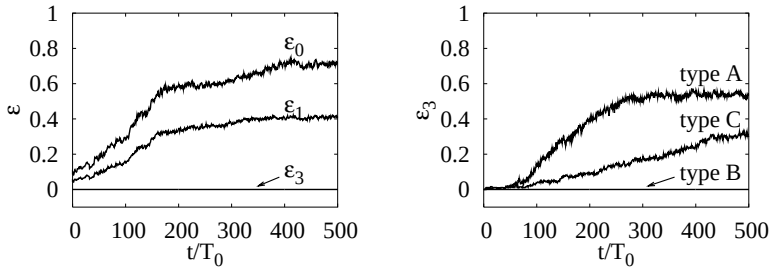

(a) ε vs time for type B. (b) ε_3 vs time for type A to C

Figure 7.5: Dependence of stirring index ε on time. Here, $T_0U_0/w = T_0cE_0^2/w\mu = 0.04$ and $T_0\Delta P/\mu = 2.4$.

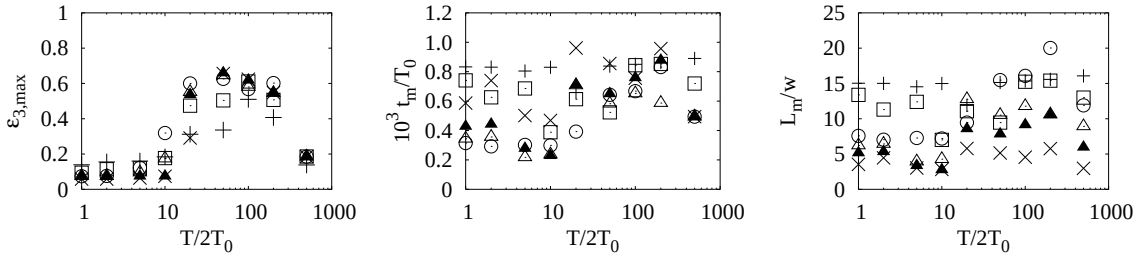

(a) ε_3 vs $T/2$ (b) t_m vs $T/2$ (c) L_m vs $T/2$

Figure 7.6: Dependence of ε_3, t_m, and L_m on $T/2$ at infinite Peclet number for type A. Symbols show numerical results; i.e., plus, open square, and open triangle show the numerical results at $T_0U_0/w = 0.01$, 0.02, and 0.04, respectively, when $T_0\Delta P/\mu = 1.8$, while cross, closed triangle, and open circle show the numerical results at $T_0\Delta P/\mu = 0.6$, 1.2, and 2.4, respectively, when $T_0U_0/w = 0.04$,

zig-zag structure of type A is more suitable for chaotic mixing in the flow channel than the linear structure of type B and the 8 particle structures of type C.

Next, we present a quantitative evaluation of the mixing problem. Here, we use ε_3 to evaluate mixing efficiency since ε_0 and ε_1 can increase even when particle 1 (red) and particle 2 (blue) are stirred independently in type B, as shown in Fig. 7.5(a). Figure 7.5(b) shows the dependence of ε_3 on time for various ICEO mixers (type A, B, and C). As shown in Fig. 7.5(b), type A shows good mixing performance, while mixing performance of type B is zero. Furthermore, although it is difficult to determine the mixing time t_{mix} from Fig. 7.2 of the trajectory method, we can obtain $t_{\mathrm{mix}} \simeq 350$ ms for type A from Fig. 7.5(b) by the box counting method.

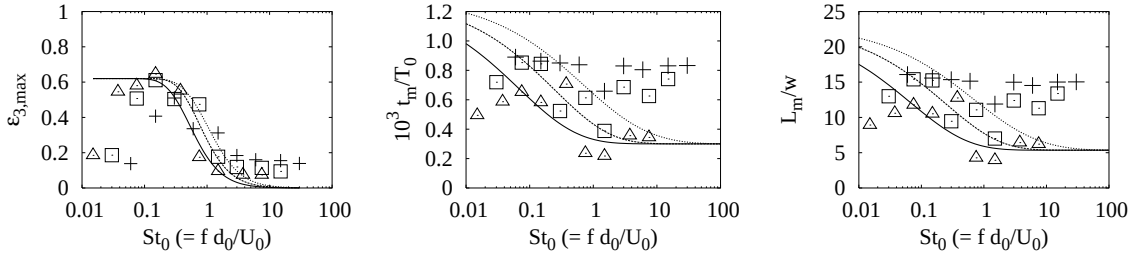

(a) ε_3 vs St_0 ($T_0\Delta P/\mu = 1.8$) (b) t_m vs St_0 ($T_0\Delta P/\mu = 1.8$) (c) L_m vs St_0 ($T_0\Delta P/\mu = 1.8$)

(d) ε_3 vs St_1 ($T_0U_0/w = 0.04$) (e) t_m vs St_1 ($T_0U_0/w = 0.04$) (f) L_m vs St_1 ($T_0U_0/w = 0.04$)

Figure 7.7: Dependence of ε_3, t_m and L_m on f at infinite Peclet number. Here, the results of Fig. 7.6 are replotted on St_0 [(a)-(c)] and St_1 [(d)-(f)]. Dotted, broken, and solid lines show the analytical results by using Eqs. (5.9) to (5.11) at $T_0U_0/w = 0.01$, 0.02, and 0.04 [at $T_0\Delta P/\mu = 0.6$, 1.2, and 2.4], respectively, in (a) to (c) [in (d) to (f)]. Symbols show numerical results; i.e., plus, open square, and open triangle show the numerical results at $T_0U_0/w = 0.01$, 0.02, and 0.04, respectively, when $T_0\Delta P/\mu = 1.8$, while cross, closed triangle, and open circle show the numerical results at $T_0\Delta P/\mu = 0.6$, 1.2, and 2.4, respectively, when $T_0U_0/w = 0.04$.

7.3.2 Effect of switching period

Next, we show the effect of the switching period. Figure 7.6 shows the dependence of ε_3, t_m, and L_m on $T/2$ at infinite Peclet number for type A. As shown in Fig. 7.6, there exists an appropriate switching period for producing chaotic mixing, and the values of ε_3 are small when the switching periods are too short or long to mix the liquids. However, as mentioned before, those results should be replotted on $St_0(= fd_0/U_0)$ and $St_1(= fd_1/U_1)$ as shown in Fig. 7.7. Here, d_0 ($= 0.6w$) and d_1 ($= 0.45w$) are characteristic lengths of vortex and directional flows. As shown in Fig. 7.7, we observe that the analytical results of ε_3, t_m, and L_m agree fairly well with the numerical results, although the agreement between numerical results and analytical results of t_m and L_m is very bad in Fig. 7.7(b) and (c). Here, we set that $C_1 = 0.62$, $C_2 = 300$, $C_3 = 400$, $C_4 = 600$, and $f(T) = 0.3(T/20)^{1.5}$ in Eqs. (5.9)-(5.11). From Figs. 7.7(a) and (d), we find that mixing efficiency is enhanced for the suitable Strouhal number ($St_0 < 1$ and $St_1 < 1$). Further, from Figs. 7.7(b), (c),

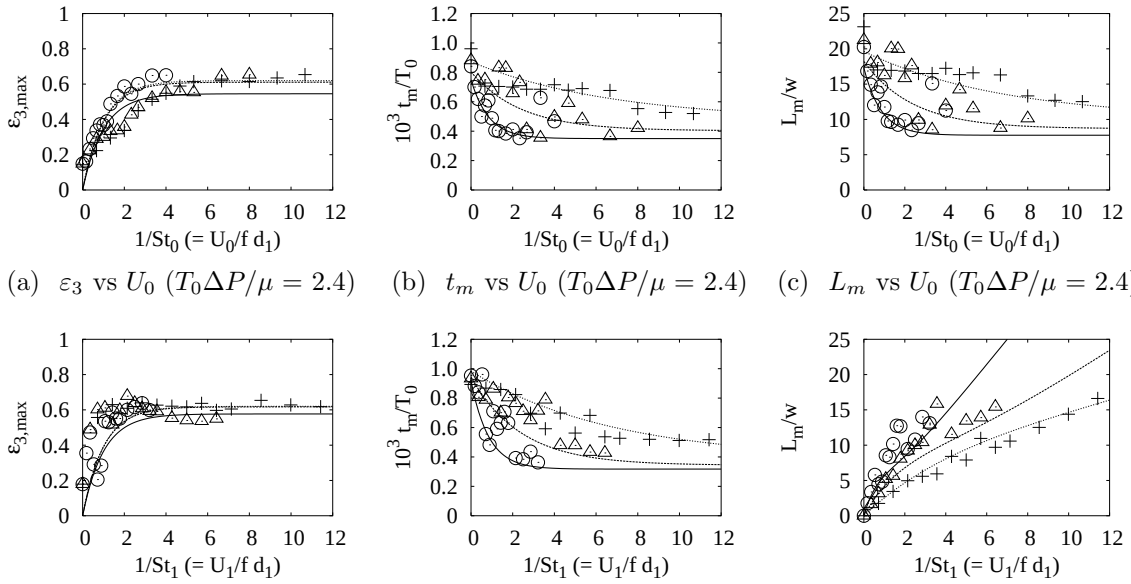

(a) ε_3 vs U_0 ($T_0\Delta P/\mu = 2.4$) (b) t_m vs U_0 ($T_0\Delta P/\mu = 2.4$) (c) L_m vs U_0 ($T_0\Delta P/\mu = 2.4$)

(d) ε_3 vs U_1 ($T_0U_0/w = 0.04$) (e) t_m vs U_1 ($T_0U_0/w = 0.04$) (f) L_m vs U_1 ($T_0U_0/w = 0.04$)

Figure 7.8: Dependence of ε_3, t_m, and L_m on U_0 and U_1 at infinite Peclet number ($D = 0$ m^2/s) for type A. Lines show the analytical results of the simple model; i.e., solid, dashed, and dotted lines show the analytical results of $T/2T_0 = 20$, 40, and 80, respectively. Symbols show numerical results; i.e., solid, dashed, and dotted lines plus, open triangle, and open circle show the numerical results of $T/2T_0 = 20$, 40, and 80, respectively.

(e), and (f), mixing time and length are approximately 1 s and 1 mm, respectively, in the suitable range of Strouhal number ($St_0 < 1$ and $St_1 < 1$).

Figures 7.8(a), (b), and (c) [(d), (e), and (f)] show the dependence of ε_3, t_m, and L_m, respectively, on U_0 (U_1) at infinite Peclet number for type A. In Fig. 7.8, lines show the analytical results of the simple model, and symbols show numerical results. As shown in Fig. 7.8, we observe that the analytical results of ε_3, t_m and L_m also agree fairly well with the numerical results. Further, from Figs. 7.8(a) and (d), we find that mixing is enhanced when $1/St_0 > 1$ and $1/St_1 > 1$ as predicted by the simple model. Furthermore, in Figs. 7.8(b), (c), (e), and (f), we also find that mixing time and length are approximately 1 s and 1 mm, respectively, in the suitable range of Strouhal number ($St_0 < 1$ and $St_1 < 1$).

7.3.3 Effect of molecular diffusivity

Next, we show the effect of molecular diffusivity. Figure 7.9 shows the dependence of ε_3, t_m and L_m on f in the presence of molecular diffusivity ($D = 1.0^{-9}$ m^2/s) for type A. Because of the presence of molecular diffusivity, mixing efficiency is not so low even in the

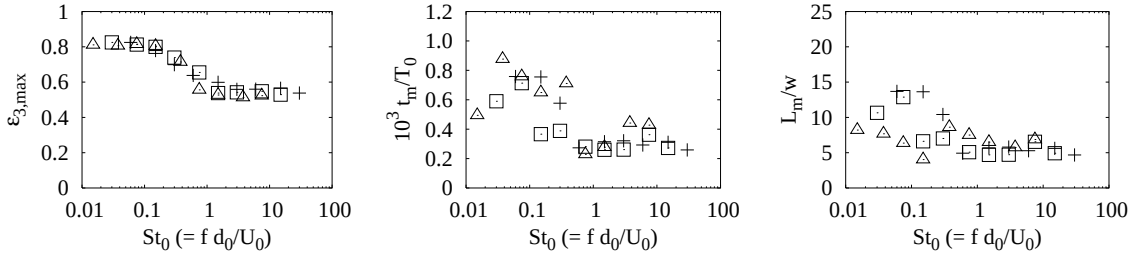

(a) ε_3 vs St_0 ($T_0\Delta P/\mu = 1.8$) (b) t_m vs St_0 ($T_0\Delta P/\mu = 1.8$) (c) L_m vs St_0 ($T_0\Delta P/\mu = 1.8$)

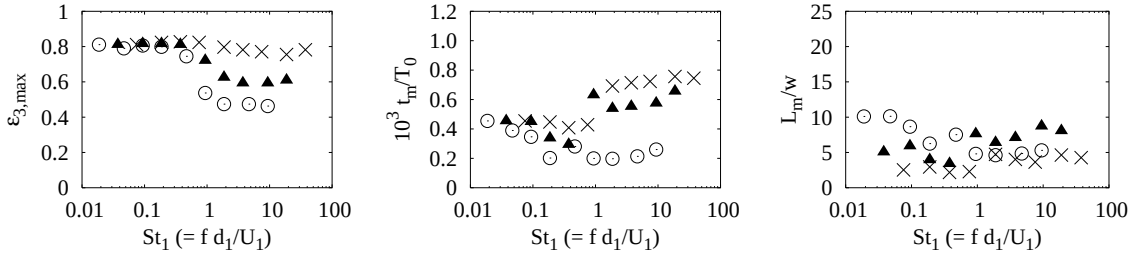

(d) ε_3 vs St_1 ($T_0U_0/w = 0.04$) (e) t_m vs St_1 ($T_0U_0/w = 0.04$) (f) L_m vs St_1 ($T_0U_0/w = 0.04$)

Figure 7.9: Dependence of ε_3, t_m, and L_m on f at finite Peclet number ($D = 1.0^{-9}$ m^2/s) for type A. Symbols show numerical results; i.e., plus, open square, and open triangle show the numerical results at $T_0U_0/w = 0.01$, 0.02, and 0.04, respectively, when $T_0\Delta P/\mu = 1.8$, while cross, closed circle, and open circle show the numerical results at $T_0\Delta P/\mu = 0.6$, 1.2, and 2.4, respectively, when $T_0U_0/w = 0.04$.

unsuitable range of Strouhal number ($St_0 > 1$ and $St_1 > 1$) as shown in Figs. 7.9(a) and (d). Nevertheless, we can see the enhancement of mixing efficiency in the suitable range of Strouhal number ($St_0 < 1$ and $St_1 < 1$). Further, for typical values, mixing time and length are approximately 400 to 800 ms and 0.5 to 1.5 mm, respectively, in the suitable range of Strouhal number.

Figure 7.10 shows the dependence of ε_3, t_m and L_m on D [(a)-(c)] and Pe_1 ($= U_1w/D$) [(d)-(f)] for type A and the simple rectangular mixer (type D) that uses just molecular diffusion, where Pe_1 is a Peclet number for a directional flow. Note that Peclet number is a dimensionless number the rate of advection of a flow to its rate of diffusion. Here, $T_0\Delta P/\mu = 2.4$ and $T_0U_0/w = 0.04$; $T_0U_1/w = 0.024$ and 0.09 for type A and D, respectively. In Figs. 7.10(d)-(f), solid and broken lines show the scaling functions that are made to fit numerical results for type D and A, respectively; i.e., for type D, $\epsilon_{\max} = 0.85$, $t_m = 0.1wPe_1/U_1$, and $L_m = 0.1wPe$; for type A, $\epsilon_{\max} = 1.96 - Pe_1^{0.033}$, $t_m/T_0 = 340[1 - e^{-Pe_1/60}]$, and $L_m/T_0U_1 = 340[1 - e^{-Pe_1/60}]$. Namely, the mixing time and mixing length of type A are almost constant, while those of type D are proportional to Peclet number. Further, as shown in Figs. 7.10(e) and (f), mixing time and length of type A are shorter than those of type D in the ranges that $Pe_1 > 300$ and $Pe_1 > 100$,

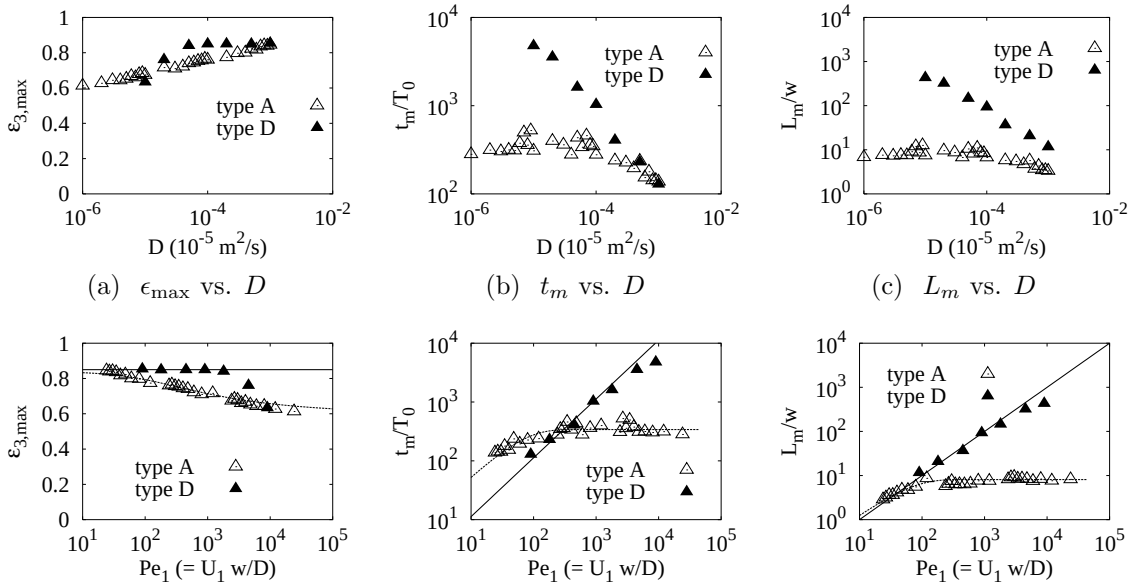

(a) $\epsilon_{\max}$ vs. D (b) t_m vs. D (c) L_m vs. D

(d) $\epsilon_{\max}$ vs. Pe (e) t_m vs. Pe (f) L_m vs. Pe

Figure 7.10: Dependence of ε_3, t_m and L_m on D [(a) and (c)] and Pe_1 ($= U_1 w/D$) [(d) and (f)] for type A and type D. Here, $T_0 \Delta P/\mu = 2.4$, $T_0 U_0/w = 0.04$, $T_0 U_1/w = 0.024$ for type A, and $T_0 U_1/w = 0.090$ for type D. In (c)-(f), solid and broken lines show the scaling functions that are made to fit numerical results for type D and type A, respectively; for type D, $\epsilon_{\max} = 1.96 - Pe_1^{0.022}$, $t_m = 0.1 w Pe_1/U_1$, and $L_m = 0.1 w Pe_1$; for type A $\epsilon_{\max} = 1.96 - Pe_1^{0.033}$, $t_m/T_0 = 340[1 - e^{-Pe_1/60}]$, and $L_m/U_1 T_0 = 340[1 - e^{-Pe_1/60}]$; typically, $T_0 = 1$ ms, $\mu = 1$ mPa·s, and $w = 100$ μm.

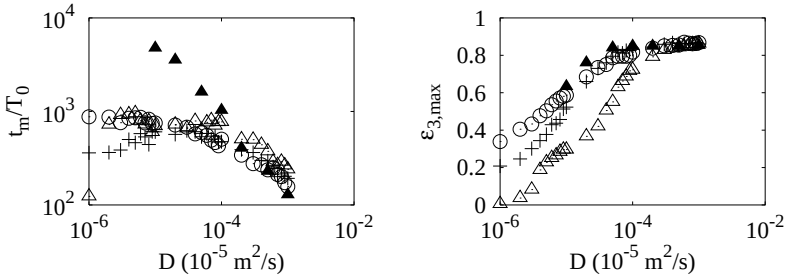

(a) t_m vs. D (b) $\epsilon_{\max}$ vs. D

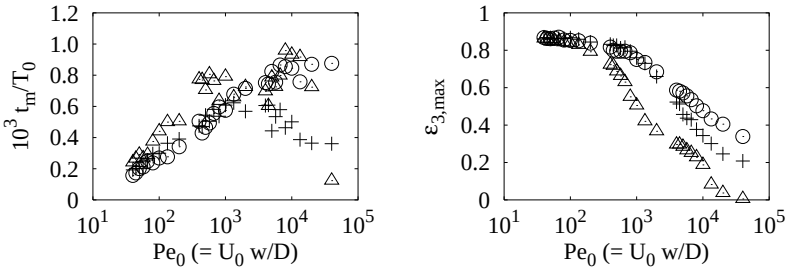

(c) t_m vs. Pe (d) $\epsilon_{\max}$ vs. Pe

Figure 7.11: Performance of simple vortex mixers without switching. Open circle, plus, and open triangle show the numerical results of the simple vortex mixers for the structures of type A, B, and C, respectively. In (a) and (b), the performance of type D (close triangle) is also plotted for the comparison. Here, $T_0\Delta P/\mu = 2.4$ and $T_0 U_0/w = 0.04$; typically, $T_0 = 1$ ms, $\mu = 1$ mPa·s, and $w = 100$ μm.

respectively.

Figure 7.11 shows the performance of simple vortex mixers without switching for the structures of type A, B, and C. Here, $T_0\Delta P/\mu = 2.4$ and $T_0 U_0/w = 0.04$; typically, $T_0 = 1$ ms, $\mu = 1$ mPa·s, and $w = 100$ μm. From Fig. 7.11, we can find that the structure of type A is more effective for mixing than those of type B and type C; i.e., the large vortex flow to across two miscible liquid regions is required for simple vortex mixers to obtain good performance. Further, as shown in Fig. 7.11(c), mixing times of simple vortex mixers are approximately proportional to logarithm of Pe_0, where Pe_0 $(= U_0 w/D)$ is a Peclet number for a vortex flow. Furthermore, in Figs. 7.11(a) and (b), the performance of type D is also plotted for the comparison. By this comparison, we can find that the values of t_m of simple vortex mixers are smaller than those of type D in the range that $D < 2\times10^{-9}$ m^2/s, and thus it is useful to use vortex flow in this range.

7.4 Discussion

At infinite Peclet number and low Reynolds number, we need to use a chaotic mixer proposed by Aref [36], and need to switch fluid orbitals finely. Nevertheless, so far, researchers have only explored the chaotic mixer using two kinds of vortex flows [105]. Thus, we have first shown that the chaotic mixer using a directional flow and a vortex flow is also useful for mixing, although Aref demonstrated that one can generate Lagrangian chaos by alternating between two (or more) different closed-orbit patterns. In particular, the chaotic mixer using a pressure-driven flow and a vortex flow due to ICEO is useful because of its simplicity and effectiveness of applying voltage. Further, different from ordinary chaotic mixers, the proposed chaotic mixer requires the specific modulation frequency to modulate fluid orbitals each other; i.e., by the analysis using the boundary element method combined with the thin double layer approximation, we have first shown that chaotic mixing is produced under the condition that that $St_0 = fd_0/U_0 < 1$ and $St_1 = fd_1/U_1 < 1$.

A simple microfluidic mixer and simple vortex mixers are also expected to work at finite Peclet number, although these mixers never work at infinite Peclet number and low Reynolds number. To clarify this problem, we have considered finite Peclet number by using random walk method along with Lagrangian tracking method, and compared our proposed mixer with a simple microfluidic mixer, simple vortex mixers, and other chaotic mixers. From the view point of the random walk theory, the mixing time of a simple mixer (type D) is estimated by the relation that $\sqrt{2Dt_m^{\rm simple}} \simeq w/2$; i.e., $t_m^{\rm simple} \simeq w^2/8D \simeq Pe_1 w/8U_1 \sim 0.1 Pe_1 w/U_1$ and $L_m^{\rm simple} \simeq Pe_1 w/8 \sim 0.1 Pe_1 w$. Thus, the numerical results of a simple mixer using the random walk method along with the Lagrangian particle tracking method are justified. Further, the values that $D = 10^{-10}$ m^2/s, $w = 100$ μm, and $U_1 = 1$ to 10 mm/s are the typical values of many BioMEMS applications. For this system, $Pe_1 = U_1 w/D = 1000$ to 10000 and $Re = U_1 w/\nu = 0.1$ to 1, where ν

is the kinematic viscosity of the fluid; the mixing length and mixing time of a simple mixer are $t_m^{\text{simple}} \sim 0.1 Pe_1 w/U_1 = 10$ to 100 s and $L_m^{\text{simple}} \sim 0.1 Pe_1 w = 1$ to 10 cm, respectively, while the mixing length and mixing time of a chaotic mixer are $t_m^{\text{chaos}} \sim 0.4$ s and $L_m^{\text{chaos}} \sim 1$ mm, respectively. Thus, the proposed chaotic mixer is more effective than the simple microfluidic mixer for many BioMEMS applications. Furthermore, the mixing time of a simple vortex mixer of the structure of type A is $t_m^{\text{vortex}} \sim 0.7$ s at $Pe_0 = 1000$, and is proportional to $\ln Pe_0$. Thus, the simple vortex mixer is also more effective than the simple microfluidic mixer. Note that we can see similar discussions in [91]. However, mixing efficiency is decreasing as the Peclet number is increasing in the range that $Pe_0 > 1000$. Therefore, the chaotic mixer is more effective than simple vortex mixers, since it works well in the wide rage of Peclet number.

To prevent sample dilution, the Harnett et al.[37] developed a ICEO mixer using many large triangular posts that form two directional channels for loading and many connecting channels for mixing. Although the ICEO mixer in [37] makes long vortex flows in the x direction and pressure flows in the y direction, it is intrinsically a simple vortex mixer because the directional flows are just used to prepare samples without mixing and the vortex flows does not cross the directional flows. Thus, the design concept is completely different from ours. Further, the performance of many passive mixers [91] that use baffles or obstacles that create a tortuous pathway are probably similar to that of a simple vortex mixer because the tortuous pathway also promotes mixing by stretching the interface between the liquids and decreasing the distance over which diffusion must take place. Note that Giona et al. [31] showed that mixing is enhanced due to the increase of the inter-material contact area by the time-periodic sine flow by using the advection-diffusion equation. Furthermore, Glasgow and Aubry [32] analyzed the effect of pulsing the classical electro-osmotic flow rate in one inlet only as well as in the two inlets, and demonstrated that the best results occur when both inlets are pulsed out of phase. In this case, interface is shown to stretch, retain one fold, and sweep through the confluence zone, leading good mixing. Although there are many similar points such that the mixer requires $St_1 \sim 1$ [33], it is not a chaotic mixer using chaotic advection and the performance is probably similar to that of a simple vortex mixer.

7.5 Conclusion

In conclusion, we have proposed chaotic ICEO mixers that switches a pressure-driven directional flow and a vortex flow and numerically examined their performance. By the boundary element method combined with the thin double layer approximation and the Lagrangian particle method along with random walk method, we find that (1) chaotic mixing can be efficiently produced by switching between a pressure-driven directional flow and a large vortex flow under the condition that $St_0 (= f d_0/U_0) < 1$ and $St_1 (= f d_1/U_1) < 1$; (2) the mixing performance of the chaotic mixer that has a large vortex flow

due to the zig-zag structure of four metal posts across a channel is better than that of chaotic mixers that have many smaller vortex flows; (3) the mixing time of the proposed chaotic mixer is almost constant in all the range of Peclet number, while the mixing times of a simple microfluidic mixer and a simple vortex mixer are approximately proportional to the Peclet number and the logarithm of the Peclet number, respectively. When Peclet number is relatively large, our proposed method can be useful to produce chaotic mixing at a low voltage in an ordinary microfluidic channel using simple electrodes.

Chapter 8

Microcolumn 1 (Theory): Microcolumn formation between electrodes in a narrow channel from metallic colloidal suspension through induced-charge electrophoresis

It is desirable to achieve the self-organization of a microcolumn between electrodes in a flow channel because the microcolumn can be used as a biosensor with high sensitivity. A direct simulation of a dispersed system of metallic particles in water is performed to show that a microcolumn between electrodes is formed by the application of an ac electric field. By the multi-physics coupled simulation technique between fluidics and electrostatics based on the boundary element method along with the double layer approximation, we find that microcolumns are formed by the growth of clusters perpendicular to the electrodes under the condition that the number density of particles is larger than the percolation threshold. Further, we propose a simple model that efficiently explains the time dependence of the probability of the formation of a microcolumn by considering standard collision theory and percolation theory. By this analysis, we can greatly contribute to developments in studies on the self-organization of microcolumns and biosensors.

8.1 Introduction

Patterned colloidal structures formed from dispersions of particles have many potential applications [101]; thus, they have been researched extensively [96, 38, 8, 56]. In particular, because of its high aspect ratio, micro or nanocolumn or wire between electrodes in a flow channel can be used as a biosensor with high sensitivity. Aksay *et al.* [96] have

reported the formation of multi-colloidal columns by generating electrohydrodynamic flow in a suspension of spherical $BaTiO_3$ by the application of a dc electric field $E_0 = 50$ to 200 kV/m. Further, Velev *et al.* [38] have reported the formation of microwires from gold nanoparticle suspensions between gold electrodes through dielectrophoresis by the application of an ac electric field $E_0 \approx 25$ kV/m. Their methods are similar in the sense that they formed microstructures between electrodes from colloidal particle suspensions by the application of ac or dc electric fields. In both these studies, it is pointed out that the electro-osmotic flow plays a major role in the assembly process; however, their findings are not directly predicted by theory, and to the best of our knowledge, a direct simulation of a colloidal multiparticle system has not been performed. Electrophoretic deposition, which can be used to form films on an electrode from colloidal suspensions by the application of dc electric fields, is known to be a related phenomenon and has been studied extensively [8, 56, 68].

Recently, Bazant and Squires [5, 83, 84] showed that an induced-charge electrokinetic phenomenon (ICEP), which includes induced-charge electro-osmosis and electrophoresis, is a key concept for understanding behaviors of metallic colloidal suspensions and flows around a metal post; e.g., it has been found that conductors in an ionic solution with a broken symmetry generate a large net flow velocity (of the order of a few millimeters per second in an electric field of approximately 10^4 V/m) due to an ICEP [5, 83, 84, 97, 16, 30, 66, 1, 57]. An ICEP is different from classical electro-osmosis and electrophoresis because it is caused by the interaction between an electric field and ions in an electric double layer formed by the polarizing effect of the electric field. Moreover, it can be driven by ac electric fields; therefore, problems due to a dc electric field can be avoided. In this study, from this unified viewpoint i.e., ICEP, we focus on the self-assembly process of a microcolumn in a narrow channel from metallic colloidal suspensions and elucidate the effect of application of an electric field to a metallic dispersion system in water in a microfluidic channel.

8.2 Theory

Figure 8.1 shows the schematic view of our simulation of the self-assembly process of a microcolumn. As shown in Fig. 8.1, we consider a dispersion system of circular metallic particles of radius c ($= 0.08w$), with N ($= 18$) number of particles between electrodes in a rectangular channel of length L ($= 2.25w$) and width w ($= 100$ μm). To evaluate the probability of the formation of a microcolumn, we generate random positions at $t = 0$ ms by considering random number for metal particles; i.e., we define regular lattice positions (X_i, Y_j) and then consider irregular lattice positions $(X_i + \delta x_{ij}, Y_j + \delta y_{ij})$, where δx_{ij} and δy_{ij} are uniform random numbers in the ranges $|\delta x_{ij}| < w/8 - c$ and $|\delta y_{ij}| < L_0/10 - c$, respectively. Here, $X_i = (i + 1/2)w/4$ for $i = 0, 1, 2, 3$ if $j = 0, 2, 4$; $X_i = (i + 1)w/4$ for $i = 0, 1, 2$ if $j = 1, 3$; and $Y_j = (j + 1/2)L_0/5 + (L - L_0)/2$ for $j = 0, 1, 2, 3, 4$. It should be

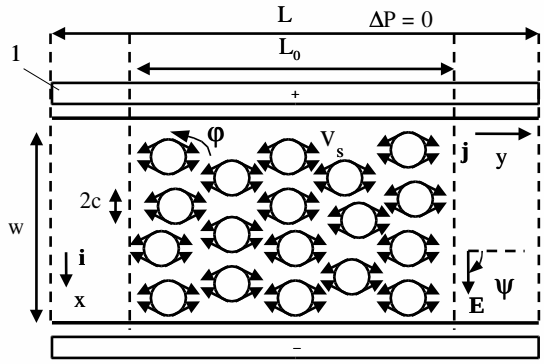

Figure 8.1: Schematic view of metallic particle dispersion system (in water) used for the simulation of microcolumns. 1: pair of electrodes. Here, length $L = 2.25w$ and width $w = 100$ μm.

noted that we introduce a limitation length L_0 to obtain samples that differ in number density under the same particle number N since number density is defined as N/L_0w. Further, we assume that particles aggregate in the direction of x if $r_{k\lambda} < 2c + d_0$ and $|x_{k\lambda}| < (2c + d_0)/2$, where $r_{k\lambda}$ is the distance between particles, $d_0 = 0.02w$, and $|x_{k\lambda}|$ is a distance in the x direction. By considering this connection in the x direction, we define an average cluster size of each sample arrangement Λ as $S_{x,\Lambda} \equiv \sum_{s=0}^{s=\infty} sP_s$, where s is the cluster size, $P_s = sn_s/N$ is the probability that one particle belongs to the cluster whose size is s, n_s is the number of clusters whose size is s, and N (= 18) is the number of particles. Further, if particles belonging to the same cluster come in contact with upper and lower electrodes at the same time, we can conclude that percolation occurs between electrodes and at least one microcolumn is formed between electrodes. We set $G_\Lambda = 1$ when percolation occurs and $G_\Lambda = 0$ when no percolation occurs.

By considering standard collision theory and percolation theory [88], we propose a simple scaling model that explains $< S_x > \equiv \sum_{\Lambda=1}^{\Lambda=N_s} S_{x,\Lambda}/N_s$ and $< G > \equiv \sum_{\Lambda=1}^{\Lambda=N_s} G_\Lambda/N_s$ as follows:

$$< S_x > \approx 1 + (S_x^{\max} - 1)(1 - e^{-t/\tau_1}), \tag{8.1}$$

$$< G > \approx P(L_0)[1 - \frac{1}{e^{(t-\tau_2)/\tau_3} + 1}], \tag{8.2}$$

respectively, where τ_1 is a clustering time, τ_2 is a threshold time of the formation of a microcolumn, τ_3 is a width of the threshold, S_x^{max} is the maximum value of $< S_x >$, $P(L_0) \equiv 1/[e^{(L_0 - L_0^{\rm th})/\Delta L_0} + 1]$ is the percolation probability between electrodes, $L_0^{\rm th}$ is the threshold of P, and ΔL is the width of the threshold of P. Although Eq. (8.1) seems to be complex, it is just the reaction equation of the first order with a time constant τ_1 in a random system, except that it is modified so that $< S_x >$ is one at the initial time and becomes S_x^{max} at the final time because of the physical limitation of the cluster in our random system. Similarly, Eq. (8.2) is just the phenomenological equation that describes the phenomenon that $< G >$ glows at $t \simeq \tau_2$ with the ambiguity time τ_3, except that it is designed so that $< G >$ becomes the percolation probability P at the final time. It should be noted that percolation theory provides the probability to form clusterings that connect to infinite or finite regions in various random systems, and can be used to explain a macroscopic conductance [88, 47]. Thus, Eq. (8.2) is an appropriate equation that describes our random system, as a first attempt. Basically, all the parameters are determined so that numerical results fit into Eqs. (8.1) and (8.2); i.e., from simulations, we set $\tau_1 = 4\tau_0$, $\tau_2 = 3\tau_0$, $\tau_3 = 0.6\tau_0$, $L_0^{\rm th}/w = 1.35$, $\Delta L_0/w = 0.3$, $U_0^{\rm eff} = U_0/7$, and $S_x^{max} \approx 2.4 + 1.8(L_0 - 2.2)^2$, where $\tau_0 = 1/[4cU_0^{\rm eff}(N/L_0 w)]$ is a collision time, $4c$ is a collision cross section, $N/L_0 w$ is a number density of the particles, U_0 $(= \epsilon c E_0^2/\mu)$ is a standard representative velocity, and E_0 $(= V_0/w)$ is a representative electric field between electrodes. It should be noted that we have derived Eqs. (8.1) and (8.2) by considering random collisions between particles that move randomly with average velocity $U_0^{\rm eff}$. In the random system, it is reasonable that $< S_x >$ is subject to the reaction equation of one order with $\tau_1 = 4\tau_0$, since clustering in the x direction occurs with the probability of 1/4. Note that clustering is apt to occur from a lower or upper electrode owing to attractive forces between a particle and a wall and attractive forces in the x direction between particles; i.e., a cluster grows in the one x direction only when a particle collide with the particle that positions at the edge of the cluster opposite to the wall. Of course, if particles collide with each other in the y direction, clustering does not occur because repulsive forces due to a ICEO flow around particles work between particles. Further, it is reasonable that the stable value of $< G >$ is an ordinary percolation probability for a random configuration problem of a finite number of particles in a finite size under the condition that $\Delta L_0 \neq 0$, and $< G >$ has a time threshold that is strongly related to τ_1.

Numerically, we consider a 2D quasi-static Stokes flow without Brownian motion: i.e., we consider the limit in which the Reynolds number Re tends to zero and the Peclet number is infinite. We assume the posts of the metal cylinder to be polarizable in an electrolytic solution under a dc or ac electric field. The motion of the surrounding fluid must satisfy Stokes equations modified by the inclusion of an electrical stress. However, by using matched asymptotic expansion [26], we can reduce them to the classical Stokes

equations as follows:

$$\mu\nabla^2\boldsymbol{v} - \nabla p = 0, \qquad \nabla\cdot\boldsymbol{v} = 0, \tag{8.3}$$

$$\text{On } S_{\mathrm{p}}^{+(j)}: \quad \boldsymbol{v}^{(j)} = \boldsymbol{U}^{(j)} + \boldsymbol{\Omega}^{(j)}\times\boldsymbol{x}^{(j)} + \boldsymbol{v}_{\mathrm{s}}^{(j)}, \tag{8.4}$$

$$\int_{S_{\mathrm{p}}^{+(j)}} \boldsymbol{f}^{(j)}\mathrm{d}l + \boldsymbol{F}_t^{\mathrm{ext},(j)} = 0, \qquad \int_{S_{\mathrm{p}}^{+(j)}} \boldsymbol{x}^{(j)}\times\boldsymbol{f}^{(j)}\mathrm{d}l + \boldsymbol{T}_t^{\mathrm{ext},(j)} = 0. \tag{8.5}$$

where $S_{\mathrm{p}}^{+(j)}$ denotes the surface defined as the outer edge of the double layer, $\boldsymbol{U}^{(j)}$ is the translational velocity, $\boldsymbol{\Omega}^{(j)}$ is the rotational angular velocity, $\boldsymbol{f}^{(j)}$ is the traction vector, $\boldsymbol{F}_t^{\mathrm{ext},(j)}$ and $\boldsymbol{T}_t^{\mathrm{ext},(j)}$ are the total external force and torque, respectively, on the j's metal cylinder (j = 1,2,...,N). Further, $\boldsymbol{x}^{(j)}$ ($= -\sin\varphi\ \boldsymbol{i} + \cos\varphi\ \boldsymbol{j}$) is the surface position of the j's metal parameterized by φ, $\boldsymbol{i}$ and $\boldsymbol{j}$ are orthogonal unit vectors in the Cartesian coordinate system, μ ($\sim$1 mPa·s) is the viscosity, $\boldsymbol{v}$ is the velocity,and p is the pressure. Under a wide range of conditions, the local slip velocity $\boldsymbol{v}_s^{(j)}$ is given by the Helmholtz-Smoluchowski formula,

$$\boldsymbol{v}_s^{(j)} = -\frac{\epsilon\zeta^{(j)}}{\mu}\boldsymbol{E}_{\mathrm{s}}{}^{(j)} \tag{8.6}$$

where $\boldsymbol{E}_{\mathrm{s}}{}^{(j)}$ is the tangential component of the electric field, ϵ ($\sim 80\epsilon_0$) is the dielectric permittivity of the solvent (typically water), and ϵ_0 is the vacuum permittivity. Here, a zeta-potential $\zeta^{(j)}$ around the j's metal is generally defined as $\zeta^{(j)} = \phi_i^{(j)} - \phi_f^{(j)}$, where $\phi_f^{(j)}$ and $\phi_i^{(j)}$ are final and initial potentials, respectively.

To consider a multi particle problem under a bounded condition, we solve the electric potential at every time step before calculating a flow field by the boundary element method based on the following Laplace's equation, $\nabla^2\phi = 0$. On the one hand, we use the Dirichlet boundary condition for the upper and lower walls (electrodes); i.e., $\phi = +0.5V_0$ at $x = 0$, $\phi = -0.5V_0$ at $x = w$, where V_0 is an applied voltage across the channel. On the other hand, we use the Neumann boundary condition for the left and right walls; i.e., $\boldsymbol{n}\cdot\nabla\phi = 0$ at $y = 0$ and L, where $\boldsymbol{n}$ is the surface normal unit vector. In addition to those boundary conditions, to obtain a final potential, we also use the Neumann boundary condition (i.e., $\boldsymbol{n}\cdot\nabla\phi = 0$) on the metal surface. Further, to obtain a initial potential, we use the condition that j's metal particle have an unknown surface potential $\phi_i^{(j)}$, and require the electrical neutral condition that $\oint_{(j)}(\boldsymbol{n}\cdot\nabla\phi)ds = 0$. Thus, we can numerically calculate a flow field for a bounded domain. It should be noted that we use the boundary condition that the velocity on the wall of the channel is zero and that the pressures of the inlet and outlet are P_1 and P_2, respectively. (Here, $P_1 = P_2 = 0$ and $\Delta P = P_2 - P_1 = 0$.) On the basis of Eqs. (8.3)-(8.6), we calculate the flow fields of the ICEP multi-particle system for a bounded domain by the boundary element method.

Further, we consider a short-range repulsive velocity $\mathbf{u}_{\mathrm{col}}(r_{ik})$ that prevents unphysical overlapping between particles; i.e., at every time step, we move particles from $\mathbf{x}_i^{\mathrm{before}}$ to

$\mathbf{x}_i^{\text{after}}$ as $\mathbf{x}_i^{\text{after}} = \mathbf{x}_i^{\text{before}} + \mathbf{u}_{\text{col}}(r_{ik})\Delta t/10$ until all the distances r_{ik} become larger than $2c + d_1$, where $d_1 = 0.01w$ ($< d_0$), Δt ($= 1$ ms) is a time interval of the numerical simulation, $\mathbf{u}_{\text{col}}(r_{ik}) = 0$ if $r_{ik} > 2c+d_1$, $\mathbf{u}_{\text{col}}(r_{ik}) = -2U_0\mathbf{x}_{ik}/r_{ik}$ if $r_{ik} < 2c$, and $\mathbf{u}_{\text{col}}(r_{ik}) = -2U_0 \exp[-(r_{ik} - 2c)/d_1]\mathbf{x}_{ik}/r_{ik}$ if $2c \le r_{ik} \le 2c + d_1$. Here, $\mathbf{x}_{ik} = (x_{ik}, y_{ik})$. Note that unphysical overlapping between particles occur mainly because particles move relatively large distances during Δt. Thus, a small factor, such as 1/10, is needed to remove unphysical overlapping. To the best of our knowledge, our developed simulator is the only tool that can directly analyze ICEP multi-particle flow automatically by considering hydrodynamic and electrostatic wall-cylinder interactions.

8.3 Results

Figure 8.2 shows an example of the formation of a microcolumn due to ICEP by a full couple simulation when $L_0/w = 1.3$, $c/w = 0.08$, $\Delta P = 0$, $\tau_0 (= L_0 w/4aNU_0^{\text{eff}}) = 79.1$ ms, $U_0 = 2$ mm/s, $U_0^{\text{eff}} = U_0/7$, and $E_0 = 18.8$ kV/m. Here, the applied voltage $V_0 = 1.88$ V for $w = 100$ μm is reasonable for an ICEP caused by an ac voltage. In fact, such strong electric fields have been used in previous experiments [96, 38, 97]. Metal particles that are placed at random positions at $t = 0$ ms generate a complex flow field, as shown in Fig. 8.2(a), and move in a complex manner due to an attractive force parallel to the electric field and a repulsive force perpendicular to the electric field between particles. Figure 8.2(b) shows an image of particles and flow fields at $t = 80$ ($\approx 1.0\tau_0$) ms. Because of the attractive force that is parallel to the electric field, particles have a tendency to aggregate in the direction of the electric field and form clusters. As shown in Fig. 8.2(c), a microcolumn is formed first at $t = 195$ ($\approx 2.5\tau_0$) ms; i.e., there is no microcolumn formation in the period $t < 195$ ms. There is a tendency that the system keeps to form a microcolumn or multi columns even though there is movement as shown in Figs. 8.2(d), 8.2(e), and 8.2(f). It should be noted that we cannot observe a remarkable flow toward the electrodes and a deposition of particles on the electrodes.

Figure 8.3 shows the results of clustering analysis by a full coupled simulation for N_s ($= 20$) initial arrangements when $L/w = 2.25$, $U_0 = 2$ mm/s, and $E_0 = 18.8$ kV/m. Figure 8.3(a) shows the time dependence of $< S_x >$. As shown in Fig. 8.3(a), the time evolution of $< S_x >$ is described by Eq. (1), which is similar to the reaction equation of one order, derived from random collisions. Figures 8.3(b) and 8.3(c) show the time evolution of $< G >$. As shown in Figs. 8.3(b) and 8.3(c), microcolumns form and then stabilize; i.e., we cannot observe a decay of $< G >$. Figure 8.3(d) shows the dependence of P on L_0/w. Here, P is defined as $P =< G >_{t=1000ms}$. As shown in Fig. 8.3(d), microcolumns are well formed in the range $L_0/w < L_0^{\text{th}} (= 1.35)$, although the width of the threshold of P is rather wide; i.e., $\Delta L_0 = 0.3$. Thus, at a specific initial arrangements of particles, the formation of microcolumn is not merely a coincidence. Further, from Fig. 8.3, we can observe that the analytical results of $< S_x >$, $< G >$, and P agree fairly well with the

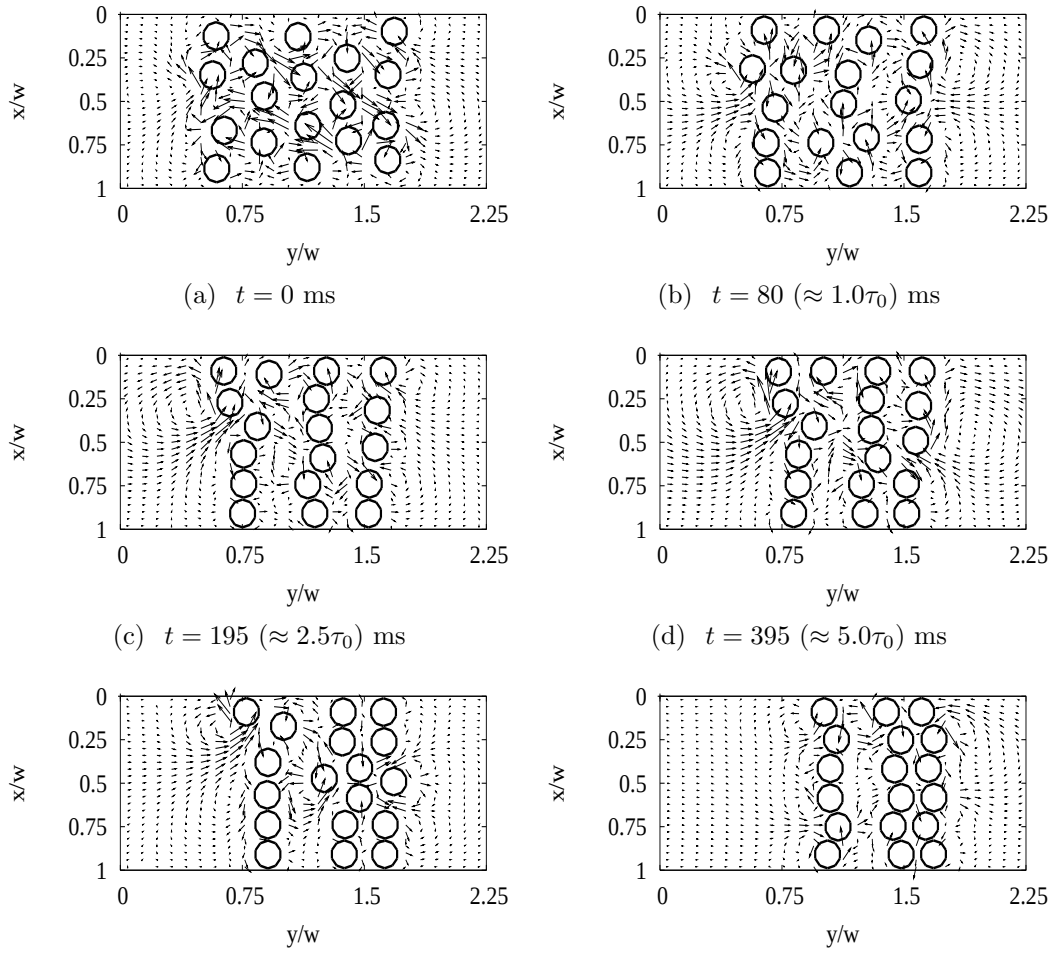

(a) $t = 0$ ms

(b) $t = 80$ ($\approx 1.0\tau_0$) ms

(c) $t = 195$ ($\approx 2.5\tau_0$) ms

(d) $t = 395$ ($\approx 5.0\tau_0$) ms

(e) $t = 700$ ($\approx 8.8\tau_0$) ms

(f) $t = 1000$($\approx 12.6\tau_0$) ms

Figure 8.2: Formation of microcolumn and ICEP flow fields of metallic particle dispersion system by a full coupled simulation. Here, $L_0/w = 1.3$, $c/w = 0.08$, $\Delta P = 0$, $\tau_0 = 79.1$ ms, $U_0 = 2$ mm/s, $U_0^{\text{eff}} = U_0/7$, and $E_0 = 18.8$ kV/m.

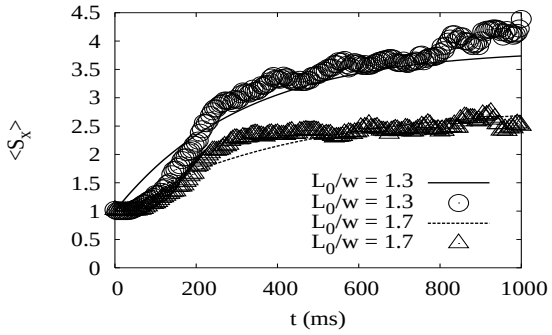

(a) Dependence of $< S_x >$ on time

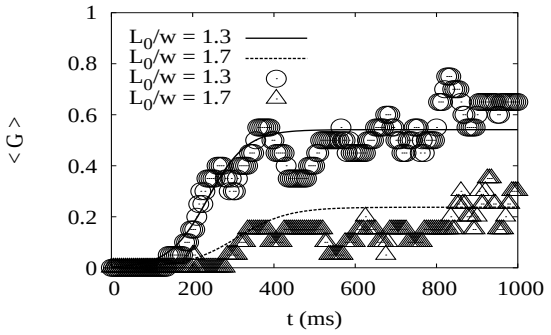

(b) Dependence of $< G >$ on time ($L_0/w > 1.0$)

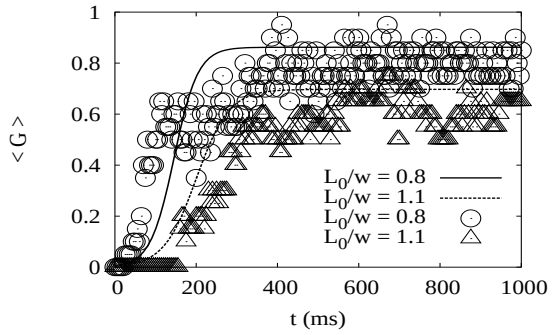

(c) Dependence of $< G >$ on time ($L_0/w < 1.0$)

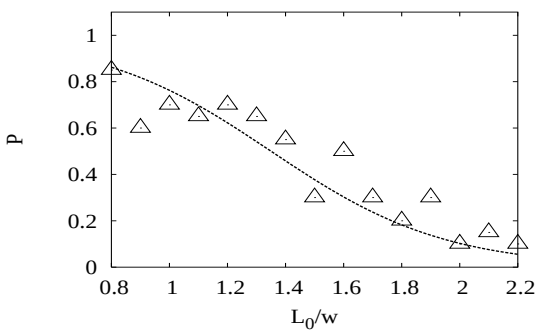

(d) Dependence of percolation probability P on L_0/w

Figure 8.3: Results of clustering analysis by a full coupled simulation. Here, $L/w = 2.25$, $\Delta P = 0$, $U_0 = 2$ mm/s, and $E_0 = 18.8$ kV/m. The lines show analytical results obtained by Eqs. (1) and (2). The symbols show numerical results obtained by the boundary element method.

numerical results.

8.4 Discussion

When $c = 8$ μm, a root mean square of Brownian motion is $\sqrt{6Dt} = \sqrt{k_B T t/\pi\mu c} = 0.13$ μm ($\ll 8$) even for $t = 100$ ms, where k_B is the Boltzmann constant and T (= 300K) is a temperature. Therefore, we can neglect Brownian motion even though our proposed system is colloidal. Thus, we have an idealized system of particles that is subject to whatever external forcing we can impose. Further, the threshold value of L_0 for P is approximately 1.2 to 1.6, which corresponds to $q \approx 0.38$-0.29, where q is the occupied ratio defined as $q = 4c^2N/L_0w$. Since the threshold of bond percolation for a 2D triangular lattice problem is approximately 0.35, we think that the current microcolumn is formed because of the percolation occurring when the percolation threshold is exceeded in the case of narrow channel. Thus, the formation mechanism of our microcolumn is different from that of other microcolumns that can be explained by the concentration of electric fields on the top of the growing tip of the microcolumn. Furthermore, though our system is not driven by dielectrophoresis, a lot of similarities may exist between an electrorheological (ER) fluid [35] and a multi particle system of ICEP since the phenomenon of organizing particles in a plane normal to electrodes is common. In an ER fluid, the formation of chains and columns parallel to the field is accompanied by a dramatic increase in the apparent viscosity of the suspension. Thus, we expect that an ICEP can be used to create a new high-performance ER fluid in the future. Further, the random configuration of particles in our system will induce a nonuniform electric field and a nonuniform slip velocity around particles. Thus, although it might not be in the unified viewpoint of ICEP, if the phenomenon seen in the relative motion of suspensoid and medium resulting from polarization forces produced by an inhomogeneous electric field is widely defined as "dielectrophoresis" [60], we may need to say that a kind of "dielectric" effect also would be automatically taken into account in our calculations through the nonuniform slip velocities resulting from a nonuniform electric field. Note that we assume that $F_t^{\mathrm{ext,(j)}}$ and $T_t^{\mathrm{ext,(j)}}$ are zero in Eq. (8.5) by considering that the electrostatic force is screened by the existence of counter ions; i.e., we consider that direct electrostatic interactions between particles do not exist in perfectly polarizable solutions, as far as we use the boundary condition that $\boldsymbol{n} \cdot \nabla\phi = 0$ on $S_{\mathrm{p}}^{+(j)}$ to obtain a steady electric field, because the boundary condition means that there is no net charge to interact with.

8.5 Conclusion

In conclusion, we have proposed the formation of microcolumns between electrodes in a narrow channel through an ICEP and percolation phenomena and numerically examined

their characteristics. By full coupled simulations, we observe the following. (1) The formation of clusters and a microcolumn in the direction of an applied electric field proceed within the time that is approximately 4 to 5 $\tau_0 (= L_0 w / 2aNU_0^{\mathrm{eff}})$. (2) A microcolumn is formed under the condition that the occupied ratio of metal particles is larger than approximately 0.35; this value approximately agrees with the threshold of bond percolation on a 2D triangular lattice. (3) The time dependence of the probability of the formation of the microcolumn is characterized by a simple scaling model that considers standard collision theory and percolation theory. (4) In a full coupled simulation that considers precise boundary conditions, there is no remarkable flow toward electrodes, and the effective velocity becomes slower than an ordinary characteristic velocity. We believe that our method for the formation of microcolumns will revolutionize the design concept of biosensors.

Chapter 9

Discussion

9.1 Bridging a gap

Microfluidic devices are important and indispensable to obtain a promising biomedical applications such as a Lab-on-a-chip (LOC) and micro-total-analysis systems (μTAS). Although Bazant and Squires [5] suggested a wide range of microfluidic applications using ICEO and ICEP in 2004, fundamental design knowledge for microfluidic devices using ICEO and ICEP were lacked in that time. Thus, our conceptual designs for stacking ICEO pumps, rotary ICEP valves, chaotic ICEO mixers, and micro-column ICEP devices are important, as a first attempt bridging a gap between fundamental physics and applications. In particular, we have clarified precise boundary effects on the devices by the multi-physics coupled simulation technique along with the thin double layer approximation, since the boundary effects play a dominant role in microfluidic device using ICEO and ICEP. Further, although classical ICEO theory sometimes cannot explain even the direction of ICEO flow [4], we have clarified the physical picture of the electric double layer that was induced by the ac electric fields and succeeded in explaining a reverse flow problem at low frequency, by the ac PNP analysis. Furthermore, our proposed devices can be fabricated on the same substrate in a same manner, and can compose a fluidic integrated circuit, such as a LOC devices. Thus, we believe that we can significantly improve the size and processing speed of a fluidic integrated circuit by using the ICEO and ICEP devices in the future.

9.2 Remained problems

However, a lot of work remains to realize innovative industrial products using ICEO and ICEP. First, we need to overcome two kinds of problems that limit ICEO and ICEP applications. One is the problem that a flow velocity of an ICEO flow reduces as the concentration of ions increases, and becomes zero at approximately 10 mM. The other is

the problem that a pressure generated by a single ICEO unit is usually very low (∼4 Pa), although the potential flow velocity is large (∼1 mm/s) with low voltage (∼V). Although the proposed stacking structure is one of solutions for the low pressure problem, we need to solve more intrinsically by increasing a performance of an ICEO working surface. Second, although we clarified the physical picture on the double layer to some extent, we need to explore more deeply the interface science between fluids and liquids, to solve the above problems. For example, by clarifying the mechanism of high viscous layer in the electric double layer, we have a possibility to overcome the 10 mM limit. Third, although pumps, valves, and mixers are important, they are not enough to create innovative systems. Thus, we need to obtain other core element technologies, such as sensors, which have a central function and compose a system with pumps, valves, and mixers. Further, we need to obtain system technologies to integrate fluidic devices, although we might use classical technologies for this problem.

9.3 Beyond the ICEK

Moreover, possibility of ICEO and ICEP does not limit within the microfluidic applications. For example, smart materials that control microscopic structures of fluidics and microscopic characters (like the micro-column device) are also promising as applications of ICEO and ICEP. Further, recently, a Janus particle, which is proposed from the view point of ICEP, has been attracted as a thermophoretic device [41]. Thus, we need to pursue a unified view point beyond ICEO and ICEP, by exploring expand interface problems, such as thermophoresis or double layer problems under the non-equilibrium conditions. Through the true understanding of the interface between solids and liquids, we believe that we can realize innovative technologies that can be used in the industrial fields.

Chapter 10

Conclusions

In conclusion, we have developed several calculation methods based on the boundary element method along with the thin electric double layer. By using these methods, we have proposed the four kinds of fundamental microfluidic devices using ICEK (i.e., ICEO and ICEP), and have elucidated their design concepts theoretically. Further, we have proven two of key issues for our predictions experimentally.

Specifically, in Chapter 2, we have developed a calculation technique (ICEP-BEM) to model ICEP using the boundary element method, and examined its validity by comparing it with analytical solutions. Further, by this method, we have shown that (1) applying an electric field tends to align polarizable elliptical particles in the same direction as the electric field thorough ICEP, even in the Poiseuille flow in a microfluidic channel; (2) in the presence of an electric field parallel to the flow channel, a polarizable elliptical particles near a wall always feels a repulsive force due to ICEP; (3) two polarizable elliptical particles are repelled each other in side-by-side conformation through ICEP, while they are attracted in head-and-tail conformation.

In Chapter 3, we have proposed ICEO pumps that employ asymmetrically stacked structures to suppress the reverse flow and examined the pumping performance by the boundary element method in conjunction with the double layer approximation and a simple model. The following are the conclusions of the numerical calculations. (1) The asymmetrical stacking configuration efficiently suppresses the reverse flow and yields ∼mm/s velocity, which is 46% to 71% of the performance of an optimum half-coating pump. (2) The velocity of the stacking pump with a thin limit with infinite N is larger than 67% of that of the half-coating pump of the circular cylinder of the same length.

In Chapter 4, (1) we have experimentally shown that asymmetrical vortices due to ICEO are generated around stacking structures consisting of conductive posts in an aqueous solution. (2) By considering boundary effects precisely, except for the problem of anomalous reverse vortex flow, we have successfully explained the experimental results that stacking structures accelerate a reverse flow rather than suppressing it. (3) By the ac PNP analysis, we find that the anomalous flow reversal in low frequency occurs owing

to the phase retardation between an induced diffuse charge and a tangential electric field, and successfully explained the observed nonlinearity of the flow velocity on the applied voltage. (3) We have shown that a large-height structure consisting of carbon posts fabricated by pyrolysis of photoresists is useful for the fabrication of an ICEO device because of its simplicity and nonreactive nature.

In Chapter 5, we have proposed rotary-ICEP microvalves in water using hydrodynamic force due to induced-charge electrophoresis and numerically examined their performance. By the multi-physics coupled simulation technique between fluidics and electro-statics based on the boundary element method along with the thin double layer approximation, we find that (1) for the general problem, an angular velocity of an elliptical metal cylinder is accelerated by the fluidic boundary effect, and is decelerated by the electric boundary effect; (2) for the valve problem, the electric boundary effect is stronger than the fluidic boundary condition and thus it usually decelerates the angular velocity of the valve, because the elliptical metal cylinder is very close to the electrode; (3) to obtain a large average velocity in an opening state and a large angular velocity in a closing motion, single or twin rotary-valves have more advantages than the multi ($N \geq 3$) rotary-ICEP valves; (4) a single rotary-ICEP valve that is positioned off the center closes at high frequency ($\sim$15 Hz) and a weak electric field (11.9 kV/m) in a microfluidic channel and can control the pulsating pressure flow in an opening state; (5) a twin rotary-ICEP valve closes at high frequency ($\sim$24 Hz) and a weak electric field (11.9 kV/m) in a microfluidic channel and can control the pulsating pressure flow in an opening state.

In Chapter 6, (1) by using an elliptical carbon conductive cylinder coated with gold, we experimentally showed that microvalves rotate near the conductive electrodes in deionized water. (2) The time evolution of the rotation angle of the elliptical conducive cylinder was obtained experimentally from the numerical analysis of an experimental image and successfully compared with the theoretical results using the multiphysics coupled simulation technique; the correction factor was very small ($\Lambda = 0.018$). (3) We have shown that a carbon cylinder of large height fabricated by the pyrolysis of a photoresist is useful for the fabrication of an ICEP device because of the simplicity of its removal from the substrate.

In Chapter 7, we have proposed chaotic ICEO mixers that switches a pressure-driven directional flow and a vortex flow and numerically examined their performance. By the boundary element method combined with the thin double layer approximation and the Lagrangian particle method along with random walk method, we find that (1) chaotic mixing can be efficiently produced by switching between a pressure-driven directional flow and a large vortex flow under the condition that $St_0 (= fd_0/U_0) < 1$ and $St_1 (= fd_1/U_1) < 1$; (2) the mixing performance of the chaotic mixer that has a large vortex flow due to the zig-zag structure of four metal posts across a channel is better than that of chaotic mixers that have many smaller vortex flows; (3) the mixing time of the proposed chaotic mixer is almost constant in all the range of Peclet number, while the mixing times of a simple microfluidic mixer and a simple vortex mixer are approximately proportional

to the Peclet number and the logarithm of the Peclet number, respectively.

In Chapter 8, we have proposed the formation of microcolumns between electrodes in a narrow channel through an ICEP and percolation phenomena and numerically examined their characteristics. By full coupled simulations, we observe the following. (1) The formation of clusters and a microcolumn in the direction of an applied electric field proceed within the time that is approximately 4 to 5 $\tau_0 (= L_0 w / 2aNU_0^{\mathrm{eff}})$. (2) A microcolumn is formed under the condition that the occupied ratio of metal particles is larger than approximately 0.35; this value approximately agrees with the threshold of bond percolation on a 2D triangular lattice. (3) The time dependence of the probability of the formation of the microcolumn is characterized by a simple scaling model that considers standard collision theory and percolation theory. (4) In a full coupled simulation that considers precise boundary conditions, there is no remarkable flow toward electrodes, and the effective velocity becomes slower than an ordinary characteristic velocity.

In the future, we believe that we can dramatically improve the size and performance of promising microfluidic systems such as lab-on-a-chip.

Chapter 11

Relevant publications

The following is a list of publications covering to contributions made thus far, as described in this work:

1. Chapter 2: Hideyuki Sugioka, "Basic analysis of induced-charge electrophoresis using the boundary element method", Colloid and Surfaces A: Physicochem. Eng. Aspects 376, 102 (2011)

2. Chapter 3: Hideyuki Sugioka, "Suppression of reverse flows in pumping by induced-charge electro-osmosis using asymmetrically stacked elliptical metal posts", Phys. Rev.E 78,057301 (2008)

3. Chapter 4: Hideyuki Sugioka, "Asymmetrical reverse vortex flow due to induced-charge electro-osmosis around carbon stacking structures", Phys. Rev. E 83,056321 (2011)

4. Chapter 5: Hideyuki Sugioka, "High-speed rotary microvalves in water using hydrodynamic force due to induced-charge electrophoresis", Phys. Rev. E 81, 036301(2010)

5. Chapter 6: Hideyuki Sugioka, "Rotation of a microvalve near conductive electrodes via induced-charge electrophoresis", Phys. Rev. E 83, 025302(R) (2011)

6. Chapter 7: Hideyuki Sugioka, "Chaotic mixer using electro-osmosis at finite Peclet number", Phys. Rev. E 81,036306 (2010)

7. Chapter 8: Hideyuki Sugioka, "Microcolumn formation between electrodes in a narrow channel from metallic colloidal suspension through induced-charge electrophoresis", Phys. Rev.E 80,016315 (2009)

Chapter 12

Acknowledgment

I would like to express my deepest gratitude to my adviser, Professor Osam Tabata, I have learned so much from you through various discussions and I am very proud of getting advice from you in my life.

I would also like to thank my dissertation committee members - Professors Kazuyoshi Nakabe and Shinji Nishiwaki. I very much appreciate your helpful comments and I am very proud of getting advice from you.

Also, I am grateful to Prof. Eric Darve for helpful discussions on the mathematical details of the calculation method. You first introduced me to the importance of induced-charge electrokinetic phenomena when I was staying at Stanford University as a visiting scholar. I am also grateful to Professor Keisuke Sasaki. You first introduced me to the attractiveness of applied physics when I was studying as a graduate school in Keio University. I am also grateful to Mr. Umeo Suzuki. You first introduced me to the scientific thinking through a lot of experiments and with group discussions.

I am also grateful to my excellent supervisors - Dr. Toshiaki Ikoma, Dr. Yuji Kawabata, Mr. Takayuki Yagi, Dr. Keishi Saitou, and Dr. Akira Asai. You all have found my ability for science and given me the great opportunities to explore from basic science to engineering problems. In particular, I greatly appreciate Mr. Yagi's wisdom and foresight to send me to Stanford University to explore advanced MEMS design technologies. I also greatly appreciate Dr. Ikoma and Dr. Kawabata's wisdom to give me the freedom to explore fluidics of interface between solids and liquids to contribute human knowledge.

Thank you also to the excellent researchers of Frontier research center. I was really encouraged when I won the 1st prize of the year's excellent research by your votes.

I would also like to thank my parents, Fujio and Chieko Kawagishi, and Akira and Emiko Sugioka. Thank you for fostering my creativity and allowing me to find my own way.

Finally, I would like to dedicate this dissertation to my lovely wife, Mie. I would not have made it without you. When I was deeply discouraged in my life, I am always helped by your understandings to myself. It is true that thanks to your existence I can pursue

my dreams.

This work was supported by Canon Inc.

Bibliography

[1] A. Ajdari. Pumping liquids using asymmetric electrode arrays. *Phys. Rev. E*, 61:R45, 2000.

[2] G.K. Batchelor. Slender body theory for particles of arbitrary cross-section in Stokes flow. *J. Fluid Mech*, 44(3):419, 1970.

[3] G.K. Batchelor. The stress system in a suspension of force-free particles. *J. Fluid Mech*, 41(3):545, 1970.

[4] M. Z. Bazant, M. S. Kilic, B. D. Storey, and A. Ajdari. Towards an understanding of induced-charge electrokinetics at large applied voltages in concentrated solutions. *Adv. Colloid Interface Sci.*, 152:48, 2009.

[5] M. Z. Bazant and T. M. Squires. Induced-charge electrokinetic phenomena: Theory and microfluidic applications. *Phys. Rev. Lett.*, 92(3):066101, 2004.

[6] M. Z. Bazant, K. Thrnton, and A. Ajdari. Induced-charge electrokinetic phenomena: Theory and microfluidic applications. *Phys. Rev. E*, 70:021506, 2004.

[7] M.Z. Bazant and Y. Ben. Theoretical prediction of fast 3d ac electro-osmotic pumps. *Lab on a Chip*, 6:1455, 2006.

[8] M. Bőhmer. In situ observation of 2-dimensional clustering during electrophoretic deposition. *Langmuir*, 12:5747, 1996.

[9] J. Bockris, A. Reddy, and M. Gamboa-Aldecd. *Modern Electrochemistry 2A: Fundamentals of Electrics*. Springer, 2001.

[10] D.A. Boy and B.D. Strey. Electrohydrodynamic instabilities in microchannels with time periodic forcing. *Phys. Rev. E*, 76:026304, 2007.

[11] J.F. Brady. Stokesian dynamics. *Annu. Rev. Fluid Mech.*, 20:111, 1988.

[12] C.A. Brebbia and M.S. Ingber, editors. *Boundary element technology VII*. Computational Mechanics Publications Southampton, 1992.

[13] C.A. Brebbia, J.C.F. Telles, and L.C. Wrobel. *Boundary Element Techniques (Theory and Application in Engineering)*. Springer-Verlag Berlin Heidelberg New York Tokyo, 1984.

[14] H. Brenner. The Stokes resistance of an arbitrary particle – IV Arbitrary fields of flow. *Chem. Eng. Sci.*, 19:703–727, 1964.

[15] A.B.D. Brown, C.G. Smith, and A.R. Rennie. Pumping of water with ac electric fields applied to asymmetric pairs of microelectrodes. *Phys. Rev. E*, 63:016305, 2000.

[16] D. Burch and M. Z. Bazant. Design principle for improved three-dimensional ac electro-osmotic pumps. *Phys. Rev. E*, 77:R055303, 2008.

[17] D. Burch and M. Z. Bazant. Design principle for improved three-dimensional ac electro-osmotic pumps. *Phys. Rev. E*, 77:R055303, 2008.

[18] J. E. Butler and E. S. G. Shaqfeh. Dynamic simulations of the inhomogeneous sedimentation of rigid fibres. *J. Fluid Mech.*, 468:205–237, 2002.

[19] H. Chen and J. Meiners. Topologic mixing on a microfluidic chip. *Appl. Phys. Lett.*, 84:2193, 2004.

[20] K. T. Chu and M. Z. Bazant. Nonlinear electrochemical relaxation around conductors. *Phys. Rev. E*, 74:011501, 2006.

[21] I. L. Claeys. Suspensions of prolate spheroids in Stokes flow. 3. Hydrodynamic transport properties of crystalline dispersions. *J. Fluid Mech.*, 251:479–500, 1993.

[22] I. L. Claeys and J. F. Brady. Suspensions of prolate spheroids in Stokes flow. 2. Statistically homogeneous dispersions. *J. Fluid Mech.*, 251:443–477, 1993.

[23] I. L. Claeys and J. Fluid Brady. Suspensions of prolate spheroids in Stokes flow. 1. Dynamics of a finite number of particles in an unbounded fluid. *J. Fluid Mech.*, 251:411–442, 1993.

[24] S.S. Dukhin. Non-equilibrium electric surface phenomena. *Adv. Colloid Interface Sci.*, 44:1, 1993.

[25] L. J. Durlofsky and J. F. Brady. Dynamic simulation of bounded suspensions of hydrodynamically interacting particles. *J. Fluid Mech.*, 200:36–67, 1989.

[26] M. C. Fair and J. L. Anderson. Electrophoresis of non-uniformly charged ellipsoidal particles. *J. Colloid Interface Sci.*, 127(2):388, 1989.

[27] R. P. Feynman. There's Plenty of Room at the Bottom. *J. Microelectromechanical Systems*, 1(1):60, 1992.

[28] Z.R. Gagnan and H.-C. Chang. Electrothermal ac electro-osmosis. *Appl. Phys. Lett.*, 94:024101, 2009.

[29] N. I. Gamayunov, V. A. Murtsovkin, and A. S. Dukhin. Pair interaction of particles in electric-field. 1. features of hydrodynamic interaction of polarized particles. *Colloid J. USSR*, 48:197–203, 1986.

[30] S. Gangwal, O. J. Cayre, M. Z. Bazant, and O.D. Velev. Induced-charge electrophoresis of metallodielectric particles. *Phys. Rev. Lett.*, 100:058302, 2008.

[31] M. Giona, S. Cerbelli, and A. Adrover. Geometry of reaction interfaces in chaotic flows. *Phys. Rev. Lett.*, 88:024501, 2002.

[32] I. Glasgow and N. Aubry. Enhancement of microfluidic mixing using time pulsing. *Lab on a Chip*, 3:114, 2003.

[33] I. Glasgow, J. Batton, and N. Aubry. Electroosmotic mixing in microchannels. *Lab on a Chip*, 4:558, 2004.

[34] A. Gonzalez, A. Ramos, N. G. Green, A. Castellanos, and H. Morgan. Fluid flow induced by nonuniform ac electric fields in electrolytes on microelectrodes. ii.?a linear double-layer analysis. *Phys. Rev. E*, 61:4019, 2000.

[35] T. C. Halsey and W. Toor. Structure of electrorheological fluids. *Phys. Rev. Lett.*, 65:2820, 1990.

[36] H.Aref. Stirring by chaotic advection. *J. Fluid Mech.*, 143:1, 1984.

[37] C.K. Harnett, J. Templeton, K.A. Dunphy-Gazman, Y.M. Senousy, and M.P. Kanouff. Model based design of a microfluidic mixer driven by induced charge electroosmosis. *Lab. Chip*, 8:565, 2008.

[38] K. D. Hermanson, S. O. Lumsdon, J. P. Williams, E. W. Kaler, and O. D. Velev. Dielectrophoretic assembly of electrically functional microwires from nanoparticle suspensions. *Science*, 294:1082, 2001.

[39] C.-C. Huang, M.Z. Bazant, and T. Thorsen. Ultrafast high-pressure ac electroosmotic pumps for portable biomedical microfluidics. *Lab on a Chip*, 10:80, 2009.

[40] G. B. Jeffery. The motion of ellipsoidal particles immersed in a viscous fluid. *Proc. Roy. Soc. Lond. Series A*, 102(715):161–179, 1922.

[41] H.-R. Jiang, N. Yoshinaga, and M. Sano. Active motion of a janus particle by self-thermophoresis in a defocused laser beam. *Phys. Rev. Lett.*, 105:268302, 2010.

[42] E.P. Kartalov and S.R. Quake. Microfluidic device reads up to four consecutive base pairs in DNA sequencing-by-synthesis. *Nucleic Acids Research*, 32(9):2873, 2004.

[43] H. J. Keh, K. D. Horig, and J. Kuo. Boundary effects on electrophoresis of colloidal cylinders. *J. Fluid Mech.*, 231:211, 1991.

[44] M. S. Kilic, M. Z. Bazant, and A. Ajdari. Steric effects in the dynamics of electrolytes at large applied voltages. i. double-layer charging. *Phys. Rev. E*, 75:021502, 2007.

[45] M. S. Kilic, M. Z. Bazant, and A. Ajdari. Steric effects in the dynamics of electrolytes at large applied voltages. ii. modified poisson-nernst-planck equations. *Phys. Rev. E*, 75:021503, 2007.

[46] H. J. Kim and A. Beskok. Quantification of chaotic strength and mixing in a micro fluidic system. *J. Micromech. Microeng.*, 17:2197, 2007.

[47] S. Kirkpatrick. Percolation and Conduction. *Rev.Mod.Phys.*, 45(4):574, 1973.

[48] H. Lamb. *Hydrodynamics*. Cambridge University Press, 6th edition edition, 1993.

[49] D. Lastochkin, R. Zhou, P. Wang, Y. Ben, and H.-C. Chang. Electrokinetic micropump and micromixer design based on ac faradaic polarization. *J. Appl. Phys.*, 96:1730, 2004.

[50] C. D. Meinhart, S. T. Wereley, and J. G. Santiago. A piv algorithm for estimating time-averaged velocity fields. *J. Fluids Eng.*, 122:289, 2000.

[51] J. Melin and S.R. Quake. Microfluidic large-scale integration: The evolution of design rules for biological automation. *Annu. Rev. Bioophys. Biomol. Struct.*, 36:213, 2007.

[52] R.J. Messinger and T.M. Squires. Suppression of electro-osmotic flow by surface roughness. *Phys. Rev. Lett.*, 105:144503, 2010.

[53] N.A. Mishchuk and P.V. Takhistov. Electroosmosis of the second kind. *Colloids Surf. A*, 95:119, 1995.

[54] V. A. Murtsovkin. Nonlinear flows near polarized disperse particles. *Colloid J.*, 58:341–349, 1996.

[55] V.A. Murtsovkin, G.I. Mantrov, and A.S. Dukhin. Study of flows in the neighborhood of a drop of mercury with the application of a variable external electric field. *Colloid J. USSR*, 53:240–4, 1991.

[56] F. Nadal, F. Argoul, P. Hanusse, B. Pouligny, and A. Ajdari. Electrically induced interactions between colloidal particles in the vicinity of a conducting plane. *Phys. Rev. E*, 65:061409, 2002.

[57] L.H. Olesen, H. Bruus, and A. Ajdari. ac electrokinetic micropumps: The effect of geometrical confinement, faradaic current injection, and nonlinear surface capacitance. *Phys. Rev. E*, 73:056313, 2006.

[58] A. J. Pascall and T. M. Squires. Induced charge electro-osmosis over controllably contaminated electrodes. *Phys. Rev. Lett.*, 104:088301, 2010.

[59] N.A. Patankar and H.H. Hu. Numerical simulation of electroosmotic flow. *Anal. Chem.*, 70(9):1870, 1998.

[60] H. A. Pohl. The motion and precipitation of suspensoids in divergent electric fields. *J. Appl. Phys.*, 22:869, 1951.

[61] H. Power and L. C. Wrobel. *Boundary Integral Methods in Fluid Mechanics*. Computation Mechanics Publications Southampton Boston, 1995.

[62] C. Pozrikidis. *Boundary integral and singularity methods for linearized viscous flow*. Cambridge University Press, 1992.

[63] C. Pozrikidis. The motion of particles in the Hele-Show cell. *J.Fluid Mech.*, 261:192, 1994.

[64] C. Pozrikidis. *Introduction to theoretical and computational fluid dynamics*. Oxford University Press, 1997.

[65] C. Pozrikidis. Orbiting motion of a freely suspended spheroid near a plane wall. *J. Fluid Mecha.*, 541:105 – 14, 2005.

[66] A. Ramos, A. Gonzalez, A. Castellanos, N. G. Green, and H. Morgan. Pumping of liquids with ac voltages applied to asymmetric pairs of microelectrodes. *Phys. Rev. E*, 67:056302, 2003.

[67] A. Ramos, H. Morgan, N. G. Green, and A. Castellanos. Ac electric-field-induced fluid flow in microelectrodes. *Journal of Colloid and Interface Science*, 217:420, 1999.

[68] W. D. Ristenpart, I. A. Aksay, and D. A. Saville. Assembly of colloidal aggregates by electrohydrodynamic flow: Kinetic experiments and scaling analysis. *Phys. Rev. E*, 69:021405, 2004.

[69] K. A. Rose, B. Hoffman, D. Saintillan, and J. G. Santiago E. S. G. Shaqfeh. Hydrodynamic interactions in metal rodlike-particle suspensions due to induced charge electroosmosis. *Phys. Rev. E*, 79:011402, 2009.

[70] K. A. Rose, J. A. Meier, G. M. Dougherty, and J. G. Santiago. Rotational electrophoresis of striped metallic microrods. *Phys. Rev. E*, 75:011503, 2007.

[71] D. Saintillan, E. Darve, and E. S. G. Shaqfeh. A smooth particle-mesh ewald algorithm for stokes suspension simulations: the sedimentation of fibers. *Phys. Fluids*, 17(3):033301–1–21, 2005.

[72] D. Saintillan, E. Darve, and E. S. G. Shaqfeh. Hydrodynamic interactions in the induced-charge electrophoresis of colloidal rod dispersions. *J. Fluid Mecha.*, 2006. In press.

[73] D. Saintillan, E. Darve, and E. S.G. Shaqfeh. Induced-charge electrophoresis in suspensions of rodlike particles: Theory and simulations. *American Society of Mechanical Engineers, Fluids Engineering Division*, 261 FED:251–256, 2005.

[74] D. Saintillan, E. Darve, and E. S.G. Shaqfeh. Microstructure in the sedimentation of anisotropic and deformable particles. *American Society of Mechanical Engineers, Fluids Engineering Division (Publication) FED*, 261:797–803, 2005.

[75] D. Saintillan, E. Darve, and S. G. Shaqfeh. Hydrodynamic interactions in the induced-charge electrophoresis of colloidal rod dispersions. *J. Fluid Mech.*, 563:223, 2006.

[76] D. Saintillan, E. S. G. Shaqfeh, and E. Darve. Effect of flexibility on the shear-induced migration of short-chain polymers in parabolic channel flow. *J. Fluid Mecha.*, 557:297 – 306, 2006.

[77] D. Saintillan, E. S. G. Shaqfeh, and E. Darve. The growth of concentration fluctuations in dilute dispersions of orientable and deformable particles under sedimentation. *J. Fluid Mecha.*, 553:347–388, 2006.

[78] D. Saintillan, E. S.G. Shaqfeh, and E. Darve. Concentration fluctuations in dilute suspensions of orientable and deformable particles under sedimentation. *AIChE Annual Meeting, Conference Proceedings*, pages 1058–1058, 2005.

[79] T.S. Simonova, V.N. Shilov, and O.A. Shramko. Low-frequency dielectrophoresis and the polarization interaction of uncharged spherical particles with an induced debye atmosphere of arbitrary thickness. *Colloid J.*, 63:108, 2001.

[80] W. R. Smythe. *Static and Dynamic Electricity (see section 4.262).* McGraw-Hill Inc., 1968.

[81] M.V. Soestbergen, P.M. Biesheuvel, and M.Z. Bazant. Diffuse-charge effects on the transient response of electrochemical cells. *Phys. Rev. E*, 81:021503, 2010.

[82] T. M. Squires. Induced-charge electro-kinetics: fundamental challenges and opportunities. *Lab. Chip*, 9:2477, 2009.

[83] T. M. Squires and M. Z. Bazant. Induced-charge electro-osmosis. *J. Fluid Mech.*, 509:217, 2004.

[84] T. M. Squires and M. Z. Bazant. Breaking symmetries in induced-charge electro-osmosis and electrophoresis. *J. Fluid Mech.*, 560:65, 2006.

[85] T.M. Squires and S.R. Quake. Microfluidics: Fluid physics at the nanoliter scale. *Rev.Mod.Phys.*, 77(3):977, 2005.

[86] M. E. Staben, A. Z. Zinchenko, and R. H. Davis. Motion of a particle between two parallel plane walls in low-Reynolds-number Poiseuille flow. *Phys. Fluids*, 15(6):1711–1733, 2003.

[87] M. E. Staben, A. Z. Zinchenko, and R. H. Davis. Dynamic simulation of spheroid motion between two parallel plane walls in low-Reynolds-number Poiseuille flow. *J. Fluid Mecha.*, 553:187–226, 2006.

[88] D. Stauffer and A. Aharony. *Introduction to Percolation Theory*. Taylor and Francis, London, 1992.

[89] B. Stoeber, D. Liepmann, and S.J. Muller. Strategy for active mixing in microdevices. *Phys. Rev. E*, 75:066314, 2007.

[90] B. Storey, L. R. Edwards, M. S. Kilic, and M. Z. Bazant. Steric effects on ac electro-osmosis in dilute electrolytes. *Phys. Rev. E*, 77:036317, 2008.

[91] A. D. Strooc, S. K. W. Dertinger, A. Ajdari, I. Mezic, H. A. Stone, and G. M. Whitesides. Chaotic mixer for microchannels. *Science*, 295:647, 2002.

[92] H. Sugioka. Suppression of reverse flows in pumping by induced-charge electro-osmosis using asymmetrically stacked elliptical metal posts. *Phys. Rev. E*, 78:057301, 2008.

[93] H. Sugioka. Microcolumn formation between electrodes in a narrow channel from metallic colloidal suspension through induced-charge electrophoresis. *Phys. Rev. E*, 80:016315, 2009.

[94] H. Sugioka. Chaotic mixer using electro-osmosis at finite peclet number. *Phys. Rev. E*, 81:036306, 2010.

[95] H. Sugioka. High-speed rotary microvalves in water using hydrodynamic force due to induced-charge electrophoresis. *Phys. Rev. E*, 81:036301, 2010.

[96] M. Trau, S. Sankaran, D. A. Saville, and I. A. Aksay. Electric-field-induced pattern formation in colloidal dispersions. *Nature*, 374:437, 1994.

[97] J. P. Urbanski, T. Thorsen, J. A. Levian, and M. Z. Bazant. Fast ac electro-osmotic micropumps with nonplanar electrodes. *Appl. Phys. Lett.*, 89:143508, 2006.

[98] C. Wang, L. Taherabadi, G. Jia, M. Madou, Y. Yeh, and B. Dunn. C-mems for the manufacture of 3d microbatteries. *Electrochem. Solid-State Lett.*, 7:A435, 2004.

[99] E. R. Weeks and H. L. Swinney. Anomalous diffusion resulting from strongly asymmetric random walks. *Phys. Rev. E*, 57:4915, 1998.

[100] S. Weinbaum, P. Gantos, and Z. Yan. Numerical multi-pole and boundary integral equation techniques in Stokes flow. *Annu. Rev. Fluid Mech.*, 22:275, 1990.

[101] G. M. Whitesides and B. Grzybowski. Self-assembly at all scales. *Science*, 295:2418, 2002.

[102] S. Yao, A. M. Myers, J. D. Posner, K. A. Rose, and J. G. Santiago. Electroosmotic pumps and their applications in microfluidic systems. *J. Microelectromech. Syst.*, 15:717, 2006.

[103] J. Zhang, G. He, and F. Liu. Electro-osmotic flow and mixing in heterogeneous microchannels. *Phys. Rev. E*, 73:056305, 2006.

[104] H. Zhao and H. Bau. On the effect of induced electro-osmosis on a cylindrical particle next to a surface. *Langmuir*, 23:4053, 2007.

[105] H. Zhao and H.H. Bau. Microfluidic chaotic stirrer utilizing induced-charge electro-osmosis. *Phys. Rev. E*, 75:066217, 2007.